AECL EACL

AECL-11249, COG-95-06

A Methodology to Analyze the Creep Behaviour of Nuclear Fuel Waste Containers

Méthode d'analyse du comportement au fluage des conteneurs de déchets de combustible nucléaire

R. Dutton

December 1995 décembre

AECL

A METHODOLOGY TO ANALYZE THE CREEP BEHAVIOUR OF NUCLEAR FUEL WASTE CONTAINERS

by

R. Dutton

Whiteshell Laboratories
Pinawa, Manitoba R0E 1L0
1995

AECL-11249
COG-95-06

A METHODOLOGY TO ANALYZE THE CREEP BEHAVIOUR OF NUCLEAR FUEL WASTE CONTAINERS

by

R. Dutton

ABSTRACT

The concept for the disposal of used-fuel waste from CANDU reactors operating in Canada comprises a system of natural and engineered barriers surrounding the waste in a mined vault situated at a depth of 500 - 1000 m in plutonic rock of the Canadian Shield. The fuel would be packaged in a highly durable metal container, within a matrix of compacted particulate. The design of the container takes into account that it would be subjected to an external hydrostatic pressure. Consideration of the rate of radioactive decay of the radionuclides contained in the fuel, suggests that the lifetime of the container should be at least 500 years. Consequently, the role of creep deformation, and the possibility of creep rupture of the container shell, must be included in the assessment of time-dependent mechanical integrity.

This report describes an analytical approach that can be used to quantify the long-term creep properties of the container material and facilitate the engineering design. The overall objective is to formulate a constitutive creep equation that provides the required input for a finite element computer model being developed to analyze the elastic-plastic behaviour of the container. Alternative forms of such equations are reviewed. It is shown that the capability of many of these equations to extrapolate over long time scales is limited by their empirical nature. Thus, the recommended equation is based on current mechanistic understanding of creep deformation and creep rupture. The pertinent mechanisms are described. It is shown that the qualitative and quantitative characteristics of these mechanisms are conveniently captured by Deformation Mechanism Maps and Fracture Mechanism Maps. These offer a guide for the design of laboratory creep tests and the extrapolation of the experimental data. Based on this mechanistic underpinning, the selected constitutive equation derives from the θ Projection Concept. The theoretical and experimental background of this concept is reviewed. Examples are described where the four characteristic θ-parameters have been used to predict the long-term creep behaviour of a number of materials. The practical success of such projections, and their established scientific base, has resulted in the widespread acceptance of the technique. Consequently, we present an analytical scheme that adopts the θ Projection Concept for the interpolation of experimental creep data and long-term prediction of creep behaviour. A criterion for determining the onset of material failure by creep rupture, that could be used in the design of containers with extended structural integrity, is proposed. Interpretation and extrapolation will be supported by the complementary Deformation and Fracture Mechanism Maps.

AECL
Whiteshell Laboratories
Pinawa, Manitoba R0E 1L0
1995

AECL-11249
COG-95-06

MÉTHODE D'ANALYSE DU COMPORTEMENT AU FLUAGE DES CONTENEURS DE DÉCHETS DE COMBUSTIBLE NUCLÉAIRE

par

R. Dutton

RÉSUMÉ

Le concept de stockage permanent des déchets de combustible irradié des réacteurs CANDU en exploitation au Canada comprend un système de barrières naturelles et artificielles entourant les déchets placés dans une enceinte creusée à une profondeur de 500 à 1 000 m dans la roche plutonique du Bouclier canadien. Le combustible y serait conditionné dans un conteneur métallique extrêmement durable, dans une matrice de particules compactées. La conception du conteneur tient compte du fait qu'il serait soumis à une pression hydrostatique externe. En tenant compte du taux de décroissance radioactive des radionucléides contenus dans le combustible, on peut avancer que la durée de vie du conteneur serait d'au moins 500 ans. En conséquence, le rôle de la déformation de fluage ainsi que la possibilité d'une rupture par contrainte de fluage de l'enveloppe du conteneur doivent faire partie de l'évaluation de l'intégrité mécanique en fonction du temps.

Le présent rapport décrit une méthode analytique pouvant servir à quantifier les propriétés de fluage sur de longues périodes du matériau de fabrication du conteneur et à faciliter les études techniques. L'objectif global est de formuler une équation constitutive du fluage qui fournit les données nécessaires à l'utilisation d'un modèle informatique d'analyse par éléments finis élaboré en vue d'étudier le comportement plastique-élastique du conteneur. On y fait une étude des variantes de ces formes d'équations. On y montre que, pour un grand nombre de ces équations, les capacités d'extrapolation sur de longues échelles de temps sont restreintes en raison de leur caractère empirique. En conséquence, l'équation recommandée est fondée sur les connaissances mécanistes actuelles de la déformation et de la rupture de fluage. On décrit également les mécanismes pertinents. On indique que les caractéristiques qualitatives et quantitatives de ces mécanismes sont représentées de façon très pratique à l'aide de cartes des mécanismes de déformation ou de cartes des mécanismes de fracture. Ces tables de correspondances servent de guide pour la conception d'essais de fluage en laboratoire ou l'extrapolation des données expérimentales. L'équation constitutive choisie, fondée sur ces principes mécanistes, découle du concept de projection θ. Le cadre expérimental et théorique de ce concept y est analysé. On y donne des exemples dans lesquels les quatre paramètres θ caractéristiques ont été employés afin de prévoir le comportement au fluage sur de longues périodes d'un certain nombre de matériaux. Les succès pratiques de telles projections, joints à leur fondement scientifique bien établi, ont entraîné l'acceptation de cette technique de façon très générale. En conséquence, nous présentons une théorie analytique dans laquelle nous adoptons le concept de projection θ aux fins de l'interpolation des données expérimentales de fluage et des prévisions à long terme du comportement au fluage. On y propose un critère de détermination du seuil de défaillance du matériau par rupture de fluage qui pourrait être utilisé dans la conception de conteneurs caractérisés par une résistance structurelle prolongée. Les cartes des mécanismes de déformation et de fracture complémentaires seront fournies à l'appui des interprétations et des extrapolations.

EACL
Laboratoires de Whiteshell
Pinawa (Manitoba) R0E 1L0
1995

AECL-11249
COG-95-06

CONTENTS

continued ...

CONTENTS (concluded)

LIST OF SYMBOLS USED IN TEXT

a, b, c	Material creep constants
A, B	Material creep constants
α, β, γ	Material creep constants
a	Area of slip plane swept out by a dislocation
a_c	Spacing between grain-boundary cavities
A	Specimen cross-sectional area
b	Dislocation Burger's vector
C	Vacancy concentration
C_o	Equilibrium vacancy concentration
C_b	Vacancy concentration in grain boundary
C_c	Vacancy concentration adjacent to grain-boundary cavity
d	Grain size (average diameter)
D	Diffusion coefficient
D_o	Diffusional constant
D_{SD}	Self-diffusion coefficient
D_{GB}	Grain-boundary diffusion coefficient
δ	Grain-boundary width
E	Young's modulus
ε	Creep strain
$\dot{\varepsilon}_s$	Steady-state secondary creep rate
$\dot{\varepsilon}_m$	Minimum creep rate

$\dot{\varepsilon}_p$	Primary creep rate
$\dot{\varepsilon}_t$	Tertiary creep rate
ε_p	Primary creep strain
ε_t	Tertiary creep strain
ε_r	Strain to rupture
ε_m	Monkman-Grant constant ($= \dot{\varepsilon}_s t_r$)
γ	Surface energy
G	Shear modulus
G_1, G_2, G_3, G_4	Constants
H_1, H_2, H_3, H_4	Constants
h	Work-hardening rate
k	Boltzmann's constant
K_1, K_2	Diffusional creep-rate constants
L	Load on creep specimen
λ	Constant ($= \varepsilon_r/\varepsilon_m$)
n	Creep-rate stress dependence
ω	Creep-damage parameter
Ω	Atomic volume
P_1, P_2	Stress-rupture correlation parameter
q	Dislocation obstacle activation energy
Q	Activation energy
Q_c	Activation energy for creep
Q_{SD}	Activation energy for self diffusion
Q_{GB}	Activation energy for grain-boundary diffusion

Q_p	Activation energy for dislocation-pipe diffusion
r	Rate of recovery
r	Grain-boundary cavity radius
σ	Stress
σ_Y	Yield stress
t	Time
t_r	Time to rupture
t_m	Time to reach minimum creep rate
t_i	Time to onset of tertiary creep
T	Temperature
θ_1, θ_2, θ_3, θ_4	Parameters of the θ Projection Concept
x	Specimen gauge length

1. INTRODUCTION

Since 1978, Atomic Energy of Canada Limited and Ontario Hydro have conducted a joint R&D program to evaluate concepts for the safe storage, transportation and disposal of Canada's nuclear fuel waste (AECL 1994). In the disposal concept, used fuel from CANDU reactors, in the form of multi-element cylindrical bundles, 500 mm long and 100 mm in diameter (Figure 1), would be placed in corrosion-resistant containers and deposited in a deep underground vault excavated to a depth of 500 - 1000 m in a plutonic rock formation. Potentially suitable rock bodies for vault construction occur within the Canadian Shield. One possible disposal-vault design is shown in Figure 2.

Based on an analysis presented by Johnson et al. (1994), the target period for which the container shell must provide full isolation has been set at a minimum of 500 years. Consequently, the choice of the material, and its thickness, to be used for the container shell must recognize the demand for assured durability over such time scales. In particular, sufficient corrosion resistance must be provided, taking into account that the container will be exposed to saline groundwater which, for a vault constructed at a depth of 1000 m, would impose a hydrostatic pressure of ~10 MPa on the container. Swelling of the clay-based buffer material that will be used to surround the container could impose an additional hydrostatic pressure of 1 - 2.5 MPa. The heat production accompanying radioactive decay is an additional factor, contributing to the ambient temperature of the vault. By specifying the design of the container and the density of container emplacement within the vault, a maximum temperature of $\leq$100°C has been prescribed for the container-shell material.

The selection of materials for the waste container has been based on an extensive investigation of comparative corrosion properties of metals suitable for container construction (Johnson et al. 1994). Attention has also been directed toward the structural behaviour of the container under hydrostatic pressure. To this end, short-term structural-performance tests have been conducted on full-scale container prototypes, using hydrostatic test facilities. Stress analyses of candidate container designs under loading have been conducted using elastic-plastic finite difference and finite element computer programs. Such information has been used to assess the mechanical integrity of the structural shell and has been compared to the measured response of the prototype during testing. The nature of these tests placed emphasis on the short-term mechanical properties of the container material.

In recognition of the required long service lifetime of the container, an R&D program has been initiated to examine the longer-term structural response of container designs during disposal. Thus, extensive materials creep testing is underway, and a finite element structural analysis computer program has been developed to take into account time-dependent plastic deformation. With a timescale of 500 years minimum, it is evident that materials creep data obtained from laboratory testing will have to be extrapolated to service lifetimes and beyond. In particular, the potential for container failure by creep rupture must be assessed. This report describes an analytical methodology proposed for the extrapolation of creep behaviour and suggests a criterion for determining the onset of material failure by creep rupture that could be used in the engineering design of containers to ensure their continued structural integrity for whatever target lifetime is selected.

2. BACKGROUND INFORMATION

2.1 CONTAINER DESIGN

Various designs of fuel-waste containers have been considered (Crosthwaite 1994). The design selected for the safety analysis of the operation of a used-fuel disposal facility was the packed-particulate container consisting of a cylindrical containment shell, 2?46 mm long and 633 mm in diameter with a wall thickness of 6.35 mm, constructed from welded ASTM Grade 2 titanium plate (Figure 3). Positioned within the container is a concentric array of 19 tubes, to act as a fuel-bundle retaining basket, which would be constructed from a material such as carbon steel. The central tube, which is thicker-walled, serves as a lifting and handling device and contains no fuel bundles. Each of the outer 18 tubes (108 mm O.D. with 3.2 mm wall thickness) are designed to accept a stack of 4 fuel bundles; thus, the container can accommodate a total of 72 used CANDU bundles. This container configuration is designed for emplacement in boreholes as shown in Figure 2. An alternative design, intended for horizontal emplacement in-room, rather than in boreholes, and constructed of copper rather than titanium, is shown in Figures 4 and 5. In this case, the basket is designed to hold 72 bundles in two levels of 36 bundles.

For both designs, the tubes comprising the fuel basket are open-ended and are not intended to provide structural support to the shell; rather, a compacted particulate matrix is used to provide this internal support. Thus, after the container is loaded with fuel bundles, all residual interstitial space is filled with compacted particulate, facilitated by mechanical vibration of the container assembly. In the design used as the reference for the engineering study for a used-fuel disposal centre, the selected particulate was industrial glass beads of about 1 mm diameter (Simmons and Baumgartner 1994).

Some potential variants of this reference design have been considered. One option, called the structurally supported design, employs the use of a sealed, more rigid internal basket that provides both retention of the used-fuel bundles and a structure to which external pressure loading on the container shell can be transferred through a compacted particulate matrix that surrounds the basket (Figure 6). Another option uses a cast-metal matrix to support the shell (Figure 7). Details of the studies conducted on these and the packed-particulate design, and the reasons for the selection of the latter as the reference for current safety and engineering analyses, are presented in Crosthwaite (1994).

2.2 MATERIALS CHARACTERIZATION

A primary focus of the container-development program has been the requirement for high corrosion durability of the container shell; therefore, a substantial research program has been conducted to evaluate the corrosion behaviour of candidate container-shell materials (Johnson et al. 1994). Taking into account the ambient chemistry associated with Canadian Shield geology, ASTM Grades 2, 12 and 16 titanium and oxygen-free copper have been selected as the most promising candidates. Titanium is a "corrosion-resistant" material, its very low corrosion rate resulting from the presence of an adherent, highly protective, surface oxide. Copper belongs to the class of "corrosion-allowance" materials that corrode slowly, but predictably: a wall thickness of about 25 mm would be required. For the reference case study for the environmental impact assessment for the Canadian Nuclear Fuel Wast Management Program, the container was designed with a shell constructed of ASTM Grade 2 titanium.

Corrosion rates measured under a variety of relevant chemistry conditions show that a 6.35-mm-thick titanium shell would not fail by penetration due to material degradation until after about 1000 - 7000 years. However, to minimize the possibility of accelerated crevice corrosion, it has been judged that the container-surface temperature should be limited to 100°C.

Grade 2 titanium is a commercially pure (~99%) product. As such, its primary constituent is the hexagonal close-packed α-phase. However, the presence of β-stabilizing trace elements (in particular, iron) causes a minor amount of the body-centred cubic β-phase to be retained at room temperature, present as an intergranular second phase. The trace elements also confer additional strength, mainly through the interstitial species such as oxygen, nitrogen and carbon. Such strengthening effects are significant at temperatures below 300°C (Conrad 1981). Grade 12 titanium is an alloy containing small quantities of molybdenum and nickel: these increase the strength and corrosion resistance of the material. The Grade 16 material contains a small amount of palladium, which increases the corrosion resistance even further. Similar to Grade 2, Grades 12 and 16 are mainly α-phase with minor fractions of residual β-phase.

2.3 MECHANICAL TESTING AND ANALYSIS

The reestablishment of the water table in the vault at a depth of 1000 m would create a hydrostatic pressure of about 10 MPa on the shell of the waste container. An additional pressure of up to 2.5 MPa could arise from moisture-induced swelling of the bentonite-clay mixture used as a buffer to surround the waste container. This material has a low diffusivity for dissolved radionuclides and therefore acts as an effective additional engineered barrier.

Full-scale hydrostatic testing of prototype containers commenced in the early 1980s. The first tests were conducted on the "stressed-shell" concept (Figure 8), where the container shell was designed to sustain the full external pressure, without any internal structural support (Crosthwaite et al. 1982). Using stainless steel as a model material, the required container wall thickness was about 29 mm for a test conducted at 20°C. Hydrostatic testing was carried out in a US facility[1]. The container shell collapsed at a pressure of about 19 MPa, in excellent agreement with an elastic-plastic finite difference analysis.

It was realized that progressive creep deformation of the container could have a significant effect on its long-term structural behaviour and that eventual collapse by creep-buckling might occur at pressures significantly less than the short-term limit of 19 MPa. A creep-buckling analysis was conducted for a titanium stressed-shell container (Hosaluk et al. 1987) by introducing time-dependent deformation into the finite difference computer code. The progressive plastic deformation of the container shell was then calculated by updating the creep strain in prescribed time increments, until the onset of plastic instability. The calculations were verified by using a finite element stress analysis code and an analytical equation based on an assumed out-of-roundness. In all cases, a steady-state creep law was used, where the creep rate ($\dot{\varepsilon}$) is given by

---

[1] At the time this test was conducted, no hydrostatic testing facilities capable of conducting tests on full-scale containers at temperatures and pressures typical of those anticipated during disposal were available in Canada. Later tests were conducted at such conditions following the construction of a facility with the appropriate capabilities at AECL's Whiteshell Laboratories.

$$\dot{\epsilon} = A\left(\frac{\sigma}{\sigma_y}\right)^n \qquad (1)$$

where A and n are constants, σ is the applied stress and σ_y is the short-term yield stress of the material, at the appropriate temperature. This equation (see Section 4.3 for further discussion of similar power-law equations) was fitted to published creep data on commercially pure titanium (Kiessel and Sinnott 1953). A sensitivity analysis showed that the time to reach plastic instability of the shell (buckling) was strongly dependent on the creep rate: a factor of 5 increase in creep rate reduced the time to buckling by about two orders of magnitude. This highlighted the need for accurate predictions of creep behaviour.

From the analysis of Hosaluk et al. (1987), it was concluded that for a Grade 2 titanium, stressed-shell design container, a minimum wall thickness of ~70 mm would be required for creep buckling to be avoided for a 500-year period, at 100°C. Due to anticipated costs and fabrication/inspection difficulties associated with a 70-mm-thick container shell, attention was subsequently focussed on internally supported thinner-shell containers.

In the test sequence performed on a full-scale prototype of the ASTM Grade 2 titanium packed-particulate container, which was conducted at up to 10 MPa at 150°C in AECL's Hydrostatic Test Facility at Whiteshell (Figure 9), the prototype was tested first in its as-received condition; only small deformations of the cylindrical portion of the shell occurred.[2] In two subsequent tests, the container was resubjected to these test conditions after artificial packing defects were introduced by removing some of the particulate. In the first of these tests, 0.2 L was removed; in the second, a further 0.8 L was removed. Although the shell deformed substantially adjacent to the packing voids, it was not breached by rupture or tearing (Teper 1985, 1987a, Teper and Reid 1989). During all tests, shell deformation was recorded by strain gauges attached to the container surface.

An analysis of the structural response of the container during the hydrostatic test was conducted by Teper (1988) in which he employed both linear-elastic and elastic-plastic finite element models. A focus of the analysis was the localized deformation associated with the unsupported void introduced by partial removal of the particulate. With this particulate removed and under hydrostatic testing, plastic strains of 0.062 compressive and 0.044 tensile were predicted. On the basis of a measured tensile ductility of 0.20 strain for titanium under uniaxial test conditions, while taking into account the biaxial stress condition in the container shell, and imposing a safety factor of 2/3, the maximum allowable (i.e., avoiding ductile tearing) tensile strain was calculated to be 0.053. However, this is based on short-term tensile testing results. It will be shown in later sections of this report that tensile ductility can be drastically reduced under long-term creep conditions.

---

[2] During transportation of the prototype from Toronto, where it was constructed, to the Whiteshell Laboratories, the glass-bead particulate within the container appeared to have settled further, causing an ~1% increase in its compacted density. This resulted in a gap forming between the top head and the upper level of the particulate, estimated from test results to have been ~14 mm in height. During an initial, low-pressure test conducted at 1 MPa and 20°C, the top head deformed downward through this gap until it recontacted the particulate. Details are presented in Teper (1988).

An important point highlighted by Teper (1987b, 1988) was that the total volume of the particulate can decrease with time. For example, further packing or settlement of the particulate can occur during container handling or under hydrostatic pressure; volumetric creep of the particulate matrix can occur due to deformation of contacting particles. This could possibly result in significant plastic strain of the container shell. The finite element analysis also demonstrates that non-uniform deformation, especially that associated with the top head and rim of the container, can cause both compressive and tensile strains to develop.

Limited creep tests have been conducted on a range of particulate materials (Teper 1987b). These were done by compressing a column of particulate contained in an open-ended cylinder with a loaded piston. At 150°C, the total creep strain for glass beads (measured as a function of the decrease in height of the glass-bead column) was about 10^{-4} after 700 h. It was not possible to determine whether the creep occurred by particle rearrangement, particle cracking, or particle plasticity. The problem with this experimental technique is the complex (and unknown) stress pattern produced in the particulate body due to boundary effects at the interface with the confining cylinder wall. Consequently, it is difficult to extract the intrinsic creep properties of the particulate. Studies are currently underway, using soils properties measurement techniques, to determine more accurately the short- and long-term mechanical properties of compacted glass beads.

3. THE ROLE OF CREEP DEFORMATION

3.1 GENERAL CONSIDERATIONS

As indicated above, both the container shell and the particulate can undergo creep deformation. Thus, the creep properties of <u>both</u> components are relevant to the overall time-dependent deformation of the container assembly. It will be apparent from the mechanical interaction between the particulate and the shell that the rate of deformation of the container will largely be determined by the creep properties of the particulate. Exceptions will be isolated areas of the container shell that are not adequately supported because of incomplete, or inhomogeneous, packing of the particulate. It is to be expected that such regions are more likely to exist in the uppermost section of the container, where settling of the particulate might create an empty void.

For containers fully supported by the particulate, the creep rate of the container shell will essentially be controlled by the volumetric creep rate of the particulate. Under these circumstances, the mechanical stress in the shell wall will be equal to the flow stress required to sustain such a creep rate. To enable such stresses and the accumulated creep strains of the container shell to be predicted, a finite element stress/strain computer program must be developed. This is being done (Rigby 1994 and Teper 1990).

The creep properties of both the container-shell material and the particulate will be required as input into the finite element model. However, laboratory-produced creep data are constrained to relatively short times (up to several years), compared with the design lifetime (~500 years) of the container. This temporal limitation requires a reliable method for extrapolating the experimental data by a factor of at least 100. Furthermore, the format of the projection methodology must serve several related purposes:

- analysis of the experimental data,
- analysis of medium-term hydrostatic testing of scale-model containers,
- extrapolation of the experimental data to long-term practical conditions,
- providing input, in suitable form, to finite element models, and
- facilitating the final design of the container.

To this end, this report will review the extant analytical tools that have been developed to accomplish such interpolation and extrapolation. From this, recommendations will be made on the most suitable methodology. Such judgement will take into account the minimum 500-year time scale, recognizing that such long-term projection is unprecedented in conventional engineering design (although there are examples of retroactive historical creep analyses covering time periods measured in centuries). Furthermore, the proposed methodology will address the fact that the imposed low creep rate of the container materials places the creep-deformation processes in an envelope of low stress and low temperature. In contrast, most conventional creep data are obtained at much higher stresses and temperatures. Above all else, the selection of the analytical tools will be guided by the need for scientific rigour in addition to engineering pragmatism. To this end, the methodology will meet the following criteria:

- must have the underpinning of scientific understanding that derives from a knowledge of creep-deformation mechanisms and phenomenology,
- must be well supported and documented in the scientific literature,
- practical application must be well demonstrated and tested, recognizing the more limited timescale of conventional engineering practice,
- must have widespread acceptance in the scientific/engineering community,
- must be able to handle creep strain and creep fracture (see below).

3.2 SPECIFIC PERSPECTIVES

It is useful to place the expected creep behaviour of the container within a perspective frame. To do this, we can assume a reasonably acceptable creep strain of 0.1 being realized over a 1000-year period. This translates to an average creep rate of ~3 x $10^{-12}s^{-1}$. Within a typical engineering context, such a creep rate is relatively low. However, recognizing the low servicee temperature of the container (~ 100°C), it is anticipated that the allowable stress in the container wall will be quite high. The displacement transducers on modern creep machines can detect specimen extensions of 10^{-7} m, i.e., strains of the order of 10^{-6}. Taking into account other testing variables, it is relatively straightforward to discriminate a creep strain of 10^{-3} over a period of one year: this is a strain rate of ~3 x $10^{-11}s^{-1}$. Indeed, measured creep rates within this range are commonly reported in the scientific literature, as shown in Figure 10 (Evans and Wilshire 1985).[3] Within the Canadian nuclear industry, it is of interest to note that the creep rates of CANDU reactor fuel channels are of this order. In addition, current creep tests conducted on the Grade 2 titanium being studied as a candidate container-construction material, are deforming at a rate of ~$10^{-11}s^{-1}$ (J.L. Crosthwaite and G.R. Kasprick, 1994, unpublished data). This means that, as far as these measured creep rates are concerned, we are required to extrapolate experimental data by about an order of magnitude - a fairly modest challenge.

---

[3] A more detailed discussion of Figure 10 is presented in Section 9.

Although the creep rate is an important parameter influencing the lifetime of the container, the time to failure by creep rupture is more crucial. This is the time (or equivalently, the creep strain) required for any internal damage processes to cause the material to fracture. For obvious reasons, this issue focusses on the creep behaviour of the container-shell material, rather than the particulate. Thus, whereas the creep rate of the container shell will largely be controlled by the creep properties of the particulate, it is the intrinsic creep (and creep-rupture) behaviour of the container-shell material that determines its design lifetime.

As we will see below, there is a link between the creep rate and the rupture time. The proposed creep analysis tools must be capable of capturing these linkages. An attractive approach is the formulation of a fracture criterion based on the strain to failure. Then, through the creep rate, the time to failure can be predicted. In this regard, it is important to emphasize that the strain to failure under creep conditions (particularly at low strain rates) can be much less than the tensile ductility measured in a short-term tensile test. Thus, the Swedish work (Henderson et al. 1992) on oxygen-free, high-purity copper being considered for constructing a fuel-waste container shell showed that whereas the strain to failure in short-term tensile tests was as high as 0.6, failure strains of <0.1 resulted under creep conditions. In addition, trace impurities can reduce the creep-rupture strain to <0.01. These low ductilities are a consequence of a change of rupture mechanism. Under short-term tensile conditions, rupture occurs by gradual necking down, or the development of transgranular cracks. In contrast, under creep conditions, cavities and cracks can form on grain boundaries, leading to premature intergranular fracture (Evans and Wilshire 1985).

It will be noticed that the above remarks on creep ductility apply to conditions of tensile stresses. It is true that the hydrostatic pressure conditions in the vault will generally produce compressive stresses in the container shell (and compressive stresses generally suppress fracture processes). However, any localized deformation, for example, that associated with end effects, or shell ovality, will result in bending deformation and therefore tensile stresses. In addition, even under nominally compressive conditions, tensile stresses can develop and produce creep cavitation on grain boundaries parallel to the compressive stress axis (Dutton 1969). The added complexity of creep fracture processes under multiaxial stress states has been described by Dyson (1992). Regardless of the actual condition of stress in the container shell, we shall adopt fracture criteria based on tensile creep test data, with the assurance that this will retain conservativeness.

4. CONVENTIONAL APPROACHES TO PROJECTION OF CREEP DATA

4.1 THE STANDARD CREEP CURVE

Typical forms of creep curves are shown in Figure 11, for the case of "high" temperature and "low" temperature. The distinction between the two is fairly arbitrary, but "high" temperature would conventionally be >0.3 of the melting point (i.e., a homologous temperature of 0.3 T_m, where all temperatures are expressed in degrees Kelvin). For both cases, there will be an

essentially instantaneous strain, ε_o, comprising an elastic and plastic component.[4] Following this, the plastic creep strain will accumulate in a time-dependent fashion.

In the higher-temperature creep regime, after the initial strain on loading, the creep rate decays with time, giving rise to the characteristic "primary" creep stage. An ostensibly constant creep rate is achieved during the "secondary stage", after which the creep rate accelerates during the "tertiary stage" that leads to fracture. The overall effect of increasing stress and increasing temperature (these are normally considered independent variables) is shown in Figures 12 and 13, respectively.

Lower-temperature creep is characterized by a continuously decreasing creep rate, and is often referred to as transient, or logarithmic creep for reasons made apparent in Section 4.2. For most practical purposes, this creep behaviour continues indefinitely (i.e., a protracted primary stage) and fracture does not occur. As creep is a thermally activated process, and occurs at any temperature above absolute zero, the distinction between low-temperature and high-temperature creep becomes rather arbitrary, being a matter of scale. For most high-performance engineering applications at elevated temperatures, materials are operated toward the upper limit of their creep temperature range and for time scales that are measured in years, up to several decades. Laboratory creep testing is therefore conducted in a temperature-stress-time envelope that allows the full expression of the primary-secondary-tertiary-fracture sequence. The "high-temperature" creep behaviour of Figure 11 then becomes the "classic" creep curve. However, as we shall see in Section 6, the underlying mechanisms responsible for creep and fracture can operate throughout the temperature-stress field. At lower temperatures, the (diffusional controlled) kinetics of these processes is slow. Consequently, within the time scale of conventional engineering application, the depiction of the "low-temperature" behaviour in Figure 11 is appropriate and representational. However, for the case of the waste container, although it operates at "low" temperatures (~0.2 T_m and ~0.3 T_m for titanium and copper respectively), its intended service lifetime is far more extended than normally encountered. Although the deformation kinetics are slow, the full expression of the creep-curve shape over very long time periods (~500 years) is of critical importance. In particular, we need to know whether a tertiary creep stage leading to creep rupture will eventually materialize. It would be unjustified to make the a priori assumption that logarithmic creep was the appropriate creep behaviour such that tertiary kinetics and fracture processes could be ignored, unless there was sound theoretical or empirical proof.

The analytical approach presented in this report assumes that the creep behaviour of the container shell will follow the normal three-stage behaviour. In fact, we embrace the long-standing principle that the three-stage creep behaviour is a universal phenomenon displayed by all materials, the temperature of operation solely determining the relative kinetic shape of the creep curve. A key objective will be to predict under what conditions of stress and temperature tertiary creep and fracture would occur, such that a design envelope can be selected to avoid failure of the container shell over its intended lifetime.

---

[4] A plastic component will be present even at quite low stress levels, below the nominal yield stress. This reflects the fact that the elastic limit is exceeded at stresses much lower than the 0.2% offset yield point. The short-term stress-strain curve is quite adequate to predict the value of ε_o as a function of stress.

At this juncture, it is instructive to examine some actual creep data for our intended container materials[5]. The conclusion of Kiessel and Sinnott (1953) following a study of the low temperature (down to room temperature) creep of commercially pure titanium, was "It would seem that second-stage creep becomes active after a relatively short testing time and any further consideration that titanium exhibits chiefly transient creep at room temperature is fallacious". Similarly, the work of Adenstedt (1949) and Luster et al. (1953) showed the full three-stage behaviour in commercial titanium at room temperature, and Evans showed this to be the case even in high strength α (1984) and α-β (1987) titanium alloys. Such alloys were developed for high-temperature creep resistance. It was a surprise to find that the low-temperature creep resistance was so poor, and, in particular, displayed a distinct tertiary stage leading to premature fracture. This is more than an academic curiosity. Such alloys are used in the low-temperature compressor of gas turbine engines. Unanticipated creep fracture failures have resulted.

Low-temperature creep studies on copper (Henderson et al. 1992 and G. Palumbo, 1994, unpublished data) also demonstrated the presence of creep fracture processes typical of the tertiary stage. All of these experiments are relatively short-term (up to several thousand hours) and therefore have been conducted at high stresses to produce high strain rates. Notwithstanding this, we cannot assume that accelerating creep, and creep fracture, will be absent under long-term conditions.

It is significant that the experimental work on titanium, referred to above, reported that the creep resistance was much lower than would be anticipated from a metal with a relatively high melting temperature (1680°C). As titanium transforms from the α-phase (close-packed hexagonal) to the β-phase (body centred cubic) at 880°C, there is some uncertainty as to the significance of the experimentally determined melting point. The measured melting point is that of the β-phase, whereas the creep measurements are performed in the α-phase. The question then arises as to what is the effective melting point of the α-phase? This situation is analogous to that of zirconium (melting point of 1850°C; α-β transformation temperature of 860°C). Whereas it has been suggested that the melting point should be equated to the transformation temperature, Carpenter (1971) has suggested (based on a consideration of diffusional-controlled creep kinetics) that the effective α-phase melting point for zirconium is 1500°C. If we draw a parallel to zirconium, the homologous temperature for creep in titanium at 100°C, could be in the range 0.3 - 0.2 T_m, i.e., approaching the "high-temperature" creep regime.

4.2 MATHEMATICAL REPRESENTATION OF CREEP CURVES

Various attempts have been made to develop constitutive equations that describe the dependence of the creep strain (ε) on time (t), stress (σ) and temperature (T) (Garofalo 1965, Evans and Wilshire 1985). In general, these will be of the form

$$\epsilon = f(\sigma, T, t) \tag{2}$$

---

[5] Creep testing of titanium and copper container materials is currently being conducted by Atomic Energy of Canada Limited and Ontario Hydro Technologies. However, data obtained to date are rather limited.

Under "low-temperature" conditions, it has been found that the strain-time relationship is logarithmic, i.e.,

$$\epsilon = a \log(bt + 1) \tag{3}$$

where a and b are material constants that depend on stress and temperature. The decreasing creep rate is generally explained by a dislocation mechanism controlled by an exhaustion process of decay (see Section 6.3.2).

The proposed container creep analysis method of Teper (1990) assumes that logarithmic creep, and Eqn. (3) applies. In principle, Eqn. (3) predicts that as $t \rightarrow \infty$, the creep strain approaches ∞, without fracture occurring. The concerns and reservations regarding such assumed behaviour were discussed in Section 4.1.

Based on the early classical work of Andrade (1910), power-law time dependencies have been used to describe the three-stage creep behaviour under "high-temperature" conditions:

$$\epsilon = \alpha t^{1/3} + \beta t + \gamma t^{4/3} \tag{4}$$

where α, β and γ are constants, the first term representing the primary stage, the second and third terms representing the secondary and tertiary stages, respectively. A similar equation was developed by Graham and Walles (1955), but with the tertiary stage represented by γt^3. For some materials, it was found that for the primary stage a better fit was obtained by using a $t^{2/3}$, or $t^{1/2}$, law rather than a $t^{1/3}$ law. The equation representing the early stages of the creep curve are then better generalized in the form,

$$\epsilon = \alpha t^p + \beta t \tag{5}$$

with the parameter p varying between zero and unity.

An example of a variant of Eqn. (5) is that due to Conway (1967):

$$\epsilon = \alpha_1 t^{1/3} + \alpha_2 t^{2/3} + \beta t \tag{6}$$

A difficulty with Eqn. (5) and its variants, is that it predicts an infinite creep rate at time zero. This objection is overcome by using an exponential function, rather than a polynomial (Garofalo et al. 1963), thus:

$$\epsilon = \alpha(1 - e^{-\beta t}) + \gamma t \tag{7}$$

where α represents the total primary creep strain and β determines the rate of exhaustion.

Evans and Wilshire (1985) have used a set of experimental creep data to test the curve-fitting capability of polynomial expressions of the form of Eqns. (4), (5) and (6), and the exponential form of Eqn. (7). The latter offered the best fit. Indeed, the derived coefficients of the polynomial expressions varied in an erratic fashion as the creep stress was varied, and even produced irrational negative values.[6]

The attractive features of expressions of the form of Eqn. (7) will be pursued later in this report (see Section 9). However, it must be emphasized that many mathematical forms can be used to fit creep curves with equivalently high accuracy (e.g., higher-order polynomials will provide the required accuracy). From the point of view of extrapolating creep data, the challenge is to find an equation that reflects the physics of the underlying deformation mechanisms, such that the coefficients will properly represent the time, stress and temperature dependencies. This will be a recurring theme of this report.

4.3 EXTRAPOLATION METHODS

Despite the efforts to obtain analytical equations to fit the full creep curve, creep-design and creep-data extrapolation in the engineering domain has centred on the steady-state creep behaviour in the secondary creep stage. No doubt this is partly due to the lack of general agreement on the mathematical forms of the creep-curve equations, together with the uncertainties in handling stress and temperature dependencies of the overall creep shape, particularly in the primary and tertiary creep stages. In addition, it is far easier to use a single-valued constant creep rate in computation, whether this be analytical or numerical.

This is not only a feature of engineering application. Other scientific researchers intent on gaining an understanding of creep mechanisms and developing theoretical models, have also concentrated on steady-state creep. This is partly justified by the reasonable assumption that primary and tertiary creep processes are relatively minor variants of the steady-state deformation mechanism. Also, in terms of the design of experiments, it is easier to measure the separate stress and temperature dependence of the secondary creep rate.

A consequence of the above trend is that most of the creep data published in the literature are simply reported as the secondary stage, steady-state creep rates (plus the stress and temperature dependence). The full creep curves are rarely available; indeed the data representing the primary and tertiary stages are discarded. This is done despite the fact that these data have typically been measured (it is difficult to be confident that steady-state creep has been achieved unless both the primary and tertiary behaviour are recorded).

The temperature dependence of the steady-state creep rate ($\dot{\varepsilon}_s$) is well represented by an Arrhenius equation:

---

[6] For example, the predicted secondary creep rate (the parameter β in Eqns (4), (5) and (6)) was significantly different from the measured value, and β was negative for some values of the stress. This problem can be avoided by measuring the secondary creep rate independently and thus inserting a fixed value of β into the equations. However, with many creep-curve shapes it is difficult to estimate the secondary creep rate with any certainty, hence the other coefficients (α and γ) will be inaccurately determined. This type of problem has been overcome by the curve-fitting procedure discussed in Section 9.

$$\dot{\epsilon}_s \propto \exp-(Q_C/kT) \tag{8}$$

where k is Boltzman's constant. Q_C is the activation energy for creep, recognizing that creep deformation is controlled by a thermally activated process (see Section 6). For the case of pure metals at higher temperatures, Q_C is generally close to the activation energy for self-diffusion (exceptions will be discussed in Section 6.1), as illustrated in Figure 14 (Sherby and Burke 1968). Note that in this figure both of our materials of interest are included: copper and titanium (both in its α and β forms).

In contrast to the universal applicability of Eqn. (8) to represent the temperature dependence, the stress dependence can take various functional forms. However, a power law (termed Norton's law) is widely used:

$$\dot{\epsilon}_s \propto \sigma^n \tag{9}$$

where n is a constant that can vary from 1 - 10 (see Section 6). Creep data for copper, illustrating the applicability of Norton's law are shown in Figure 15 ($n \approx 5$).

Combining Eqns. (8) and (9), the steady-state creep rate is given by

$$\dot{\epsilon}_s = A\sigma^n \exp-(Q_C/kT) \tag{10}$$

where A is a constant. The values of A, n and Q_C are obtained from the analysis of experimental creep data. When this equation is used to extrapolate to other conditions of interest, caution must be taken because A, n and Q_C can vary according to the applicable range of stress and temperature. In addition, as already mentioned, it does not include any primary or tertiary strains.

Equation (10) has been modified (Graham and Walles 1955) to include representation of the primary and tertiary stages, as follows:

$$\dot{\epsilon} = A\sigma^n \exp-(Q_C/kT)(a + bt^{-2/3} + ct^2) \tag{11}$$

where a, b and c are additional constants. The integrated form of this will yield a polynomial form very similar to the equation for creep strain given in Section 4.2.

Equations (10) and (11) can be used only to predict accumulated creep strain. However, they contain no information about creep rupture, and therefore the ultimate lifetime limit of components. This predictive capability is generally provided by the experimental measurement of rupture time (t_r). Although t_r can be determined from the measurement of the full (three-stage) creep curve, in practice much simpler (i.e., less costly) methods are used. Creep specimens are loaded at various stresses and temperatures until failure, the rupture

time being recorded. No strain transducers are used to measure the creep strains: the creep curve is, consequently, unavailable.

The basis for interpolation and extrapolation of time to rupture data derives from the inverse proportionality between t_r and $\dot{\varepsilon}_s$, referred to as the Monkman-Grant relationship (Monkman and Grant 1956):

$$\frac{1}{t_r} \propto \dot{\epsilon}_s = A\sigma^n \exp(-Q_C/kT) \tag{12}$$

This facilitates plots of log t_r against log σ, as shown in Figure 16 (obtained from the creep data shown in Figure 15). However, the confidence in extrapolation relies on the value of n remaining constant over the full stress range. This is usually not the case, particularly at low stresses, where n decreases. Such a tendency will overestimate creep lives at low stress.

It is significant to note that the Monkman-Grant relationship represented in Eqn. (12) establishes a behavioural linkage between time to rupture and the creep rate. This indicates that the fracture-related damage occurring during the tertiary stage must be controlled by the rate of creep deformation. Any proposed micromechanisms must include this feature.

Extrapolation methods have been developed using parametric procedures. In these, a correlation parameter (P) is used to superimpose stress-rupture data obtained over a range of temperature onto a single master design curve. In this case, if a reliable correlation parameter can be found, short-term tests can be conducted at higher stresses and temperatures, and the rupture times under long-term service conditions (lower stresses and temperatures) can be predicted by extrapolation. An approach to this scheme can be achieved by writing the logarithmic form of Eqn. (12) as

$$\log t_r = \frac{P_1}{T} - P_2 \tag{13}$$

The correlation parameter advocated by Orr et al. (1954) is P_2. Thus, the stress-rupture data are plotted as log stress against (log t_r - P_1/T). Such data for a chromium-molybdenum-vanadium steel are shown in Figure 17(a), with P_1 = 17,300. An alternative, suggested by Larson and Miller (1952), is to use the P_1 parameter (i.e., a plot of log stress against T (log t_r + P_2)), also shown in Figure 17(b) with P_2 = 23.3. Using modifications of this approach, more than 30 alternative variants of P have been proposed. A selection of these (including P_1 and P_2), and their practical application, is described in the Metals Handbook (Voorhees 1985). The very existence of such a large number of proposed correlation parameters signals the lack of a definitive engineering design tool to project rupture times in a reliable fashion. This is partly due to the inherent scatter in the experimental data, e.g., there can be a hundred-fold spread in rupture times measured for a given stress and temperature. Furthermore, the correlation parameters themselves have significant limitations. Thus, the data in Figure 17 cover a wide range of stress and temperature and illustrate the point made above that such plots are generally non-linear. Thus, while these approaches can be useful for data collation and interpolation, parametric relationships cannot be used reliably for extrapolation, except over very limited time spans (an extrapolation factor of about 3).

An alternative engineering approach is to use a continuum mechanical concept of accumulated damage (Kachanov 1958, Rabotnov 1969). Damage is described by a generalized scalar parameter, ω, which varies from zero at the start of life, to unity at failure. The precise mechanistic nature of the damage is not specified, but we may relate it to the progressive development of internal cavities and cracks. Both damage and creep strain are assumed to increase as a function of stress, temperature and the current state of damage. The creep rate and damage rate are then expressed as

$$\dot{\epsilon} = A\sigma^n / (1 - \omega)^n \tag{14}$$

$$\dot{\omega} = B\sigma^r (1 - \omega)^s \tag{15}$$

where A, B, n, r and s are temperature-dependent constants. An examination of Eqn. (14), with a focus on its applicability to the accelerating tertiary stage (the essence of the ω parameter), will provide some understanding of the phenomenological nature of ω. Thus, the term $1 - \omega$ accounts for the increase in effective stress arising from grain-boundary decohesion. Explicitly, ω can be considered to be the number fraction of cavitated grain boundaries such that the stress operating on the remaining intact boundaries is $[\sigma/(1 - \omega)]$. In principle, then, ω can be evaluated at any strain, or time, by measuring the total cavity volume in a metallographic section. However, this is a somewhat impractical procedure. Alternatively, we could fit Eqn. (14) to the tertiary creep data to obtain an analytical expression for ω, hence obtaining estimates for A, r and s in Eqn. (15). However, there is no certainty that this provides a sound basis for extrapolation. In addition, Eqn. (14) predicts that $\dot{\epsilon} = \infty$ at the point of fracture, where $\omega = 1$. This is inconsistent with experimental observation, demonstrating that final rupture (plastic instability) occurs when $\omega < 1$, i.e., $\omega = 1$ is not a good fracture criteria. Despite these shortcomings, the damage-parameter concept does effectively represent the phenomenology of tertiary creep and we can proceed by integrating Eqns. (14) and (15), whence by simple manipulation, using the fact that the time to rupture (t_r) and the strain rupture (ϵ_r) are reached when $\omega = 1$, we obtain the following:

$$\frac{\epsilon}{\epsilon_r} = 1 - (1 - t/t_r)^{1/\lambda} \tag{16}$$

$$\dot{\epsilon} = (\epsilon_m / t_r)(1 - t/t_r)^{1/\lambda} \tag{17}$$

$$\omega = 1 - (t - t/t_r)^{\lambda - 1} \tag{18}$$

where ϵ_r is the strain to rupture, $\epsilon_m = \dot{\epsilon}_s t_r$ (i.e., the Monkman-Grant constant) and $\lambda = \epsilon_r/\epsilon_m$. In Eqns. (16) and (17), the parameter ω does not appear. The major utility of these equations has been to provide a means for relating the strain or strain rate measured in actual plant components to the life fraction consumed, or the remnant life fraction $(1 - t/t_r)$. Practical application of this approach is explained elsewhere (Cane and Aplin 1994, Metals Handbook 1985). The analysis also offers the concept of required creep ductility during tertiary creep.

Thus, λ is used as a creep-damage tolerance parameter. In terms of measurable creep properties, it can be shown that

$$\lambda = \epsilon_r / \epsilon_m = \epsilon_r / \dot{\epsilon}_s t_r \tag{19}$$

In engineering practice, $\lambda > 10$ is used as a design criterion that ensures sufficient ductility during tertiary creep to avoid premature failure of a component.

5. PROPOSED ANALYTICAL TOOLS

It should be evident from Sections 2 and 3 that the design of the container requires reliable analytical tools to predict the creep behaviour, particularly the time (and/or strain) to failure. Section 4 has reviewed alternative methodologies that have been typically used in engineering practice to extrapolate creep strains and creep-rupture lifetimes. However, the inadequacies of these processes have been highlighted. A cursory perusal of the core references of Section 4 will reveal the rather early origin of the underlying ideas and principles. This is perhaps to be expected within the mainstream of traditional engineering design. There are, however, more recent and innovative approaches to the problem. These have arisen from advances in the understanding of creep and creep-rupture processes, plus the incentives emerging from the high-performance challenges encountered in the advanced technologies being developed in industries such as aerospace. One might also observe that the advent of modern computers has facilitated the exploration of new data analysis techniques and exploitation of elaborate curve-fitting techniques.

It is from this milieu that we have selected two complementary analytical tools. One is, in essence, a constitutive equation that can be used to fit the full three-stage creep curve, but avoiding the problems outlined in Section 4.2. It is the θ Projection Concept developed by Evans and Wilshire (1985) and includes the capability of predicting time, or strain, to rupture, while avoiding the problems indicated in Section 4.3. This analytical procedure is described in Section 9, together with the supporting theoretical formulation that underlies the functional form of the constitutive equation.

The second analytical tool employs the concept of the Deformation Mechanism Maps developed by Frost and Ashby (1982) and their complementary Fracture Mechanism Maps (Ashby et al. 1979). These provide a vehicle, in concert with the θ Projection Concept, for ensuring that the overall approach is entrenched in a scientific understanding of creep processes. In fact, the Mechanism Maps are a convenient repository of the collective world-wide knowledge of creep behaviour and creep mechanisms. A detailed description will be found in Sections 7 and 8.

Because a central theme of our proposed approach is the understanding of creep behaviour, we will now present a summary of the major creep-deformation and creep-rupture mechanisms.

6. PRINCIPAL CREEP-DEFORMATION AND -RUPTURE MECHANISMS

6.1 THE ROLE OF DIFFUSION

The kinetics of creep deformation and creep rupture are controlled by thermally activated processes, hence the Arrhenius form of the temperature dependence contained in the typical strain-rate equation (given above):

$$\dot{\epsilon} = A\sigma^n \exp -(Q_c / kT) \tag{20}$$

The thermal energy, Q_C, is that required to activate the individual process responsible for producing a unit of creep strain. In many cases, as illustrated in Figure 14 (see Section 4.3), Q_C is equal to the activation energy for self-diffusion (as defined below), Q_{SD}, where the self-diffusion coefficient (D_{SD}) is given by

$$D_{SD} = D_o \exp -(Q_{SD} / kT) \tag{21}$$

where D_o is a constant. This establishes the fact that creep deformation is usually controlled by diffusion processes.

The relevant diffusion process involves the thermally induced migration of vacancies. The link between vacancy migration and deformation processes will be made clear below. The vacancy diffusion process can occur within various locations in the solid. Thus, diffusion in the crystal lattice is called self-diffusion, with a characteristic activation energy of Q_{SD}. Although $Q_C = Q_{SD}$ at higher temperatures, Q_C is significantly less than Q_{SD} at lower temperatures. This reflects the fact that there are diffusion paths other than the crystal lattice, where vacancy migration is much easier, i.e., the associated activation energy is much less than Q_{SD}. Such easy diffusion paths exist within grain boundaries and along the cores of dislocations (termed "pipe" diffusion), where the activation energies are Q_{GB} and Q_P, respectively (Q_{GB} and Q_P are equal to 0.5 Q_{SD}, or less).[7]

This effect is illustrated in Figure 18. It will be seen from this Arrhenius plot that whereas easy diffusion paths exist, they are dominant only at lower temperatures (below T on the diagram). They make a negligible contribution to the overall diffusion rate at higher temperatures because the effective volume of grain boundaries and dislocations is very small compared with the total volume of lattice. Hence, within the (low homologous temperature) container shell, we can anticipate low activation energies (low temperature dependence) for creep, with creep rates controlled by diffusion along grain boundaries and dislocations. Creep data for copper (Feltham and Meakin 1959), shown in Figure 19, illustrate this point.

6.2 DIFFUSIONAL CREEP

This term is used to describe a creep process that arises directly from the diffusion of vacancies. Figure 20 shows, schematically, a cube-shaped grain subjected to a system of

---

[7] Grain Boundaries and dislocation cores (central axis of the dislocation) define regions where the atomic arrangements are less regular than the crystal lattice.

tensile and compressive stress. Elongation of the grain in the tensile direction can be achieved by displacing an atom from a position just below the surface to a position on top of the surface. In doing this, the stress does an amount of work, $\sigma\Omega$, where Ω is the volume of the atom. The addition of atoms on the tensile surface creates vacancies in the sub-surface region. The resulting increase in concentration of vacancies, in equilibrium with the stressed surface is given by

$$C = C_o \exp(\sigma\Omega / kT) \tag{22}$$

where C_0 is the equilibrium concentration under zero stress. Concomitantly, the concentration of vacancies at the surface under compressive stress is reduced, according to

$$C = C_o \exp(-\sigma\Omega / kT) \tag{23}$$

The resulting concentration gradient causes a flow of vacancies from the surface under tension to the surface under compression. This is equivalent to a flow of atoms in the opposite direction. The overall result is that atoms are removed from the compression surface and added to the tension surface, thus producing the creep strain.

A polycrystalline material is, of course, an assembly of a large number of grains, of the type shown in Figure 20. The diffusional flow described above, occurs in each grain, the collective microscopic behaviour being the total macroscopic creep elongation of the specimen or component. The vacancy-producing or -absorbing "surfaces" referred to above are, actually, grain boundaries. The rate at which this diffusional creep occurs is now dependent on the diffusional path, in accordance with those described in Section 6.1.

If the diffusion path is primarily through the lattice (see Figure 20), this is called Nabarro-Herring creep (Nabarro 1948, Herring 1950). The application of standard diffusional theory, using the boundary values established by Eqns. (22) and (23), yields the following creep-rate expression:

$$\dot{\epsilon} = K_1 \frac{D_{SD}}{d^2} \cdot \frac{\sigma\Omega}{kT} \tag{24}$$

where K_1 is a constant (≈ 10), D_{SD} is the diffusion coefficient for lattice self-diffusion and d is the average grain diameter.

Alternatively, if the preferred/dominant diffusion path is the grain-boundary (see Figure 20), the process is called Coble creep (Coble 1963). The governing equation is

$$\dot{\epsilon} = K_2 \frac{D_{GB}}{d^3} \cdot \frac{\delta\sigma\Omega}{kT} \tag{25}$$

where K_2 is a constant (≈ 40), D_{GB} is the grain-boundary self-diffusion coefficient and δ is the width of the narrow zone in the grain boundary that contains the diffusive flow. Note that the grain size dependence of Coble creep is different from that of Nabarro-Herring creep.

Taking into account that the temperature dependence of the diffusion coefficient is given by Eqn. (15), both Eqns. (24) and (25) have the same form as that for the secondary creep rate given in Eqn. (10). The value of the activation energy, Q, will be that for self diffusion (Q_{SD}) for Nabarro-Herring creep (at higher temperatures), and that for grain-boundary diffusion (Q_{GB}) for Coble creep (at lower temperatures). However, the value for n will be unity in both cases. Referral to Figure 10 will show that power-law creep with $n \approx 1$ typically occurs at low stress levels, i.e., diffusional creep dominates at low stress and low creep rates. We may, therefore, anticipate this mechanism being present in certain regions of the container shell. The significance of a low value for n (i.e., a low stress dependence of the creep rate) will become apparent when we discuss creep rupture and creep ductility in Section 6.4.1.

6.3 DISLOCATION CREEP

The role of the diffusion of vacancies is less direct in dislocation-creep mechanisms than in diffusional creep. In the latter, the strain is produced directly by the selective deposition of atoms at grain boundaries. The strain arising from dislocation-creep mechanisms is produced by the generation and movement of dislocations in the crystal lattice. In this case, diffusion serves to assist the dislocations in their movement. Consequently, a much higher strain is produced per unit of diffusional flux and the creep rate is dominated by the dislocation processes at the higher levels of stress (where dislocation movement is encouraged). To better understand the dislocation processes, it will be useful to examine their phenomenological characteristics before looking at micromechanisms.

6.3.1 Work Hardening and Recovery

Dislocation mechanisms must fall into a general framework where two competing phenomena are occurring simultaneously, namely work hardening and recovery. This is a long-standing principle (Bailey 1926) that has been substantiated through extensive theoretical and experimental investigation. At low temperatures, where recovery is absent, continued plastic deformation requires an increase in the applied stress. This produces the familiar form of the stress-strain curve recorded in a tensile test, see Figure 21. At any stress level, it is possible to define a rate of work hardening, h, as the gradient of the stress-strain curve, where

$$h = \partial\sigma / \partial\epsilon \tag{26}$$

The hardening is due to the fact that the density of dislocations is increasing with increasing strain (i.e., the deformation is generating additional dislocations). Consequently, the dislocations interact with each other and hence become increasingly immobilized such that further deformation strain is possible only if the stress is increased.

If the strained metal is now heated to a higher temperature, the material gradually softens with time. This would result in a decrease in the stress necessary to produce further strain (i.e., the flow stress), see Figure 21. Such a process is called recovery and the rate of recovery (r) is defined as

$$r = - \partial\sigma / \partial t \tag{27}$$

Recovery occurs because the dislocation density decreases, as dislocations are annihilated by thermally activated processes.

During creep deformation, the creep strain increases by a small amount ($d\varepsilon$) during a small time interval (dt). Work hardening and recovery are taking place simultaneously and the change in flow stress ($d\sigma$) is a function of both strain and time and is dependent on the rate of work hardening, compared to the rate of recovery:

$$d\sigma = \frac{\partial \sigma}{\partial \epsilon} d\epsilon + \frac{\partial \sigma}{\partial t} dt = h d\epsilon - r dt \tag{28}$$

If the work-hardening rate is dominant, the flow stress will progressively increase and the creep rate will decrease with time/strain. This is the situation during the primary stage. In contrast, if the recovery process is dominating, the flow stress will decrease and the creep rate will accelerate, as in the tertiary stage. During the secondary stage, the rate of work hardening is exactly balanced by the rate of recovery, $d\sigma = 0$ and the creep rate is constant and is given by

$$\dot{\epsilon}_s = \frac{d\epsilon}{dt} = - \frac{\partial \sigma / \partial t}{\partial \sigma / \partial \epsilon} = \frac{r}{h} \tag{29}$$

This concept forms the basis of most dislocation theories. Furthermore, the dynamic competition between work hardening and recovery is the fundamental rationale underlying the θ Projection Concept presented in Section 9. It remains to investigate the details of the dislocation arrangements and interactions that determine the values of r and h.

6.3.2 Generic Dislocation Model

During creep, the microstructural distribution of dislocations develops in a non-uniform fashion. In some areas, there will be a high density of dislocation tangles and networks, forming barriers, or obstacles, to further dislocation flow. Adjacent to these will be areas that are comparatively free of dislocations. These regions are relatively soft and dislocation movement will be comparatively facile. The rate of continuing creep deformation will now be controlled by the ability of the mobile dislocations to overcome the hard-barrier regions.

Although the details of this process are complex, we will explore its generic kinetics because this illustrates the competing nature of the work-hardening and recovery processes outlined in Section 6.3.1. Furthermore, the desired equations form the basis of understanding that underlies the θ Projection Concept referred to in Section 5 and discussed more fully in Section 9. Our discussion will draw from the generalized dislocation-barrier theory of McLean (1966) and the dislocation microstructural model of Nix and Ilschner (1979). Further details will be found in Evans and Wilshire (1985 and 1993).

The basic strain-rate equation is obtained by considering the activation energy (q) necessary to overcome the obstacles:

$$\frac{d\epsilon}{dt} = B \exp(-q / kT) \tag{30}$$

where B is a constant and represents the detailed dislocation configuration.

If the applied stress, σ, is equal to the mechanical strength of the barrier, σ_b, the required activation energy will be zero (i.e., q = 0). When σ is less than this value, the thermal energy necessary to assist the stress in overcoming the barrier will be $q(\sigma_b - \sigma)/\sigma_b$. The rate equation then becomes

$$\frac{d\epsilon}{dt} = B \exp\left[-\frac{q}{kT}\left(1 - \frac{\sigma}{\sigma_b}\right)\right] \tag{31}$$

A key concept is that the strength of the barrier is being continuously modified by the work-hardening and recovery processes:

$$\sigma_b - \sigma = h\epsilon - rt \tag{32}$$

A consideration of the work done in overcoming the barrier (the force on the barrier x the distance moved in overcoming the barrier) leads to

$$q = \sigma_b b a \tag{33}$$

where b is the Burgers vector of the dislocation and a is the area of the slip plane swept out by the dislocation in overcoming the obstacle. Substitution of Eqns. (32) and (33) into (31) yields

$$\frac{d\epsilon}{dt} = B \exp\left[-\frac{ba}{kT}(h\epsilon - rt)\right] \tag{34}$$

In the early stages of creep (i.e., the primary creep stage), the exponential term can be approximated by the first two terms of its Taylor series, leading to the first-order differential equation

$$\frac{d\epsilon}{dt} + \frac{Bbah}{kT}\epsilon = B\left[1 + \frac{rba}{kT}t\right] \tag{35}$$

which has the solution

$$\epsilon = \frac{kT}{Bbah}\left[B + \frac{r}{h}\right]\left\{1 - \exp\left(-\frac{rba}{kT}t\right)\right\} + \frac{r}{h}t \tag{36}$$

In general form, Eqn. (36) can be written as

$$\epsilon = \theta_1(1 - e^{-\theta_2 t}) + \dot{\epsilon}_S t \tag{37}$$

with the θ_1 and θ_2 parameters describing the primary creep curve, where

$$\theta_1 = \frac{kT}{Bbah}\left[B + \frac{r}{h}\right] \quad \textit{and} \quad \theta_2 = \frac{rba}{kT}$$

Equation (37) (which is identical to Eqn. (7)) is a key element of the θ Projection Concept and will be discussed further in Section 9. At this point, it is worth noting that the θ parameters contain information on the detailed dislocation configuration, and the competing recovery and work-hardening processes. At very long times, Eqn. (37) shows that the total primary creep strain is limited to the value of θ_1, while θ_2 represents the rate of decay of the creep rate (i.e., the shape of the primary creep curve) and is often referred to as a process of "exhaustion", similar to the logarithmic form of Eqn. (3). However, the second term of Eqn. (37) predicts that the exhaustion process undergoes a gradual transition into the steady-state creep rate, $\dot{\varepsilon}_s$ (equal to r/h). In the next section, we examine more specific dislocation models that provide further understanding of recovery and work hardening.

6.3.3 Specific Dislocation Model

Numerous specific dislocation mechanisms have been put forward to describe creep phenomena. A review of these will be found in the textbook of Gittus (1975). We will examine one of these to illustrate their genus. This is the classical theory of Weertman (1955), based on the seminal idea that the recovery process is contained in the kinetics of dislocation climb. The mechanism is illustrated schematically in Figure 22.

Deformation has its origin in the generation of dislocations from numerous sources, one of which is shown in Figure 22. The emitted dislocations initially move relatively freely along their glide plane. However, the leading dislocations inevitably encounter an obstacle that prevents further glide. Subsequent dislocations emitted from the source interact with each other and become piled up against the obstacle. The resulting back-stress prevents the source from creating further dislocations: deformation ceases, this representing the strain hardening effect. Under the action of the stress (which modifies the local vacancy concentration in equilibrium with the dislocation in a manner identical to that represented in Eqn. (22)), diffusion causes vacancies to flow to or away from the dislocation, resulting in its climb motion normal to the slip plane. The released dislocation is now free to move on an adjacent slip plane, or may be annihilated by an encounter with another dislocation of opposite sign. In this manner, the obstacle is circumvented and the source can continue to operate. The climb process is the recovery event, controlled by diffusional kinetics.

When the details of this process are worked out, it is found that the climb rate of the dislocation is proportional to σ^2 and the ratio of the distance of dislocation glide to the height of dislocation climb is proportional to $\sigma^{2.5}$. This results in the following (steady-state) creep-rate equation

$$\dot{\epsilon} = A\sigma^{4.5} \exp(-Q_{SD}/kT) \tag{38}$$

which is identical to Eqn. (10), with n = 4.5. Other dislocation theories (which also depend on climb-induced recovery) predict values of n ranging from 2 to 10. Under low-temperature conditions, where dislocation-pipe diffusion is more effective than lattice self diffusion, Q_{SD} will be replaced by Q_P.

6.4 FRACTURE MECHANISMS

6.4.1 General Considerations

Materials subjected to tensile deformation may fail in a variety of ways. The broad classes of fracture are illustrated in Figure 23. For relatively ductile materials subjected to short-term tensile testing, failure is generally initiated by the development of a localized necked region, which progresses until the local cross-sectional area reduces to zero. Materials that have less ductility will form internal voids, usually transgranular, but sometimes intergranular when grain boundaries are weakened by impurities. These voids form by plastic tearing and are usually confined to regions of local necking. At low (usually cryogenic) temperatures, brittle cleavage fracture (transgranular or intergranular) can occur. Under creep conditions, voids and cracks can form by a combination of diffusion and creep plasticity. These are virtually always intergranular in nature, but can be transgranular at higher stresses.

Tertiary creep mechanisms are intrinsically linked with creep-rupture mechanisms. There is, however, one exception to this rule. An accelerating creep rate can occur as a result of microstructural instability, or softening. An example of this would be dynamic recrystallization, which effectively annihilates the dislocation microstructure by a process akin to annealing. Such behaviour is not expected to occur in the materials being considered for fuel-waste container construction because of the relatively low homologous temperature, which is below the recrystallization temperature. Another common source of softening would be the modification (particularly coarsening) of precipitates. This generally applies to high-strength alloys whose high creep resistance is achieved by precipitation hardening. Again, this does not apply to the candidate container materials, which are not precipitation-hardened materials.

Before we describe specific creep-rupture mechanisms, it is important to examine the general phenomenology of plastic instability. This is manifest as the development of a localized region of necking. Not only does this result in premature failure at low average creep strains, but the rapid local deformation occurring at the elevated stress present in the necked region produces an accelerating deformation rate. Although this is a localized plastic instability, it gives rise to an apparent macroscopic tertiary stage.

As the propensity for necking is highly dependent on the stress sensitivity of the creep rate, we must place this phenomenon in the context of the container shell. We start by representing the stress dependence of the creep rate (Eqn. (10)) in simplified form:

$$\dot{\epsilon} = B\sigma^n \tag{39}$$

As necking proceeds, the localized stress becomes higher, resulting in an increase in the local creep rate. An increase in the creep rate produces an acceleration of the reduction of load bearing area in the neck, giving rise to a runaway instability. The higher the value of n, the greater is the increase in the creep rate for a given reduction in the cross-sectional area, and

hence a greater tendency for necking. We can be more specific. Consider a creep specimen with a gauge length of x and a cross-sectional area of A. The strain rate can be written

$$\dot{\epsilon} = \frac{1}{x}\frac{dx}{dt} = -\frac{1}{A}\frac{dA}{dt} \tag{40}$$

Using Eqn. (39) and recognizing that $\sigma = L/A$, where L is the load on the specimen, the rate of decrease in specimen cross-sectional area is

$$-\frac{dA}{dt} = BL^n A^{1-n} \tag{41}$$

Thus, when $n \rightarrow 1$, the rate of decrease in cross-sectional area becomes independent of the area. Consequently, the rate of reduction in area is identical throughout the specimen gauge length, and localized necking is hence inhibited[8]. This has been confirmed in an extensive survey of creep-rupture data on a variety of materials (Woodford 1969). Over a range of n values from 200 to 1.6, the strain to rupture increased from 0.04 to 20. Similarly, Figure 24 (Evans and Wilshire 1985) illustrates the overall consequence of progressive neck development, and its dependence on the value of n. The average strain rate of a tensile specimen is plotted as a function of average strain, according to a simple finite element analysis of the necked region. This figure effectively demonstrates the increase in the measured creep rate as deformation progresses i.e., the development of a tertiary creep stage. As expected, the acceleration of the creep rate is more rapid for high values of n. When n = 1, the creep rate is essentially constant, in accordance with the analysis presented above. In principle, if n = 1, the material should extend indefinitely. This is the basis of the so-called superplastic materials, where $n \approx 1$ and extremely large strains of 1 to 10 are typically realized (Sherby and Wadsworth 1989).

As shown in Section 6.2, a creep process that is characterized by $n \simeq 1$ is that of diffusional creep. It would, therefore, be advantageous to operate the container under conditions where diffusional creep dominates. Plastic stability would then prevail. However, we could not guarantee that the extremely high strains characteristic of superplastic materials would be maintained. The intergranular fracture processes described in Section 6.4.2 could still occur, placing some limit on creep ductility. Actual superplastic materials are designed to avoid this problem by using extremely fine grain sizes to suppress grain-boundary cavitation. Nevertheless, conditions with n = 1 would favour high ductilities and long creep lives.

---

[8] In the general case, the effect of work hardening should be considered, in addition to the strain rate sensitivity. This is made explicit in the classical analysis of Hart (1967). Thus, if the rate of work hardening (h in Eqn. (26)) is high, the local deformation associated with necking causes a significant increase in the flow stress, hence resisting further neck formation. This would seem to be beneficial under creep conditions, where the values of h are typically very high (Evans 1973). However, as explained in Section 6.3.1, the hardening process is continuously being opposed by the recovery process. This makes it difficult to assess the benefit of work hardening in resisting neck formation under creep conditions.

6.4.2 Creep Fracture Mechanisms

The mechanisms of creep fracture are quite different from the time-independent ductile fracture processes occurring in short-term tensile tests. Whereas the latter usually fail by the development of transgranular cracks, creep rupture is more typically an intergranular phenomenon. These creep-rupture processes cause a marked reduction in strain to failure compared with short-term tensile tests. At higher creep stresses, microcracks form at grain-boundary triple-points (the point of intersection of three grain boundaries), and are wedge-like in shape, whereas at lower stresses, cracking occurs by the link up of spherical voids nucleated along the grain boundary. Both triple-point cracking and cavity formation occur primarily on grain boundaries lying normal to the tensile stress. They both nucleate fairly early in the creep life, but their growing presence is not evident until they are responsible for the accelerating creep of the tertiary stage. A comprehensive summary of creep-rupture mechanisms is provided in a book written by Evans (1984).

The formation of triple-point wedge-cracks is a direct result of the fact that adjacent grains within a polycrystalline material move relative to each other under creep conditions. This shearing process, termed grain-boundary sliding, is illustrated in Figure 25. Such sliding results in stress concentrations at triple-points, large enough to nucleate a crack. Continued sliding causes a wedge-shaped crack to grow along the grain boundary normal to the tensile stress. The relative movement of the adjacent grains must be accommodated by deformation in the surrounding grains. Grain-boundary sliding, and hence triple-point crack development, is then controlled by the rate of grain deformation by creep. This coupling of fracture and deformation is the basis of the Monkman-Grant relationship discussed in Section 4.3.

The grain-boundary shear stresses, and therefore the applied tensile stress, must be sufficiently high to decohere the grain boundary at the triple-point. At lower stress ranges, intergranular failure occurs by grain-boundary cavitation, depicted in Figure 26. As with triple-point cracking, the nucleation of grain-boundary cavities is typically caused by grain-boundary sliding. The stress-concentration sites are now associated with particles at the grain boundaries, or irregularities formed by the intersection of planes of deformation with the grain boundaries. Following nucleation, grain-boundary sliding can make a contribution to cavity growth, but evidence is in favour of diffusional growth being the major process. Thus, when a cavity has reached a critical size (dependent on the applied stress), growth continues by absorption of vacancies from the surrounding grain boundary (Balluffi and Siegle 1955).

In keeping with Eqn. (22), the vacancy concentration, C_b, at a grain boundary normal to the stress, σ, is given by

$$C_b = C_o \exp(\sigma\Omega / kT) \tag{42}$$

where C_o is the equilibrium concentration of vacancies at zero stress, and Ω is the atomic volume. However, the vacancy concentration near the cavity surface, C_c, is also increased above C_o. This is due to the presence of the surface tension, γ, such that the work done to form a vacancy at this location is $2\gamma\Omega/r$, where r is the cavity radius, and the local vacancy concentration is

$$C_c = C_o \exp(2\gamma\Omega / rkT) \tag{43}$$

For the cavity to preferentially absorb vacancies from the grain boundary, $C_b > C_c$. This condition is reached when the cavity size exceeds $r = 2\gamma/\sigma$. Based on the boundary conditions represented by Eqns. (42) and (43), a diffusional model (grain-boundary diffusion) was developed by Hull and Rimmer (1959), from which the rate of growth of a cavity is predicted to be

$$\frac{dr}{dt} = \frac{D_{GB}\delta\Omega(\sigma - 2\gamma/r)}{2kTa_c r} \tag{44}$$

where a_c is the spacing between cavities. Other variants and refinements of this equation have also been developed (Gittus 1975).

There are a number of difficulties in using equations such as (44) to calculate, for example, the time to rupture:

- The cavity spacing, a_c is not well characterized. Experiments show that it can vary with stress, temperature, strain and time in ways that are not well understood. This makes integration of Eqn. (44) very difficult.

- There is no definitive fracture criterion. This will be associated with cavity growth and interlinkage, but requires an understanding of the plastic failure of the inter-cavity ligaments. It is worth noting that the plastic instability phenomenon discussed in Section 6.4.1 plays a role in this context. Thus, creep rupture by cavitation is delayed in materials with $n = 1$.

- Surface diffusion plays a role. This has the effect of changing the spherical cavity into an elongated lenticular shape, a phenomenon that has an important influence on cavity linkage, and hence the fracture criterion.

- A plastic accommodation factor must be taken into account. This is discussed below.

In the description of the cavity-growth model above, emphasis was placed on the key role of vacancy diffusion. However, there is an equivalent counterflow of atoms, and these must be deposited on the grain boundary adjacent to the cavities. The volume increase associated with this plating out of atoms must be accommodated by local plastic deformation (Beere and Speight 1978). In addition, the ligaments separating the cavities and removed from the region of diffusional flow, will undergo creep deformation as shown in Figure 27. Such creep deformation contributes to the growth of the cavities and the overall elongation rate of the material. A second, related, phenomenon occurs because grain-boundary cavitation is inhomogeneous. The situation is illustrated in Figure 26. The atoms that are depositing on the cavitated grain boundary are "jacking" grains A and B apart. This jacking action is constrained by grains C and D. The rate at which A and B move apart, and hence the rate of cavity growth, is controlled by the creep deformation of C and D (Dyson 1976). Further information on this deformation-controlled fracture mechanism will be found in the discussion of Fracture Mechanism Maps, Section 8. Not only does this complicate the cavity-growth rate

and determination of the ultimate time to rupture, it provides the coupling between creep fracture and deformation, essential to explain the Monkman-Grant relationship.

Whereas the theory of creep rupture is highly complex, the associated strain/time behaviour in the tertiary stage is even more complicated. We have shown above how enhanced plastic creep strain is initiated by the cavity-growth process itself. Another factor is the effective increase in stress because of the net loss in cross-sectional area resulting from cavity formation. However, further discussion of the characteristic shape of the tertiary creep stage will be postponed until we return to this important issue in Section 9.

7. DEFORMATION MECHANISM MAPS

7.1 CONSTRUCTION OF THE MAPS

Although Ashby (1972) is the recognized champion of the deformation mechanism map concept, the basic diagrammatic format originated with Weertman (1963). However, it was Ashby and his co-workers at Cambridge university who refined the mapping process, collected vast amounts of data, and constructed maps for many metals and ceramics. A major collection of their work is to be found in the book by Frost and Ashby (1982). This book reviews the relevant creep mechanisms (i.e., a more detailed version of Section 6) and includes maps for titanium and copper, separately published by Sargent and Ashby (1982) and Cocks and Ashby (1982), respectively.

The deformation maps are drawn using axes of normalized stress (σ/E, or σ/G, where E and G are the Young's modulus and shear modulus of elasticity, respectively) and homologous temperature, as shown schematically in Figure 28. The various fields of the map (about five of them) represent the range of stress and temperature within which a particular mechanism is dominant. The boundaries of these fields represent the stress-temperature locus where the applicable creep rates of adjacent mechanisms are equal. The mechanisms considered in the construction of the maps conform with those described in Section 6. The creep rates are calculated from the corresponding constitutive equations, being a combination of theoretical prediction and empirical interpolation (see below). In addition to representing the stress-temperature regimes within which a given mechanism is expected to be dominant, contours of constant creep rate are superimposed on the map, these contour lines traversing the various mechanistic fields. These contour lines are shown on the specific maps for titanium and copper shown in Figures 29 and 30. In a similar manner, actual experimental creep data are plotted on the map. Thus, the deformation map is a compendium of theoretical and experimental information, represented in a compact, highly visual form.

As shown in Figure 28, the upper limit of the diagram is determined by yield-point phenomena, and is of no interest to us. The lower limit of the diagram is set by diffusional creep, with a distinction between Nabarro-Herring and Coble creep. Calculations within these regions are performed using Eqns. (24) and (25): the relevant parameters (diffusion coefficients, elastic moduli, etc.) for titanium and copper are collected in Table 1. The deformation equation used for the dislocation-creep field (termed power-law creep in Figures 29 and 30) is a modified form of Eqns. (10) and (38):

$$\dot{\epsilon} = A \frac{DGb}{kT} \left(\frac{\sigma}{G}\right)^n \tag{45}$$

where the diffusion coefficient, D, is put equal to D_{SD} for high temperatures and equal to D_P at lower temperatures. The parameters A and n are determined from actual experimental data, and are collected in Table 1.

A limitation of the deformation maps is that they represent steady-state (secondary creep stage) creep conditions only. Frost and Ashby (1982) have made an attempt to capture transient creep (primary creep stage) in the deformation map format. However, these are cumbersome and less useful as they come in multiple sets; each map is appropriate to a specified time. In addition, transient-creep data are rather limited in scope; the only set of maps provided by Frost and Ashby are for stainless steel. Furthermore, the deformation maps do not include information on tertiary creep. Some of this information is, however, contained in the complementary Fracture Mechanism Maps, discussed in Section 8.

7.2 APPLICATION OF THE MAPS

For our purposes, the attractive feature of the deformation maps is that they are based on established mechanisms for creep, supported by a wide-ranging set of experimental data. As a result, they contain the authority of the mainstream of international scientific knowledge on creep processes. Any selected subsection of the map is supported by the complete body of information subsumed into the map taken as a whole. It is from this that the utility of the maps emerge. Take titanium as an example (Figure 29). The container shell will operate at a homologous temperature (based on the β-phase melting temperature used in the map) of 0.2. We observe that experimental data at this temperature are confined to the region of very high stress. However, we can, with some degree of confidence, focus on the strain-rate contour of $10^{-12}s^{-1}$ (recalling that this would be the approximate range of acceptability discussed in Section 3.2). Such a strain rate would allow a design stress of about 10^{-3} G. The map tells us that this deformation rate falls in the area of power-law (i.e., dislocation) creep, with (see Table 1) a stress exponent of n = 4.3 and an activation energy of 97 kJ/mole (dislocation core diffusion). Such parameters facilitate the engineering design of the container, together with the experimental design of a test matrix for conducting additional creep tests in this region. The appropriate constitutive equation for steady-state creep would be that of Eqn. (45).

It might be judged advantageous to operate the titanium shell in the diffusional creep mode. This would allow benefit from the high ductility that is predicted from a stress exponent of n = 1, which prevents the onset of plastic instability. We discover from the map that this would require a stress level of about 10^{-4} G. The creep mechanism would be Coble creep, for which an accurate constitutive equation is known (Eqn. (25)), together with its relevant parameters (from Table 1). Using such an equation (or adding the appropriate strain-rate contours to the map), the preferred maximum creep strain rate of the particulate matrix could be determined.

Another general message contained in the maps is that the steady-state creep regimes (whether of dislocation or diffusion origin) extend throughout the entire temperature range, despite the fact that the actual deformation rates at homologous temperatures of 0.2 and below, are very low. This substantiates the arguments made in Section 4 that even at low temperatures we might expect (over very long time scales) the full expression of creep

behaviour typified by primary, secondary and tertiary stages. This position will be supported by similar consideration of Fracture Mechanism Maps described in Section 8.

The deformation map will also be useful when we consider the θ Projection Concept, elucidated in Section 9. Thus, it will allow us to exercise caution if the θ Projection is extended from one creep region to another, i.e., if we cross a field boundary from one dominant mechanism to its neighbour. The information in the map will also provide some ballpark comparison with the creep rates predicted by any θ Projection equations that are eventually developed. Such equations will require the generation of experimental creep data to extract the essential θ-parameters. The deformation map will provide useful guidance in setting the range of stress and temperature to be explored in these experiments. The relevance of these points will be more evident following the discussion of the θ Projection Concept in Section 9.

Finally, it must be acknowledged that although the Deformation Mechanism Maps summarize our current knowledge of steady-state creep, they undoubtedly are incomplete. Within the context of the long history of mechanical metallurgy, there is likely to emerge future modification of theoretical models and experimental data. We can, however, say with conviction that the maps currently represent the entire state of understanding of creep and plastic flow processes.

7.3 SPECIFIC CASE STUDIES

In their book on Deformation Mechanism Maps, Frost and Ashby (1982) provide several case studies illustrating the application of the deformation maps to practical problems. Examples from industrial metal-forming procedures, including rolling, forming and extrusion, fall into the upper end of the strain-rate range (10 - 10^5 s^{-1}). The maps are used for a variety of materials to obtain estimates for the forming forces that are required, and the way in which these forces will change if the rate of the process, or the temperature at which it is performed, are altered.

Maps constructed for tungsten have been used to improve the lifetime of electric light bulb filaments. For these to last ~1000 h, the filament creep rate must be $<10^{-9}$ s^{-1}. The maps show that for pure tungsten, the operating conditions place the filament in the power-law creep regime, with an unacceptable creep rate of 10^{-4} s^{-1}. However, doping the tungsten with minor alloy additions causes the power-law creep region to shrink, thus placing the filament in the diffusional creep area. The creep rate is now reduced to 4×10^{-10} s^{-1}, and ductility is also enhanced by the fact that $n = 1$. A similar scenario emerges for the analysis of nickel-based alloys used in high-temperature turbine blades (maximum acceptable creep rates of ~10^{-8} s^{-1}). Alloying again places the blade in the diffusional creep field, but with unacceptably high creep rates. The solution to this is to increase the grain size, thus reducing the diffusional creep rate. As a result, the power-law creep field expands such that it contains the turbine blade and precipitation-strengthening strategies can be used to lower the creep rate further.

Examples of application of the maps to longer time scales (~30 years) are taken from the nuclear industry. Reactor components made of stainless steel are considered. Allowable creep rates are in the range of 10^{-10} s^{-1}, placing them in the diffusional creep field. Because allowable strains are small, of the order of 0.01, transient-creep maps are found to be necessary to obtain accurate predictions.

Apart from the above examples, there are several case studies that deal with much longer time scales, of historical and geological proportion. As these are of greater significance to the waste-container problem, we will look at these separately, in greater detail.

7.3.1 Creep of Architectural Lead

Since pre-Roman times, lead has been used for roof coverings and water pipes. Because of its good corrosion resistance, ancient lead piping installations have survived in various architectural forms. Present-day inspections sometimes reveal that creep deformation has occurred, even under relatively low stress conditions. This is due to the fact that the low melting point of lead places room temperature in the range of 0.5 T_m homologous temperature. It has been observed that whereas Roman lead piping shows negligible creep over periods of about 2000 years, Victorian piping of about 75 years old has crept by significant amounts. Thus, an analysis of the sag of Victorian piping (drain pipe and hot-water pipe) showed that creep rates of about 5×10^{-12} s^{-1} had occurred under stresses of $\sim 5 \times 10^{-5}$ G. An examination of the relevant deformation map (Figure 31) shows that the observed creep rates are consistent with those predicted, falling in the field of diffusional creep (Coble creep).

Note that the grain size for this map is 50 μm, in keeping with the measured grain size of 10 - 100 μm in Victorian lead piping. In contrast, the grain size of Roman lead piping is >1 mm. This is a consequence of the fact that Roman piping was made by a casting process, whereas Victorian piping was produced by extrusion. Figure 31 also shows the deformation map for a 1 mm grain size (bearing in mind that diffusional creep is strongly dependent on grain size, as explained in Section 6.2). This places the water piping in a position straddling the diffusional creep and power-law creep boundary. The predicted creep rates are several orders of magnitude slower, adequately explaining the lack of creep deformation in Roman piping over a period of thousands of years.

7.3.2 Creep in the Polar Ice Cap

Studies of the South Polar Ice Cap show a maximum depth of 4000 m at its centre, sloping gently outwards for 1000 km or more, before falling steeply into the open sea. Based on this gradient and depth of ice, the shear stresses in the ice can be calculated. Similarly, borehole measurements have determined the temperature as a function of depth.

Deformation maps have been used to analyze the outward flow of the ice cap. The relevant map is shown in Figure 32, onto which is plotted the range of temperature and stress present in the ice cap (at the Byrd Station), as a function of depth. This shows that the Antarctic ice cap deforms by power-law creep, with the creep rate being greatest ($\sim 10^{-9}$ s^{-1}) next to the bedrock, where the stress and temperature are maximum.

7.3.3 Continental Drift

It is well established that the major continental plates positioned in the earth's upper mantle are drifting apart, over distances of about 5000 km in a period of 2×10^8 years. This translates to a creep strain rate of 10^{-12} - 10^{-15} s^{-1}. The major mineral phase present in the mantle and sustaining this creep strain is olivine, a silicate material. The deformation map is presented in Figure 33.

The creep-rate contours in Figure 33 have been modified to take into account the extreme pressures present in the earth's mantle (much larger than for the polar ice cap). The theoretical-creep equations facilitate this by including the effects of pressure on the creep-activation energies. The net effect is to reduce the creep rates by about 10^3, compared to creep rates at atmospheric pressure. The range of creep stress and temperature is uncertain, but is bounded by the hatched area shown in Figure 33. This shows that the predicted creep rates are consistent with those estimated from geological observation of continental drift. The map also predicts that the creep mechanism will be power-law creep at the higher stresses (deeper layers) and diffusional creep at lower stresses, based on a grain size of 0.1 mm. If the grain size is larger, say 1 mm, the dominant flow mechanism will be power-law creep.

8. FRACTURE MECHANISM MAPS

The format and layout of the Fracture Mechanism Maps is similar to that of the Deformation Mechanism Maps. However, during their historical development, the method of construction has progressed through two phases. The first of these (Ashby et al. 1979) followed a largely empirical process. The resulting map for copper (to the author's knowledge, no map for titanium has been published) is shown in Figure 34. The mechanistic fields of this map are derived from direct observation of the characteristic fracture mode from metallographic examination of creep specimens. Thus, the narrow region at the higher stress levels is designated "ductile fracture", or "transgranular creep fracture" (the differentiation between the two is rather arbitrary), based on observation of plasticity-induced voids and cracks. Below this is the extensive field of "intergranular creep fracture" characterized by the observation of intergranular voids and cracks. The upper right sector, at higher temperatures, marks the regime where extensive dynamic recrystallization is evident.

Also plotted on the map are contours of equal fracture times, the included numbers being the logarithm, to the base 10, of the time to rupture in seconds. Solid symbols mean that the fracture was identified as intergranular (open symbols, transgranular). The shaded areas indicate a mixed mode of fracture.

The information contained in such fracture maps is, in reality, rather limited. The diagram basically divides the microscopic observations into two classes: transgranular and intergranular. The experimental rupture times included on the maps provide supplementary information, necessarily of limited temperature and stress ranges. As such, the maps are largely of pedagogical value, at best. They provide little basis for extrapolation, having a very limited theoretical basis, somewhat at variance with the claim of a "mechanistic" map.

These fundamental limitations were partially improved in later versions of the maps (Cocks and Ashby 1982), the published version for copper (titanium unavailable) being shown in Figure 35. Such maps are now more firmly based on the mechanistic understanding outlined in Section 6.4. The boundaries of the map are derived from kinetic equations that describe cavity growth, mainly on grain boundaries. With the aid of these theoretical equations (with parameters such as diffusion coefficients and creep rates derived from experimental data), the map is divided into regions that are primarily controlled by surface diffusion, grain-boundary diffusion and power-law creep, as described in Section 6.4. The lower boundary on the map (the heavily dashed line) marks the threshold stress below which the voids are unstable (sub-critical) and therefore disappear by sintering, under the action of the surface tension. The

contours on the map represent constant values of damage rate, df_h/dt, where f_h represents the fractional area of cavities, r^2/ℓ^2, where r is the radius of the cavity and 2ℓ their spacing apart on the grain boundary. Note that the initial values of ℓ and f_h (and therefore r) have to be pre-designated. The authors use the values of df_h/dt to calculate the times to rupture, by integration. However, the considerable difficulties associated with this are pointed out in Section 6.4. Not least of these is the determination of a suitable fracture criterion. Cocks and Ashby adopt a value of $f_h = 0.25$. Clearly, when $f_h = 1$, the cavities are fully linked and fracture is guaranteed. The preferred (and rather arbitrary) value of $f_h = 0.25$ assumes that the remaining ligaments fail rapidly by plastic tearing. In addition, it is assumed that the inter-cavity spacing (2ℓ) remains constant. This is at variance with experimental information that typically demonstrates that cavity nucleation is an ongoing process as creep proceeds. In addition, the time required to nucleate the cavities has to be estimated (and may represent a significant fraction of the rupture time).

The integration procedure also yields the increasing creep strain resulting from the cavitation growth process. Thus, an expression is obtained for the tertiary creep stage, and the strain to failure. However, this procedure is subject to the same limitations underlying the assumptions used to calculate the times to rupture.

In summary, the Fracture Mechanism Maps (in contrast to the utility of the Deformation Mechanism Maps) are of limited practical use. In particular, their reliability is questionable for the purposes of extrapolation outside the experimental database. However, the theoretical analysis of Cocks and Ashby (1982) represents a superb representation of the current understanding of creep-fracture mechanisms. In fact, their paper serves the admirable task of emphasizing the enormous complexity of the fracture mechanisms, and their subtle coupling with the deformation process. As has been mentioned previously, this latter observation is a key characteristic of creep, being entrenched in the Monkman-Grant relationship (Section 4.3) and utilized in the θ Projection Concept (Section 9).

9. THE θ PROJECTION CONCEPT

9.1 GENERAL CONSIDERATIONS

The θ Projection Concept was introduced by Evans et al. (1982) in 1982 and has been a topic of intense investigation and application by the Swansea University research group. Extensive reviews of this development have been published in their 1985 textbook (Evans and Wilshire 1985) and a more recent update (Evans and Wilshire 1993).

The concept embraces the maxim that the creep behaviour of a material finds its full expression in the total creep curve, classically represented by the three stages of primary, secondary and tertiary creep. Thus, as pointed out in Section 4.3, creep and creep fracture have been traditionally described by reference to only a few standard parameters, the secondary creep rate ($\dot{\varepsilon}_s$), the time to rupture (t_r) and the strain to rupture (ε_r). While the values of t_r and ε_r precisely identify the point of creep failure, measurement of only the steady-state creep rate disregards the primary and tertiary stages, so that a major portion of the information available from a creep curve is totally ignored. The significance of this omission can be illustrated using Figure 36. Thus, the three curves have the same values of $\dot{\varepsilon}_s$, t_r and ε_r, but the curve shapes differ markedly, reflecting the different proportion of lifetime

spent in primary or tertiary. Actual examples of this, for the case of copper, are shown in Figure 37. In general, this shows the common trend for the primary stage to become less pronounced, and the tertiary stage to become more dominant, with decreasing applied stress (the likely scenario for the container shell). Such disparate behaviour is of crucial importance for the modelling of complex structures using finite element stress analysis codes. Clearly, then, a comprehensive description of creep behaviour requires constitutive equations that accurately describe the full creep-curve shape and its dependence on test conditions. Such a process will ensure that the constitutive equations contain the primary and fundamental phenomena that are universal to the creep behaviour of all classes of materials.

9.2 FORMULATION OF THE CONSTITUTIVE EQUATIONS

An early attempt by the Swansea group (Davies et al. 1969) to quantify the whole creep curve was based on the use of the exponential equation of Garofalo et al. (1963) to represent primary and secondary creep. This is Eqn. (7) of Section 4.2. This equation can be extended to include a tertiary term, as

$$\epsilon = \alpha_1(1 - e^{-\beta_1 t}) + \gamma t + \alpha_2 e^{\beta_2(t - t_i)} \tag{46}$$

where the constants α_2 and β_2 define the shape of the tertiary stage that begins after t_i. Unfortunately, the time to the onset of tertiary is subjective and can produce significant errors in long-term extrapolation. In addition, it was realized that the mechanistic precursors of the tertiary stage are present throughout the creep curve. Thus, for example, the onset of tertiary does not coincide with the nucleation of grain-boundary cavities. Such cavities form and grow early in the creep life, even during primary creep. Tertiary creep only becomes evident when the intergranular damage develops to an extent sufficient to cause an acceleration in the creep rate. This conceptual reasoning quickly leads to an alternative view of the form of conventional creep curves. We can consider the deformation behaviour to be a consequence of competing events, a primary creep process that decays throughout the entire creep life and a tertiary creep process that accelerates from the commencement of creep. This view is also in complete harmony with the idea of a competing work-hardening rate (h) and a recovery rate (r), as discussed in Section 6.3.1. Within this mechanistic framework, a minimum creep rate rather than a steady-state creep rate would be attained. Indeed, it seems fortuitous to expect that a perfect balance between r and h (bearing in mind that both r and h are themselves time-dependent quantities reflecting the evolution of the creep microstructure) will be maintained for any prolonged period to result in a protracted period of secondary creep. Depending on the precise rates of primary decay and tertiary acceleration, the minimum creep rate could appear to be essentially constant over the period of inflection. Examples of this will be given below.

We might consider a polynomial expression that is compatible with this concept, in keeping with Eqn. (5) and suggested by de Lacombe (1939)

$$\epsilon = \alpha_1 t^{\beta_1} + \alpha_2 t^{\beta_2} \tag{47}$$

with $\beta_1 < 1$ and $\beta_2 > 1$. However, as explained in Section 4.2, the coefficients of polynomial expressions vary erratically with stress and therefore are unsuitable for longer-term extrapolations. The evidence from experimental data indicates that the exponential form of equation holds more promise (Evans and Wilshire 1985).

We can begin the development of an exponential constitutive equation by examining that used to represent the primary and secondary stages:

$$\epsilon = \theta_1(1 - e^{-\theta_2 t}) + \dot{\epsilon}_s t \tag{48}$$

This, in its empirical form, is that suggested by Garofalo et al. (1963) (see Eqn. (7) in Section 4.2). We learned in Section 6.3.2 (Eqn. (37)) that this equation has full theoretical justification, being derived from a dislocation-creep mechanism applicable to primary creep, and based on the fundamental idea of the competing interaction between the work-hardening and recovery rates. Differentiation of Eqn. (48) then shows the creep rate decays as

$$\dot{\epsilon} = \theta_1\theta_2 e^{-\theta_2 t} + \dot{\epsilon}_s \tag{49}$$

which, on rearrangement becomes

$$\dot{\epsilon}_p = \theta_1\theta_2 e^{-\theta_2 t} = \theta_2(\theta_1 - \epsilon_p) \tag{50}$$

where $\dot{\epsilon}_p$ is the primary creep rate given by $\dot{\epsilon} - \dot{\epsilon}_s$.

In Eqn. (50), the primary creep rate ($\dot{\epsilon}_p$) decays linearly with increasing primary creep strain (ϵ_p). This means that primary creep obeys first-order reaction-rate kinetics, in keeping with the mechanistic predictions. A rationalization of this is as follows. The strain rate is a function of the pertaining microstructure (dislocation configuration, density of cavities, etc.), which evolves in proportion to the accumulated strain. A natural consequence is that $\dot{\epsilon}_p \propto \epsilon_p$. The kinetic rate constant is given by the parameter θ_2, while θ_1 determines the maximum primary strain as $t \rightarrow \infty$. This is illustrated in Figure 38. As shown in Eqn. (37), the θ parameters contain information on the dislocation configuration and the work-hardening/recovery rates. Equation (50) therefore describes a continuously decaying creep curve which, as the primary creep strain approaches θ_1 at long times, eventually attains a steady-state creep rate of $\dot{\epsilon}_s$.

We must now consider the tertiary creep stage. The required expression must recognize that the tertiary damage processes initiate early in the creep life and advance in a progressive manner. Thus, even when intergranular cavities and cracks nucleate early in the primary stage, the low initial damage levels will be insufficient to have any significant effect on the rapid decay in creep rate. However, as the size and number of cavities increase with increasing strain, the resulting acceleration in creep rate will offset the gradual decay in creep rate towards $\dot{\epsilon}_s$. This process can be modelled by introducing the damage parameter, ω, (see Section 4.3) which is initially zero for undamaged material (t = 0). The value of ω then

increases such that instead of approaching $\dot{\varepsilon}_s$, the creep rate will accelerate with the tertiary creep rate ($\dot{\varepsilon}_t$) given by

$$\dot{\epsilon}_t = \dot{\epsilon}_s (1 + \omega) = \frac{r}{h} (1 + \omega) \tag{51}$$

with the rate of damage accumulation $\dot{\omega}$ increasing as

$$\dot{\omega} = C (d\epsilon_t / dt) \tag{52}$$

where C is a constant. On integrating, we can then replace the steady-state term in Eqn. (48) to give

$$\epsilon = \theta_1(1 - e^{-\theta_2 t}) + (1/C)(\epsilon^{C\dot{\epsilon}_s t} - 1) \tag{53}$$

which can be written as

$$\epsilon = \theta_1(1 - e^{-\theta_2 t}) + \theta_3(e^{\theta_4 t} - 1) \tag{54}$$

Differentiation shows that the tertiary creep rate ($\dot{\varepsilon}_t$) increases linearly with increasing tertiary creep strain, $\varepsilon_t = \varepsilon - \varepsilon_p$ as

$$\dot{\epsilon}_t = \theta_3\theta_4 e^{\theta_4 t} = \theta_4(\theta_3 + \epsilon_t) \tag{55}$$

which is the same form as Eqn. (50) and demonstrates that the tertiary stage also obeys first-order reaction-rate kinetics. The significance of the θ_3 and θ_4 parameters is indicated in Figure 38.

Evans and Wilshire (1985) show that such first-order kinetics are inconsistent with a phenomenological explanation of tertiary creep based on the loss of load-bearing area. Thus, for example, Figure 24 shows that $\dot{\varepsilon}_t$ is <u>not</u> directly proportional to ε_t when the acceleration of creep deformation is the result of plastic instability arising from neck formation. Similarly, simple calculation shows that first-order kinetics would not be produced by the lack of grain-boundary load-bearing area resulting from the growth of cavities, regardless of the assumed cavity spacing. In addition, since the total cavity volume is usually less than 1%, the reduction in load-bearing area is insufficient to account for the typical magnitude of tertiary creep. Furthermore, experiments show that the deformation acceleration occurs only if the cavities are associated with grain boundaries (cavities produced within the grains do not increase the creep rate). However, the correct kinetics would derive from a micromechanism where dislocation climb is enhanced by the absorption of vacancies by the developing cavities

(Evans and Wilshire 1981). In this case, $\dot{\varepsilon}_t \propto \varepsilon_t$, in accordance with Eqn. (55). It is typically observed that significant necking occurs only in the final stages of tertiary creep.

9.3 INTERPOLATION OF EXPERIMENTAL DATA

Equation (54) is the primary constitutive equation emerging from the θ Projection Concept. Figure 39 demonstrates the capability of the equation to accurately represent experimental data obtained for a steel. This shows that the use of the four θ parameters allows a good fit to a creep curve that shows an apparent period of secondary creep, although the equation contains only a minimum creep rate. Through differentiation of Eqn. (54), the creep rate at any instant is given by

$$\dot{\epsilon} = \theta_1\theta_2\theta^{-\theta_2 t} + \theta_3\theta_4\theta^{\theta_4 t} \tag{56}$$

and the minimum creep rate is produced at a time t_m given by

$$t_m = \frac{1}{\theta_2 + \theta_4} \ln \frac{\theta_1\theta_2^2}{\theta_3\theta_4^2} \tag{57}$$

which, substituted with Eqn. (56) will yield the minimum creep rate, $\dot{\varepsilon}_m$. The value of $\dot{\varepsilon}_m$ will be greater than the secondary creep rate, $\dot{\varepsilon}_s$, in Eqn. (48), which would have been attained eventually in the absence of tertiary processes. Figure 37 shows some examples for copper (Brown et al. 1987), and demonstrates the capability of the equation to fit a variety of creep curves.

9.4 EXTRAPOLATION OF EXPERIMENTAL DATA

The major utility of Eqn. (54) lies in its capability for prediction and extrapolation. Such projection is achieved through the four θ parameters. The values of these (plus their statistical variability) can be extracted by fitting the equation to each experimental creep curve obtained for a particular material, using suitable computer programs (available from the Swansea group). The set of θ parameters for copper (obtained from creep curves such as those shown in Figure 37), plus their systematic variation with stress and temperature, is shown in Figure 40. This provides the basis for a quantitative description of the gradual change in curve shape with changing test conditions.

Figure 40 shows that a linear relationship is found in the plot of stress versus log θ. For the θ_1 and θ_3 parameters, the temperature dependence is represented by the temperature dependence of the short-term yield stress (σ_Y), whereas θ_2 and θ_4 are best fitted to an Arrhenius relationship. Both stress and temperature dependencies can thus be written as

$$\begin{aligned}
\theta_1 &= G_1 \exp H_1(\sigma/\sigma_Y) \\
\theta_2 &= G_2 \exp -[(Q_2 - H_2\sigma)/kT] \\
\theta_3 &= G_3 \exp H_3(\sigma/\sigma_Y) \\
\theta_4 &= G_4 \exp -[(Q_4 - H_4\sigma)/kT]
\end{aligned} \tag{58}$$

where G and H are constants and Q is the activation energy. The fact that $Q_2 = Q_4 = 110$ kJ/mol is consistent with the fact that the creep of copper is controlled by pipe diffusion (see Table 1). This applies to primary creep (θ_2) and tertiary creep (θ_4).

It is now necessary to verify whether the θ parameters facilitate long-term extrapolation. This has been demonstrated by an extensive investigation of a chromium-molybdenum-vanadium ferritic steel (Wilshire 1989, Wilshire and Evans 1994). This steel is used in the high-temperature (~550°C) steam generating section of a thermal-electric power station. The appropriate θ parameters are shown in Figure 41. The activation energy for θ_2 is equal to 224 kJ/mol, a value close to that for lattice self-diffusion in ferrite. The temperature dependence of θ_4 is more complex, a stress-dependent activation energy being required. This reflects the fact that, in addition to the formation of grain-boundary cavities, the tertiary creep in this material is affected by the coarsening of the carbide precipitates that are deliberately provided for added creep strength.

Figure 41 shows that the experimental stress range used to obtain the θ parameters for steel is 150 - 350 MPa. The θ parameters can now be used to extrapolate the creep data to much lower stresses. Thus, Figure 42 shows the complete curves predicted for the stress range 70 - 110 MPa. This demonstrates the capability of the θ Projection technique to extrapolate creep data obtained over a period of about one month to periods in excess of ten years.

The extrapolation capability is further illustrated by reference to Figure 10. This is a logarithmic plot of the minimum creep rate ($\dot{\varepsilon}_m$), obtained through Eqns. (56) and (57), versus stress. In Figure 10, the solid line is derived from short-term data (~1000 h), represented by the symbol, +. To this plot has been added long-term creep data (up to 100,000 h), subsequently obtained at lower stresses. It can be seen that the long-term data are remarkably well predicted by the θ parameters derived from short-term data. This is an impressive demonstration of the extrapolative power of the θ Projection Concept. It has been successfully applied (and verified) to project experimental data obtained from creep tests performed over several months to the 30-year lifetime conditions of an electricity generating plant.

Although this is far short of the levels of extrapolation (at least 500 years and possibly much longer) required for the waste-container shell, a glance at Figure 10 will show that the continued projection to a creep rate of $\sim 10^{-12}$ s^{-1} is a modest step. This is the range of the anticipated operating creep rate of the container shell (see Section 3.2).

Evans and Wilshire (1993) point out that the form of the θ equations represented by Eqns. (58) are not, in practice, convenient, particularly for use in finite element computer programs. They have therefore recommended the use of the following equation for long-term extrapolation:

$$\ln \theta_i = a_i + b_i\sigma + c_iT + d_i\sigma T \qquad (59)$$

This applies to conditions in which the experimental data used to derive the θ parameters do not depart significantly from the temperature of the intended application. Under such conditions, the 1/T relationship of Eqn. (58) is closely equivalent to a linear T dependence.

The constants a, b, c and d can be evaluated rapidly by a multilinear least-squares regression analysis. Their values for copper and steel are shown in Table 2.

The Swansea group has applied the θ Projection Concept to analyze the creep behaviour of a variety of materials, summarized as follows:

- oxygen-free high conductivity copper (Evans and Wilshire 1987a, Brown et al. 1987),
- three varieties of aluminum alloy used for airframe construction (Evans et al. 1990, Evans et al. 1993a),
- three high-performance structural steels (Brown 1987, Wilshire 1989, 1993a, Evans et al. 1984, 1993a, Wilshire and Evans 1994),
- oxide dispersion-strengthened steel (Evans et al. 1993, b and c), which has very high apparent values of n and Q_c: $n \approx 40$ and $Q_c \approx 3 \times Q_{SD}$,
- nickel-based superalloy (Brown et al. 1986a, Evans and Wilshire 1987b), and
- a variety of structural ceramics (Wilshire 1993b).

It will be noted from the above references that many of the papers were co-authored with collaborators from other laboratories. In addition, other workers, independent of the Swansea group, have utilized the θ Projection Concept. A selection of such studies includes

- four ferritic Cr-Mo-V steels (Maruyama and Oikawa 1987a),
- nickel-based superalloys (Li et al. 1987, Henderson and McLean 1984),
- low alloy steel (Shen and Plumtree 1990), and
- several high-temperature steels (Taylor et al. 1990, Li et al. 1990).

The further use of Eqn. (54) to extrapolate creep lifetimes (time, and strain to failure) will be discussed in Section 9.6, but first we pause to examine the relationship between the θ Projection Concept and the Deformation Mechanism Maps.

9.5 θ PROJECTION AND DEFORMATION MAPS

An inspection of Figure 10 shows that the stress dependence of the minimum creep rate follows a power law, with the stress exponent, n, varying with stress. We discussed the corresponding Norton law for steady-state creep in Section 4.3. Similar to the case of the secondary creep rate (Eqn. (10)), we can write

$$\dot{\varepsilon}_m = A\sigma^n \exp -Q_c/kT \tag{60}$$

In Figure 43, the plotted lines represent $\dot{\varepsilon}_m$ calculated from the θ parameters for copper. The data points (for a variety of temperatures) are measured from the actual creep curves, assuming that there exists a secondary stage, i.e., these are the "steady-state" creep rates, $\dot{\varepsilon}_s$. It can be seen that there is good agreement between the interpolated values of $\dot{\varepsilon}_m$ and the measured values of $\dot{\varepsilon}_s$, demonstrating (as expected) the equivalence between Eqn. (60) and Eqn. (10). At the higher stress levels, $n \approx 5$, in accordance with the climb mechanism represented by Eqn. (38) in Section 6.3.3. However, the n value decreases continually with decreasing stress, approaching $n = 1$, typifying the diffusional creep process, Section 6.2.

Using Eqn. (60), together with the θ data of Figure 40, the full range of Norton's n values can be plotted as in Figure 44, and range from n = 12 to 1 over the extrapolated stress field.

In a similar fashion, we can plot the full set of activation energies, Q_c in Eqn. (60). These are also shown in Figure 44.

Using the "rules" that correlate values of n and Q_c with the classical creep mechanisms in Section 6, we can superimpose the information in Figure 44 on the Deformation Mechanism Maps for copper shown in Figure 30 of Section 7. This is shown in Figure 45. It is evident that the predicted n = 1 contour separates the regions of dislocation power-law and diffusional creep. Similarly, the projected line for Q_c = 125 kJ/mol divides the map into the appropriate fields controlled by lattice self diffusion at high temperature and that controlled by preferential diffusion (grain-boundary or dislocation-core paths) at lower temperatures.

This is convincing demonstration of the consistent equivalency between the θ Projection Concept and the Deformation Mechanism Maps. However, it must be remembered that the two approaches (although complementary) are based on a fundamental difference of logic. The deformation maps are based on the concept of a true secondary creep region. In contrast, the θ Projection Concept focusses on the stress and temperature dependence of the characteristic shape of the entire creep curve. The fact that $\dot{\varepsilon}_m \approx \dot{\varepsilon}_s$ can be considered fortuitous, although it is a direct consequence of mechanistic viewpoint. Although this may seem a trivial point of graphical plotting perspective, there are deeper implications.

We have seen that the mechanistic base of the θ Projection Concept, Eqn. (8) is rooted in a consideration of creep deformation occurring via dislocation motion characterized by the work-hardening and recovery rates. The immediate question is why, then, does the projection of creep data based on the θ-parameter equation apparently enter the diffusional creep field, at lower stresses (outside the experimental database).

This apparent anomaly has encouraged the Swansea group to take a rather radical stance on mechanistic issues. First they reject the actuality of diffusional creep, in practical terms. They claim that even in stress-temperature regimes where n = 1, the governing mechanism is based on dislocations, not direct diffusion. They offer experimental support to their claims (Wilshire 1990). However, this contravention of extant understanding (and a holistic denial of published experimental evidence) is extreme and unnecessary (in this author's opinion). Indeed, personal discussion with Evans and Wilshire (R. Dutton, 1994, memorandum to J.L. Crosthwaite) has revealed some compromise on this position. Thus, an alternative (and preferred) viewpoint is as follows. From the inception of the deformation map concept, and entrenched in all mechanistic theory, it is always understood that all acceptable deformation mechanisms occur simultaneously. The fields of the mechanism maps represent, only, regions in the stress-temperature plane where an individual deformation mechanism is dominant. Therefore it is feasible (required, actually) that the θ parameters capture the concurrent existence of all relevant mechanisms. The variation of θ with stress and temperature reflects the moving contribution of all of these mechanisms. However, for this crucial information to be contained in the derived θ-parameters, it is vital to ensure that they are obtained from a data set that adequately samples the full expression of all of the deformation mechanisms. Thus, in the specific case of the container-shell material, particularly with long-term projection in mind, we must ensure that the range (particularly stress range) of our experimental database is sufficiently wide. This emphasizes the utility of combining the use of Deformation Mechanism Maps with the θ Projection Concept. The map

will force us to pay particular attention to extrapolation across mechanism field boundaries. The examples for steel and copper described above (and the referenced application to other materials, both metals and ceramics) clearly demonstrate that this is readily achieved in practice.

9.6 PROJECTION OF RUPTURE LIFETIMES

While Eqns. (54) and (59) appear to offer a highly satisfactory means of predicting creep curves, this type of analysis does not specifically refer to fracture. Hence, to complete the description of creep behaviour, it is necessary to define some suitable failure criterion. Although the mechanistic understanding of the precursors to fracture is in place (Section 6.4), the critical damage level at which final rupture occurs is ill-defined, as explained in Section 8. A convenient way of marking the termination of the creep curve (e.g., those shown in Figure 42) is to specify either the rupture time or the rupture strain. The Swansea group has recommended the limiting creep strain, or ductility, as the parameter more amenable to long-term projection. This choice is largely based on the observation that the creep ductility does not vary markedly with stress (Figure 46), whereas the creep life changes by several orders of magnitude over the same range of test conditions (Figure 47).

Figure 46 shows that the creep ductility, ε_f, decreases gradually with decreasing stress at each creep temperature. This suggests that the applicable relationship, equivalent to Eqn. (59), is

$$\epsilon_f = a + b\sigma + cT + d\sigma T \tag{61}$$

where the constants a, b, c and d can be evaluated by multilinear least squares regression analysis of the data shown in Figure 46. These values, for copper and steel are included in Table 2.

Having obtained the appropriate value for ε_f, the θ parameters can be used to estimate the time to rupture, t_r. This is the time taken for the accumulated creep strain to reach the total ductility, ε_f. For this purpose, the time (t') to reach some specified creep strain (ε') is obtained by solving (numerically) the equation

$$\theta_1(1 - e^{-\theta_2 t'}) + \theta_3(e^{\theta_4 t'} - 1) - \epsilon' = 0 \tag{62}$$

By setting $\varepsilon_f = \varepsilon'$, the rupture time is given at $t_r = t'$. Note also that the strain rate at any strain, ε', can be obtained simply by substituting t' into Eqn. (56).

Using the strain to failure criterion, a variety of creep-curve equations have been compared to assess their capability of predicting the rupture time (Brown 1987). The polynomial equations described in Section 4.2 were included. It was demonstrated that the θ Projection Concept provided the most accurate prediction.

It is expected that there will be relatively little error in the projection of rupture life, even if the material ductility does change unexpectedly at low-stress levels. Thus, in low stress tests, the creep curves are typically dominated by the tertiary process, defined by θ_3 and θ_4. The

strain/time behaviour may then be considered simply in terms of a gradually increasing creep rate throughout virtually the entire life. In the late stages of the tertiary process, the creep rate is accelerating very rapidly. As a consequence, even a substantial change in ductility should cause only a relatively small variation in rupture life under these conditions.

Using the coefficients in Table 2, the predicted stress-rupture curves for the 0.5Cr-0.5Mo-0.25V steel are shown in Figure 47. It is important to note that the experimental data used for the creep-curve analysis were from tests lasting less than 1200 h. Despite the short-term nature of these data, Figure 47 shows that the predictions are accurate for times in excess of 100,000 h, as confirmed by the long-term stress-rupture data (Johnson et al. 1967) included in the graph. Furthermore, the θ Projection Concept can be used to test the Monkman-Grant relationship. The relevant plot is shown in Figure 48, where again, the theoretical predictions are in excellent agreement with the experimental data. Although the extrapolated lines show appreciable curvature (reflecting the pronounced curvature of Figure 10), they are reasonably linear over quite extended times, and the plots obtained at different temperatures superimpose reasonably well.

Although the results described above on the 0.5Cr-0.5Mo-0.25V steel are impressive, the Swansea group did not consider them to be a definitive test of the θ Projection Concept because the creep tests (to obtain the θ parameters) were performed on a different batch of material to that used to measure the creep-rupture lives. In fact, the creep-rupture data (Johnson et al. 1967) were obtained from multi-laboratory testing (e.g., such as those shown in Figure 17), hence the relatively large scatter band (up to ± 20% in stress) indicated in Figure 47. Thus, even rather poor predictions may well have fitted within such broad scatter bands. To avoid this shortcoming, a large ongoing collaborative study (Swansea University, GEC, Babcocks Energy, National Power, Power Gen and Nuclear Electric) was undertaken on a 1Cr-Mo-V rotor steel. The initial results have been published (Evans et al. 1993c, Wilshire and Evans 1994), and are shown in Figure 49. The short-term data (up to about 1000 h), shown as open symbols, were used to extrapolate the times to rupture. These extrapolations are seen to be in excellent agreement with the long-term rupture data (full symbols). This comparison was conducted with a "double blind" protocol in place, to avoid any bias in the analysis. Note that the short-term creep tests were performed under constant-stress conditions and the long-term tests under constant-load conditions. Using the θ Projection Concept, it is relatively easy to produce predictive plots for either loading mode. It is instructive to observe the better agreement of the long-term experimental data with the appropriate constant-load prediction, a graphic illustration of the power and accuracy of the derived θ parameters.

Figures 47, 48 and 49 provide a convincing demonstration of the applicability of the θ Projection Concept to rupture times and creep ductility. It is clear that long-term rupture lives can be estimated from short-term measurements of creep behaviour. However, care should be taken in using the methodology to extrapolate outside the temperature range of the experimental data. This is due to the fact that although Eqn. (58) has a sound theoretical foundation (e.g., the activation energies of the rate parameters θ_2 and θ_4 are related directly to their controlling mechanisms), Eqns. (59) and (61) are essentially empirical (i.e., their coefficients have no mechanistic significance). In this regard, additional guidance can be obtained from the Deformation Mechanism Maps, and to a lesser extent, the Fracture Mechanism Maps.

10. CONCLUDING REMARKS

10.1 GENERAL COMMENTS

We have seen that the constitutive equation embedded in the θ Projection Concept is specifically formulated to capture the phenomenological shape of the entire creep curve. This axiomatic principle has immediate appeal. Through its representation of the complete creep behaviour, it facilitates the precise calculation of creep strain, deformation rates and times to failure. As the mathematical formulation is based on established mechanistic understanding, it lends confidence to long-term extrapolation outside of the experimental database. Whereas the classical approach is generally based on the concept of a single-valued steady-state creep rate, expressed as a function of stress and temperature, the θ Projection Concept employs four rate constants to represent the stress and temperature dependence of the complete creep-curve shape. Combined with a simple fracture criterion, this facilitates the computation of rupture life at any stress or temperature. The accuracy of this predictive capability has been well demonstrated. In their latest paper (Wilshire and Evans 1994), the Swansea group has shown that the predicted behavioural pattern determined from tests lasting up to 1000 h correlated extremely well with the independently measured long-term data for conditions that would have resulted in creep lives well in excess of 100,000 h. It is significant to note that this impressive projection was made for a 0.5Cr-0.5Mo-0.25V steel, which is known to exhibit marked changes in carbide precipitate dispersion during prolonged creep exposure. The θ-relationships are obviously capable of quantifying the complex long-term effects associated with such progressive changes in microstructure. Because of the simple single-phase composition of the relatively pure titanium and copper intended for the fuel waste container, these microstructural changes will not occur. Therefore, it is reasonable to expect that even longer-term extrapolations (up to ~5,000,000 h) for these materials will be reliable. A conservative fracture criterion will serve to provide added confidence. The level of confidence can be estimated from a statistical analysis of the θ-parameters. A formal procedure for accomplishing this has been published (Evans 1989, 1990).

Since its introduction in 1982, the θ Projection Concept has found international acceptance in the scientific and engineering communities. Thus, as shown in Section 9.4, the methodology has been applied to a wide range of materials, including pure metals, steels, superalloys and ceramics. The Swansea group has, naturally, spearheaded this effort. They have been successful in attracting substantial external financial support which has enabled them to develop a large and sophisticated creep laboratory, with over 50 modern creep machines and supporting equipment (Dutton 1994). As a result, extensive collaborative and contractual research is being conducted with major companies including Nuclear Electric, GEC, Babcocks Energy, National Power, Power Gen, Rolls Royce, Pratt and Whitney, etc. Whereas much of this work is published in the open literature, a large fraction of the data are protected by proprietary interests. Other European, North American and Japanese laboratories are also adopting the same approach. In some instances, the commercial interest is in data interpolation. An example would be in high-temperature gas turbine blades. The challenge is to predict creep strains and creep lives with great precision, and in a format suitable for complex finite element analysis. In this case, creep testing spans the actual operating temperatures, stresses, and the expected component lifetimes. In contrast, an emphasis on extrapolation of the creep data to longer service lifetimes is the focus of studies on high-temperature steam generating components used in thermal power plants. This widespread adoption of the θ Projection Concept reflects substantial endorsement of the technique as a

practical solution to a long-standing problem. Such interest and effort ensures the ongoing refinement and extension of the methodology.

The fact that the θ Projection Concept casts some doubt on the reality of a period of constant creep rate during the secondary stage, does not imply that we should discard the extensive body of literature dealing with steady-state creep mechanisms. A useful starting point to examine this issue is to revisit the role of the work-hardening rate (h) and the recovery rate (r), discussed in Section 6.3.1. Thus, Eqn. (29) can be rewitten as

$$\dot{\epsilon} = \left(\frac{\partial \epsilon}{\partial t}\right)_{\sigma} = -\left(\frac{\partial \sigma}{\partial t}\right)_{\epsilon} \Big/ \left(\frac{\partial \sigma}{\partial \epsilon}\right)_{t} = \frac{r}{h} \tag{63}$$

It has been pointed out by Davies and Stevens (1993) that Eqn. (63) should apply throughout the creep curve, not just in the steady-state region.[9] Primary and tertiary creep then arises because the values of r and h vary with time, or strain. Differentiation with respect to time gives

$$\frac{\partial \dot{\epsilon}}{\partial t} = \ddot{\epsilon} = \frac{h\dot{r} - r\dot{h}}{h^2} \tag{64}$$

where

$$\dot{r} = \left(\frac{\partial}{\partial t}\right)_{\sigma}\left(\frac{\partial \sigma}{\partial t}\right)_{\epsilon} \quad \textit{and} \quad \dot{h} = \left(\frac{\partial}{\partial t}\right)_{\sigma}\left(\frac{\partial \sigma}{\partial \epsilon}\right)_{t}$$

and since h > 0 for plastic stability, then during primary creep we have

$$\ddot{\epsilon} < 0 \qquad \frac{\dot{r}}{r} < \frac{\dot{h}}{h} \tag{65}$$

while during tertiary creep

$$\ddot{\epsilon} > 0 \qquad \frac{\dot{r}}{r} > \frac{\dot{h}}{h} \tag{66}$$

The condition prevailing in secondary creep is represented by

$$\frac{\dot{r}}{r} = \frac{\dot{h}}{h} \tag{67}$$

---

[9] In the context of Section 6.3.1, the rate of hardening is always balanced by the rate of recovery such that $d\sigma = 0$ applies throughout the creep curve. This is a necessary condition because under creep conditions, the flow stress is always equal to the applied stress.

This equality can be accomplished in two ways. The first is that Eqn. (67) is equal to zero. This would represent the fact that a state of constant structure exists, e.g., that the dislocation density is constant, leading to a finite period of constant creep, i.e., an extended steady-state secondary stage. The second possibility is that Eqn. (67) is not equal to zero. This would correspond to the situation where no steady-state creep exists, but rather the secondary creep is only a point of inflection. Such a minimum creep rate is the situation proposed within the θ Projection Concept. In actuality, within a dynamic system of interacting mechanisms, it would be fortuitous to expect the existence of an extended time period over which the microstructure (including the dislocation density) remains precisely constant. Regardless of whether Eqn. (67) is equal to zero, or not,[10] this analysis highlights the role of the evolving microstructure in determining the values of r and h, and their variation with time (or strain). This is the essence of the derivation of the primary creep mechanism described in Section 6.3.2. Within the theories of steady-state creep, the parameters characterizing the microstructure are generally contained in a preexponential constant. This is the constant A in the general creep equation (Eqn. (10)), the constant B in the generic dislocation-creep equation (Eqn. (34)), and the constant A in the specific creep equation based on dislocation climb (Eqn. (38)). Thus, the existence of a constant creep rate in the steady-state mechanisms discussed in Section 6 is contingent on the constancy of the preexponential structural parameter. This does not refute the reality, or application, of the established creep mechanisms, and their attendant rate equations. Indeed, we note that the values of the preexponential constants are evaluated directly from experimental creep-rate data, using the assumption that a steady state exists (within the limitation of current theoretical understanding, there is no a prior method to calculate the preexponential constant). Accordingly, to the extent that this represents a reasonable representation of experimental data, while retaining the essential mechanistic understanding, the Deformation Mechanism Maps described in Section 7 are valid and representational. Indeed, there has been no claim that the Maps capture the total creep behaviour, including primary and tertiary creep. This limitation is understood.

Within this framework, we are justified in using the mechanistic equations and the Deformation Mechanism Maps as a guide to interpretation and extrapolation. Thus, the Maps can be used to identify the prominent mechanism that prevails within prescribed boundaries of stress and temperature. Furthermore, the mechanistic equations will provide reasonable estimates of the characteristic creep rate. Accordingly, it is reasonable to use Figures 29 and 30 to determine that, at the maximum operating temperature (100°C) of the fuel-waste container, deformation at high stresses will occur by power-law creep and at lower stresses, by diffusional creep. In both instances, the creep rate will be controlled by diffusion along easy paths, such as grain boundaries or dislocations. Creep rates of 10^{-11} sec^{-1}, or less, are to be expected. Of course, these statements do not exclude the possibility that alternative mechanisms exist, and have not been identified on the Maps. In this context, we must bear in mind that there is a dearth of experimental data available within the extreme left-hand portion of the Maps. One of the objectives of our experimental creep program will be to provide some of these data. An analysis of the temperature and stress dependence of the θ-parameters will enable these mechanisms to be identified. For example, the work of Zeyfang et al. (1971) indicates that the creep rate of titanium at ~80°C is controlled by dislocations overcoming interstitial solute barriers in a (unspecified) thermally activated fashion. It is interesting to note that their data

---

[10] Davies and Stevens present some experimental evidence supporting the conclusion that $\dot{r}/r = \dot{h}/h = 0$ and hence it is "probable" that a secondary stage truly exists, at variance with the θ Projection Concept. However, they point out that this conclusion is "subject to some experimental uncertainty".

show that the change in strain rate during primary creep was proportional to the strain, i.e., that it followed the first-order rate kinetics predicted by the θ Projection Concept. However, the creep rates examined were quite high, ~10^{-4} sec^{-1}. This would place (quite appropriately) the mechanism within the obstacle-controlled plasticity region of the Deformation Map in Figure 29. It will be important to establish, for our material, the stress level that defines the lower boundary of this deformation field. At this juncture, it is important to emphasize that the θ Projection Concept makes no assumption regarding the precise deformation micromechanism that controls the creep rate. Thus, the rate equation developed in Section 6.3.2, on which the formulation of primary creep (i.e., θ_1 and θ_2) is based, is generic in nature. It is only necessary to assume that deformation occurs when thermally activated events manage to overcome internal activation barriers, and that when such events occur, they are governed by Boltzmann statistics. If the activation barriers are allowed to have strengths that can increase by work hardening, or decrease by recovery processes, the general form of primary creep behaviour can be derived, and the kinetics obey first-order rate theory. In a similar manner, the representation of the tertiary region, through the θ_3 and θ_4 parameters, is based on the assumption that damage mechanisms are becoming prominent. Furthermore, the rate of damage accumulation is linked to the deformation rate (and hence the work-hardening and recovery rates), as explained in Sections 4.3 and 9.2, and obeys first-order rate kinetics.

The θ Projection approach is not unique in its use of the mechanistic understanding of creep mechanisms to develop a constitutive equation describing the complete creep curve. Thus, Chandler (1990) has modified the steady-state deformation equations from the Deformation Mechanism Maps to describe primary creep. This was achieved by replacing the applied stress by a driving stress that is progressively reduced in strength by a work-hardening term that is essentially introduced as a microstructural factor within the preexponential parameter. Similarly, the equations derived from the Fracture Mechanism Maps are added to introduce the accelerating tertiary stage. A similar procedure is used by Dyson and McLean (1990), as discussed further below. A hybrid approach was used by Shen and Plumtree (1990). They used the standard θ-equation to describe the primary stage, but a modified formulation to describe the tertiary stage. In this case, a damage accumulation parameter was used to represent a continual increase in the effective stress due to a progressive loss of load-bearing area. Such an approach is parallel to that of Kachanov (1958) and Rabotnov (1969), discussed in Section 4.3. The resulting equation gives a better fit to tertiary creep that exhibits a rapid acceleration of creep rate, a phenomenon described in Section 10.3. However, similar to the form of Eqn. (17), the rupture time enters the equation as an essential parameter, hence somewhat defeating the objective of predicting the lifetime.

Of the alternative analytical approaches mentioned above, that of Dyson and McLean (1990) warrants further discussion. This work represents the development of a creep analysis methodology by the National Physics Laboratory (NPL) in the UK. Their constitutive equations are based on strain <u>rate</u> expressions (rather than strains as in the θ Projection Concept), the creep curve then being obtained via numerical integration. Despite this difference, the NPL group also consider the shape of the creep curve to be determined by the decreasing creep rate of the primary stage being superseded by an accelerated tertiary stage, leading to fracture. Similar to the θ Projection Concept, four parameters are used to capture this overall process. These include parameters that represent the strain hardening and recovery processes. Most of the creep modelling emphasis is placed on those recovery, or "softening", processes that characterize the tertiary creep stage. Within the mathematical formulation, the creep damage parameter of Kachanov (1958) and Rabotnov (1969) is used. Depending on

the material, a wide range of damage mechanisms can be included in the tertiary softening process. These have been classified by Dyson (1992) and include cavity growth, microstructural instability and corrosion processes. Based on these considerations, NPL has developed a software package called CRISPEN (Dyson and McLean 1990) to extract the four constitutive parameters from experimental creep data, integrate the rate equations to obtain the creep curves, and facilitate predictive extrapolation. More complex conditions, such as those involving multiaxial stress states can be handled by the more sophisticated numerical integration schemes contained in the CREEPSIM software package (Osgerby et al. 1992).

The NPL group have used their methodology to analyze the creep behaviour of high-strength steels (Dyson and Osgerby 1993, Osgerby and Dyson 1994a) and nickel-based superalloys (McLean et al. 1992). The creep curves of all of these materials are dominated by tertiary creep, most of which is characterized by softening due to precipitate coarsening. Using the CREEPSIM software, the creep data have been used to predict stress-strain (Osgerby and Dyson 1993) and stress relaxation (Osgerby and Dyson 1994b) behaviour. Within all of these applications, the NPL group has not demonstrated the capability of their methodology to perform long-term projection of creep data, equivalent to that of the θ Projection Concept, as described in Section 9.6. In fact, based on the fact that both methods use four parameters to describe similar strain hardening and softening phenomenon, Dyson and McLean (1990) acknowledge the equivalence of the two approaches, but claim an advantage of using CREEPSIM for more complex multiaxial bonding conditions.

10.2 DATA ANALYSIS AND PERFORMANCE PROJECTION

As mentioned earlier, a program of creep testing of titanium has been initiated at the Whiteshell Laboratories. At the time of writing, one of these tests, conducted at 100°C and 187 MPa, has proceeded to failure after a total lifetime of about 24,000 h. The creep curve is shown in Figure 50. This confirms that at this temperature considerable creep strain (>0.2) occurs in titanium and the classical three-stage behaviour is evident. Most of the creep life is composed of primary creep, with a rather abrupt onset of the tertiary stage: a definitive secondary stage is not apparent. There will be more detailed discussion of this and other current creep data in a future report.

The creep data, such as those shown in Figure 50, will be subsequently analyzed using the θ Projection Concept. This will be facilitated by employing a commercial computer software package, the "Theta Projection Analysis Suite", acquired from Swansea University. This package consists of a suite of 19 computer programs (including a comprehensive user manual), which is designed to accomplish tasks such as:

- edit the experimental data,
- plot the experimental creep curves,
- fit the theoretical θ-parameter creep curves,
- extract the θ parameters,
- statistical analysis of the parameters,
- determine stress and temperature dependence of parameters, and
- predict long-term creep strains, rates and rupture times.

These capabilities are precisely those needed to analyze our experimental creep data, provide a constitutive equation suitable for the finite element code we are developing, and extrapolate the creep behaviour characteristics over the lifetime of the container. The software suite is

being used by a significant number of other researchers, and hence is well tested and has found general acceptance in the scientific/engineering community.

Since the θ Projection Concept, supported by the software package, allows any creep-strain or creep-rate parameter to be calculated in a highly computer-efficient manner, it is ideally suited to engineering design and assessment. In many circumstances, the thermal and mechanical conditions vary in some structural components during operation: the prevailing conditions often change with time. With the computer-based finite element methods, procedures must be developed for handling changes in stress and temperature during service.

If the operating conditions change from $\sigma_1 T_1$ to $\sigma_2 T_2$, there is no practical difficulty in computing the θ values at $\sigma_2 T_2$, and hence in constructing the new creep curve. However, it is not immediately apparent how the new creep rate is to be calculated from the new curve. The problem is illustrated in Figure 51 where two schematic creep curves are shown for the conditions $\sigma_1 T_1$ and $\sigma_2 T_2$. It is possible to proceed from the first curve to the second along many alternative paths, the extreme cases being referred to as time-hardening (A) and strain-hardening (B). In many circumstances, studies of the effects of changes in stress and temperature have shown that the strain-hardening path is very nearly correct and a simple constitutive relationship can be constructed on this basis (Evans and Wilshire 1987, Wilshire 1989). Thus, if a strain ε_1 has been attained at $\sigma_1 T_1$, then the corresponding θ-values are (from Eqn. 59) θ_i such that

$$\log \theta_i = f(\sigma_1 T_1) \tag{68}$$

and (see Eqn. (56))

$$\dot{\epsilon}_1 = \theta_1\theta_2 \exp(-\theta_2 t^*) + \theta_3\theta_4 \exp(\theta_4 t^*) \tag{69}$$

where, from Eqn. (62), t^* is the root of

$$\theta_1(1 - e^{-\theta_2 t}) + \theta_3(e^{\theta_4 t} - 1) - \epsilon_1 = 0 \tag{70}$$

When the operating conditions are changed to $\sigma_2 T_2$, the new creep rate $\dot{\varepsilon}_2$ will be given by

$$\dot{\epsilon}_2 = \theta_1'\theta_2' \exp(-\theta_2' t') + \theta_3'\theta_4' \exp(\theta_4' t') \tag{71}$$

where $\log \theta_i' = h(\sigma_2 T_2)$ and t' is the root of

$$\theta_1'(1 - e^{-\theta_2' t}) + \theta_3'(e^{\theta_4' t} - 1) - \epsilon_1 = 0 \tag{72}$$

In this way, the θ Projection Concept provides the complete constitutive relationship for the material, which is required to be able to apply the computer-based analysis to conditions of various stresses and temperatures. This method was used (Evans et al. 1993c) to convert constant-stress creep data into constant-load creep-rupture data, as shown in Figure 49. Similar examples are presented by Taylor et al. (1990). The technique has also been used successfully in the design of, and service lifetime calculations for superalloy turbine blades (Evans and Wilshire 1987).

In Section 3.1, it was pointed out that for the packed-particulate container to be used for storing fuel waste, the deformation rate of the container shell may be controlled by the creep rate of the particulate. An understanding of material behaviour (such as the container shell) under conditions of constant strain rate is frequently required for the design of components subjected to creep deformation. However, the experimental acquisition of such constant strain-rate data is expensive compared to the procurement of creep data, because of the more sophisticated test equipment required. Fortunately, methods have been developed to predict constant strain-rate behaviour from creep data. A recent example comes from the work of Osgerby and Dyson (1993). The methodology uses the fact that the total strain rate, $\dot{\varepsilon}_T$, under changing stress conditions is given by

$$\dot{\epsilon}_T = \frac{\dot{\sigma}}{E} + \dot{\epsilon} \tag{73}$$

where E is the elastic modulus. The rate of change of stress under constant strain-rate conditions, $\dot{\varepsilon}_T = K$ is then given by

$$\dot{\sigma} = E\,(K - \dot{\epsilon}) \tag{74}$$

By numerically integrating the constitutive equation for $\dot{\varepsilon}$, under the constraint imposed by Eqn. (74), the stress-strain curve appropriate to the constant strain rate K is obtained. Osgerby and Dyson did not employ the θ Projection equation. However, they used the constitutive equation developed at NPL (see Section 10.1), which is similar to the θ Projection Concept. An example creep curve for the Nimonic 101 alloy is shown in Figure 52, with the fit to their constitutive equation. Such creep data was then used to construct the stress-strain curve shown in Figure 53. Also shown on this figure is an actual experimental plot of a constant strain-rate test. As can be seen, there is good agreement between the experimental data and the behaviour predicted from the model that utilized the constant-load creep data. The model can be used to predict the stress-strain curve for any given constant strain rate. Figure 53 shows the stress rising initially to a peak value, corresponding to the hardening-dominated primary creep behaviour. Then, as the softening processes accompanying tertiary creep become more dominant, the stress decays monotonically. A similar procedure can be carried out using the θ-equation.

The above examples demonstrate the capability and flexibility of the θ Projection Concept in analyzing and predicting creep strains and creep rates. As has already been discussed, to be in a position to project creep-rupture times, there is a need to specify a fracture criterion. This is the topic of the next section.

10.3 FRACTURE CRITERION

The discussion of fracture mechanisms in Section 6.4 and Fracture Mechanism Maps in Section 8 pointed out that the micromechanisms responsible for fracture can be varied and complex. Consequently, the form of the tertiary stage cannot be defined with the same precision as that of the primary stage, reflecting the generally poorer qualitative understanding of rupture processes and their coupling with tertiary deformation. The θ Projection Concept assumes that the rate-controlling process follows first-order kinetics. However, for example, Figure 24 shows that if gross necking is prevalent, first-order kinetics does not apply, the acceleration of the creep rate proceeding in a more rapid fashion. This effect is illustrated by the creep curve for titanium, shown in Figure 50. Thus, compared with the creep curve for steel shown in Figure 39, the later stage of tertiary creep in titanium accelerates much faster, due to the early onset of necking. These inherent uncertainties can cause some error in the prediction of times to rupture based on the derivation of the θ_3 and θ_4 parameters from the experimental data. In particular, it is the rate constant θ_4 that loses its capability of fitting the complete tertiary stage when the apparent creep rate increases rapidly under the rising stress conditions in the necked region. These deficiencies have been addressed by several workers.

In a study of four ferritic steels, Maruyama and Oikawa (1987a) used the θ Projection Concept to identify the nature of the creep mechanisms. The later stages of tertiary creep deviate from the θ-equation, because of gross necking instability. This deficiency was solved by truncating the experimental data before fitting the θ-equation. Not only did this improve the fit with the tertiary stage, but also improved the fit in the earlier primary stage. To avoid arbitrariness in the truncation, the values of θ_2 and θ_4 were calculated over a range of cut-off strains. The strain at which $\theta_2 = \theta_4$ was chosen as a standard criterion (Maruyama and Oikawa 1987b). Such a constitutive equation that equates θ_2 and θ_4 has been criticized by Brown et al. (1986b), who revealed several analytical inadequacies. This procedure was also found to be inapplicable for a nickel-based superalloy (Li et al. 1987). The values of θ_1, θ_2, θ_3 and θ_4 become constant above a specific cut-off strain. This characteristic, together with an examination of the standard error of fitting, was used for the truncation criterion.

The utilization of the truncation strategy has also been used for the projection of creep properties and times to rupture for steels (Taylor et al. 1990, Li et al. 1990). Again, it was observed that in the absence of truncation, the θ_3 and θ_4 parameters were so scattered that their predictive capability was poor. The situation was significantly improved by truncating the creep curves to eliminate the period of gross necking. An investigation of the sensitivity of the calculated θ values to the level of truncation showed that provided the final stage of the creep curves was removed, the results were not significantly affected by the cut-off point. A standard truncation criterion of the strain at seven times the minimum creep rate was established, and was found to be successful in offering accurate predictability.

The problem of the shape of the tertiary creep stage being disturbed by necking has been recognized by the Swansea group. To overcome this difficulty, their θ Projection software suite includes a data truncation criterion based on the onset of rapid creep-rate acceleration. In addition, they have prepared (Evans and Wilshire 1993) a modified form of the θ Projection equation for a material that displays little or no tertiary creep, as depicted in Figure 54. Such behaviour is related to the necking phenomenon, but in this case the instability is a result of an intolerance to tertiary damage. For example, in an exceedingly brittle material (a ceramic would be a primary case) internal damage is likely to result in the formation of a microcrack that propagates very rapidly, in an unstable manner. This causes premature termination of

the primary creep stage so that little tertiary stage is discernable. To accurately describe such a creep curve, Eqn. (54) must be modified by expanding the tertiary exponential term by means of its Taylor series so that

$$\epsilon = \theta_1(1 - e^{-\theta_2 t}) + \theta_3\theta_4 t \tag{75}$$

This equation is identical to that of Garafalo et al. (1963), shown as Eqn. (7) in Section 4.2. It consists of a primary stage that enters a steady-state secondary stage. Such an equation has been successfully used to analyze the creep behaviour of ceramics (Wilshire 1993b).

In Section 9.6, we saw how the θ Projection Concept employs a fracture criterion based on the total strain to rupture following the ultimate termination of tertiary creep. The rupture time, which is the primary engineering parameter used to predict the useful lifetime of a component, is obtained by using the θ-based deformation equation to compute the time required to reach the rupture strain. However, we have seen from the discussion presented above that in many cases there is reduced confidence in the capability of the θ_3 and θ_4 parameters to predict the total shape of the complete tertiary stage. This uncertainty is associated with the complexity and coexistence of multiple damage processes leading to fracture. In addition, the precise quantitative understanding of the detailed micromechanisms of intergranular cavity and crack formation is imperfectly understood. In many practical instances, these shortcomings are offset by the fact that the errors of prediction are not significant. This fortunate circumstance arises because in a condition of rapid acceleration of the creep rate, an uncertainty in the rupture strain does not have a large effect on the calculated rupture time. Notwithstanding the general validity of this conclusion, we think it prudent to employ a more conservative fracture criterion into the design of the fuel waste container. We don't wish to operate the container under extended periods of tertiary creep, particularly recognizing that at the relatively low operating temperatures, premature instability due to the necking phenomenon is a likely scenario. Recognizing that we will forfeit available lifetime, we will adopt a fracture criterion where the maximum allowable design strain is less than the actual rupture strain. A considerable safety margin would be secured by setting this limiting strain to that which exists at the onset of tertiary creep, i.e., the strain to reach the minimum creep rate. The θ-based equation is ideally suited to the determination of this condition. Thus, the lifetime would then be defined by the employment of Eqn. (57). However, our experimental program, and the θ Projection equation that arises may show that the majority of the long-term creep curve is actually dominated by the tertiary stage. In this case, the onset of tertiary creep may represent a criterion that is unsatisfactorily limiting, excessively conservative. Under such circumstances, a more suitable, yet acceptible criterion may be set by choosing a creep strain where the creep rate has increased to some modest level, e.g., three times the minimum creep rate[11]. In this context, we may recall the truncation criterion of Taylor et al. (1990) and Li et al. (1990) of seven times the minimum creep rate, as described above. The eventual decision on the precise value of the multiplying factor can be made after we have completed our experimental creep program and formulated our appropriate θ-equation. Whatever

---

[11] This criterion strictly applies to creep conditions, where the prevailing stress is less than the yield-stress. As discussed in Section 2.3, it is possible that small-scale plastic deformation may initially occur in localized areas where the yield-stress is exceeded. Under these rapid strain-rate conditions, the appropriate maximum strain criterion is obtained from short-term tensile tests, as described by Teper (1988).

criterion we ultimately set, the θ Projection Concept, supported by the complementary Deformation Mechanism Map, provides an immediate tool to compute the container lifetime. In addition, the Fracture Mechanism Map will provide a comparative estimate of rupture time, from which we can extract a supplementary evaluation of the safety factor.

ACKNOWLEDGEMENTS

This document was prepared in support of the Canadian Nuclear Fuel Waste Management Program, which is funded jointly by AECL and Ontario Hydro under the auspices of the CANDU Owners Group.

The author would like to thank Drs. B. Wilshire and R.W. Evans of Swansea University, and Drs. R.N. Stevens and C.K.L. Davies of the University of London for extensive and penetrating discussions on the θ Projection Concept and Deformation Mechanism Maps. While these researchers offered valuable insight into these methodologies, the author is solely responsible for any nuances of interpretation that might deviate from their viewpoint. Within this spirit, the carefull review of the manuscript, and the useful comments provided by my colleagues, J.L. Crosthwaite, B.W. Leitch and B. Teper, are gratefully acknowledged.

REFERENCES

Adenstedt, H. 1949. Creep of titanium at room temperatures. Metal Progress 56, 658-660.

Andrade, E.N. da C. 1910. The viscous flow in metals, and allied phenomena. University College, London. Proceedings of the Royal Society, London (A) 84, 1-12.

AECL (Atomic Energy of Canada Limited). 1994. Environmental impact statement on the concept for disposal of Canada's nuclear fuel waste. Atomic Energy of Canada Limited Report, AECL-10711, COG-93-1. Available in English and French.

Ashby, M.F. 1972. A first report on deformation-mechanism maps. Acta Metallurgica 20, 887-897.

Ashby, M.F., C. Gandhi and D.M.R. Taplin. 1979. Fracture-mechanism maps and their construction for F.C.C. metals and alloys. Acta Metallurgica 27, 699-729.

Bailey, R.W. 1926. Note on the softening of strain-hardened metals and its relation to creep. Engineering 121, 351-352.

Balluffi, R.W. and L. Siegle. 1955. Effect of grain boundaries upon formation and dimensional changes during diffusion. Acta Metallurgica 3, 170-177.

Beere, W. and M.V. Speight. 1978. Creep cavitation by vacancy diffusion in plastically deforming solid. Metal Science Journal 12, 172-176.

Brown, S.G.R. 1987. Extrapolation by creep-curve shape analysis. In Creep and Fracture of Engineering Materials and Structures (B. Wilshire and R.W. Evans, editors), Proceedings of the Third International Conference, University College, Swansea, 1987, 829-838.

Brown, S.G.R., R.W. Evans and B. Wilshire. 1986a. Creep strain and creep life prediction for cast nickel-based superalloy IN-100. Materials Science and Engineering 84, 147-156.

Brown, S.G.R., R.W. Evans and B. Wilshire. 1986b. Exponential descriptions of normal creep curves. Scripta Metallurgica 20, 855-860.

Brown, S.G.R., R.W. Evans and B. Wilshire. 1987. New approach to creep of pure metals with special reference to polycrystalline copper. Materials Science and Technology 3, 23-27.

Cane, B.J. and P.F. Aplin. 1994. Creep life assessment methods. The Journal of Strain Analysis 29, 225-232.

Carpenter, G.J.C. 1971. Diffusion coefficient as a guide to prospects for high temperature zirconium alloys. Atomic Energy of Canada Limited Report, AECL-3967.

Chandler, H.D. 1990. Creep-curve descriptions in terms of deformation and damage accumulation mechanisms. In Creep and Fracture of Engineering Materials and Structures (B. Wilshire and R.W. Evans, editors), Proceedings of the Fourth International Conference, Swansea, 1990, 975-984.

Coble, R.L. 1963. A model for boundary diffusion controlled creep in polycrystalline materials. Journal of Applied Physics 34, 1679-1682.

Cocks, A.C.F. and M.F. Ashby. 1982. On creep fracture by void growth. Progress in Materials Science 27, 189-244.

Conrad, H. 1981. Effect of interstitial solutes on the strength and ductility of titanium. Progress in Materials Science 26, 123-403.

Conway, J.B. 1967. Numerical Methods for Creep and Rupture Analyses. Gordon and Breach Science Publishers, Incorporated, Newark, N.J.

Crosthwaite, J.L. 1994. The performance, assessment and ranking of container design options for the Canadian Nuclear Fuel Waste Management Program. Atomic Energy of Canada Limited Technical Record, TR-500, COG-93-410.

Crosthwaite, J.L., J.N. Barrie and K. Nuttall. 1982. Design, fabrication and testing of a prototype stressed-shell fuel isolation container. Atomic Energy of Canada Limited Report, AECL-6823.

Davies, C.K.L. and R.N. Stevens. 1993. Constant steady-state creep in a Cu-9 atomic % Al alloy? In Creep and Fracture of Engineering Materials and Structures (B. Wilshire and R.W. Evans, editors), Proceedings of the Fifth International Conference, Swansea, 1993, 31-40.

Davies, P.W., W.J. Evans, K.R. Williams and B. Wilshire. 1969. An equation to represent strain/time relationships during high temperature creep. Scripta Metallurgica 3, 671-674.

de Lacombe, J. 1939. Method for expressing creep curves. Revue de Metallurgie 36, 178-188.

Dutton, R. 1969. A survey of compression creep testing of metals. Materials Research and Standards 9, 11-17.

Dyson, B.F. 1976. Constraints on diffusional cavity growth rates. Metal Science Journal 10, 349-353.

Dyson, B.F. 1992. Materials data requirements, creep damage mechanisms, and predictive models. In High Temperature Structural Design (L.H. Larson, editor). Mechanical Engineering Publications, London, 335-354.

Dyson, B.F. and M. McLean. 1990. Creep deformation of engineering alloys - developments from physical modelling. Iron and Steel Institute of Japan International 30, 802-811.

Dyson, B.F. and S. Osgerby. 1993. Modelling and analysis of creep deformation and fracture in a 1 Cr ½ Mo ferritic steel. National Physics Laboratory Report, DMM(A)116.

Evans, H.E. 1973. A model of strain hardening during high-temperature creep. Philosophical Magazine 28, 227-230.

Evans, H.E. 1984. Mechanisms of Creep Fracture. Elsevier Applied Science Publishers, London.

Evans, R.W. 1989. Statistical scatter and variability of creep property estimates in theta projection method. Materials Science and Technology 5, 699-707.

Evans, R.W. 1990. Statistics of creep property estimation. In Creep and Fracture of Engineering Materials and Structures (B. Wilshire and R.W. Evans, editors), Proceedings of the Fourth International Conference, Swansea, 1990, 1017-1028.

Evans, R.W. and B. Wilshire. 1981. The role of grain-boundary cavities during tertiary creep. In Creep and Fracture of Engineering Materials and Structures (B. Wilshire and D.R.J. Owen, editors), Proceedings of the International Conference, Swansea, 1981, 303-314.

Evans, R.W. and B. Wilshire. 1985. Creep of Metals and Alloys. The Institute of Materials, London. Ashgate Publishing Company, Brookfield, VT.

Evans, R.W. and B. Wilshire. 1987a. Power-law creep of polycrystalline copper. In Creep and Fracture of Engineering Materials and Structures (B. Wilshire and R.W. Evans, editors), Proceedings of the Third International Conference, Swansea, 1987, 59-70.

Evans, R.W. and B. Wilshire, 1987b. Creep behaviour of superalloy blade materials. Materials Science and Technology 3, 701-705.

Evans, R.W. and B. Wilshire. 1993. Introduction to Creep. The Institute of Materials, London. Ashgate Publishing Company, Brookfield, VT.

Evans, R.W., I. Beden and B. Wilshire. 1984. Creep life prediction for ½Cr½Mo¼V ferritic steel. In Creep and Fracture of Engineering Materials and Structures (B. Wilshire and D.R.J. Owen, editors), Proceedings of the Second International Conference, Swansea 1984, 1277-1290.

Evans, R.W., A.A. Fadlalla and B. Wilshire. 1990. Prediction of long-term creep rupture properties for an aluminum alloy for airframe application. In Creep and Fracture of Engineering Materials and Structures (B. Wilshire and R.W. Evans, editors), Proceedings of the Fourth International Conference, Swansea, 1990, 1009-1016.

Evans, R.W., E.A. Little, J.A. Preston and B. Wilshire. 1993. Rationalization of the creep behaviour of oxide-dispersion-strengthened alloys. In Creep and Fracture of Engineering Materials and Structures (B. Wilshire and R.W. Evans, editors), Proceedings of the Fifth International Conference, Swansea, 1993, 565-572.

Evans, R.W., J.D. Parker and B. Wilshire. 1982. An extrapolation procedure for long-term creep strain and creep life prediction, with special reference to 0.5Cr0.5Mo0.25V ferritic steels. In Recent Advances in Creep and Fatigue of Engineering Materials and Structures (B. Wilshire and O.R.J. Owen, editors), Pineridge Press, Swansea, U.K., 135-167.

Evans, R.W., I. Pearce, B. Wilshire, R.I. Butt and R.N. Wilson. 1993a. Creep fracture of aluminum airframe alloys. In Creep and Fracture of Engineering Materials and Structures (B. Wilshire and R.W. Evans, editors), Proceedings of the Fifth International Conference, Swansea, 1993, 109-116

Evans, R.W., J.A. Preston, B. Wilshire and E.A. Little. 1993b. Creep and creep fracture of an oxide-dispersion-strengthened 13% chromium ferritic steel. Materials Science and Engineering A167, 65-72.

Evans, R.W., M.R. Willis, B. Wilshire, S. Holdsworth, B. Senior, A. Fleming, M. Spindler and J.A. Williams. 1993c. Prediction of long-term creep and creep fracture data for 1 CrMoV Rotor steel. In Creep and Fracture of Engineering Materials and Structures (B. Wilshire and R.W. Evans, editors), Proceedings of the Fifth International Conference, Swansea, 1993, 633-642.

Evans, W.J. 1984. Low-temperature creep and fracture of near α titanium alloys. In Creep and Fracture of Engineering Materials and Structures (B. Wilshire and D.R.J. Owen, editors), Proceedings of the Second International Conference, Swansea, 1984, 395-406.

Evans, W.J. 1987. Creep-fatigue interactions in Ti-6Al-4V at ambient temperatures. In Creep and Fracture of Engineering Materials and Structures (B. Wilshire and R.W. Evans, editors), Proceedings of the Third International Conference, Swansea, 1987, 603-613.

Feltham, P. and J.D. Meakin. 1959. Creep in face-centred cubic metals with special reference to copper. Acta Metallurgica 7, 614-627.

Frost, H.J. and M.F. Ashby. 1982. Deformation-Mechanism Maps: The Plasticity and Creep of Metals and Ceramics. Franklin Book Company, Incorporated, Elkins Park, PA.

Garofalo, F. 1965. Fundamentals of Creep-Rupture in Metals. Macmillan Publishing Co., Inc., New York, NY.

Garofalo, F., C. Richmond, W.F. Domis and F. von Gemminger. 1963. Joint International Conference on Creep, Institute of Mechanical Engineering, London.

Gittus, J. 1975. Creep, Viscoelasticity and Creep Fracture in Solids. Elsevier Science, Inc., New York, NY.

Graham, A. and K.F.A. Walles. 1955. Relationships between long and short-time creep and tensile properties of a commercial alloy. Journal of the Iron and Steel Institute, 179, 105-120.

Hart, E.W. 1967. Theory of the tensile test. Acta Metallurgica 15, 351-355.

Henderson, P.J. and M. McLean. 1984. An evaluation of the factors influencing tertiary creep in nickel-based superalloys. In Creep and Fracture of Engineering Materials and Structures (B. Wilshire and D.R.J. Owen, editors), Proceedings of the Second International Conference, Swansea, 1984, 319-332.

Henderson, P.J., J-O. Österberg and B. Ivarsson. 1992. Low-temperature creep of copper intended for nuclear waste containers. Swedish Institute for Metals Research. Swedish Nuclear Fuel and Waste Management Company Report, SKB-TR-92-04.

Herring, C. 1950. Diffusional viscosity of a polycrystalline solid. Journal of Applied Physics 21, 437-445.

Hosaluk, L.J., H.Y.S. Ko and K.J. Truss. 1987. The effects of creep on the long-term performance of titanium stressed-shell fuel isolation containers. Atomic Energy of Canada Limited Technical Record, TR-402.

Hull, D. and D.E. Rimmer. 1959. The growth of grain-boundary voids under stress. Philosophical Magazine 4, 673-687.

Johnson, L.H., J.C. Tait, D.W. Shoesmith, J.L. Crosthwaite and M.N. Gray. 1994. The disposal of Canada's nuclear fuel waste: Engineered barriers alternatives. Atomic Energy of Canada Limited Report, AECL-10718, COG-93-8.

Johnson, R.F., M.J. May, R.J. Trueman and J. Mickleraith. 1967. Elevated-temperature tensile, creep, and rupture properties of 1%Cr-½%Mo, 2¼%Cr-1%Mo, and ½%Cr-½%Mo-¼%V steels. In High Temperature Properties of Steels, Proceedings of the Joint Conference, Eastbourne, 1966, 229-264.

Kachanov, L.M. 1958. Long-time strength and creep. Izvestiya Akademii Nauk. SSSR, Otdelenie Tekhnicheskikh Nauk, 8, 26-31.

Kiessel, W.R. and M.J. Sinnott. 1953. Creep properties of commercially pure titanium. Transactions A.I.M.E., Journal of Metals, 5, 331-338.

Larson, F.R. and J. Miller. 1952. A time-temperature relationship for rupture and creep stresses. Transactions ASME 74, 765-771.

Li, G., T. Sakai and T. Endo. 1987. An application of creep time law to the life prediction of a nickel-base superalloy. In Creep and Fracture of Engineering Materials and Structures (B. Wilshire and R.W. Evans, editors), Proceedings of the Third International Conference, Swansea, 1987, 803-813.

Li, Y.Z., M.C. Nguyen and H.H. Over. 1990. Creep and creep crack growth evaluation within the European High Temperature Materials Databank, PETTEN. In Creep and Fracture of Engineering Materials and Structures (B. Wilshire and R.W. Evans, editors), Proceedings of the Fourth International Conference, Swansea, 1990, 961-974.

Luster, D.R., W.W. Wentz and D.W. Kaufmann. 1953. Creep properties of titanium. Materials and Methods 37, 100-103.

Maruyama, K. and H. Oikawa. 1987a. On physical bases of the modified θ projection concept. In Creep and Fracture of Engineering Materials and Structures (B. Wilshire and R.W. Evans, editors), Proceedings of the Third International Conference, Swansea, 1987, 815-828.

Maruyama, K. and H. Oikawa. 1987b. Comments on "exponential descriptions of normal creep curves by S.G.R. Brown, W.R. Evans and B. Wilshire". Scripta Metallurgica 21, 233-237.

McLean, D. 1966. The physics of high temperature creep in metals. Reports on Progress in Physics 29, 1-33.

McLean, M., B.F. Dyson and R.N. Ghosh. 1992. Recent evaluation of gas turbine materials and the development of models for life prediction. In Mechanical Behaviour of Materials, Volume 2, Pergamon Press, Oxford, 49-57.

Monkman, F.C. and N.J. Grant. 1956. An empirical relationship between rupture life and minimum creep-rate in creep-rupture tests. Proceedings ASTM 56, 593-605.

Nabarro, F.R.N. 1948. Deformation crystals by the motion of single ions. In Report on Conference on Strength of Solids, The Physical Society, London, 75-90.

Nix, W.D. and B. Ilschner. 1979. Mechanisms controlling creep of single phase metals and alloys. In Strength of Metals and Alloys (P. Haasen, V. Gerold and G. Kostorz, editors), Proceedings of the Fifth International Conference, Aachen, West Germany, 1979, Pergamon Press, New York, NY, 1503-530.

Orr, R.L., O.D. Sherby and J.E. Dorn. 1954. Correlations of rupture data for metals at elevated temperatures. Transactions American Society for Metals 46, 113-128.

Osgerby, S and B.F. Dyson. 1993. Constant strain-rate testing: Prediction of stress-strain curves from constant-load creep data. In Creep and Fracture of Engineering Materials and Structures (B. Wilshire and R.W. Evans, editors), Proceedings of the Fifth International Conference, Swansea, 1993, 53-61.

Osgerby, S. and B.F. Dyson. 1994a. Validation of a constitutive model for creep deformation and fracture in a 1 Cr ½ Mo ferritic steel. In Materials for Advanced Power Engineering, Part 1 (D. Coutsouradis et al., editors) 573-582.

Osgerby, S. and B.F. Dyson. 1994b. Physically-based modelling of stress-relaxation in superalloys and ferritic steels. In Proceedings of Conference on Performance of Bolting Materials in High Temperature Plant Applications, York, June 1994, to be published.

Osgerby, S.,A. Barbosa and B.F. Dyson. 1992. CREEPSIM-2: a software package for numerical integration of 1st order differential equations. National Physics Laboratory Report, DMM(A)35.

Rabotnov, Y.N. 1969. Creep rupture (Creep rupture and fatigue growth in solid body mechanics, considering triaxial stress state and simplified creep rupture theory variant). In Applied Mechanics, Proceedings of the 12th International Union of Theoretical and Applied Mechanics, Stanford University, CA, 1968, Springer-Verlag, New York, 342-349.

Rigby, G.L. 1994. A finite element model for creep in titanium. Atomic Energy of Canada Limited Technical Record, TR-647, COG-I-94-365.

Sargent, P.M. and M.F. Ashby. 1982. Deformation maps for titanium and zirconium. Scripta Metallurgica 16, 1415-1422.

Shen, G. and A. Plumtree. 1990. Combination of continuum damage mechanics and θ-projection concept for creep life prediction. In Creep and Fracture of Engineering Materials and Structures (B. Wilshire and R.W. Evans, editors), Proceedings of the Fourth International Conference, Swansea, 1990, 999-1008.

Sherby, O.D. and P.M. Burke. 1968. Mechanical behavior of crystalline solids at elevated temperature. Progress in Materials Science 13, 325-390.

Sherby, O.D. and J. Wadsworth. 1989. Superplasticity - Recent advances and future directions. Progress in Materials Science 33, 169-221.

Simmons, G.R. and P. Baumgartner. 1994. The disposal of Canada's nuclear fuel waste: engineering for a disposal facility. Atomic Energy of Canada Limited Report, AECL-10715, COG-93-5.

Taylor, N.G., B.R. Twaddle and R.C. Hurst. 1990. Prediction of alloy 800H and 2¼Cr 1 Mo component creep behaviour from uniaxial specimen data. In Creep and Fracture of Engineering Materials and Structures (B. Wilshire and R.W. Evans, editors), Proceedings of the Fourth International Conference, Swansea, 1990, 985-998.

Teper, B. 1985. Test programs of the prototype of the TWPP container: Part 2 - Post-hydrostatic tests. Ontario Hydro Research Division Report, 85-313-K.

Teper, B. 1987a. Test program of the prototype of the thin-wall particulate-packed (TWPP) container 1. Hydrostatic tests. Atomic Energy of Canada Limited Technical Record, TR-369-1. Also available as Ontario Hydro Research Division Report, 84-293-K.

Teper, B. 1987b. Test program of granular materials for the thin-walled, particulate-packed container. Ontario Hydro Research Division Report, 87-154-K.

Teper, B. 1988. Test program of the prototype of the TWPP container: Part 3 - Detailed stress analysis and comparison with test results. Ontario Hydro Research Division Report, 87-296-K.

Teper, B. 1990. Long-term creep assessment of candidate metals for high-level nuclear waste containers - interim report. Ontario Hydro Research Division Report, 90-241-K.

Teper, B. and S.A. Reid. 1989. Recent developments in design of containers for disposal of high-level waste from CANDU reactors. In Waste Management '89, Proceedings of the Symposium on Waste Management, Tucson, AZ, 1989, Volume 1, 623-631.

Voorhees, H.R. 1985. Assessment and use of creep-rupture properties. In Metals Handbook, Ninth edition, Volume 8, Mechanical Testing. ASM International, Metals Park, OH, 329-342.

Weertman, J. 1955. Theory of steady-state creep based on dislocation climb. Journal of Applied Physics 26, 1213-1217.

Weertman, J. 1963. An empirical relationship defining the stress dependence of minimum creep rate in metals. Metallurgical Society of AIME Transactions, 227, 1475-1476.

Wilshire, B. 1989. New high-precision creep procedures for accurate life extension of plant. International Journal of Pressure Vessel and Piping 39, 73-82.

Wilshire, B. 1990. On the evidence for diffusional creep processes. In Creep and Fracture of Engineering Materials and Structures (B. Wilshire and R.W. Evans, editors), Proceedings of the Fourth International Conference, Swansea, 1990, 1-9.

Wilshire, B. 1993a. Creep data prediction for high-performance steels. In Advanced Materials (T. Kishi, N. Tanaka and Y. Kagawa, editors), Proceedings of the Third Japan International SAMPE Symposium, Tokyo, 1993, 2011-2018.

Wilshire, B. 1993b. High temperature properties of monolithic ceramics. Materials and Design 14, 39-43.

Wilshire, B. and R.W. Evans. 1994. Acquisition and analysis of creep data. Journal of Strain Analysis 29, 159-165.

Woodford, D.A. 1969. Strain-rate sensitivity as a measure of ductility. Transactions of the ASM 62, 291-293.

Zeyfang, R., R. Martin and H. Conrad. 1971. Low-temperature creep of titanium. Materials Science and Engineering 8, 134-140.

---

* Internal report, available from SDDO, AECL Research, Chalk River Laboratories, Chalk River, Ontario K0J 1J0.

** Unpublished report available from the principal author at Ontario Hydro Research Division, 800 Kipling Avenue, Toronto, Ontario M8Z 5S4.

TABLE 1

VALUES OF THE PARAMETERS USED TO CONSTRUCT THE DEFORMATION MECHANISM MAPS (Frost and Ashby 1982)

Materials	α-Titanium	Copper
Crystallographic and thermal data		
Atomic volume, Ω (m^3)	1.76×10^{-29}	1.18×10^{-29}
Burç r's vector, b (m)	2.95×10^{-10}	2.56×10^{-10}
Melting temperature, T_m(K)	1933	1356
Modulus*		
Shear modulus at 300 K, G_o (MN/m^2)	4.36×10^4	4.21×10^4
Temperature dependence of modulus, $\frac{T_m}{G_o}\frac{dG}{dT}$	-1.2	-0.54
Lattice diffusion		
Pre-exponential, D_o (m^2/s)	8.6×10^{-10}	2.0×10^{-5}
Activation energy, Q_{SD} (kJ/mole)	150	197
Boundary diffusion		
Pre-exponential, δD_o (m^3/s)	3.6×10^{-16}	5.0×10^{-15}
Activation energy, Q_{GB} (kJ/mole)	97	104
Core diffusion†		
Pre-exponential, $a_c D_o$ (m^4/s)	7.3×10^{-29}	1.0×10^{-24}
Activation energy, Q_P (kJ/mole)	97	117
Power-law creep		
Exponent, n	4.3	4.8
Constant, A	7.7×10^4	7.4×10^5
Activation energy, Q_C (kJ/mole)††	242	-
Pre-exponential for creep, D_o (m^2/s)	1.3×10^{-2}	-

* $$G = G_o\left(1 + \frac{T - 300}{T_m}\right)\frac{T_m}{G_o}\frac{dG}{dT}$$

† a_c = effective diffusive section of a dislocation core.

†† for titanium, these values were used for power-law creep, the activation energies Q_{SD} or Q_P giving a poor fit to the data.

TABLE 2

COEFFICIENTS FOR ln θ and ε_r ACCORDING TO EQNS. (59) AND (61)
(Units are in s, K and MPa)

COPPER				
Parameter	a_i	b_i	c_i	d_i
$\log_e \theta_1$	-15.8241	-0.02419	0.01190	0.0001392
$\log_e \theta_2$	-23.3920	-0.09676	0.01359	0.0003669
$\log_e \theta_3$	-12.9852	-0.06501	0.00766	0.0001495
$\log_e \theta_4$	-22.7161	-0.05707	0.01336	0.0002519
ε_r	-0.02247	-0.03668	-0.16511	0.04695
½ Cr ½ Mo ¼ V STEEL				
Parameter	a_i	b_i	c_i	d_i
$\log_e \theta_1$	-20.11538	0.01060	-0.00103	0.0001569
$\log_e \theta_2$	-54.01865	0.00051	0.00051	-0.0000449
$\log_e \theta_3$	-4.30353	-0.00468	-0.00127	0.0001840
$\log_e \theta_4$	-37.83147	0.02107	-0.00109	0.0001644
ε_r	-2.58580	0.00349	0.00126	-0.0000011

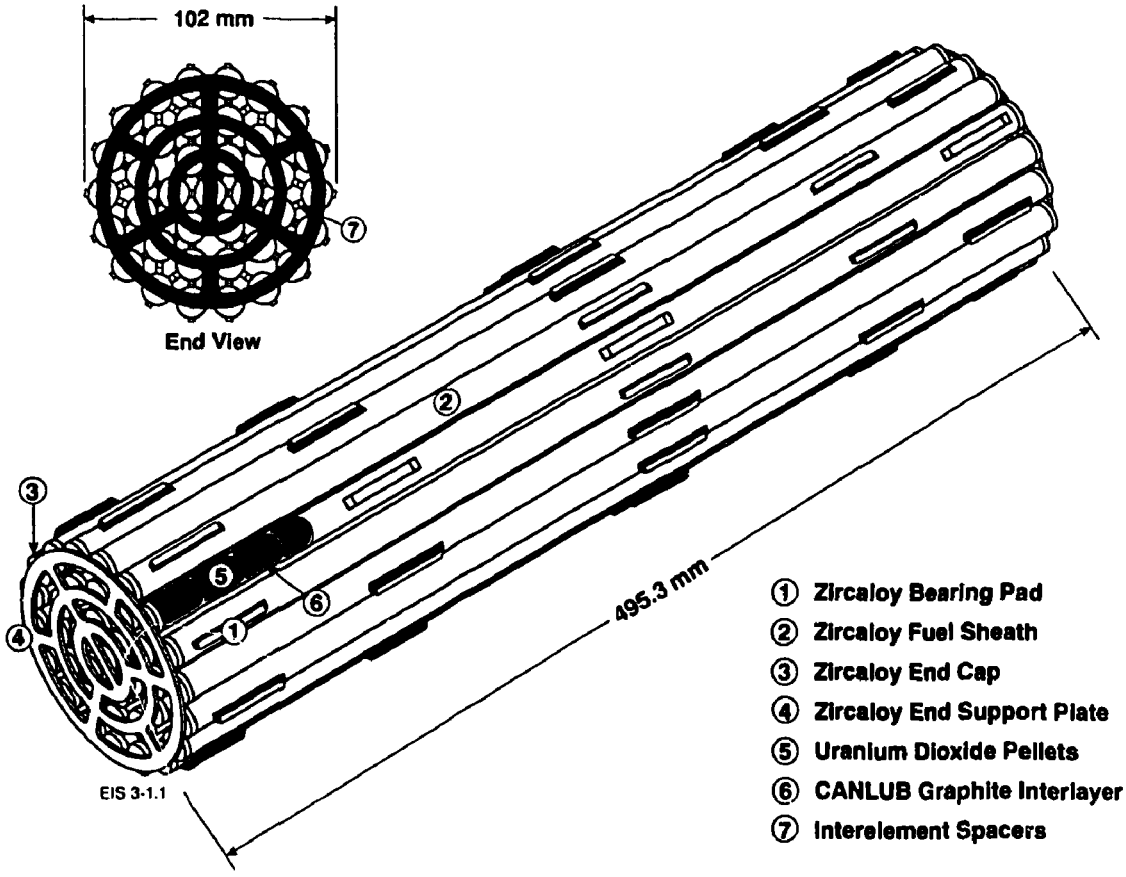

FIGURE 1: A CANDU 37-Element Fuel Bundle

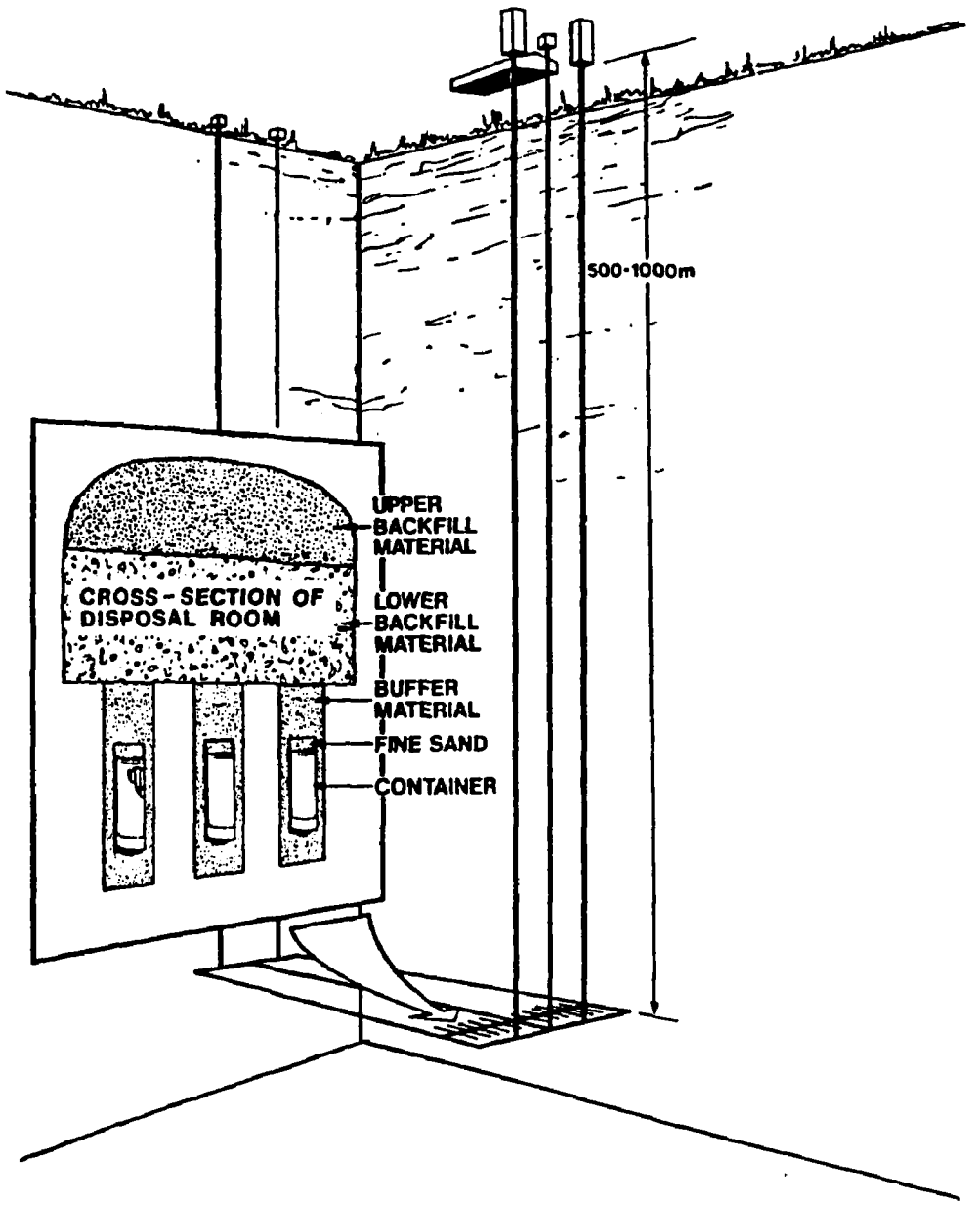

FIGURE 2: Conceptual Disposal Vault Design

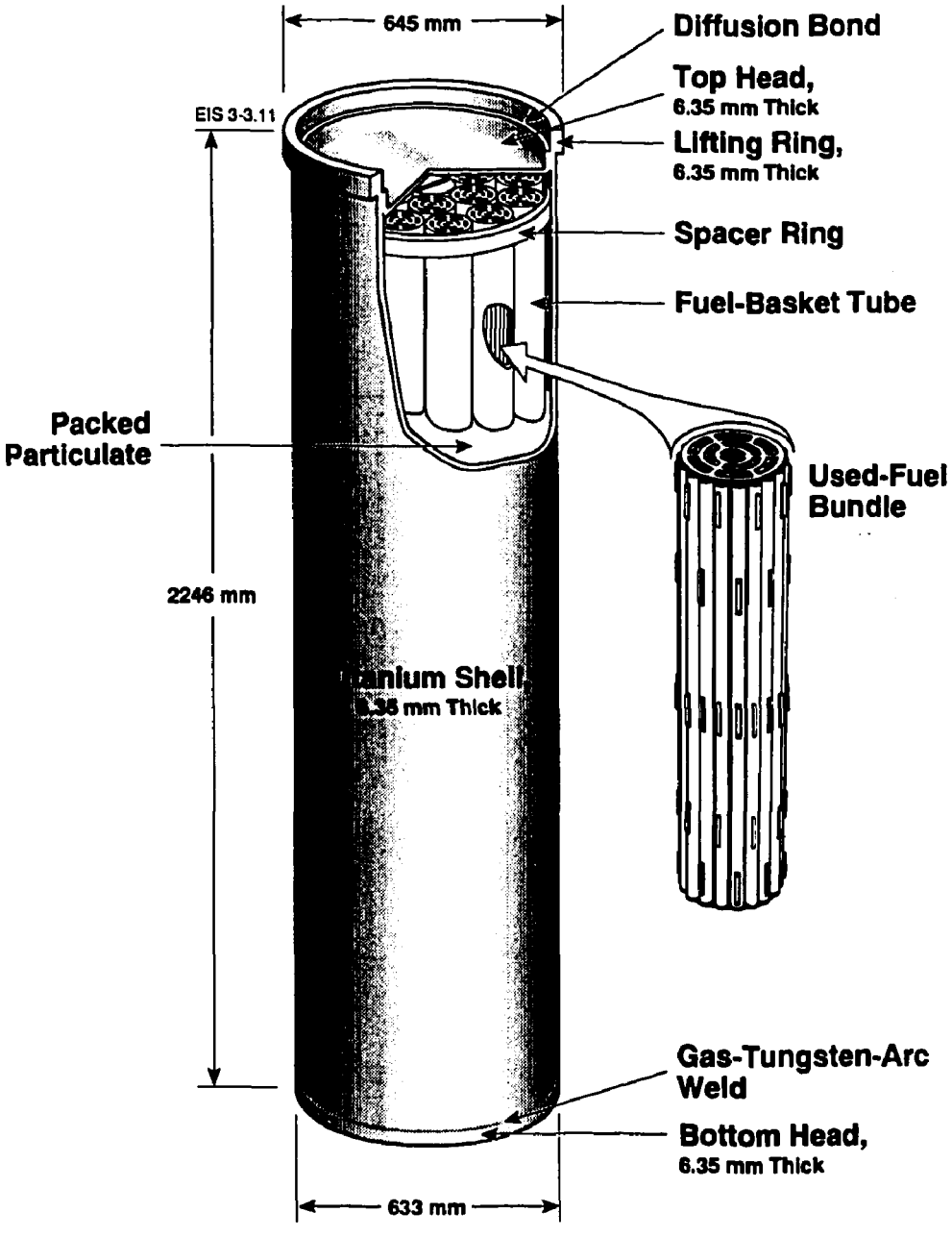

FIGURE 3: Titanium-Shell, Packed-Particulate Fuel Disposal Container

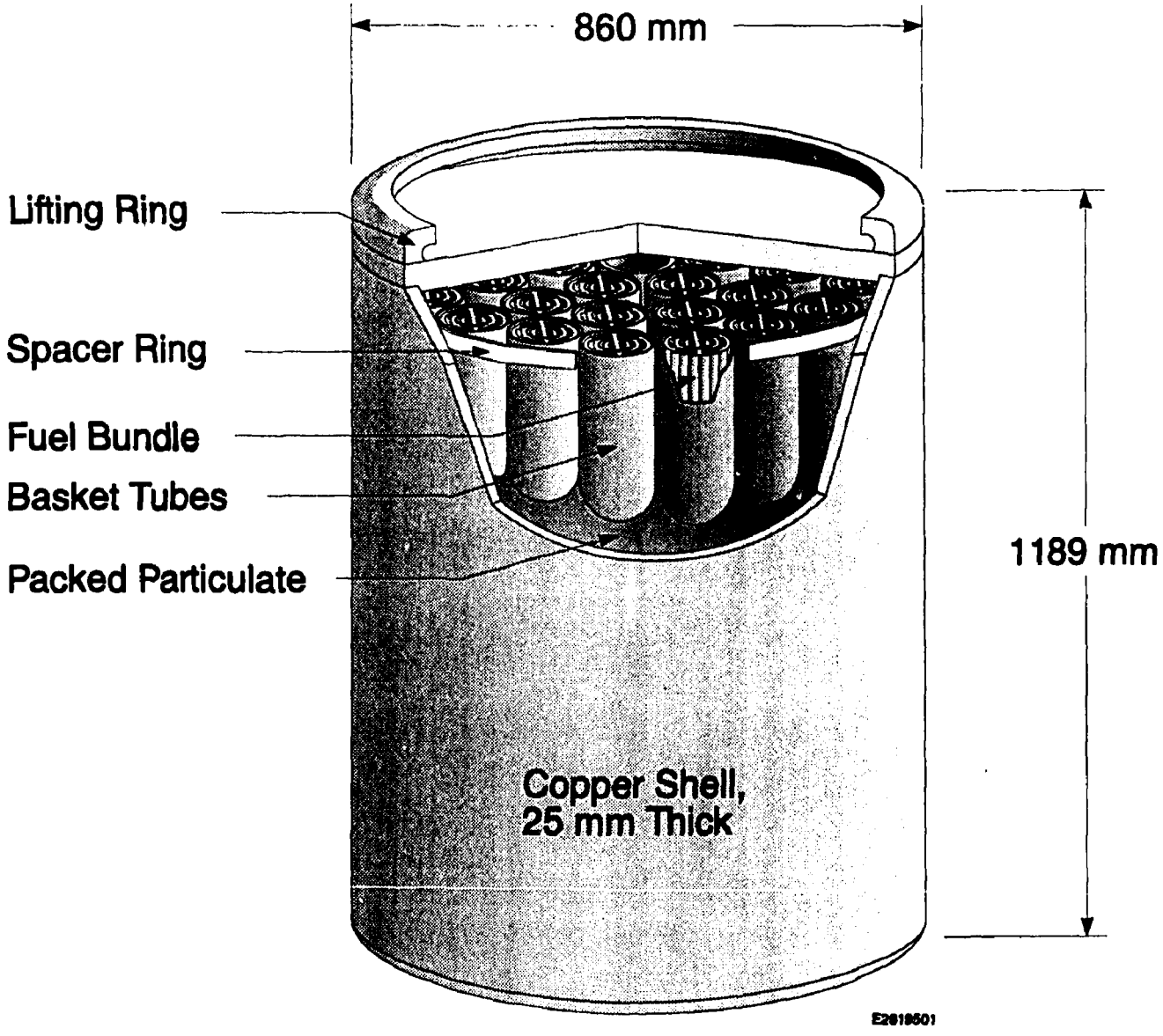

FIGURE 4: Copper-Shell, Packed-Particulate Container Designed for In-Room Emplacement

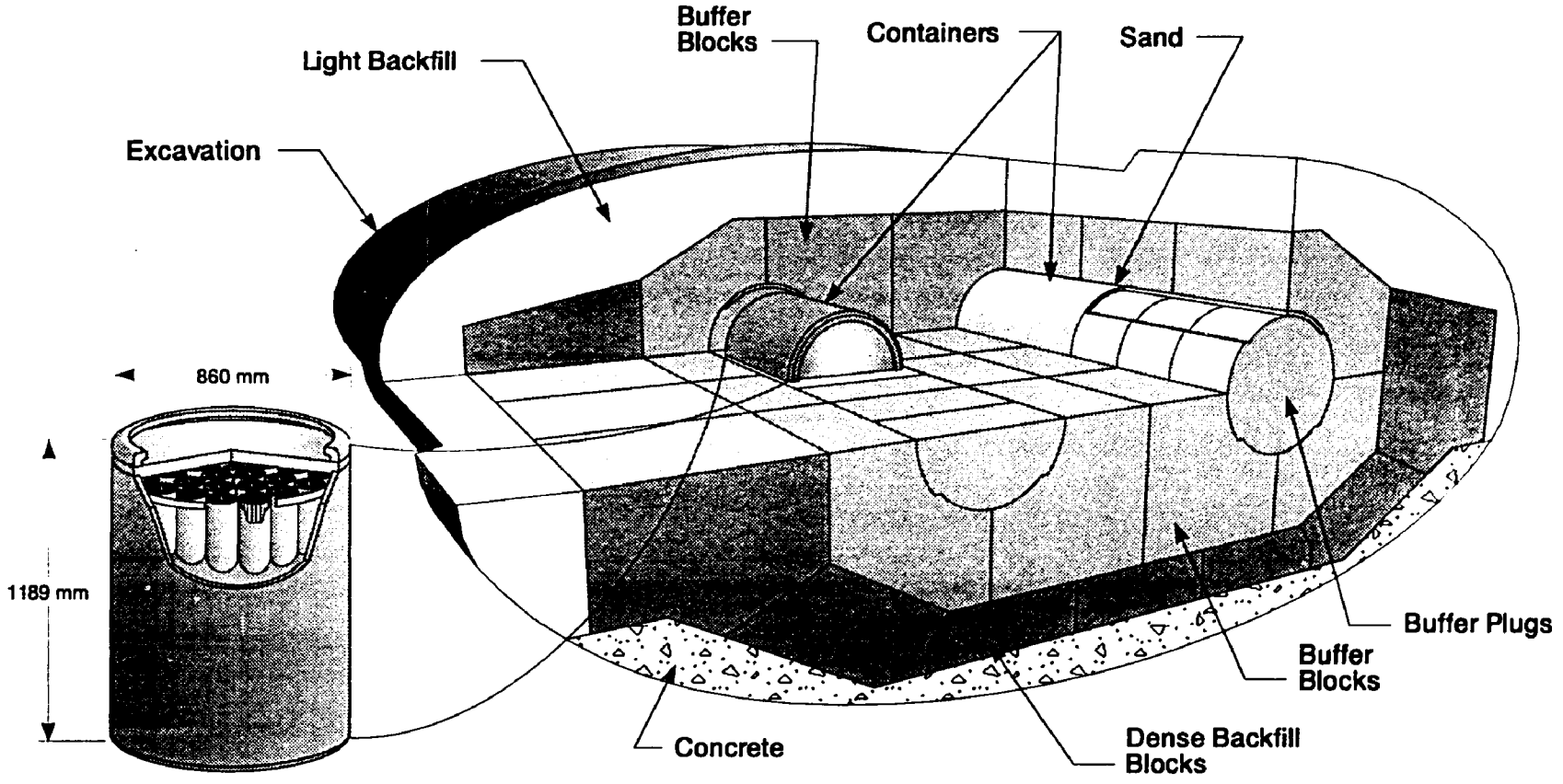

FIGURE 5: Disposal Room Showing the In-Room Emplacement of Disposal Container

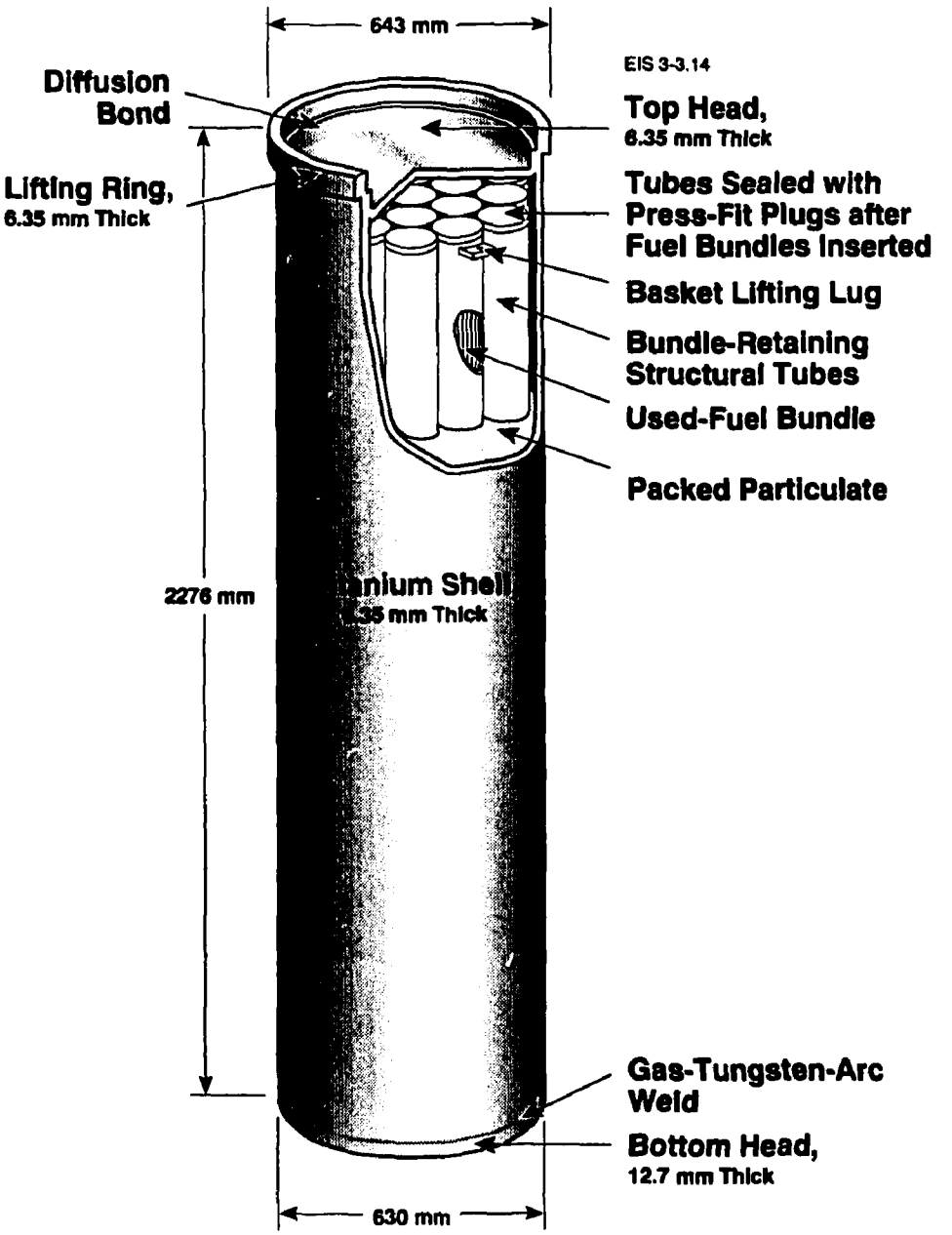

FIGURE 6: Titanium-Shell, Structurally Supported Fuel Disposal Container

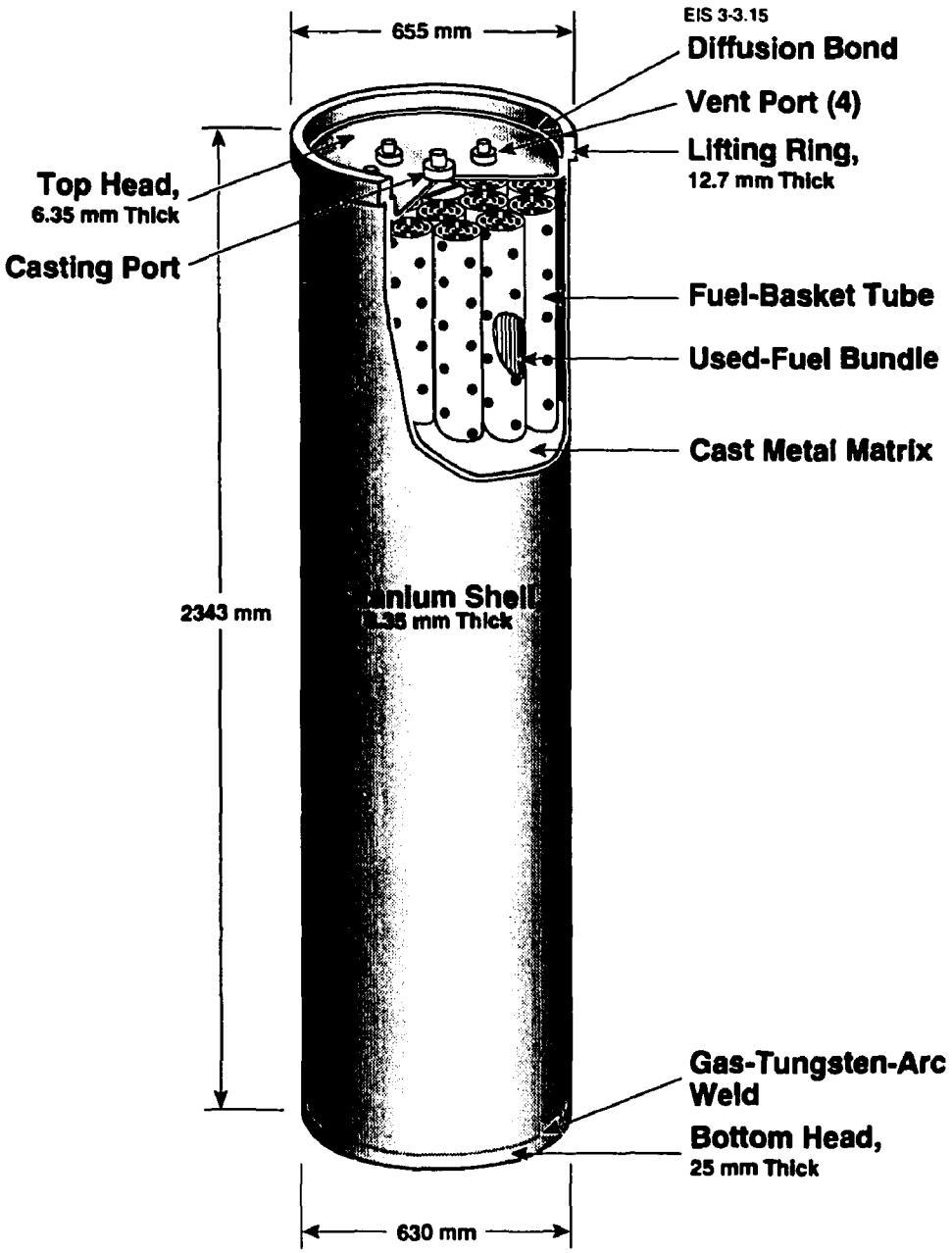

FIGURE 7: Titanium-Shell, Metal-Matrix Fuel Disposal Container

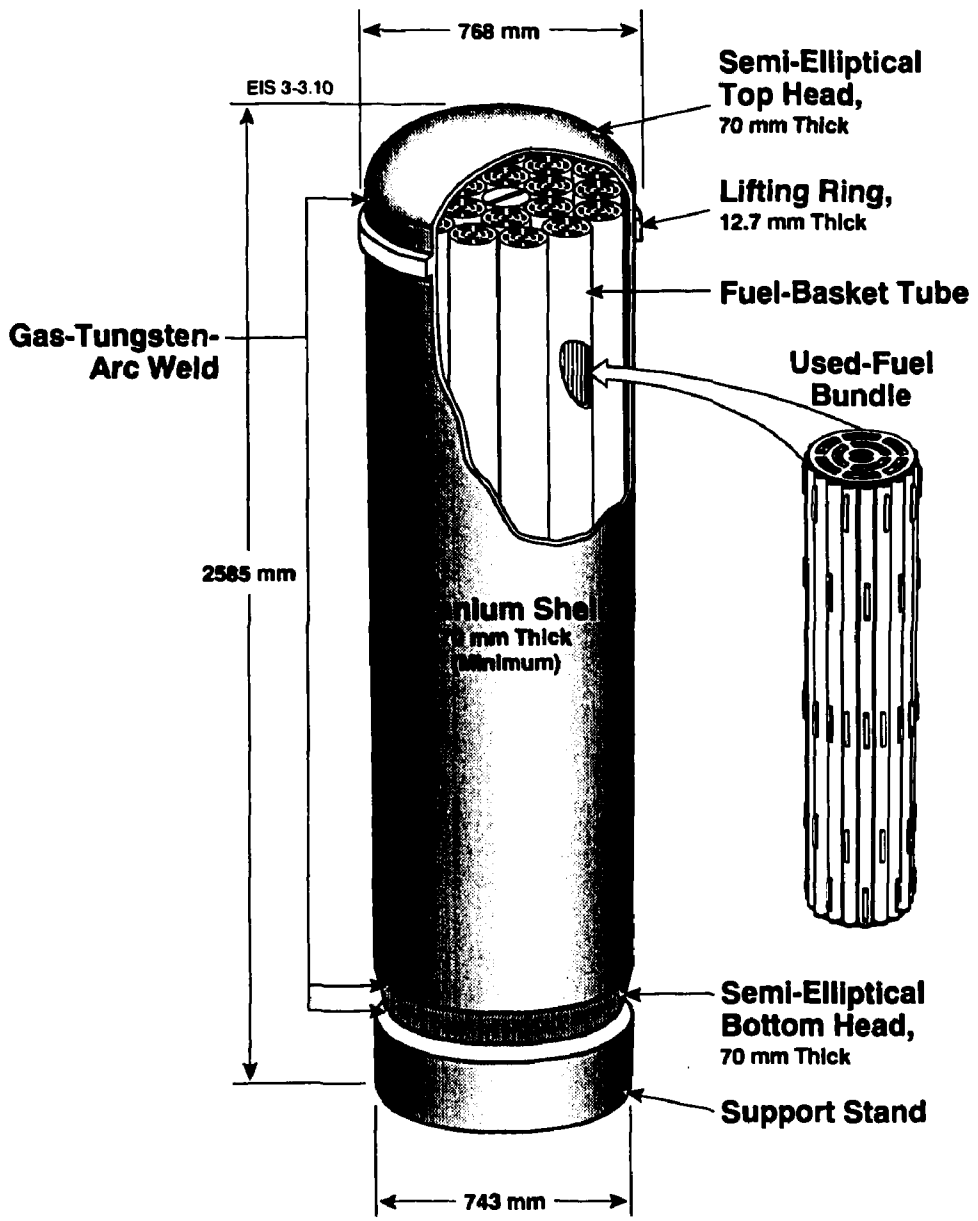

FIGURE 8: Titanium Stressed-Shell Fuel Disposal Container

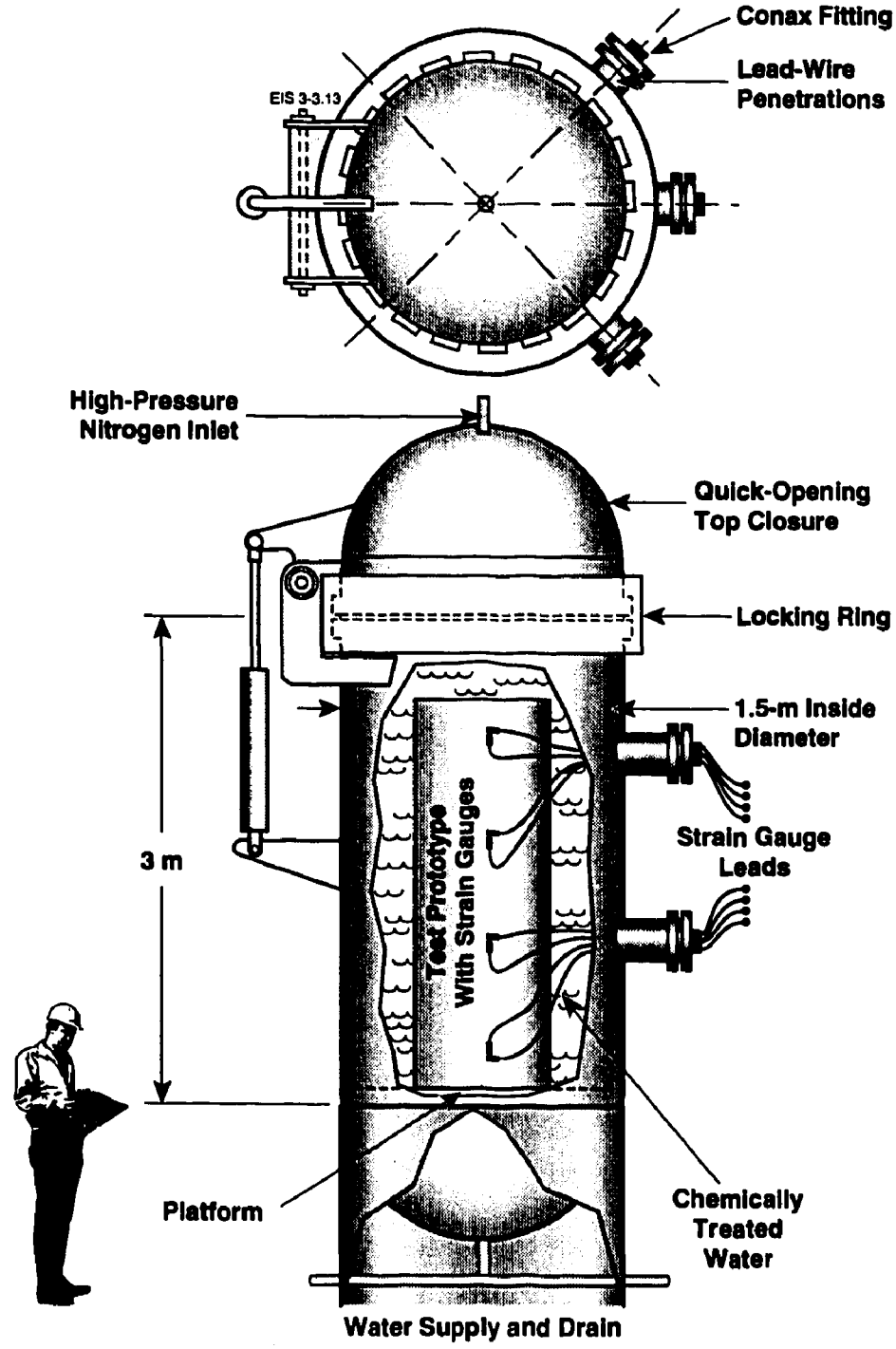

FIGURE 9: Whiteshell Laboratories Hydrostatic Test Facility

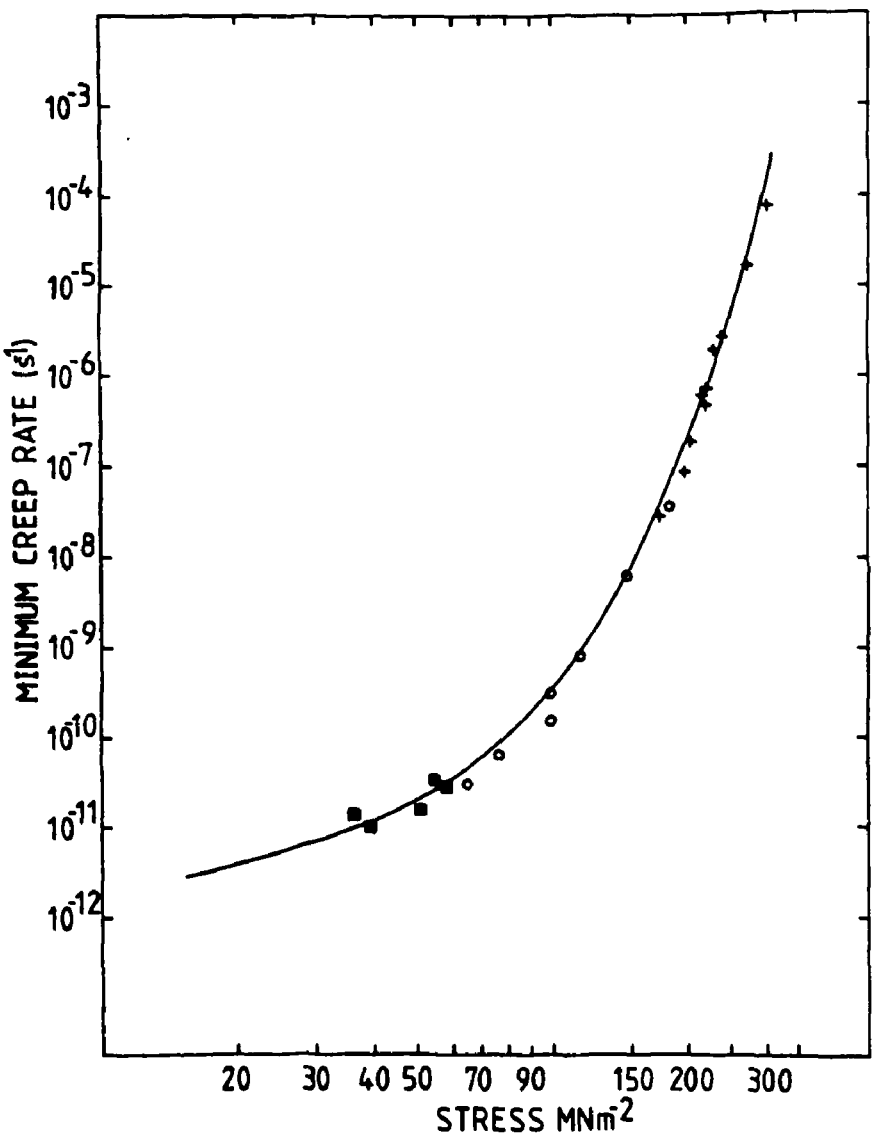

FIGURE 10: The Stress Dependence of the Minimum Creep Rate of 0.5Cr-0.5Mo-0.25V Ferritic Steel at 565°C. The solid line is calculated from the short-term data (marked +), using the θ Projection methodology (Section 9). The long-term data (marked o and ■) was subsequently obtained (Evans and Wilshire 1985).

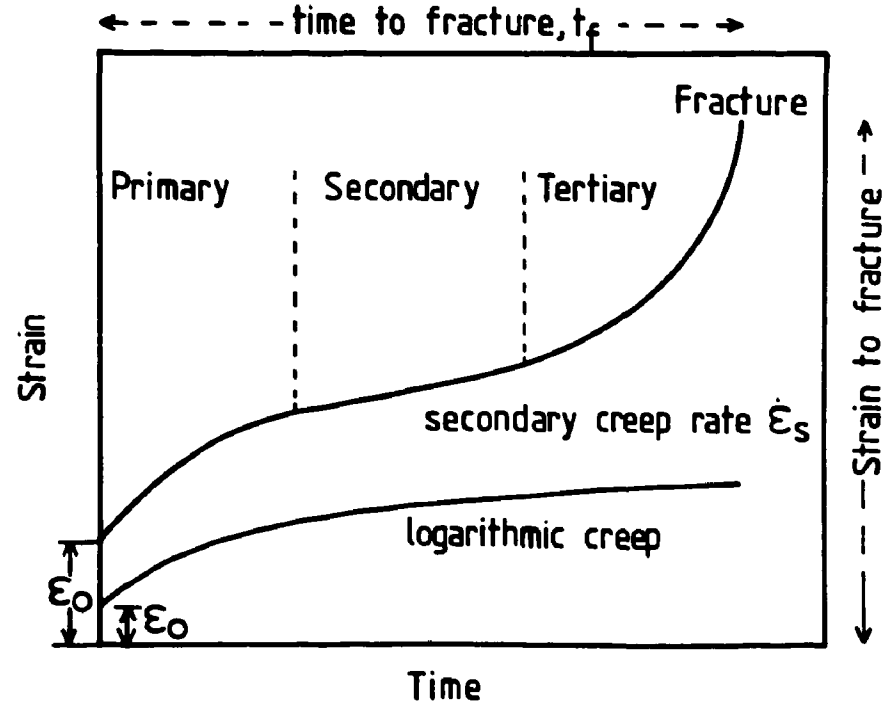

FIGURE 11: Schematic Creep Curves Illustrating Logarithmic Behaviour at Lower Temperatures and Normal Three-Stage Behaviour at Higher Temperatures

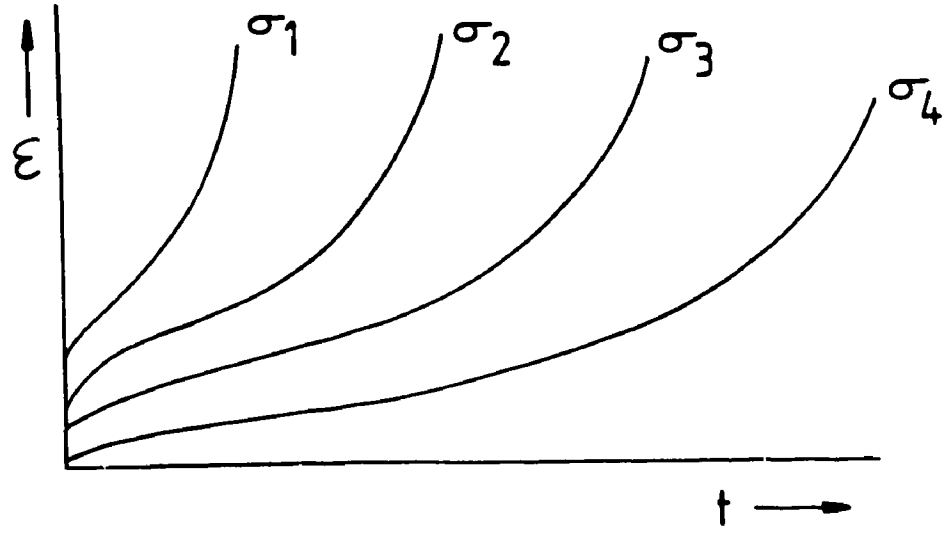

FIGURE 12: Schematic Creep Curves at the Same Temperature, but Various Stresses (σ), Where $\sigma_1 > \sigma_2 > \sigma_3 > \sigma_4$

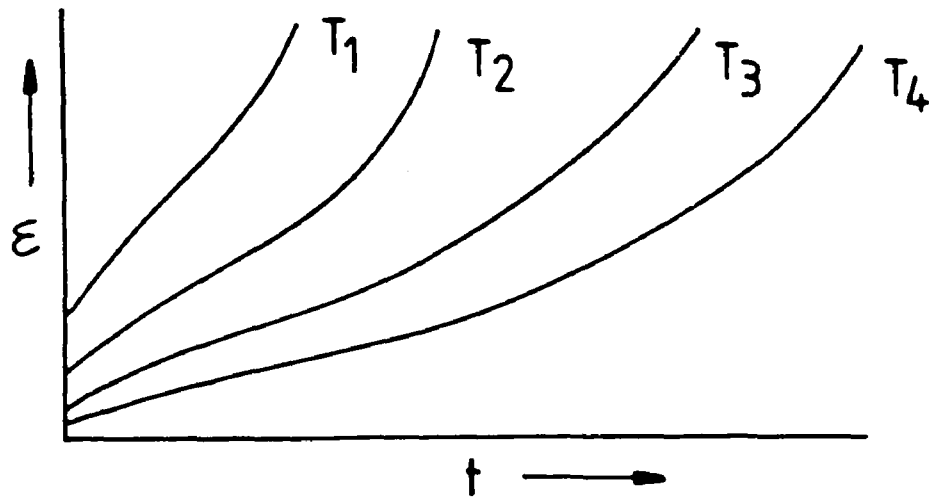

FIGURE 13: Schematic Creep Curves at the Same Stress, but Various Temperatures (T), Where $T_1 > T_2 > T_3 > T_4$

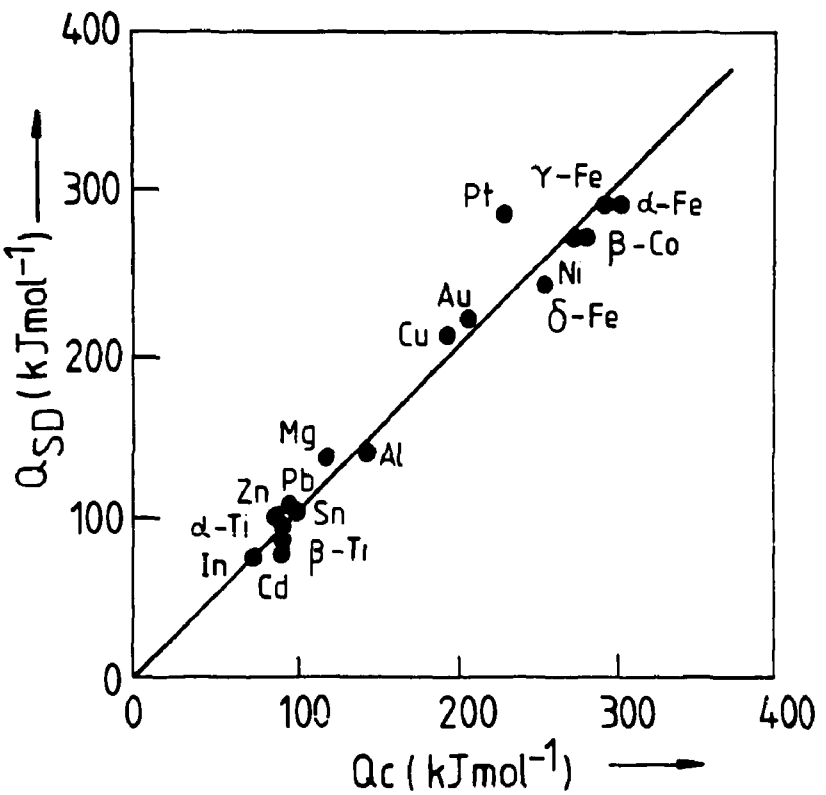

FIGURE 14: The Relationship Between the Activation Energy for Creep (Q_c) and the Activation Energy for Lattice Self Diffusion (Q_{SD}) for a Number of Pure Metals at High Temperature (Sherby and Burke 1967)

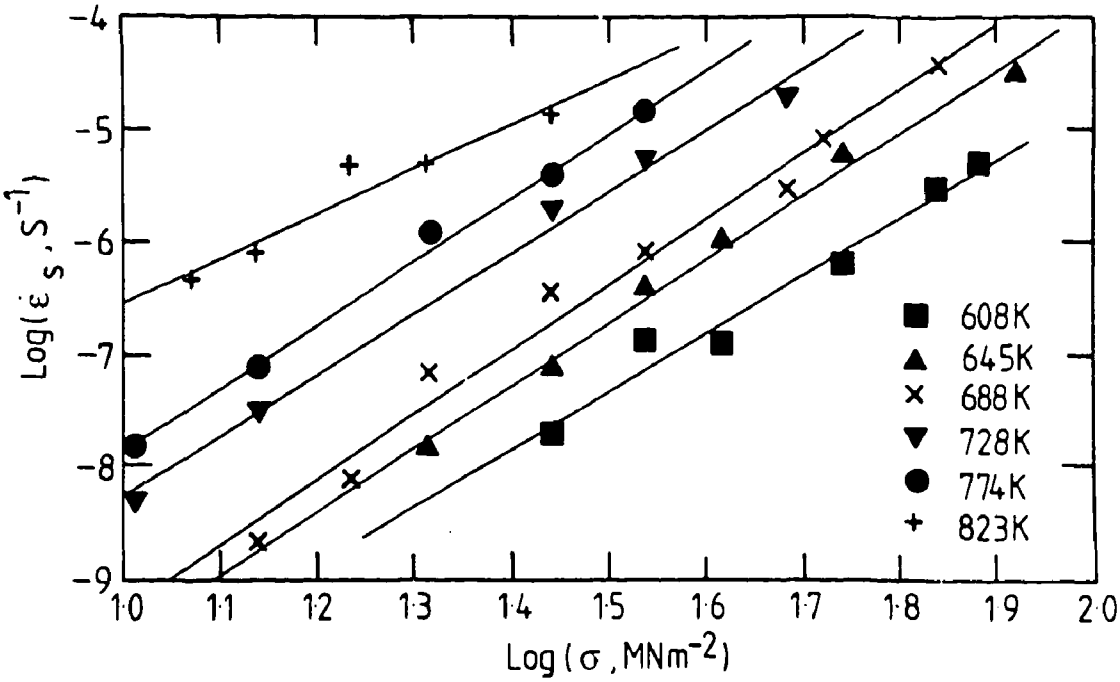

FIGURE 15: Power-Law Form of Steady-State Creep Rates Measured at Various Temperatures for Polycrystalline Copper. Stress exponent (n) is about 5 (Evans and Wilshire 1993).

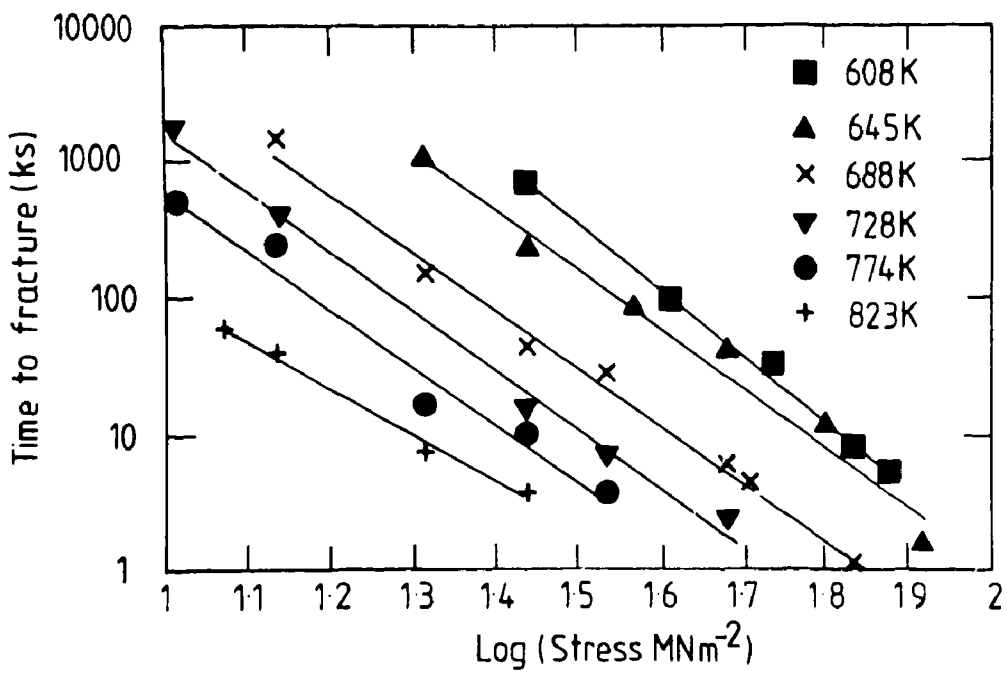

FIGURE 16: Dependence of Time to Rupture on Stress, at Various Temperatures, for the Polycrystalline Copper Data Shown in Figure 15 (Evans and Wilshire 1993)

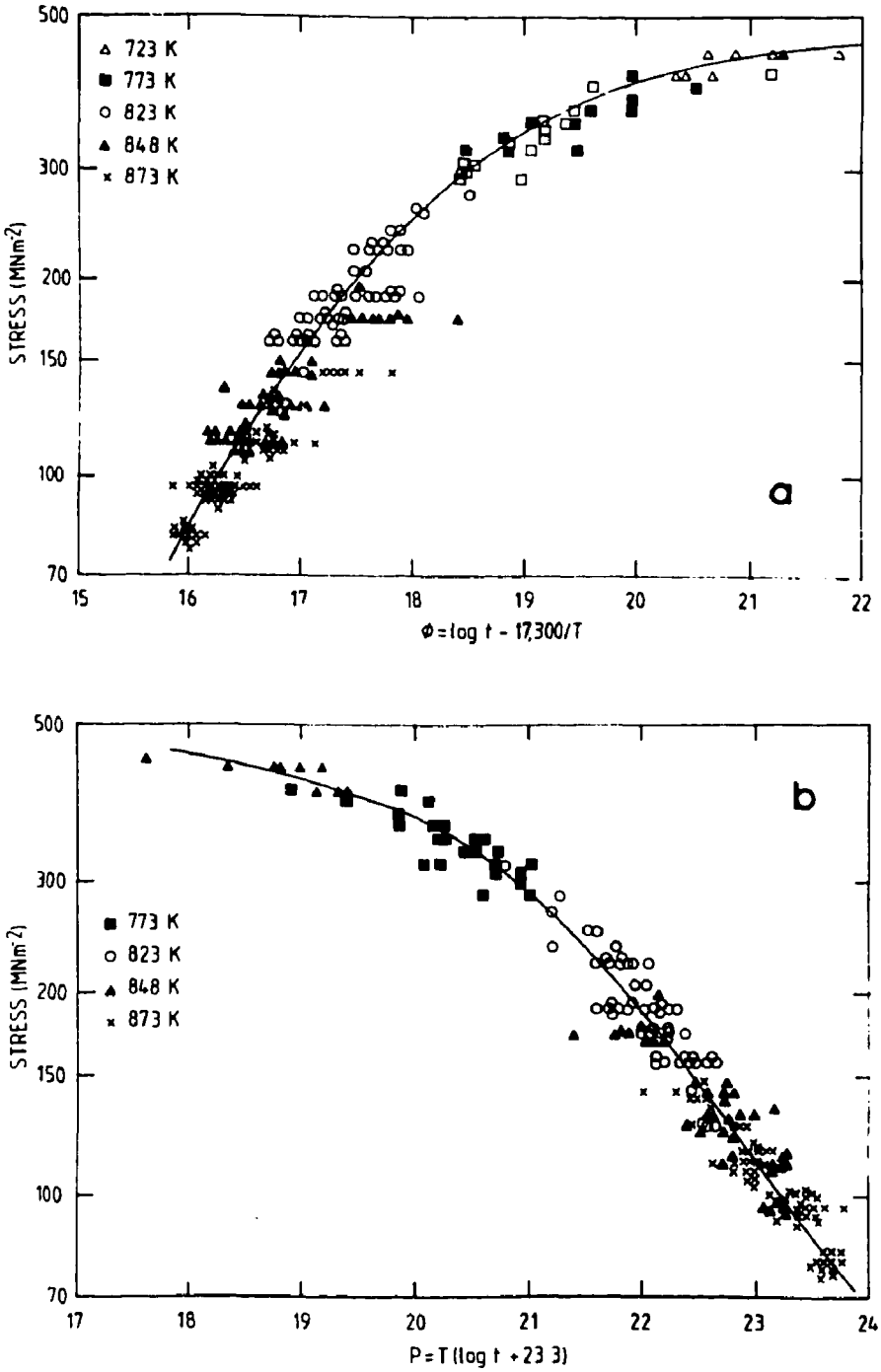

FIGURE 17: Stress-Rupture Data for 0.5Cr-0.5Mo-0.25V Steel, Using the Parametric Relationship Suggested by (a) Orr, Sherby and Dorn (1954) and (b) Larson and Miller (1952)

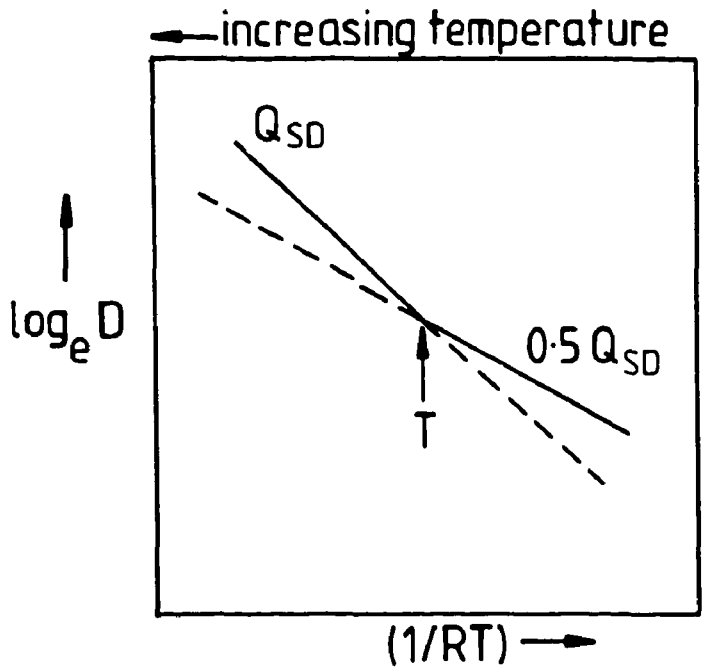

FIGURE 18: Schematic Illustration of the Variation in Diffusion Rate with Temperature for Lattice Diffusion ($Q = Q_{SD}$) and for Preferential Diffusion Along Preferred Paths ($Q = 0.5\,Q_{SD}$)

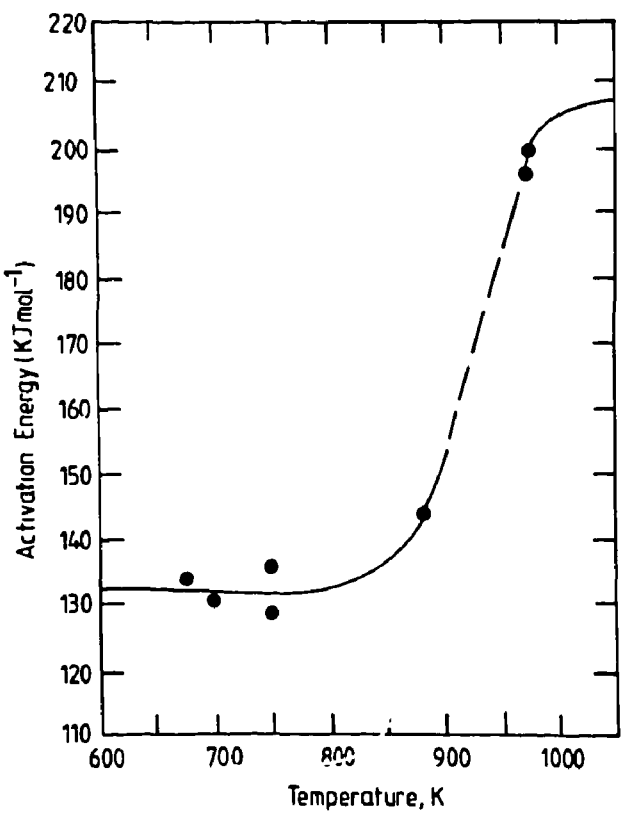

FIGURE 19: The Temperature Dependence of the Activation Energy for Creep of Polycrystalline Copper (Feltham and Meakin 1959)

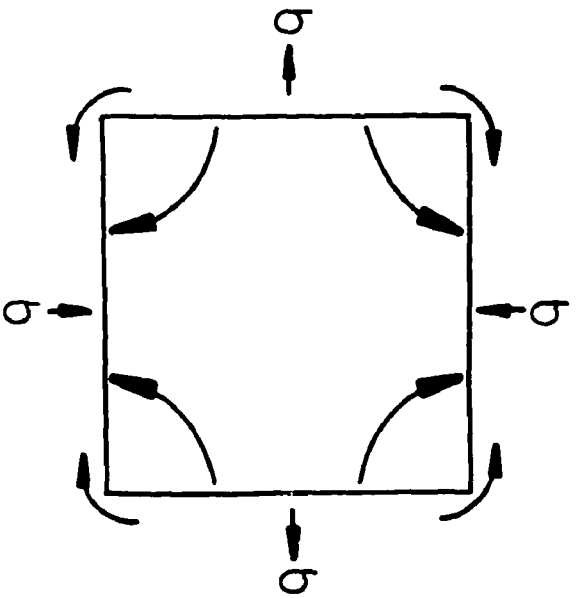

FIGURE 20: Schematic Representation of Diffusional Creep. The flow of vacancies may be through the grains (Nabarro-Herring creep) or along the grain boundaries (Coble creep)

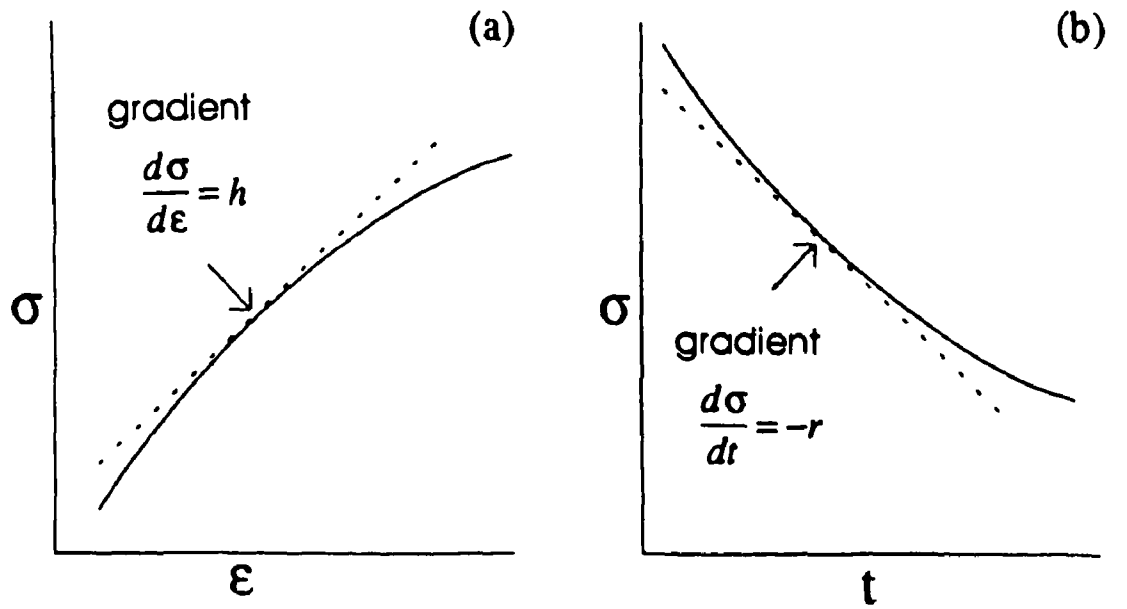

FIGURE 21: Graphical Representation of the Work-Hardening Rate (h) and Recovery Rate (r)

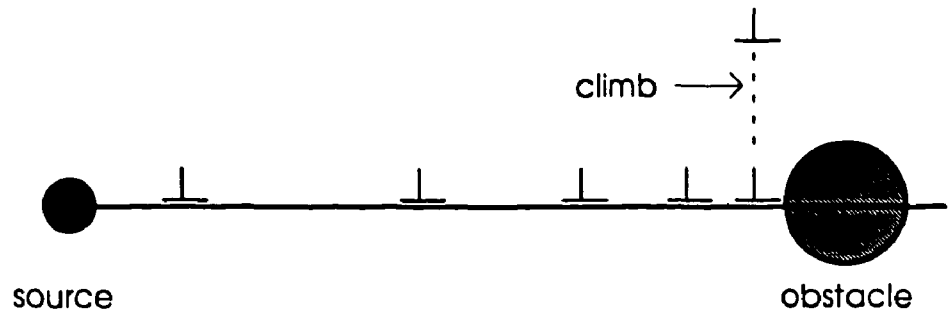

FIGURE 22: Schematic Representation of Climb of the Leading Dislocation in a Pile Up Against an Obstacle on the Slip Plane

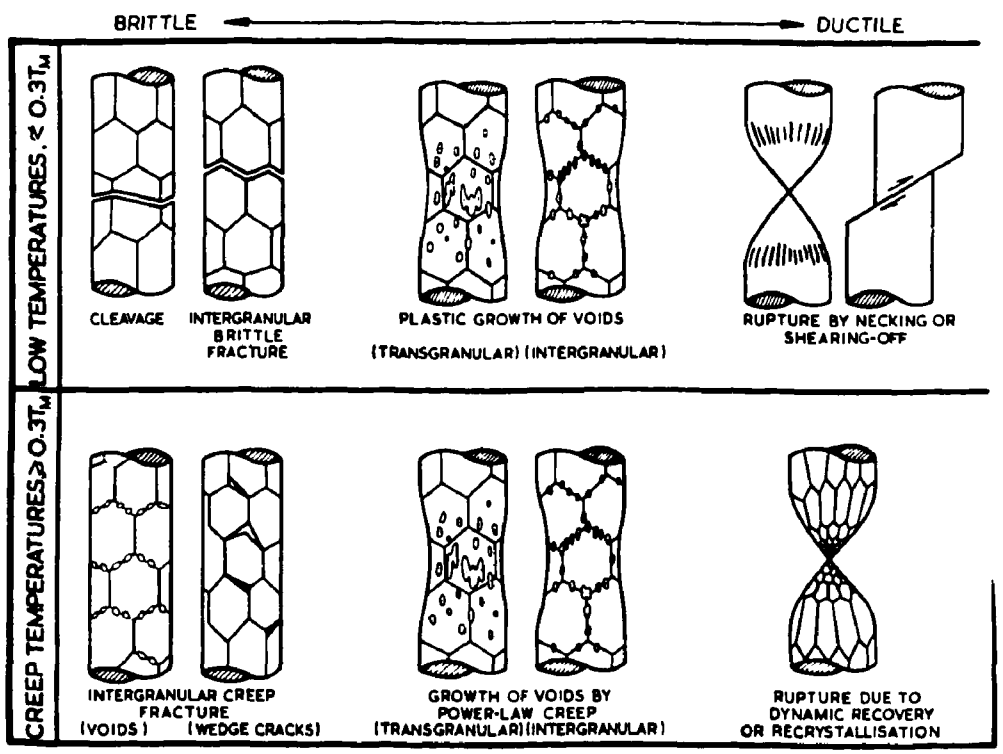

FIGURE 23: Schematic Diagram Showing the Broad Classes of Fracture Mechanisms (Ashby et al. 1979)

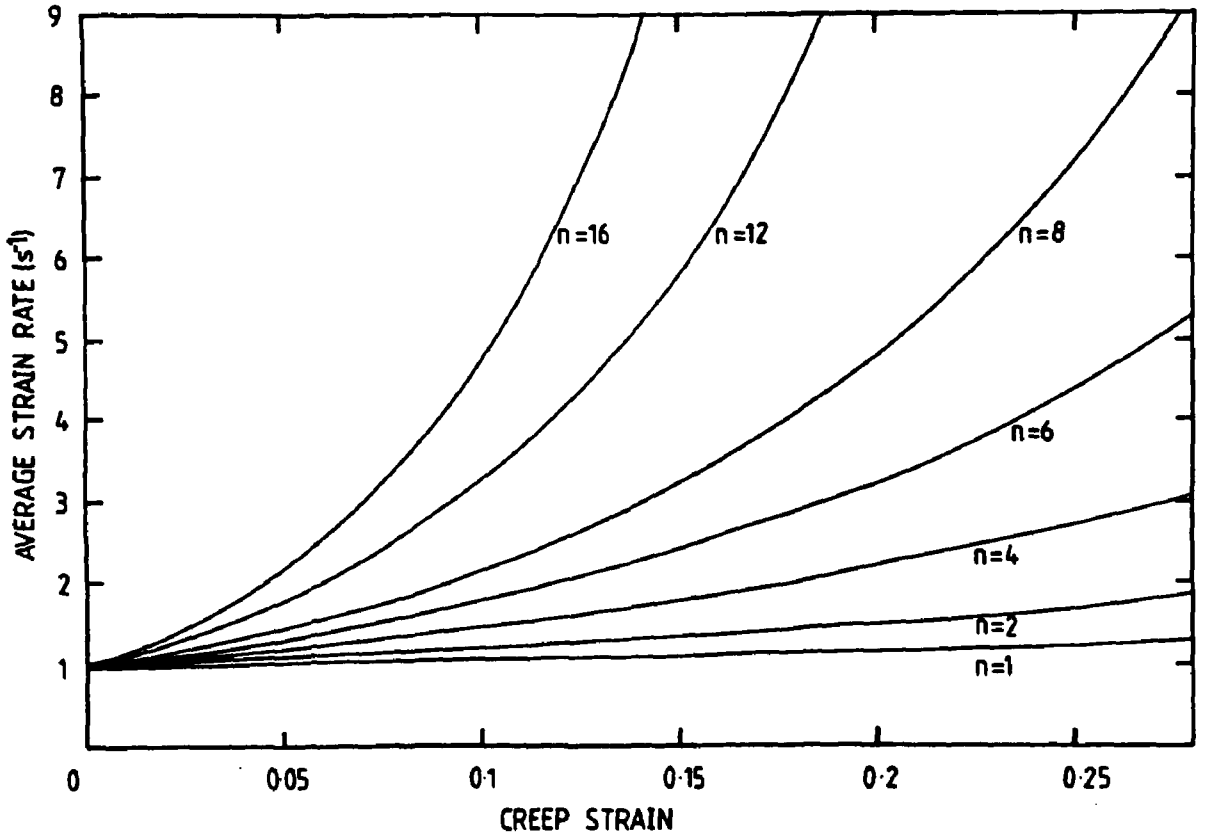

FIGURE 24: Average Specimen Strain Rate as a Function of Average Strain for a Tensile Creep Specimen Undergoing Progressive Necking for Various Values of the Stress Exponent, n (Evans and Wilshire 1985)

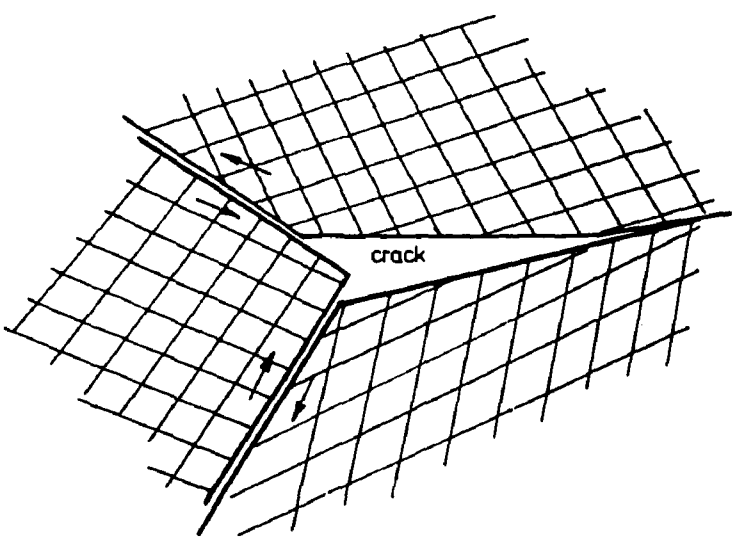

FIGURE 25: Schematic Representation of the Development of Wedge-Cracks at a Triple-Point, Due to Grain-Boundary Sliding

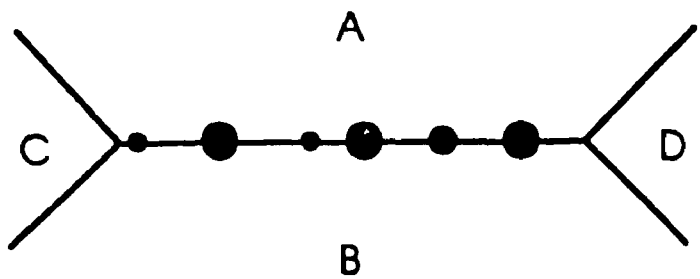

FIGURE 26: Depiction of a Series of Cavities Growing by Vacancy Absorption on a Grain Boundary Under a Tensile Stress

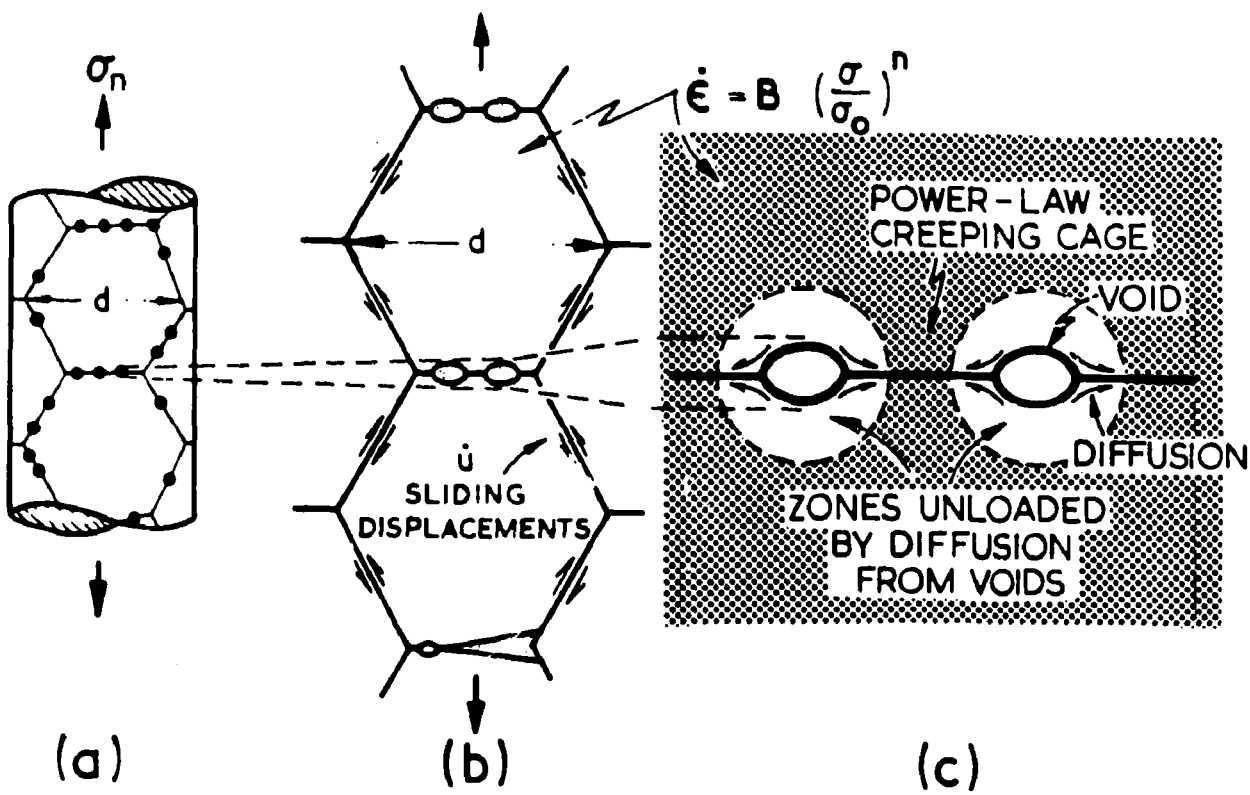

FIGURE 27: Diagrams (a) and (b) Show the Development of Grain-Boundary Voids, Accompanied by Grain-Boundary Sliding. In (c) the diffusional growth of voids is indicated. The diffusion fields of neighbouring voids do not, in general, overlap, so that each void is contained in a cage of material deforming by power-law creep (Ashby et al. 1979).

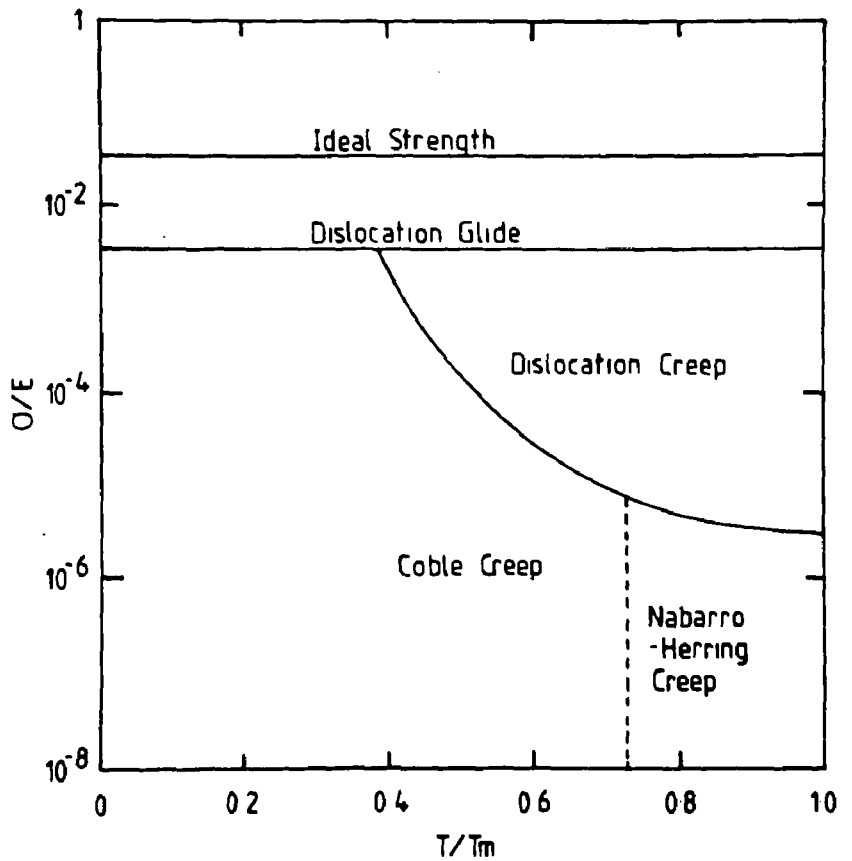

FIGURE 28: Schematic Version of a Deformation Mechanism Map, Showing Regions in the Stress/Temperature Plane Where Various (Steady-State) Creep Mechanisms Dominate the Deformation Process

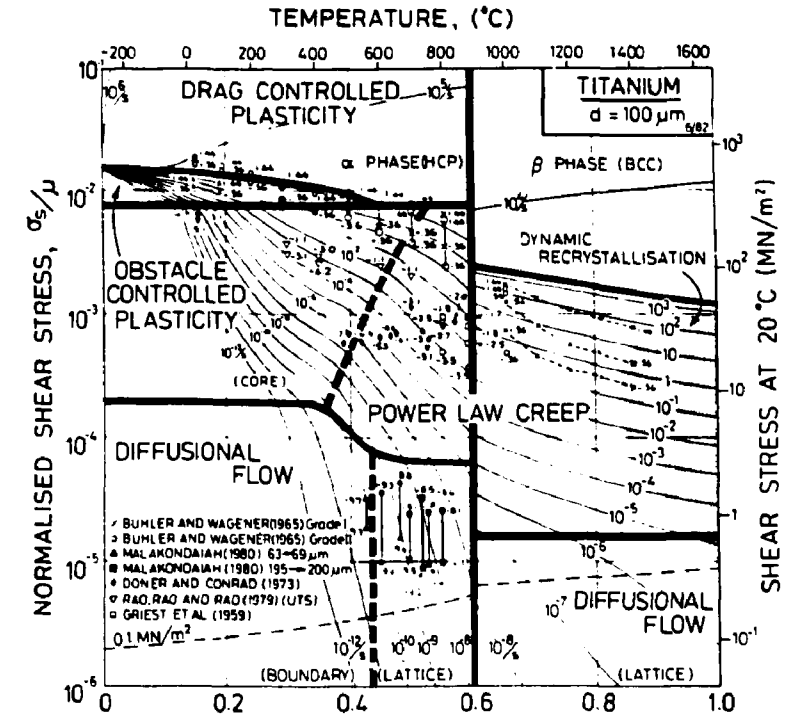

(a)

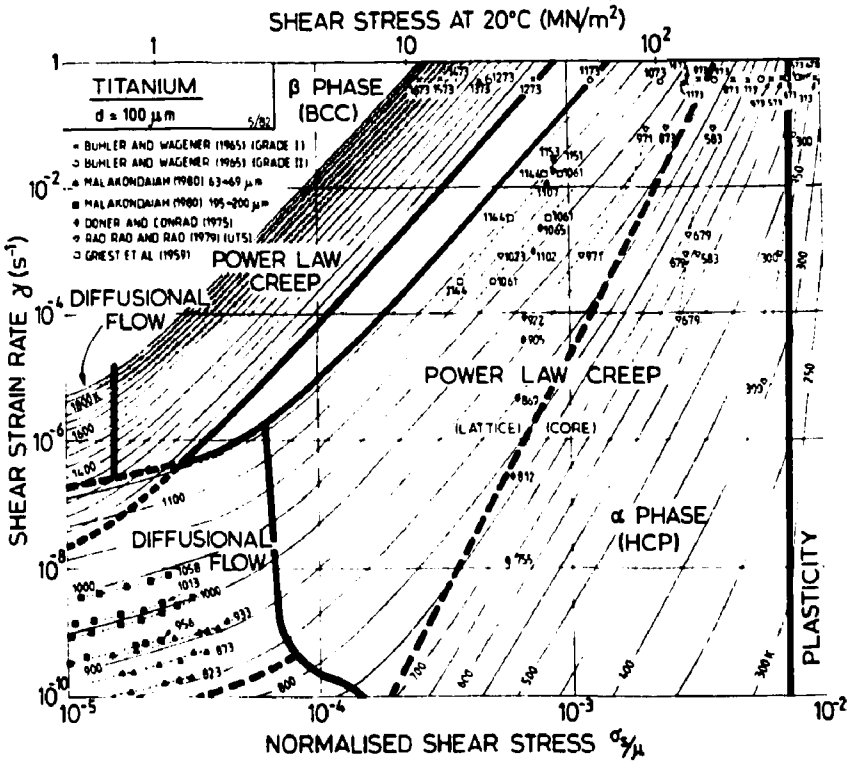

(b)

FIGURE 29: Deformation Mechanism Map for Titanium with a Grain Size of 100 μm. Diagram (a) is the normal form of the Map, corresponding to Figure 28. In this stress/temperature plane, contours of constant strain rate are plotted, and the experimental data indicated by various symbols. An alternative (but equivalent) form is shown in (b), using the strain-rate/stress plane, where the contour lines represent equal temperature conditions. Note the symbol μ is used for the elastic shear modulus, rather than G in the text. (Sargent and Ashby 1982).

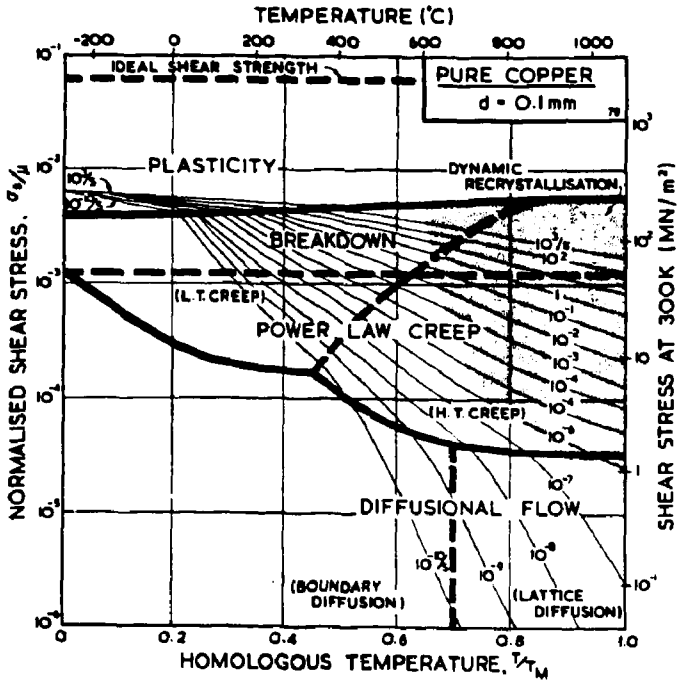

(a)

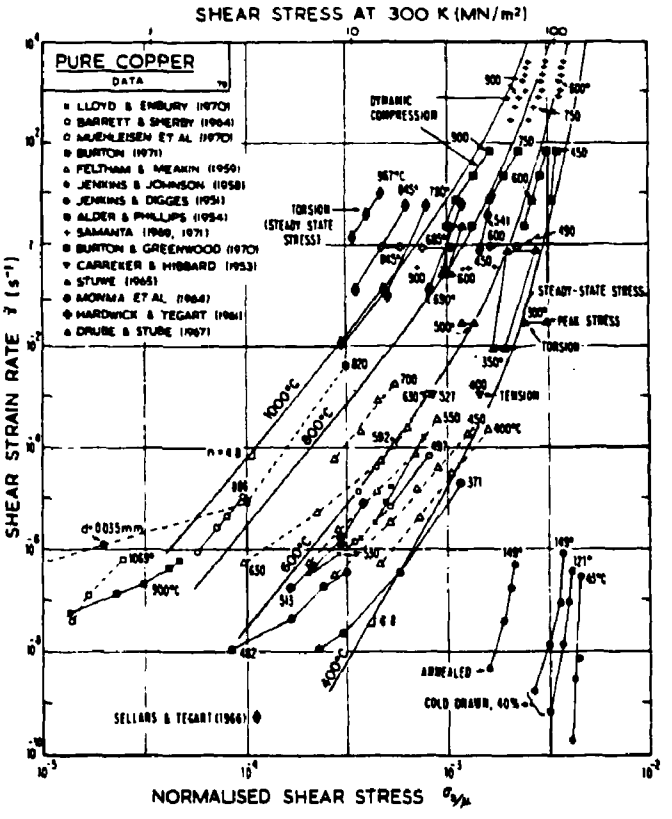

(c)

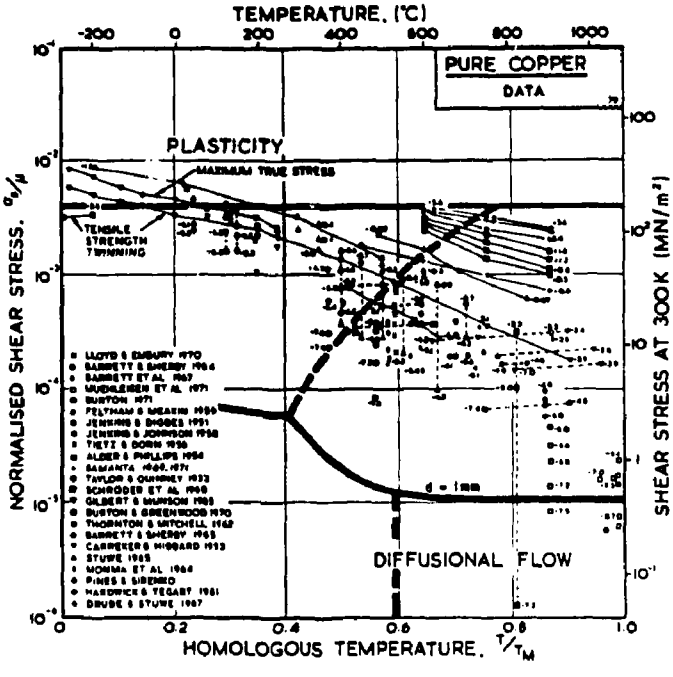

(b)

FIGURE 30: Deformation Mechanism Map for Copper with a Grain Size of 0.1 mm, Shown in (a). Diagram (b) shows the experimental data superimposed on the Map, while (c) shows the data in the strain-rate/stress plane. Note the symbol μ is used for the elastic shear modulus, rather than G in the text. (Frost and Ashby 1982).

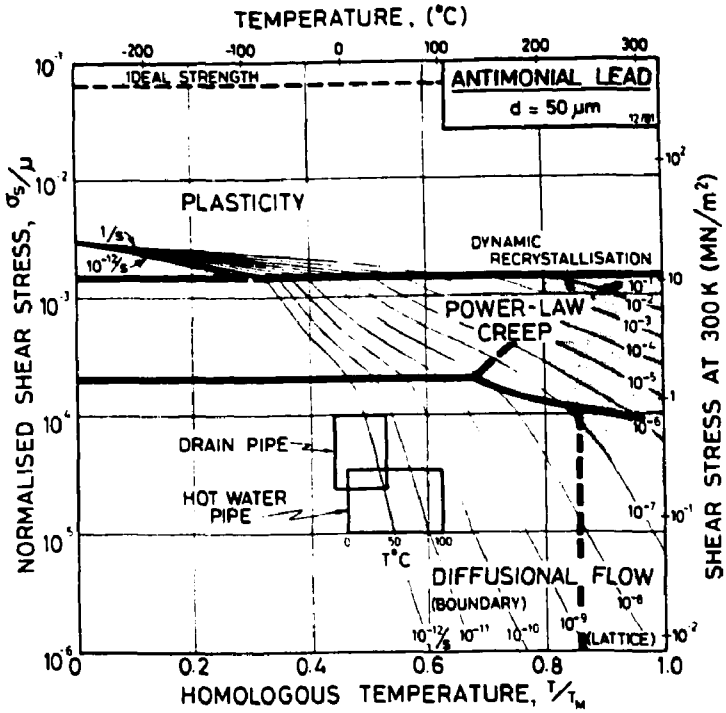

(a)

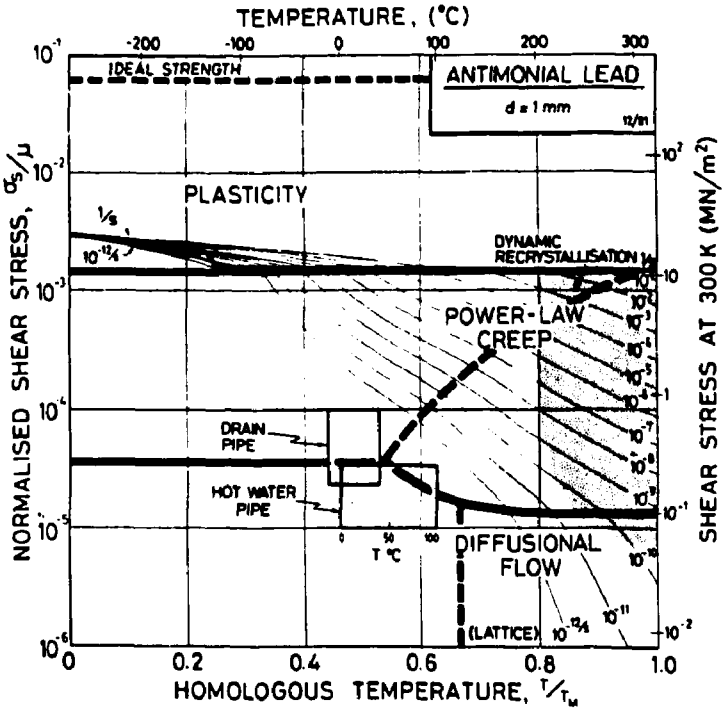

(b)

FIGURE 31: Deformation Mechanism Map for Antimonial Lead with a Grain Size of 50 μm (a) and 1 mm (b). On each of these Maps is plotted the stress/temperature range of the water pipes. Note the symbol μ is used for the elastic shear modulus, rather than G in the text. (Frost and Ashby 1982).

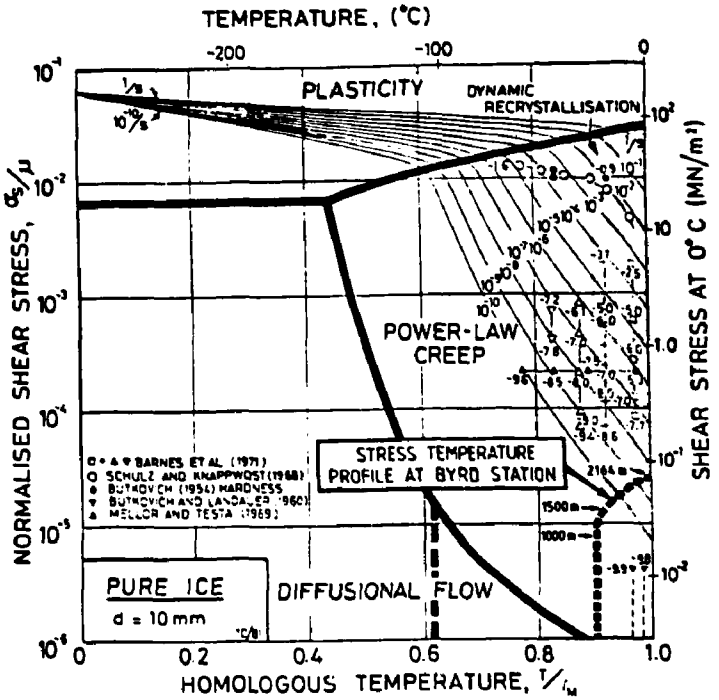

FIGURE 32: Deformation Mechanism Map for Ice with a Grain Size of 10 mm. The stress-temperature profile of the Antarctic ice derived from boreholes at the Byrd Station is also plotted, showing deformation in this region is mainly by power-law creep. Note the symbol μ is used for the elastic shear modulus, rather than G in the text. (Frost and Ashby 1982).

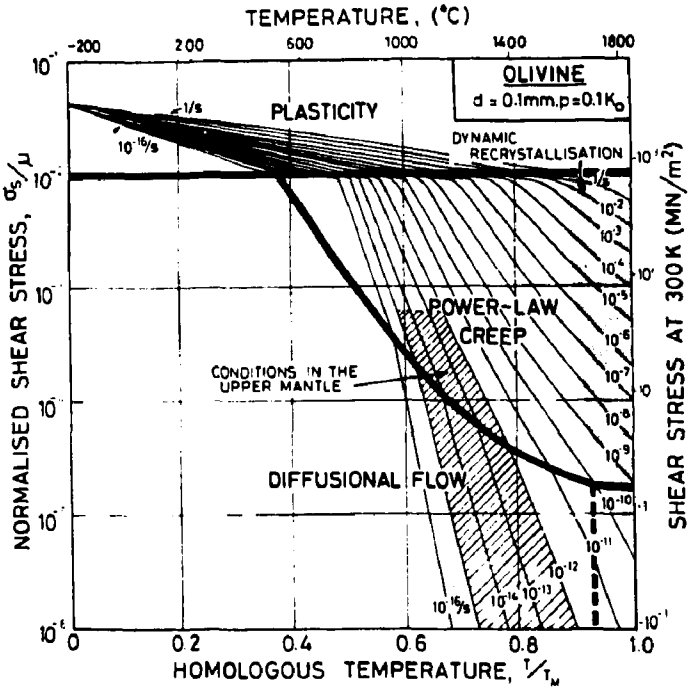

FIGURE 33: Deformation Mechanism Map for Olivine (Grain Size of 0.1 mm) Relevant to a Hydrostatic Pressure of 1.3×10^4 MPa, Corresponding to a Depth of 380 km. The range of conditions in the earth's upper mantle is shown. Note the symbol μ is used for the elastic shear modulus, rather than G in the text. (Frost and Ashby 1982).

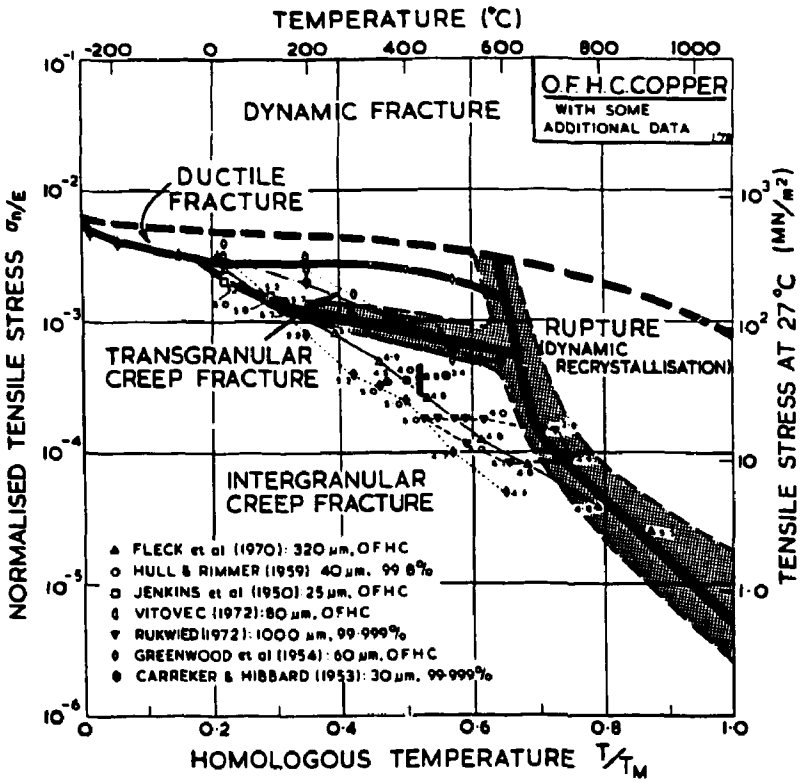

FIGURE 34: Fracture Mechanism Map for OFHC Copper, Based on Empirical Metallographic Evidence from the Experimental Data Indicated (Ashby et al. 1979)

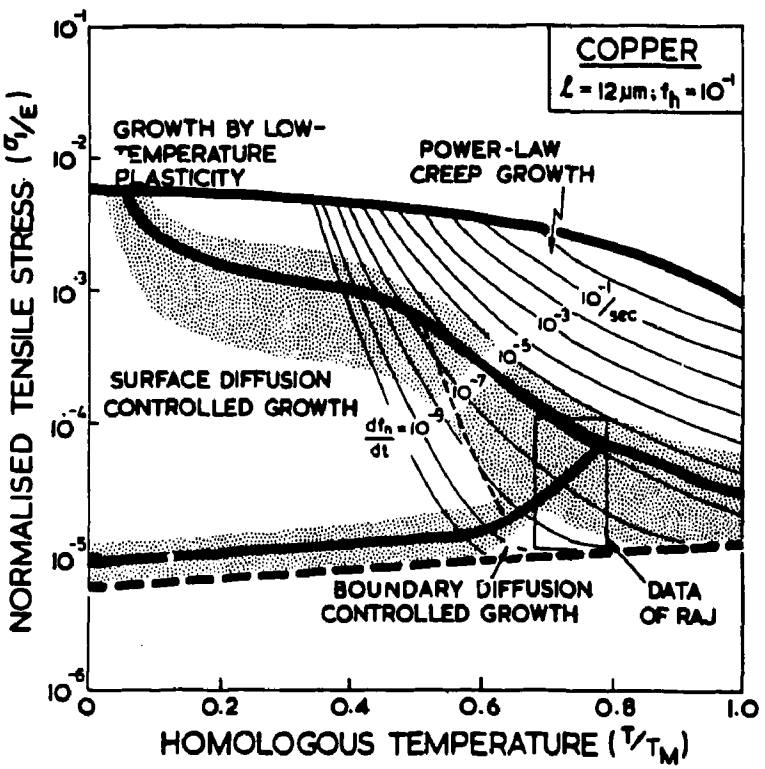

FIGURE 35: Fracture Mechanism Map for Copper, Based on Intergranular Creep Cavity Growth Mechanisms Where f_h is the Fractional Area of Cavities, Spaced 2 ℓ Apart (Cocks and Ashby 1982)

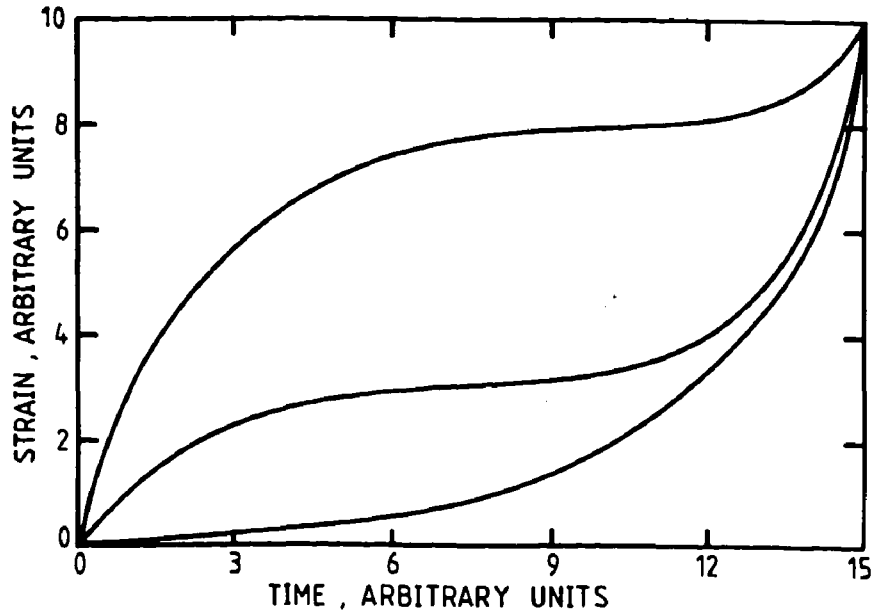

FIGURE 36: Schematic Creep Curves of Different Shape but Characterized by the Same Steady-State Creep Rate, Time and Strain to Fracture (Evans and Wilshire 1993)

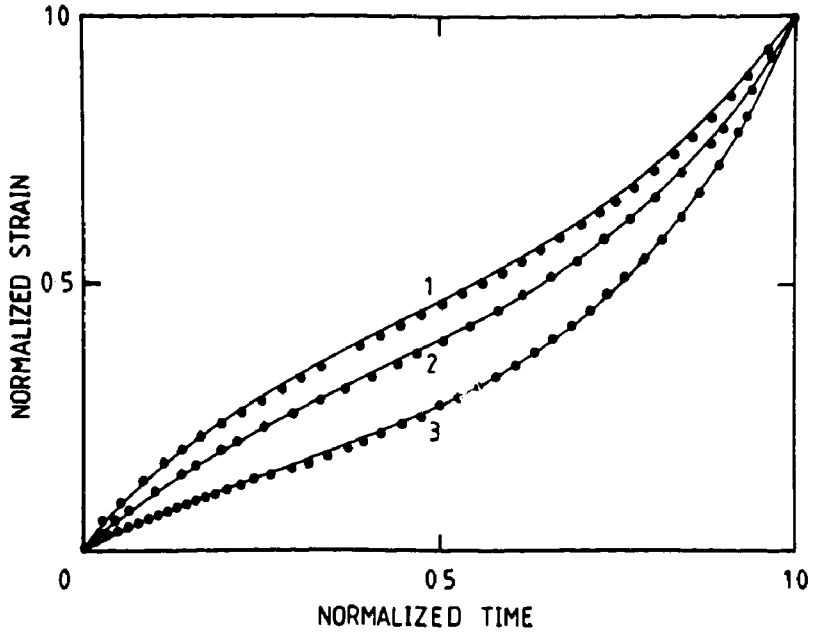

FIGURE 37: Constant-Stress Creep Curves for Copper Plotted as Normalized Strain ($\varepsilon/\varepsilon_f$) Against Normalized Time (t/t_f) for Stresses of (1) 48, (2) 34 and (3) 14 MPa at 455°C. The points are experimental data, while the lines are constructed using the θ Projection Concept (Evans and Wilshire 1993).

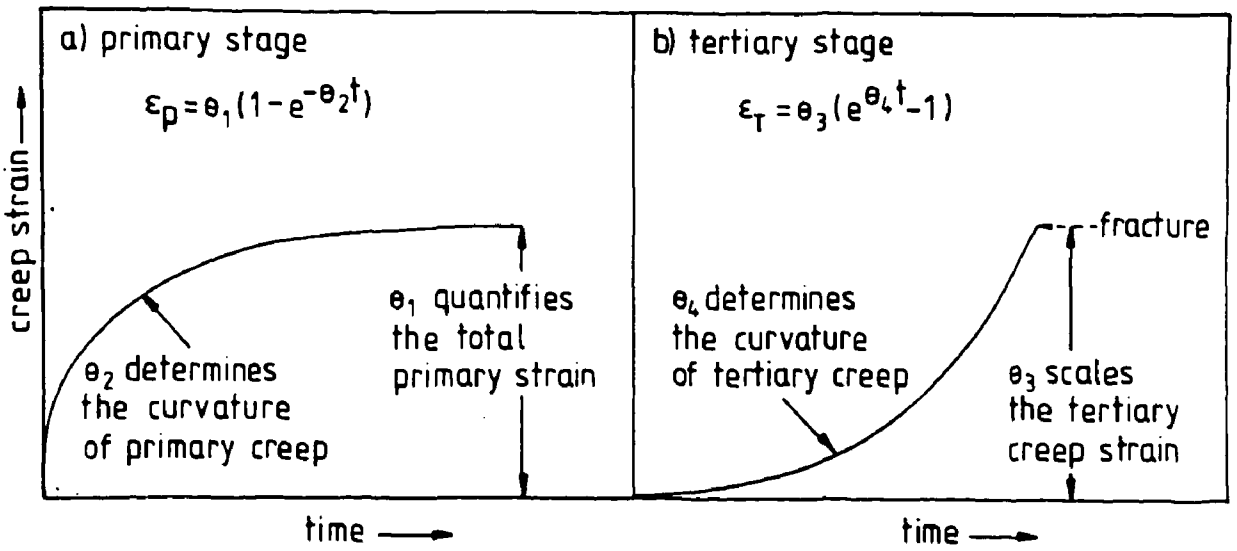

FIGURE 38: This Illustrates that the θ Projection Concept is Based on the Principle that Normal Creep Curves Comprise a Decaying Primary Component (ε_p) and an Accelerating Tertiary Concept (ε_t). The parameters θ_1 and θ_3 scale the primary and tertiary stages with respect to strain. The terms θ_2 and θ_4 are then rate parameters that describe the curvatures of the primary and tertiary stages, respectively (Evans and Wilshire 1993).

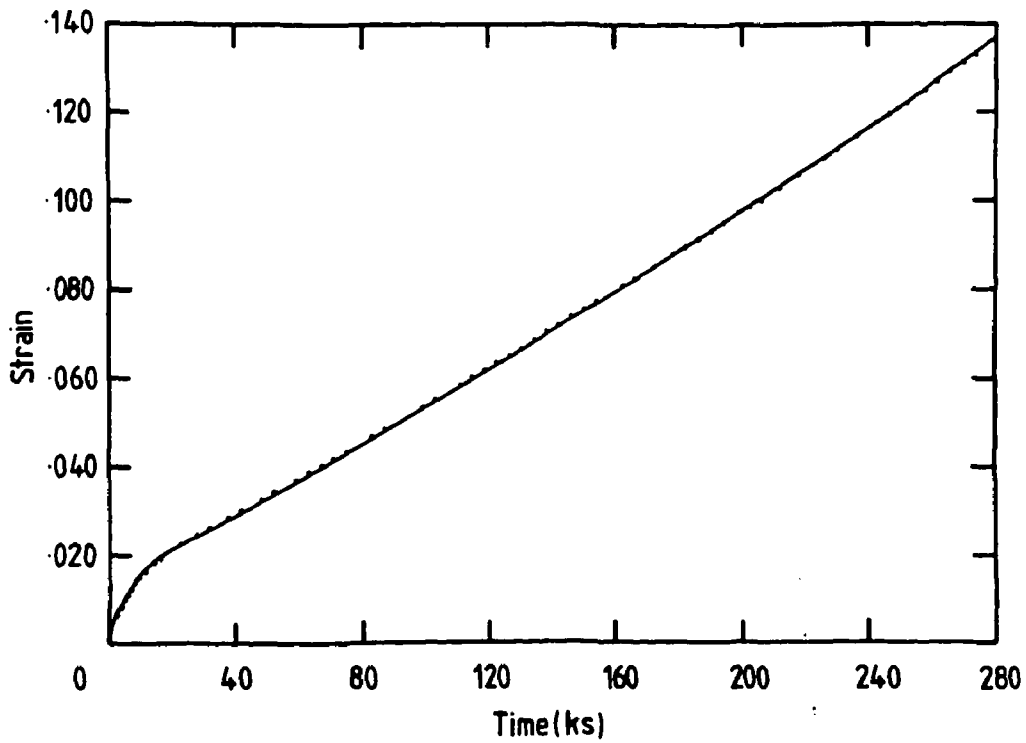

FIGURE 39: Actual (Data Points) and Predicted (θ Projection) Creep Curve for 0.5Cr0.5Mo0.25V Steel Tested at 310 MPa and 530°C (Evans et al. 1984)

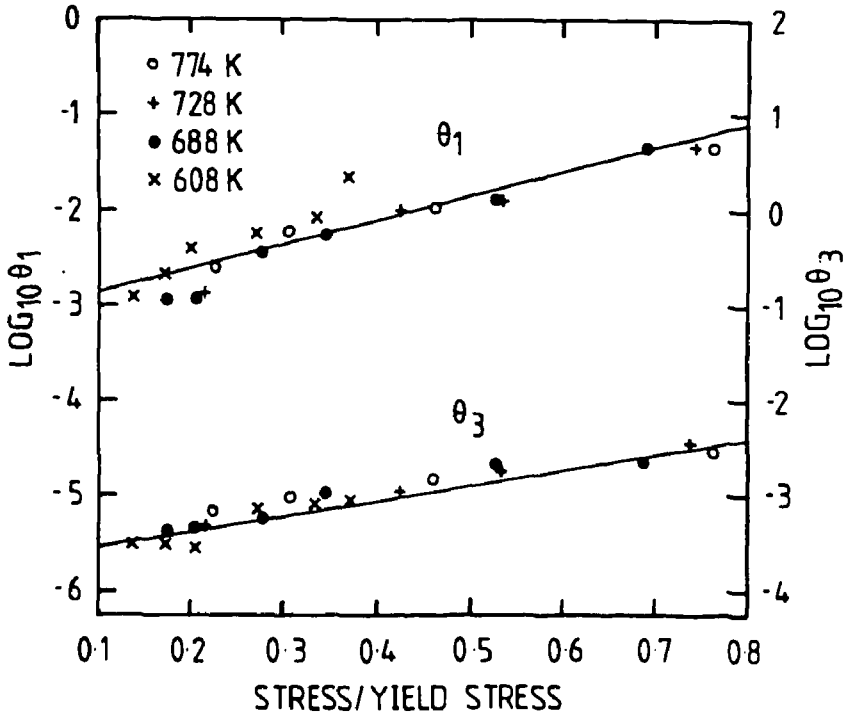

(a)

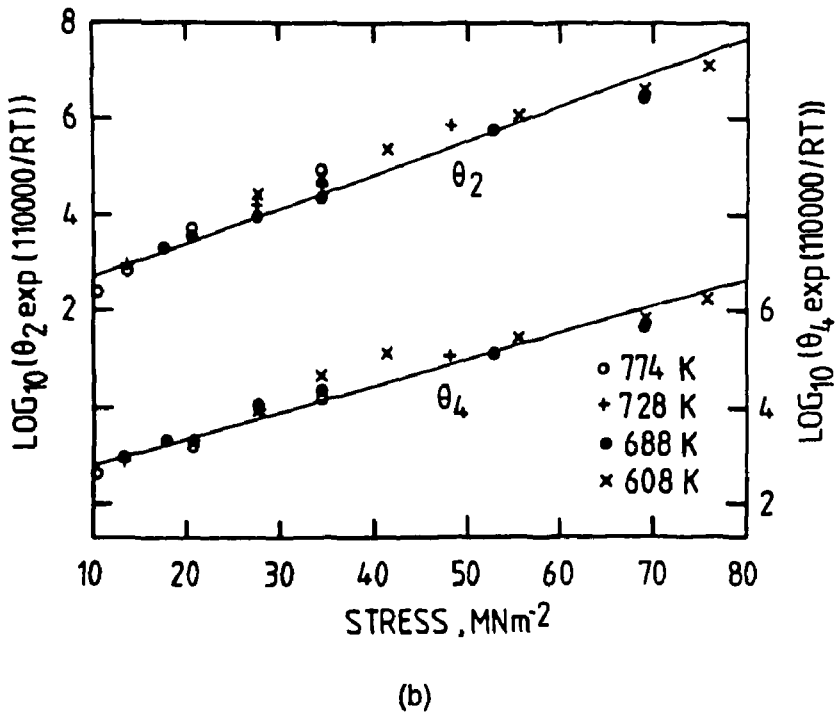

(b)

FIGURE 40: The Stress and Temperature Dependencies of (a) the Strain-Like Parameters θ_1 and θ_3, and (b) the Rate Constants θ_2 and θ_4 for Copper (Evans and Wilshire 1983)

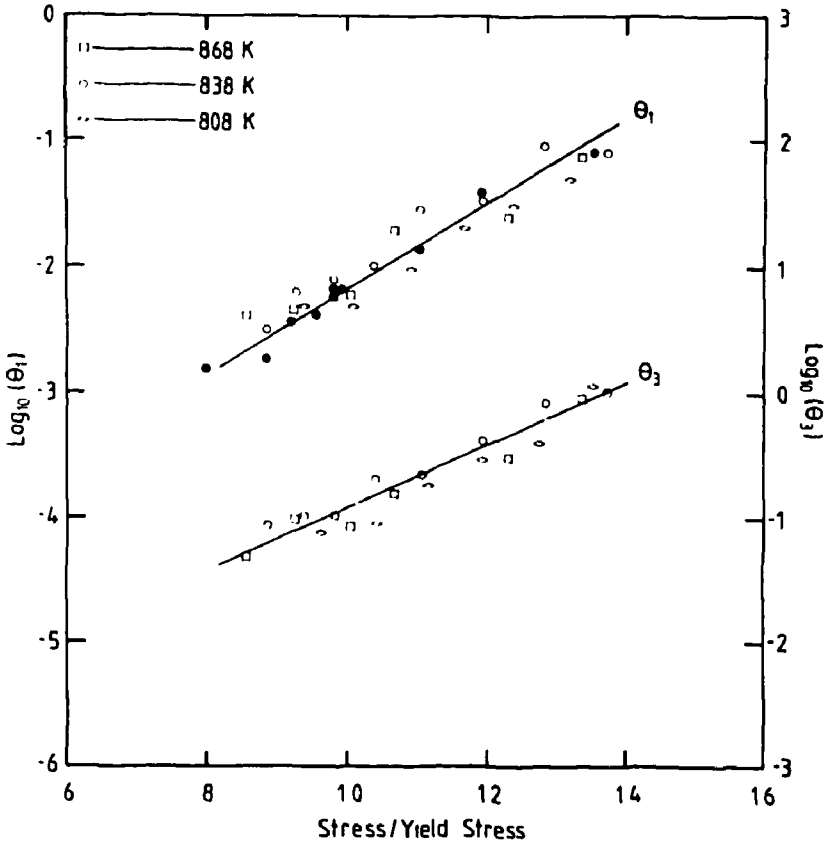

(a)

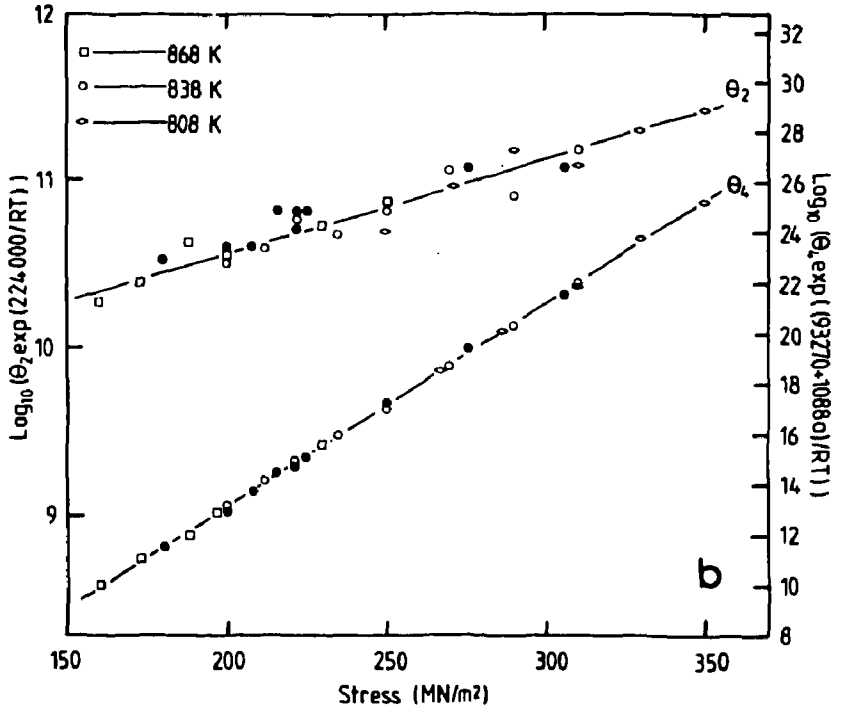

(b)

FIGURE 41: The Stress and Temperature Dependencies of (a) θ_1 and θ_2, and (b) θ_3 and θ_4 for 0.5Cr-0.5Mo-0.25V Steel (Evans and Wilshire 1993)

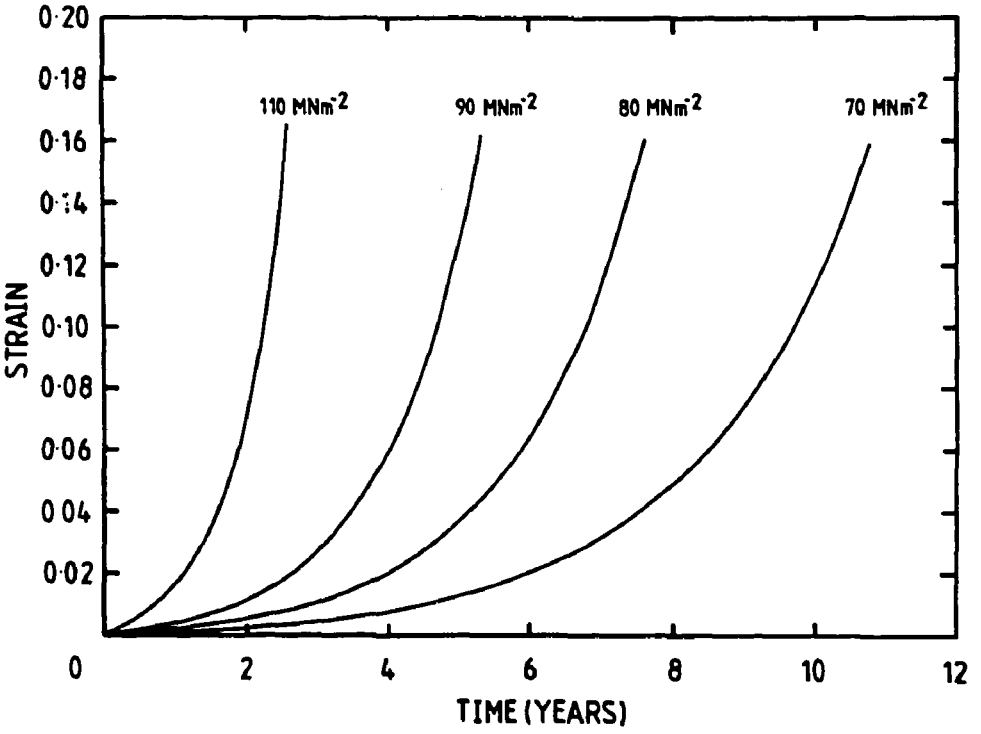

FIGURE 42: Long-Term Creep Curves Calculated from the θ Data (Figure 41) for 0.5Cr0.5Mo0.25V Steel at 565°C (Evans and Wilshire 1985)

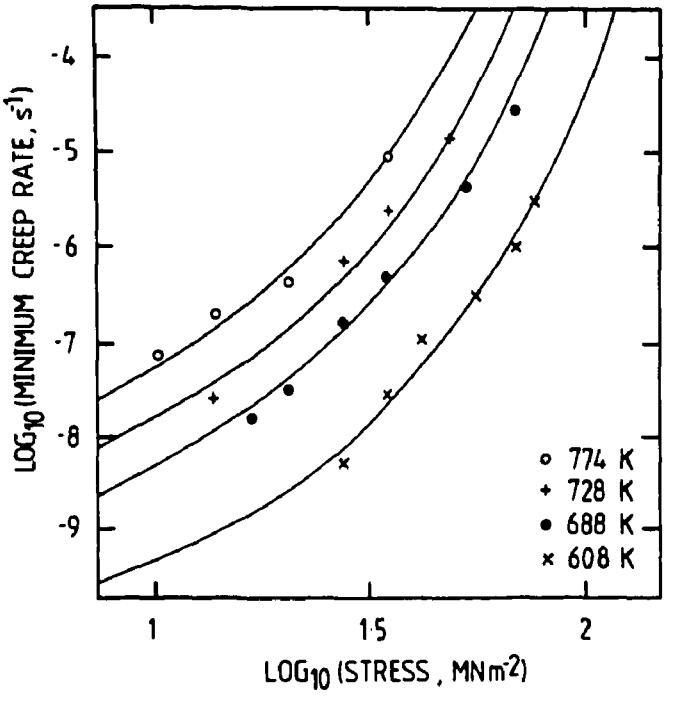

FIGURE 43: Stress Dependence of the Minimum Creep Rate for Polycrystalline Copper. The lines predicted from the stress dependence of the θ parameters (Figure 40) are compared with experimental data at various temperatures (Evans and Wilshire 1993).

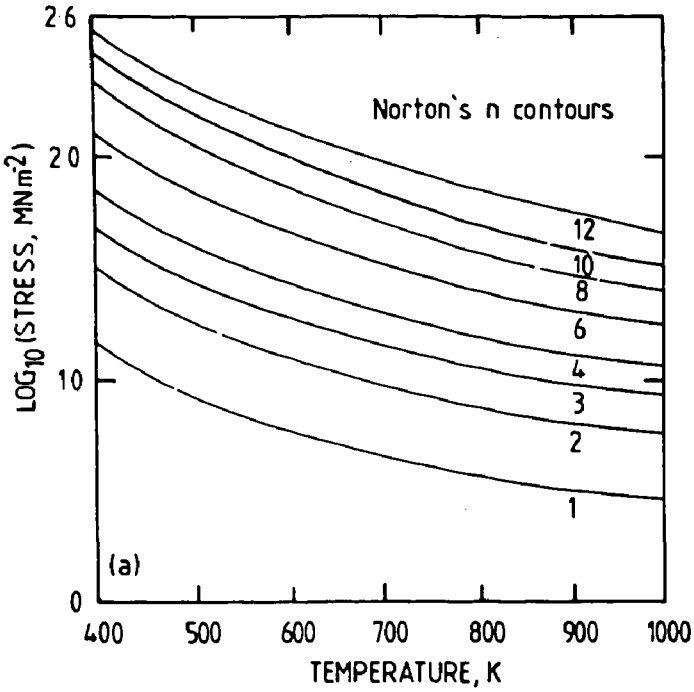

(a)

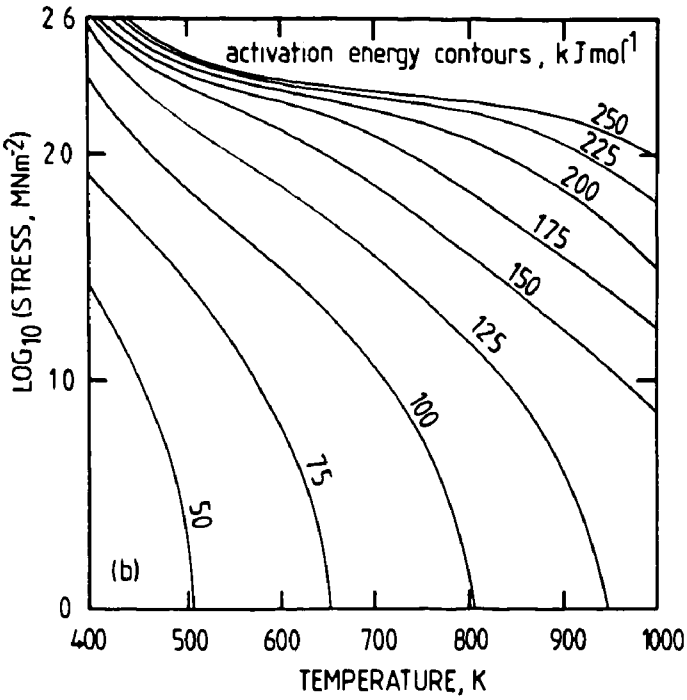

(b)

FIGURE 44: Variation of (a) the Stress Exponent, n, and (b) the Activation Energy for Creep, Q_c, of Polycrystalline Copper. The plots were derived from minimum creep rates calculated from a knowledge of the stress and temperature dependencies of the θ parameters shown in Figure 40 (Evans and Wilshire 1993).

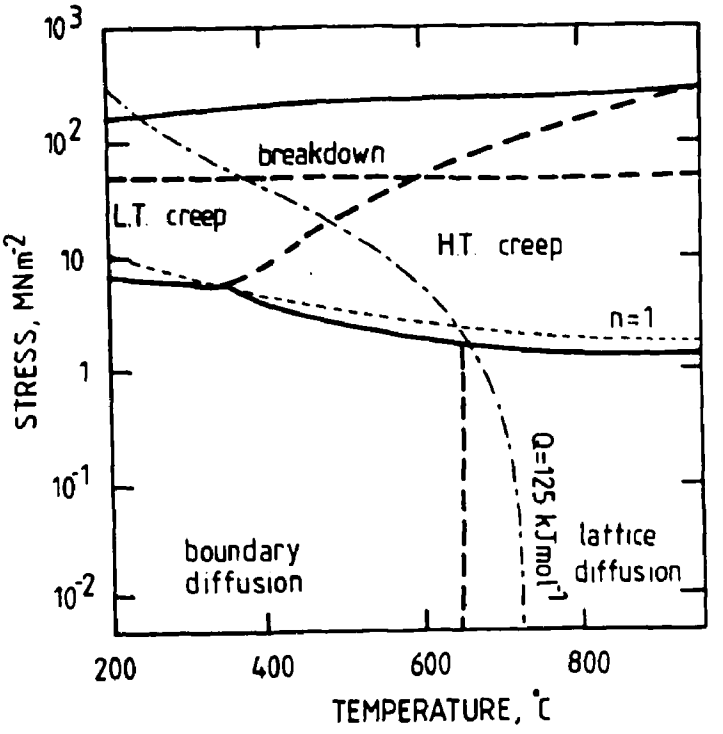

FIGURE 45: Deformation Mechanism Map for Polycrystalline Copper (see Figure 30) with Lines of $n \approx 1$ and $Q_c = 110$ kJ mol^{-1} Calculated from the Stress and Temperature Dependencies of the θ Parameters (Figure 40). LT and HT indicate the regimes where dislocation creep is controlled by core diffusion and lattice diffusion at low and high temperatures, respectively (Evans and Wilshire 1993).

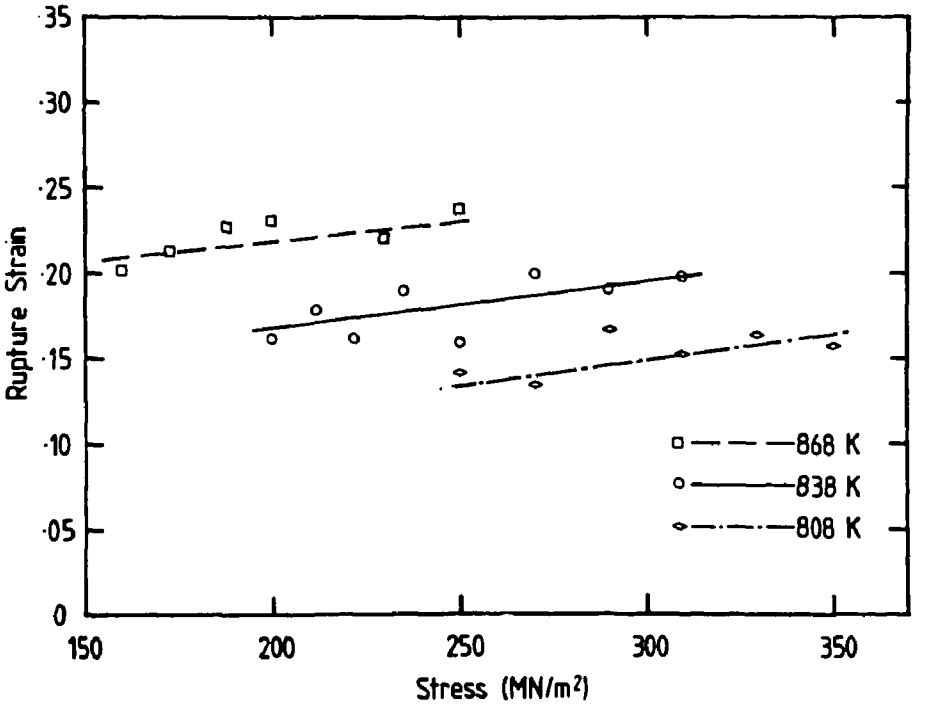

FIGURE 46: The Variation of the Creep Ductility, ε_f, with Stress and Temperature for 0.5Cr0.5Mo0.25V Steel (Evans and Wilshire 1993)

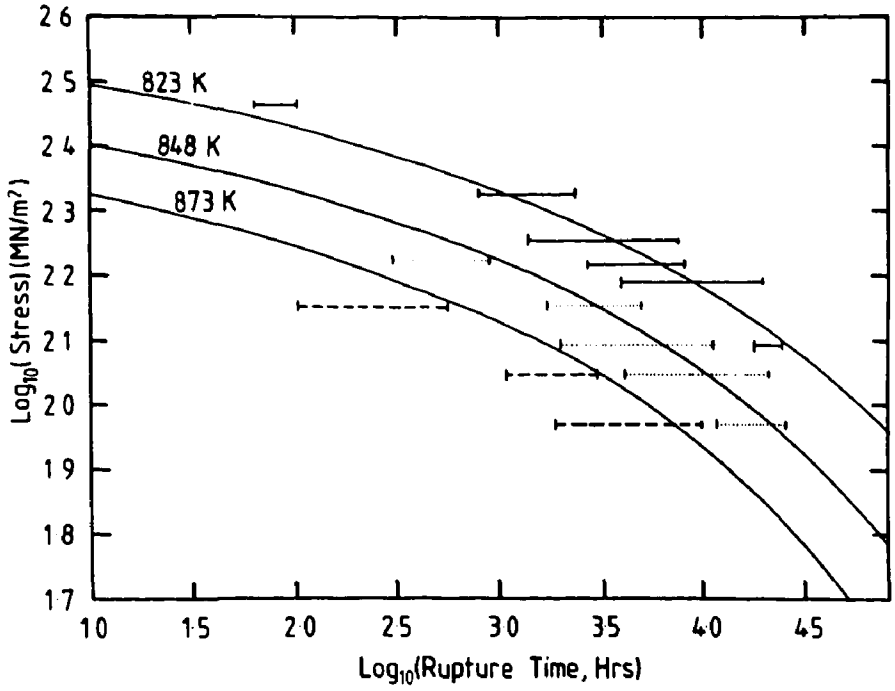

FIGURE 47: Predicted Stress-Rupture Curves for 0.5Cr-0.5Mo-0.25V Steel. The error bars represent the scatter for various stress/temperature conditions in multi-laboratory long-term stress-rupture data (Evans and Wilshire 1993).

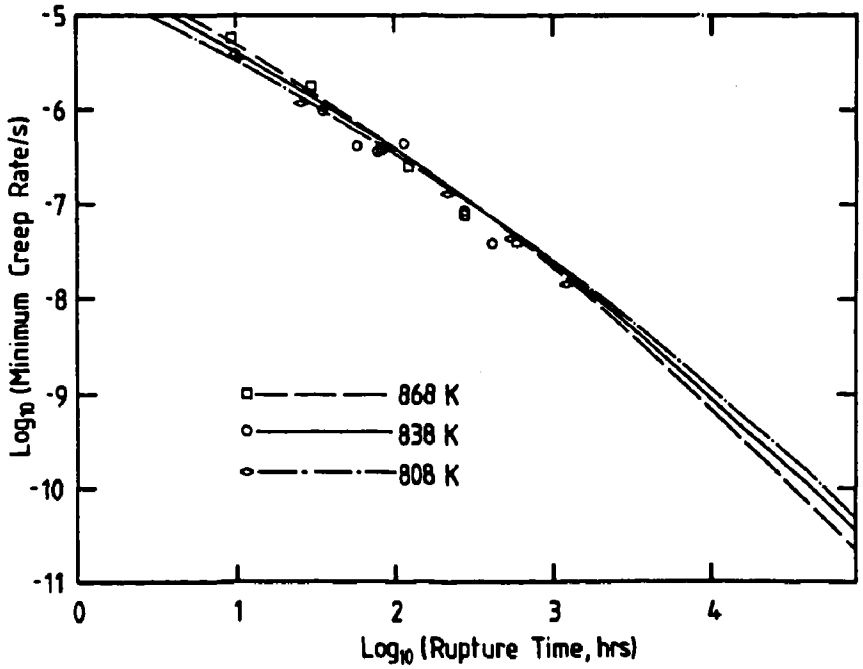

FIGURE 48: The Relationship Between the Minimum Creep Rate- and the Rupture Life of 0.5Cr0.5Mo0.25V Steel Calculated from the θ Data (lines), Together with the Available Experimental Points (Evans and Wilshire 1985)

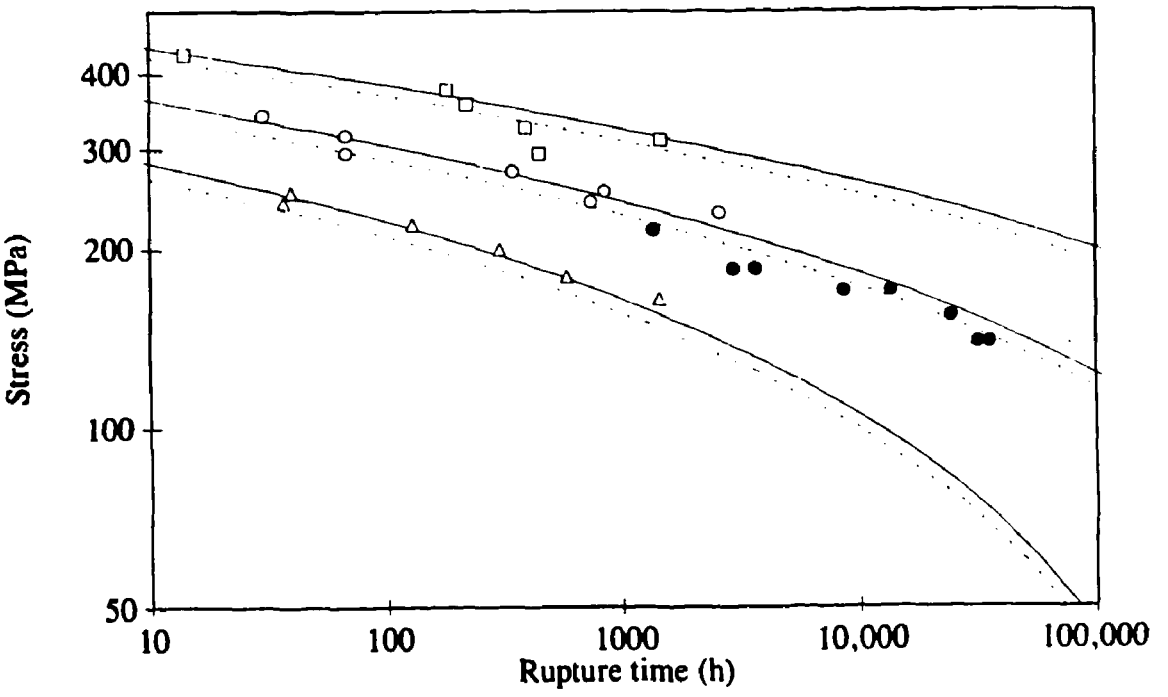

FIGURE 49: Predicted (θ Parameter) log σ/log t_r Plots for Constant-Stress (Solid Lines) and Constant-Load (Broken Lines) Conditions, Compared with Measured t_r Values Obtained from Short-Term Constant-Stress Tests at 510, 550 and 590°C (Open Symbols) and Long-Term Constant-Load Tests (Full Symbols) at 550°C, for 1CrMoV Steel (Wilshire and Evans 1994)

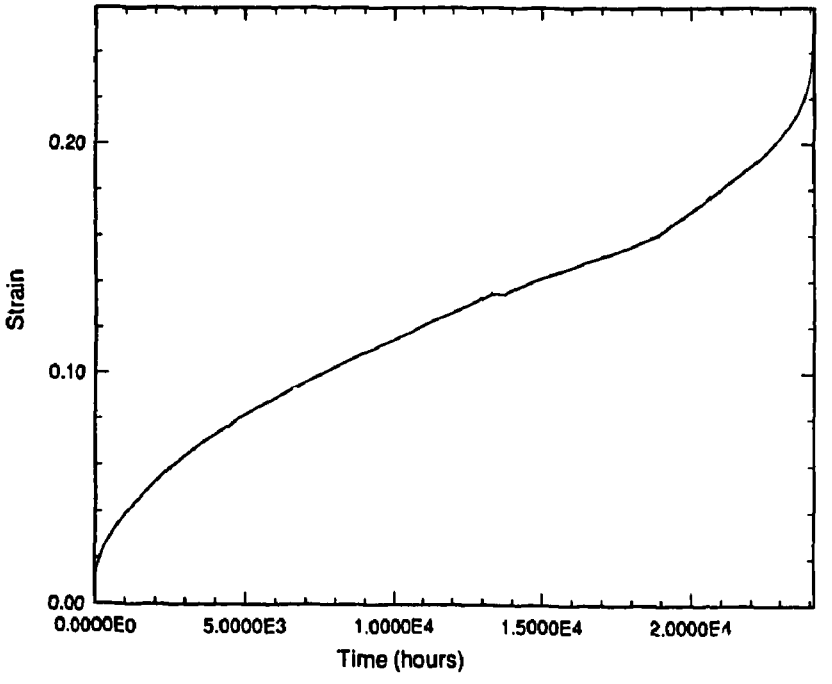

FIGURE 50: Creep Curve for ASTM Grade 2 Titanium, Tested at 100°C and 187 MPa

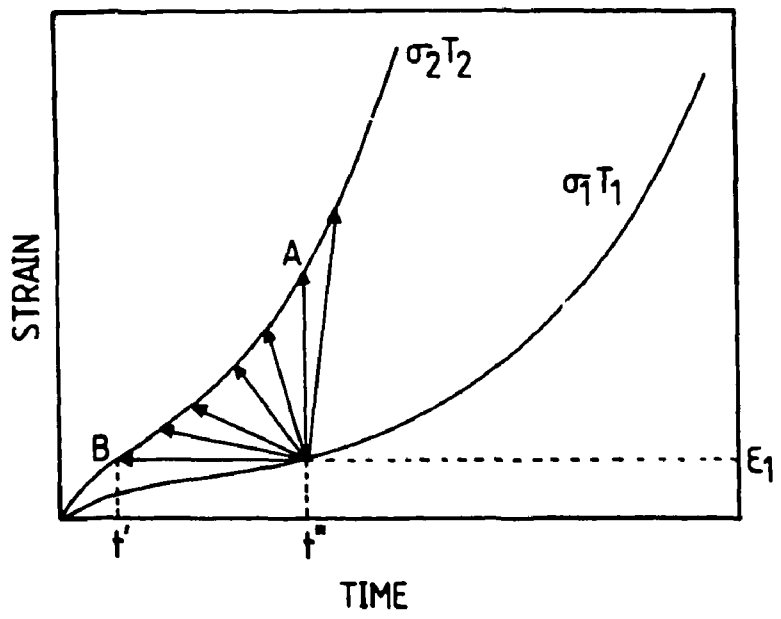

FIGURE 51: Schematic Diagram Showing Alternative Paths when Prevailing Conditions Change from $\sigma_1 T_1$ to $\sigma_2 T_2$ (Evans and Wilshire 1987b)

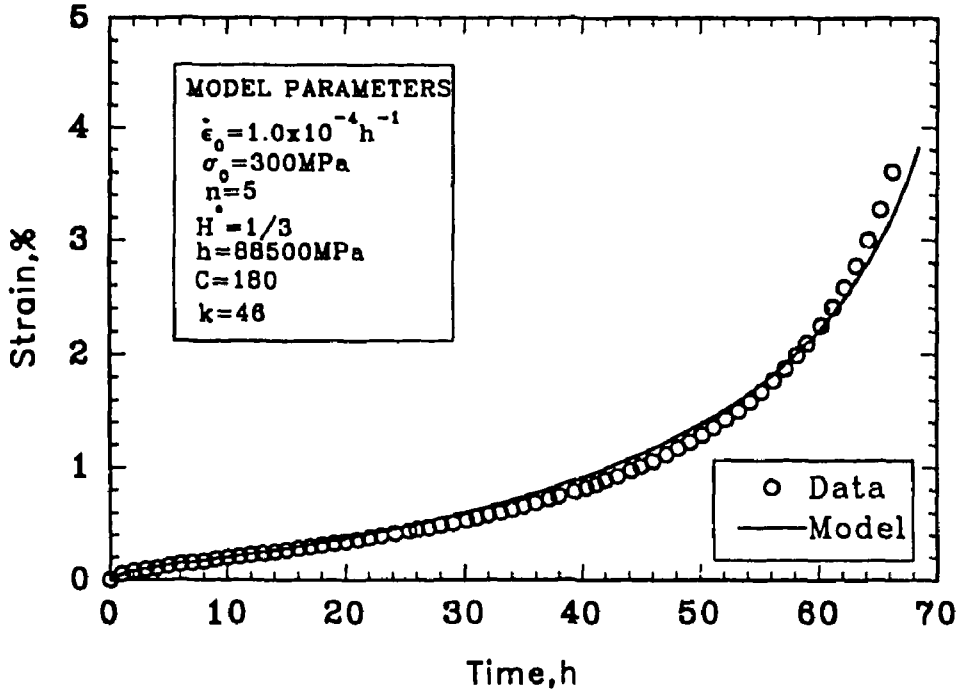

FIGURE 52: Creep Curve for Nimonic 101 Alloy (Osgerby and Dyson 1993)

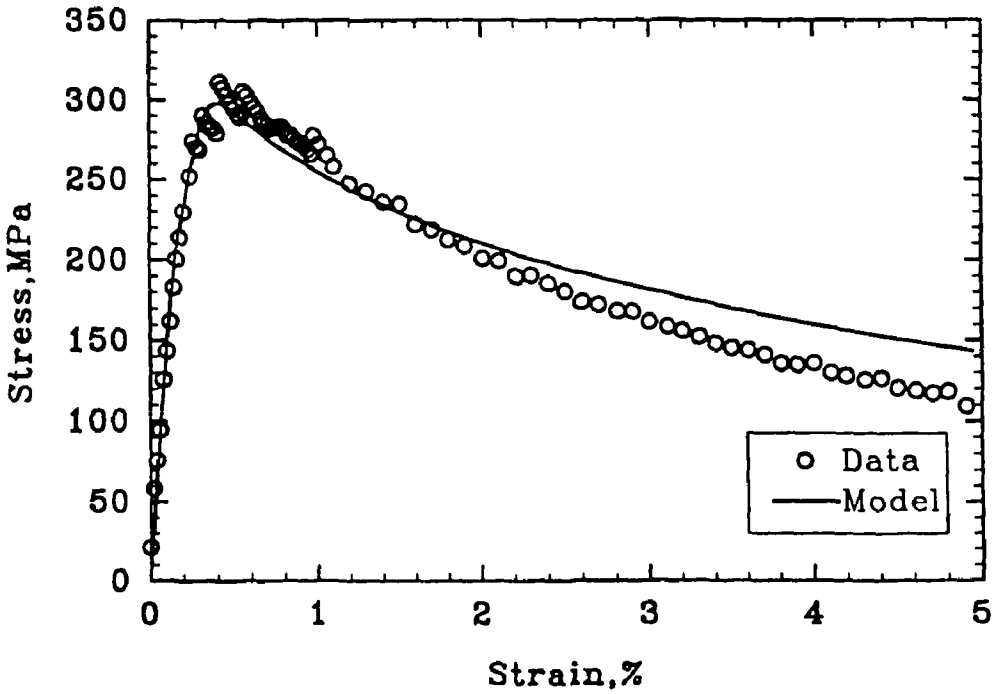

FIGURE 53: Stress-Strain Curve (Constant-Strain Rate of 1.4 x 10^{-4} h^{-1}) for Nimonic 101 Alloy, Predicted from Creep Data and Compared with Experiment (Osgerby and Dyson 1993)

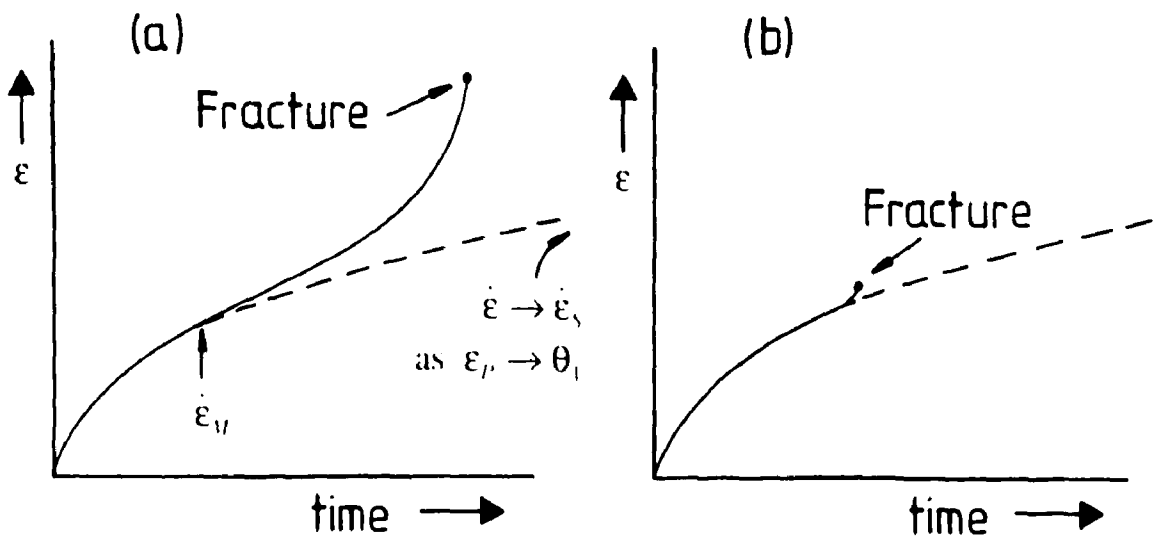

FIGURE 54: Schematic Representation of (a) Extensive Tertiary Stage for Creep-Ductile Materials and (b) Contracted Tertiary Stage for Creep-Brittle Materials (Evans and Wilshire 1993)

Cat. No. / N° de cat.: CC2-11249E
ISBN 0-660-16281-4
ISSN 0067-0367

To identify individual documents in the series, we have assigned an AECL- number to each. Please refer to the AECL- number when requesting additional copies of this document from

Scientific Document Distribution Office (SDDO)
AECL
Chalk River, Ontario
Canada K0J 1J0

Fax: (613) 584-1745 Tel.: (613) 584-3311
ext. 4623

Price: C

Pour identifier les rapports individuels faisant partie de cette série, nous avons affecté un numéro AECL- à chacun d'eux. Veuillez indiquer le numéro AECL- lorsque vous demandez d'autres exemplaires de ce rapport au

Service de Distribution des documents officiels (SDDO)
EACL
Chalk River (Ontario)
Canada K0J 1J0

Fax: (613) 584-1745 Tél.: (613) 584-3311
poste 4623

Prix: C

AECL EACL

AECL-11249, COG-95-06

A Methodology to Analyze the Creep Behaviour of Nuclear Fuel Waste Containers

Méthode d'analyse du comportement au fluage des conteneurs de déchets de combustible nucléaire

R. Dutton

December 1995 décembre

AECL

A METHODOLOGY TO ANALYZE THE CREEP BEHAVIOUR OF NUCLEAR FUEL WASTE CONTAINERS

by

R. Dutton

Whiteshell Laboratories
Pinawa, Manitoba R0E 1L0
1995

AECL-11249
COG-95-06

A METHODOLOGY TO ANALYZE THE CREEP BEHAVIOUR OF NUCLEAR FUEL WASTE CONTAINERS

by

R. Dutton

ABSTRACT

The concept for the disposal of used-fuel waste from CANDU reactors operating in Canada comprises a system of natural and engineered barriers surrounding the waste in a mined vault situated at a depth of 500 - 1000 m in plutonic rock of the Canadian Shield. The fuel would be packaged in a highly durable metal container, within a matrix of compacted particulate. The design of the container takes into account that it would be subjected to an external hydrostatic pressure. Consideration of the rate of radioactive decay of the radionuclides contained in the fuel, suggests that the lifetime of the container should be at least 500 years. Consequently, the role of creep deformation, and the possibility of creep rupture of the container shell, must be included in the assessment of time-dependent mechanical integrity.

This report describes an analytical approach that can be used to quantify the long-term creep properties of the container material and facilitate the engineering design. The overall objective is to formulate a constitutive creep equation that provides the required input for a finite element computer model being developed to analyze the elastic-plastic behaviour of the container. Alternative forms of such equations are reviewed. It is shown that the capability of many of these equations to extrapolate over long time scales is limited by their empirical nature. Thus, the recommended equation is based on current mechanistic understanding of creep deformation and creep rupture. The pertinent mechanisms are described. It is shown that the qualitative and quantitative characteristics of these mechanisms are conveniently captured by Deformation Mechanism Maps and Fracture Mechanism Maps. These offer a guide for the design of laboratory creep tests and the extrapolation of the experimental data. Based on this mechanistic underpinning, the selected constitutive equation derives from the θ Projection Concept. The theoretical and experimental background of this concept is reviewed. Examples are described where the four characteristic θ-parameters have been used to predict the long-term creep behaviour of a number of materials. The practical success of such projections, and their established scientific base, has resulted in the widespread acceptance of the technique. Consequently, we present an analytical scheme that adopts the θ Projection Concept for the interpolation of experimental creep data and long-term prediction of creep behaviour. A criterion for determining the onset of material failure by creep rupture, that could be used in the design of containers with extended structural integrity, is proposed. Interpretation and extrapolation will be supported by the complementary Deformation and Fracture Mechanism Maps.

AECL
Whiteshell Laboratories
Pinawa, Manitoba R0E 1L0
1995

AECL-11249
COG-95-06

MÉTHODE D'ANALYSE DU COMPORTEMENT AU FLUAGE DES CONTENEURS DE DÉCHETS DE COMBUSTIBLE NUCLÉAIRE

par

R. Dutton

RÉSUMÉ

Le concept de stockage permanent des déchets de combustible irradié des réacteurs CANDU en exploitation au Canada comprend un système de barrières naturelles et artificielles entourant les déchets placés dans une enceinte creusée à une profondeur de 500 à 1 000 m dans la roche plutonique du Bouclier canadien. Le combustible y serait conditionné dans un conteneur métallique extrêmement durable, dans une matrice de particules compactées. La conception du conteneur tient compte du fait qu'il serait soumis à une pression hydrostatique externe. En tenant compte du taux de décroissance radioactive des radionucléides contenus dans le combustible, on peut avancer que la durée de vie du conteneur serait d'au moins 500 ans. En conséquence, le rôle de la déformation de fluage ainsi que la possibilité d'une rupture par contrainte de fluage de l'enveloppe du conteneur doivent faire partie de l'évaluation de l'intégrité mécanique en fonction du temps.

Le présent rapport décrit une méthode analytique pouvant servir à quantifier les propriétés de fluage sur de longues périodes du matériau de fabrication du conteneur et à faciliter les études techniques. L'objectif global est de formuler une équation constitutive du fluage qui fournit les données nécessaires à l'utilisation d'un modèle informatique d'analyse par éléments finis élaboré en vue d'étudier le comportement plastique-élastique du conteneur. On y fait une étude des variantes de ces formes d'équations. On y montre que, pour un grand nombre de ces équations, les capacités d'extrapolation sur de longues échelles de temps sont restreintes en raison de leur caractère empirique. En conséquence, l'équation recommandée est fondée sur les connaissances mécanistes actuelles de la déformation et de la rupture de fluage. On décrit également les mécanismes pertinents. On indique que les caractéristiques qualitatives et quantitatives de ces mécanismes sont représentées de façon très pratique à l'aide de cartes des mécanismes de déformation ou de cartes des mécanismes de fracture. Ces tables de correspondances servent de guide pour la conception d'essais de fluage en laboratoire ou l'extrapolation des données expérimentales. L'équation constitutive choisie, fondée sur ces principes mécanistes, découle du concept de projection θ. Le cadre expérimental et théorique de ce concept y est analysé. On y donne des exemples dans lesquels les quatre paramètres θ caractéristiques ont été employés afin de prévoir le comportement au fluage sur de longues périodes d'un certain nombre de matériaux. Les succès pratiques de telles projections, joints à leur fondement scientifique bien établi, ont entraîné l'acceptation de cette technique de façon très générale. En conséquence, nous présentons une théorie analytique dans laquelle nous adoptons le concept de projection θ aux fins de l'interpolation des données expérimentales de fluage et des prévisions à long terme du comportement au fluage. On y propose un critère de détermination du seuil de défaillance du matériau par rupture de fluage qui pourrait être utilisé dans la conception de conteneurs caractérisés par une résistance structurelle prolongée. Les cartes des mécanismes de déformation et de fracture complémentaires seront fournies à l'appui des interprétations et des extrapolations.

EACL
Laboratoires de Whiteshell
Pinawa (Manitoba) R0E 1L0
1995

AECL-11249
COG-95-06

CONTENTS

continued ...

CONTENTS (concluded)

LIST OF SYMBOLS USED IN TEXT

a, b, c	Material creep constants
A, B	Material creep constants
α, β, γ	Material creep constants
a	Area of slip plane swept out by a dislocation
a_c	Spacing between grain-boundary cavities
A	Specimen cross-sectional area
b	Dislocation Burger's vector
C	Vacancy concentration
C_o	Equilibrium vacancy concentration
C_b	Vacancy concentration in grain boundary
C_c	Vacancy concentration adjacent to grain-boundary cavity
d	Grain size (average diameter)
D	Diffusion coefficient
D_o	Diffusional constant
D_{SD}	Self-diffusion coefficient
D_{GB}	Grain-boundary diffusion coefficient
δ	Grain-boundary width
E	Young's modulus
ε	Creep strain
$\dot{\varepsilon}_s$	Steady-state secondary creep rate
$\dot{\varepsilon}_m$	Minimum creep rate

$\dot{\varepsilon}_p$	Primary creep rate
$\dot{\varepsilon}_t$	Tertiary creep rate
ε_p	Primary creep strain
ε_t	Tertiary creep strain
ε_r	Strain to rupture
ε_m	Monkman-Grant constant ($= \dot{\varepsilon}_s t_r$)
γ	Surface energy
G	Shear modulus
G_1, G_2, G_3, G_4	Constants
H_1, H_2, H_3, H_4	Constants
h	Work-hardening rate
k	Boltzmann's constant
K_1, K_2	Diffusional creep-rate constants
L	Load on creep specimen
λ	Constant ($= \varepsilon_r/\varepsilon_m$)
n	Creep-rate stress dependence
ω	Creep-damage parameter
Ω	Atomic volume
P_1, P_2	Stress-rupture correlation parameter
q	Dislocation obstacle activation energy
Q	Activation energy
Q_c	Activation energy for creep
Q_{SD}	Activation energy for self diffusion
Q_{GB}	Activation energy for grain-boundary diffusion

Q_p	Activation energy for dislocation-pipe diffusion
r	Rate of recovery
r	Grain-boundary cavity radius
σ	Stress
σ_Y	Yield stress
t	Time
t_r	Time to rupture
t_m	Time to reach minimum creep rate
t_i	Time to onset of tertiary creep
T	Temperature
θ_1, θ_2, θ_3, θ_4	Parameters of the θ Projection Concept
x	Specimen gauge length

1. INTRODUCTION

Since 1978, Atomic Energy of Canada Limited and Ontario Hydro have conducted a joint R&D program to evaluate concepts for the safe storage, transportation and disposal of Canada's nuclear fuel waste (AECL 1994). In the disposal concept, used fuel from CANDU reactors, in the form of multi-element cylindrical bundles, 500 mm long and 100 mm in diameter (Figure 1), would be placed in corrosion-resistant containers and deposited in a deep underground vault excavated to a depth of 500 - 1000 m in a plutonic rock formation. Potentially suitable rock bodies for vault construction occur within the Canadian Shield. One possible disposal-vault design is shown in Figure 2.

Based on an analysis presented by Johnson et al. (1994), the target period for which the container shell must provide full isolation has been set at a minimum of 500 years. Consequently, the choice of the material, and its thickness, to be used for the container shell must recognize the demand for assured durability over such time scales. In particular, sufficient corrosion resistance must be provided, taking into account that the container will be exposed to saline groundwater which, for a vault constructed at a depth of 1000 m, would impose a hydrostatic pressure of ~10 MPa on the container. Swelling of the clay-based buffer material that will be used to surround the container could impose an additional hydrostatic pressure of 1 - 2.5 MPa. The heat production accompanying radioactive decay is an additional factor, contributing to the ambient temperature of the vault. By specifying the design of the container and the density of container emplacement within the vault, a maximum temperature of $\leq$100°C has been prescribed for the container-shell material.

The selection of materials for the waste container has been based on an extensive investigation of comparative corrosion properties of metals suitable for container construction (Johnson et al. 1994). Attention has also been directed toward the structural behaviour of the container under hydrostatic pressure. To this end, short-term structural-performance tests have been conducted on full-scale container prototypes, using hydrostatic test facilities. Stress analyses of candidate container designs under loading have been conducted using elastic-plastic finite difference and finite element computer programs. Such information has been used to assess the mechanical integrity of the structural shell and has been compared to the measured response of the prototype during testing. The nature of these tests placed emphasis on the short-term mechanical properties of the container material.

In recognition of the required long service lifetime of the container, an R&D program has been initiated to examine the longer-term structural response of container designs during disposal. Thus, extensive materials creep testing is underway, and a finite element structural analysis computer program has been developed to take into account time-dependent plastic deformation. With a timescale of 500 years minimum, it is evident that materials creep data obtained from laboratory testing will have to be extrapolated to service lifetimes and beyond. In particular, the potential for container failure by creep rupture must be assessed. This report describes an analytical methodology proposed for the extrapolation of creep behaviour and suggests a criterion for determining the onset of material failure by creep rupture that could be used in the engineering design of containers to ensure their continued structural integrity for whatever target lifetime is selected.

2. BACKGROUND INFORMATION

2.1 CONTAINER DESIGN

Various designs of fuel-waste containers have been considered (Crosthwaite 1994). The design selected for the safety analysis of the operation of a used-fuel disposal facility was the packed-particulate container consisting of a cylindrical containment shell, 2?46 mm long and 633 mm in diameter with a wall thickness of 6.35 mm, constructed from welded ASTM Grade 2 titanium plate (Figure 3). Positioned within the container is a concentric array of 19 tubes, to act as a fuel-bundle retaining basket, which would be constructed from a material such as carbon steel. The central tube, which is thicker-walled, serves as a lifting and handling device and contains no fuel bundles. Each of the outer 18 tubes (108 mm O.D. with 3.2 mm wall thickness) are designed to accept a stack of 4 fuel bundles; thus, the container can accommodate a total of 72 used CANDU bundles. This container configuration is designed for emplacement in boreholes as shown in Figure 2. An alternative design, intended for horizontal emplacement in-room, rather than in boreholes, and constructed of copper rather than titanium, is shown in Figures 4 and 5. In this case, the basket is designed to hold 72 bundles in two levels of 36 bundles.

For both designs, the tubes comprising the fuel basket are open-ended and are not intended to provide structural support to the shell; rather, a compacted particulate matrix is used to provide this internal support. Thus, after the container is loaded with fuel bundles, all residual interstitial space is filled with compacted particulate, facilitated by mechanical vibration of the container assembly. In the design used as the reference for the engineering study for a used-fuel disposal centre, the selected particulate was industrial glass beads of about 1 mm diameter (Simmons and Baumgartner 1994).

Some potential variants of this reference design have been considered. One option, called the structurally supported design, employs the use of a sealed, more rigid internal basket that provides both retention of the used-fuel bundles and a structure to which external pressure loading on the container shell can be transferred through a compacted particulate matrix that surrounds the basket (Figure 6). Another option uses a cast-metal matrix to support the shell (Figure 7). Details of the studies conducted on these and the packed-particulate design, and the reasons for the selection of the latter as the reference for current safety and engineering analyses, are presented in Crosthwaite (1994).

2.2 MATERIALS CHARACTERIZATION

A primary focus of the container-development program has been the requirement for high corrosion durability of the container shell; therefore, a substantial research program has been conducted to evaluate the corrosion behaviour of candidate container-shell materials (Johnson et al. 1994). Taking into account the ambient chemistry associated with Canadian Shield geology, ASTM Grades 2, 12 and 16 titanium and oxygen-free copper have been selected as the most promising candidates. Titanium is a "corrosion-resistant" material, its very low corrosion rate resulting from the presence of an adherent, highly protective, surface oxide. Copper belongs to the class of "corrosion-allowance" materials that corrode slowly, but predictably: a wall thickness of about 25 mm would be required. For the reference case study for the environmental impact assessment for the Canadian Nuclear Fuel Wast Management Program, the container was designed with a shell constructed of ASTM Grade 2 titanium.

Corrosion rates measured under a variety of relevant chemistry conditions show that a 6.35-mm-thick titanium shell would not fail by penetration due to material degradation until after about 1000 - 7000 years. However, to minimize the possibility of accelerated crevice corrosion, it has been judged that the container-surface temperature should be limited to 100°C.

Grade 2 titanium is a commercially pure (~99%) product. As such, its primary constituent is the hexagonal close-packed α-phase. However, the presence of β-stabilizing trace elements (in particular, iron) causes a minor amount of the body-centred cubic β-phase to be retained at room temperature, present as an intergranular second phase. The trace elements also confer additional strength, mainly through the interstitial species such as oxygen, nitrogen and carbon. Such strengthening effects are significant at temperatures below 300°C (Conrad 1981). Grade 12 titanium is an alloy containing small quantities of molybdenum and nickel: these increase the strength and corrosion resistance of the material. The Grade 16 material contains a small amount of palladium, which increases the corrosion resistance even further. Similar to Grade 2, Grades 12 and 16 are mainly α-phase with minor fractions of residual β-phase.

2.3 MECHANICAL TESTING AND ANALYSIS

The reestablishment of the water table in the vault at a depth of 1000 m would create a hydrostatic pressure of about 10 MPa on the shell of the waste container. An additional pressure of up to 2.5 MPa could arise from moisture-induced swelling of the bentonite-clay mixture used as a buffer to surround the waste container. This material has a low diffusivity for dissolved radionuclides and therefore acts as an effective additional engineered barrier.

Full-scale hydrostatic testing of prototype containers commenced in the early 1980s. The first tests were conducted on the "stressed-shell" concept (Figure 8), where the container shell was designed to sustain the full external pressure, without any internal structural support (Crosthwaite et al. 1982). Using stainless steel as a model material, the required container wall thickness was about 29 mm for a test conducted at 20°C. Hydrostatic testing was carried out in a US facility[1]. The container shell collapsed at a pressure of about 19 MPa, in excellent agreement with an elastic-plastic finite difference analysis.

It was realized that progressive creep deformation of the container could have a significant effect on its long-term structural behaviour and that eventual collapse by creep-buckling might occur at pressures significantly less than the short-term limit of 19 MPa. A creep-buckling analysis was conducted for a titanium stressed-shell container (Hosaluk et al. 1987) by introducing time-dependent deformation into the finite difference computer code. The progressive plastic deformation of the container shell was then calculated by updating the creep strain in prescribed time increments, until the onset of plastic instability. The calculations were verified by using a finite element stress analysis code and an analytical equation based on an assumed out-of-roundness. In all cases, a steady-state creep law was used, where the creep rate ($\dot{\varepsilon}$) is given by

---

[1] At the time this test was conducted, no hydrostatic testing facilities capable of conducting tests on full-scale containers at temperatures and pressures typical of those anticipated during disposal were available in Canada. Later tests were conducted at such conditions following the construction of a facility with the appropriate capabilities at AECL's Whiteshell Laboratories.

$$\dot{\epsilon} = A\left(\frac{\sigma}{\sigma_y}\right)^n \qquad (1)$$

where A and n are constants, σ is the applied stress and σ_y is the short-term yield stress of the material, at the appropriate temperature. This equation (see Section 4.3 for further discussion of similar power-law equations) was fitted to published creep data on commercially pure titanium (Kiessel and Sinnott 1953). A sensitivity analysis showed that the time to reach plastic instability of the shell (buckling) was strongly dependent on the creep rate: a factor of 5 increase in creep rate reduced the time to buckling by about two orders of magnitude. This highlighted the need for accurate predictions of creep behaviour.

From the analysis of Hosaluk et al. (1987), it was concluded that for a Grade 2 titanium, stressed-shell design container, a minimum wall thickness of ~70 mm would be required for creep buckling to be avoided for a 500-year period, at 100°C. Due to anticipated costs and fabrication/inspection difficulties associated with a 70-mm-thick container shell, attention was subsequently focussed on internally supported thinner-shell containers.

In the test sequence performed on a full-scale prototype of the ASTM Grade 2 titanium packed-particulate container, which was conducted at up to 10 MPa at 150°C in AECL's Hydrostatic Test Facility at Whiteshell (Figure 9), the prototype was tested first in its as-received condition; only small deformations of the cylindrical portion of the shell occurred.[2] In two subsequent tests, the container was resubjected to these test conditions after artificial packing defects were introduced by removing some of the particulate. In the first of these tests, 0.2 L was removed; in the second, a further 0.8 L was removed. Although the shell deformed substantially adjacent to the packing voids, it was not breached by rupture or tearing (Teper 1985, 1987a, Teper and Reid 1989). During all tests, shell deformation was recorded by strain gauges attached to the container surface.

An analysis of the structural response of the container during the hydrostatic test was conducted by Teper (1988) in which he employed both linear-elastic and elastic-plastic finite element models. A focus of the analysis was the localized deformation associated with the unsupported void introduced by partial removal of the particulate. With this particulate removed and under hydrostatic testing, plastic strains of 0.062 compressive and 0.044 tensile were predicted. On the basis of a measured tensile ductility of 0.20 strain for titanium under uniaxial test conditions, while taking into account the biaxial stress condition in the container shell, and imposing a safety factor of 2/3, the maximum allowable (i.e., avoiding ductile tearing) tensile strain was calculated to be 0.053. However, this is based on short-term tensile testing results. It will be shown in later sections of this report that tensile ductility can be drastically reduced under long-term creep conditions.

---

[2] During transportation of the prototype from Toronto, where it was constructed, to the Whiteshell Laboratories, the glass-bead particulate within the container appeared to have settled further, causing an ~1% increase in its compacted density. This resulted in a gap forming between the top head and the upper level of the particulate, estimated from test results to have been ~14 mm in height. During an initial, low-pressure test conducted at 1 MPa and 20°C, the top head deformed downward through this gap until it recontacted the particulate. Details are presented in Teper (1988).

An important point highlighted by Teper (1987b, 1988) was that the total volume of the particulate can decrease with time. For example, further packing or settlement of the particulate can occur during container handling or under hydrostatic pressure; volumetric creep of the particulate matrix can occur due to deformation of contacting particles. This could possibly result in significant plastic strain of the container shell. The finite element analysis also demonstrates that non-uniform deformation, especially that associated with the top head and rim of the container, can cause both compressive and tensile strains to develop.

Limited creep tests have been conducted on a range of particulate materials (Teper 1987b). These were done by compressing a column of particulate contained in an open-ended cylinder with a loaded piston. At 150°C, the total creep strain for glass beads (measured as a function of the decrease in height of the glass-bead column) was about 10^{-4} after 700 h. It was not possible to determine whether the creep occurred by particle rearrangement, particle cracking, or particle plasticity. The problem with this experimental technique is the complex (and unknown) stress pattern produced in the particulate body due to boundary effects at the interface with the confining cylinder wall. Consequently, it is difficult to extract the intrinsic creep properties of the particulate. Studies are currently underway, using soils properties measurement techniques, to determine more accurately the short- and long-term mechanical properties of compacted glass beads.

3. THE ROLE OF CREEP DEFORMATION

3.1 GENERAL CONSIDERATIONS

As indicated above, both the container shell and the particulate can undergo creep deformation. Thus, the creep properties of <u>both</u> components are relevant to the overall time-dependent deformation of the container assembly. It will be apparent from the mechanical interaction between the particulate and the shell that the rate of deformation of the container will largely be determined by the creep properties of the particulate. Exceptions will be isolated areas of the container shell that are not adequately supported because of incomplete, or inhomogeneous, packing of the particulate. It is to be expected that such regions are more likely to exist in the uppermost section of the container, where settling of the particulate might create an empty void.

For containers fully supported by the particulate, the creep rate of the container shell will essentially be controlled by the volumetric creep rate of the particulate. Under these circumstances, the mechanical stress in the shell wall will be equal to the flow stress required to sustain such a creep rate. To enable such stresses and the accumulated creep strains of the container shell to be predicted, a finite element stress/strain computer program must be developed. This is being done (Rigby 1994 and Teper 1990).

The creep properties of both the container-shell material and the particulate will be required as input into the finite element model. However, laboratory-produced creep data are constrained to relatively short times (up to several years), compared with the design lifetime (~500 years) of the container. This temporal limitation requires a reliable method for extrapolating the experimental data by a factor of at least 100. Furthermore, the format of the projection methodology must serve several related purposes:

- analysis of the experimental data,
- analysis of medium-term hydrostatic testing of scale-model containers,
- extrapolation of the experimental data to long-term practical conditions,
- providing input, in suitable form, to finite element models, and
- facilitating the final design of the container.

To this end, this report will review the extant analytical tools that have been developed to accomplish such interpolation and extrapolation. From this, recommendations will be made on the most suitable methodology. Such judgement will take into account the minimum 500-year time scale, recognizing that such long-term projection is unprecedented in conventional engineering design (although there are examples of retroactive historical creep analyses covering time periods measured in centuries). Furthermore, the proposed methodology will address the fact that the imposed low creep rate of the container materials places the creep-deformation processes in an envelope of low stress and low temperature. In contrast, most conventional creep data are obtained at much higher stresses and temperatures. Above all else, the selection of the analytical tools will be guided by the need for scientific rigour in addition to engineering pragmatism. To this end, the methodology will meet the following criteria:

- must have the underpinning of scientific understanding that derives from a knowledge of creep-deformation mechanisms and phenomenology,
- must be well supported and documented in the scientific literature,
- practical application must be well demonstrated and tested, recognizing the more limited timescale of conventional engineering practice,
- must have widespread acceptance in the scientific/engineering community,
- must be able to handle creep strain and creep fracture (see below).

3.2 SPECIFIC PERSPECTIVES

It is useful to place the expected creep behaviour of the container within a perspective frame. To do this, we can assume a reasonably acceptable creep strain of 0.1 being realized over a 1000-year period. This translates to an average creep rate of ~3 x $10^{-12}s^{-1}$. Within a typical engineering context, such a creep rate is relatively low. However, recognizing the low servicee temperature of the container (~ 100°C), it is anticipated that the allowable stress in the container wall will be quite high. The displacement transducers on modern creep machines can detect specimen extensions of 10^{-7} m, i.e., strains of the order of 10^{-6}. Taking into account other testing variables, it is relatively straightforward to discriminate a creep strain of 10^{-3} over a period of one year: this is a strain rate of ~3 x $10^{-11}s^{-1}$. Indeed, measured creep rates within this range are commonly reported in the scientific literature, as shown in Figure 10 (Evans and Wilshire 1985).[3] Within the Canadian nuclear industry, it is of interest to note that the creep rates of CANDU reactor fuel channels are of this order. In addition, current creep tests conducted on the Grade 2 titanium being studied as a candidate container-construction material, are deforming at a rate of ~$10^{-11}s^{-1}$ (J.L. Crosthwaite and G.R. Kasprick, 1994, unpublished data). This means that, as far as these measured creep rates are concerned, we are required to extrapolate experimental data by about an order of magnitude - a fairly modest challenge.

---

[3] A more detailed discussion of Figure 10 is presented in Section 9.

Although the creep rate is an important parameter influencing the lifetime of the container, the time to failure by creep rupture is more crucial. This is the time (or equivalently, the creep strain) required for any internal damage processes to cause the material to fracture. For obvious reasons, this issue focusses on the creep behaviour of the container-shell material, rather than the particulate. Thus, whereas the creep rate of the container shell will largely be controlled by the creep properties of the particulate, it is the intrinsic creep (and creep-rupture) behaviour of the container-shell material that determines its design lifetime.

As we will see below, there is a link between the creep rate and the rupture time. The proposed creep analysis tools must be capable of capturing these linkages. An attractive approach is the formulation of a fracture criterion based on the strain to failure. Then, through the creep rate, the time to failure can be predicted. In this regard, it is important to emphasize that the strain to failure under creep conditions (particularly at low strain rates) can be much less than the tensile ductility measured in a short-term tensile test. Thus, the Swedish work (Henderson et al. 1992) on oxygen-free, high-purity copper being considered for constructing a fuel-waste container shell showed that whereas the strain to failure in short-term tensile tests was as high as 0.6, failure strains of <0.1 resulted under creep conditions. In addition, trace impurities can reduce the creep-rupture strain to <0.01. These low ductilities are a consequence of a change of rupture mechanism. Under short-term tensile conditions, rupture occurs by gradual necking down, or the development of transgranular cracks. In contrast, under creep conditions, cavities and cracks can form on grain boundaries, leading to premature intergranular fracture (Evans and Wilshire 1985).

It will be noticed that the above remarks on creep ductility apply to conditions of tensile stresses. It is true that the hydrostatic pressure conditions in the vault will generally produce compressive stresses in the container shell (and compressive stresses generally suppress fracture processes). However, any localized deformation, for example, that associated with end effects, or shell ovality, will result in bending deformation and therefore tensile stresses. In addition, even under nominally compressive conditions, tensile stresses can develop and produce creep cavitation on grain boundaries parallel to the compressive stress axis (Dutton 1969). The added complexity of creep fracture processes under multiaxial stress states has been described by Dyson (1992). Regardless of the actual condition of stress in the container shell, we shall adopt fracture criteria based on tensile creep test data, with the assurance that this will retain conservativeness.

4. CONVENTIONAL APPROACHES TO PROJECTION OF CREEP DATA

4.1 THE STANDARD CREEP CURVE

Typical forms of creep curves are shown in Figure 11, for the case of "high" temperature and "low" temperature. The distinction between the two is fairly arbitrary, but "high" temperature would conventionally be >0.3 of the melting point (i.e., a homologous temperature of 0.3 T_m, where all temperatures are expressed in degrees Kelvin). For both cases, there will be an

essentially instantaneous strain, ε_o, comprising an elastic and plastic component.[4] Following this, the plastic creep strain will accumulate in a time-dependent fashion.

In the higher-temperature creep regime, after the initial strain on loading, the creep rate decays with time, giving rise to the characteristic "primary" creep stage. An ostensibly constant creep rate is achieved during the "secondary stage", after which the creep rate accelerates during the "tertiary stage" that leads to fracture. The overall effect of increasing stress and increasing temperature (these are normally considered independent variables) is shown in Figures 12 and 13, respectively.

Lower-temperature creep is characterized by a continuously decreasing creep rate, and is often referred to as transient, or logarithmic creep for reasons made apparent in Section 4.2. For most practical purposes, this creep behaviour continues indefinitely (i.e., a protracted primary stage) and fracture does not occur. As creep is a thermally activated process, and occurs at any temperature above absolute zero, the distinction between low-temperature and high-temperature creep becomes rather arbitrary, being a matter of scale. For most high-performance engineering applications at elevated temperatures, materials are operated toward the upper limit of their creep temperature range and for time scales that are measured in years, up to several decades. Laboratory creep testing is therefore conducted in a temperature-stress-time envelope that allows the full expression of the primary-secondary-tertiary-fracture sequence. The "high-temperature" creep behaviour of Figure 11 then becomes the "classic" creep curve. However, as we shall see in Section 6, the underlying mechanisms responsible for creep and fracture can operate throughout the temperature-stress field. At lower temperatures, the (diffusional controlled) kinetics of these processes is slow. Consequently, within the time scale of conventional engineering application, the depiction of the "low-temperature" behaviour in Figure 11 is appropriate and representational. However, for the case of the waste container, although it operates at "low" temperatures (~0.2 T_m and ~0.3 T_m for titanium and copper respectively), its intended service lifetime is far more extended than normally encountered. Although the deformation kinetics are slow, the full expression of the creep-curve shape over very long time periods (~500 years) is of critical importance. In particular, we need to know whether a tertiary creep stage leading to creep rupture will eventually materialize. It would be unjustified to make the a priori assumption that logarithmic creep was the appropriate creep behaviour such that tertiary kinetics and fracture processes could be ignored, unless there was sound theoretical or empirical proof.

The analytical approach presented in this report assumes that the creep behaviour of the container shell will follow the normal three-stage behaviour. In fact, we embrace the long-standing principle that the three-stage creep behaviour is a universal phenomenon displayed by all materials, the temperature of operation solely determining the relative kinetic shape of the creep curve. A key objective will be to predict under what conditions of stress and temperature tertiary creep and fracture would occur, such that a design envelope can be selected to avoid failure of the container shell over its intended lifetime.

---

[4] A plastic component will be present even at quite low stress levels, below the nominal yield stress. This reflects the fact that the elastic limit is exceeded at stresses much lower than the 0.2% offset yield point. The short-term stress-strain curve is quite adequate to predict the value of ε_o as a function of stress.

At this juncture, it is instructive to examine some actual creep data for our intended container materials[5]. The conclusion of Kiessel and Sinnott (1953) following a study of the low temperature (down to room temperature) creep of commercially pure titanium, was "It would seem that second-stage creep becomes active after a relatively short testing time and any further consideration that titanium exhibits chiefly transient creep at room temperature is fallacious". Similarly, the work of Adenstedt (1949) and Luster et al. (1953) showed the full three-stage behaviour in commercial titanium at room temperature, and Evans showed this to be the case even in high strength α (1984) and α-β (1987) titanium alloys. Such alloys were developed for high-temperature creep resistance. It was a surprise to find that the low-temperature creep resistance was so poor, and, in particular, displayed a distinct tertiary stage leading to premature fracture. This is more than an academic curiosity. Such alloys are used in the low-temperature compressor of gas turbine engines. Unanticipated creep fracture failures have resulted.

Low-temperature creep studies on copper (Henderson et al. 1992 and G. Palumbo, 1994, unpublished data) also demonstrated the presence of creep fracture processes typical of the tertiary stage. All of these experiments are relatively short-term (up to several thousand hours) and therefore have been conducted at high stresses to produce high strain rates. Notwithstanding this, we cannot assume that accelerating creep, and creep fracture, will be absent under long-term conditions.

It is significant that the experimental work on titanium, referred to above, reported that the creep resistance was much lower than would be anticipated from a metal with a relatively high melting temperature (1680°C). As titanium transforms from the α-phase (close-packed hexagonal) to the β-phase (body centred cubic) at 880°C, there is some uncertainty as to the significance of the experimentally determined melting point. The measured melting point is that of the β-phase, whereas the creep measurements are performed in the α-phase. The question then arises as to what is the effective melting point of the α-phase? This situation is analogous to that of zirconium (melting point of 1850°C; α-β transformation temperature of 860°C). Whereas it has been suggested that the melting point should be equated to the transformation temperature, Carpenter (1971) has suggested (based on a consideration of diffusional-controlled creep kinetics) that the effective α-phase melting point for zirconium is 1500°C. If we draw a parallel to zirconium, the homologous temperature for creep in titanium at 100°C, could be in the range 0.3 - 0.2 T_m, i.e., approaching the "high-temperature" creep regime.

4.2 MATHEMATICAL REPRESENTATION OF CREEP CURVES

Various attempts have been made to develop constitutive equations that describe the dependence of the creep strain (ε) on time (t), stress (σ) and temperature (T) (Garofalo 1965, Evans and Wilshire 1985). In general, these will be of the form

$$\epsilon = f(\sigma, T, t) \tag{2}$$

---

[5] Creep testing of titanium and copper container materials is currently being conducted by Atomic Energy of Canada Limited and Ontario Hydro Technologies. However, data obtained to date are rather limited.

Under "low-temperature" conditions, it has been found that the strain-time relationship is logarithmic, i.e.,

$$\epsilon = a \log(bt + 1) \tag{3}$$

where a and b are material constants that depend on stress and temperature. The decreasing creep rate is generally explained by a dislocation mechanism controlled by an exhaustion process of decay (see Section 6.3.2).

The proposed container creep analysis method of Teper (1990) assumes that logarithmic creep, and Eqn. (3) applies. In principle, Eqn. (3) predicts that as $t \rightarrow \infty$, the creep strain approaches ∞, without fracture occurring. The concerns and reservations regarding such assumed behaviour were discussed in Section 4.1.

Based on the early classical work of Andrade (1910), power-law time dependencies have been used to describe the three-stage creep behaviour under "high-temperature" conditions:

$$\epsilon = \alpha t^{1/3} + \beta t + \gamma t^{4/3} \tag{4}$$

where α, β and γ are constants, the first term representing the primary stage, the second and third terms representing the secondary and tertiary stages, respectively. A similar equation was developed by Graham and Walles (1955), but with the tertiary stage represented by γt^3. For some materials, it was found that for the primary stage a better fit was obtained by using a $t^{2/3}$, or $t^{1/2}$, law rather than a $t^{1/3}$ law. The equation representing the early stages of the creep curve are then better generalized in the form,

$$\epsilon = \alpha t^p + \beta t \tag{5}$$

with the parameter p varying between zero and unity.

An example of a variant of Eqn. (5) is that due to Conway (1967):

$$\epsilon = \alpha_1 t^{1/3} + \alpha_2 t^{2/3} + \beta t \tag{6}$$

A difficulty with Eqn. (5) and its variants, is that it predicts an infinite creep rate at time zero. This objection is overcome by using an exponential function, rather than a polynomial (Garofalo et al. 1963), thus:

$$\epsilon = \alpha(1 - e^{-\beta t}) + \gamma t \tag{7}$$

where α represents the total primary creep strain and β determines the rate of exhaustion.

Evans and Wilshire (1985) have used a set of experimental creep data to test the curve-fitting capability of polynomial expressions of the form of Eqns. (4), (5) and (6), and the exponential form of Eqn. (7). The latter offered the best fit. Indeed, the derived coefficients of the polynomial expressions varied in an erratic fashion as the creep stress was varied, and even produced irrational negative values.[6]

The attractive features of expressions of the form of Eqn. (7) will be pursued later in this report (see Section 9). However, it must be emphasized that many mathematical forms can be used to fit creep curves with equivalently high accuracy (e.g., higher-order polynomials will provide the required accuracy). From the point of view of extrapolating creep data, the challenge is to find an equation that reflects the physics of the underlying deformation mechanisms, such that the coefficients will properly represent the time, stress and temperature dependencies. This will be a recurring theme of this report.

4.3 EXTRAPOLATION METHODS

Despite the efforts to obtain analytical equations to fit the full creep curve, creep-design and creep-data extrapolation in the engineering domain has centred on the steady-state creep behaviour in the secondary creep stage. No doubt this is partly due to the lack of general agreement on the mathematical forms of the creep-curve equations, together with the uncertainties in handling stress and temperature dependencies of the overall creep shape, particularly in the primary and tertiary creep stages. In addition, it is far easier to use a single-valued constant creep rate in computation, whether this be analytical or numerical.

This is not only a feature of engineering application. Other scientific researchers intent on gaining an understanding of creep mechanisms and developing theoretical models, have also concentrated on steady-state creep. This is partly justified by the reasonable assumption that primary and tertiary creep processes are relatively minor variants of the steady-state deformation mechanism. Also, in terms of the design of experiments, it is easier to measure the separate stress and temperature dependence of the secondary creep rate.

A consequence of the above trend is that most of the creep data published in the literature are simply reported as the secondary stage, steady-state creep rates (plus the stress and temperature dependence). The full creep curves are rarely available; indeed the data representing the primary and tertiary stages are discarded. This is done despite the fact that these data have typically been measured (it is difficult to be confident that steady-state creep has been achieved unless both the primary and tertiary behaviour are recorded).

The temperature dependence of the steady-state creep rate ($\dot{\varepsilon}_s$) is well represented by an Arrhenius equation:

---

[6] For example, the predicted secondary creep rate (the parameter β in Eqns (4), (5) and (6)) was significantly different from the measured value, and β was negative for some values of the stress. This problem can be avoided by measuring the secondary creep rate independently and thus inserting a fixed value of β into the equations. However, with many creep-curve shapes it is difficult to estimate the secondary creep rate with any certainty, hence the other coefficients (α and γ) will be inaccurately determined. This type of problem has been overcome by the curve-fitting procedure discussed in Section 9.

$$\dot{\epsilon}_s \propto \exp-(Q_C/kT) \tag{8}$$

where k is Boltzman's constant. Q_C is the activation energy for creep, recognizing that creep deformation is controlled by a thermally activated process (see Section 6). For the case of pure metals at higher temperatures, Q_C is generally close to the activation energy for self-diffusion (exceptions will be discussed in Section 6.1), as illustrated in Figure 14 (Sherby and Burke 1968). Note that in this figure both of our materials of interest are included: copper and titanium (both in its α and β forms).

In contrast to the universal applicability of Eqn. (8) to represent the temperature dependence, the stress dependence can take various functional forms. However, a power law (termed Norton's law) is widely used:

$$\dot{\epsilon}_s \propto \sigma^n \tag{9}$$

where n is a constant that can vary from 1 - 10 (see Section 6). Creep data for copper, illustrating the applicability of Norton's law are shown in Figure 15 ($n \approx 5$).

Combining Eqns. (8) and (9), the steady-state creep rate is given by

$$\dot{\epsilon}_s = A\sigma^n \exp-(Q_C/kT) \tag{10}$$

where A is a constant. The values of A, n and Q_C are obtained from the analysis of experimental creep data. When this equation is used to extrapolate to other conditions of interest, caution must be taken because A, n and Q_C can vary according to the applicable range of stress and temperature. In addition, as already mentioned, it does not include any primary or tertiary strains.

Equation (10) has been modified (Graham and Walles 1955) to include representation of the primary and tertiary stages, as follows:

$$\dot{\epsilon} = A\sigma^n \exp-(Q_C/kT)(a + bt^{-2/3} + ct^2) \tag{11}$$

where a, b and c are additional constants. The integrated form of this will yield a polynomial form very similar to the equation for creep strain given in Section 4.2.

Equations (10) and (11) can be used only to predict accumulated creep strain. However, they contain no information about creep rupture, and therefore the ultimate lifetime limit of components. This predictive capability is generally provided by the experimental measurement of rupture time (t_r). Although t_r can be determined from the measurement of the full (three-stage) creep curve, in practice much simpler (i.e., less costly) methods are used. Creep specimens are loaded at various stresses and temperatures until failure, the rupture

time being recorded. No strain transducers are used to measure the creep strains: the creep curve is, consequently, unavailable.

The basis for interpolation and extrapolation of time to rupture data derives from the inverse proportionality between t_r and $\dot{\varepsilon}_s$, referred to as the Monkman-Grant relationship (Monkman and Grant 1956):

$$\frac{1}{t_r} \propto \dot{\epsilon}_s = A\sigma^n \exp(-Q_C/kT) \tag{12}$$

This facilitates plots of log t_r against log σ, as shown in Figure 16 (obtained from the creep data shown in Figure 15). However, the confidence in extrapolation relies on the value of n remaining constant over the full stress range. This is usually not the case, particularly at low stresses, where n decreases. Such a tendency will overestimate creep lives at low stress.

It is significant to note that the Monkman-Grant relationship represented in Eqn. (12) establishes a behavioural linkage between time to rupture and the creep rate. This indicates that the fracture-related damage occurring during the tertiary stage must be controlled by the rate of creep deformation. Any proposed micromechanisms must include this feature.

Extrapolation methods have been developed using parametric procedures. In these, a correlation parameter (P) is used to superimpose stress-rupture data obtained over a range of temperature onto a single master design curve. In this case, if a reliable correlation parameter can be found, short-term tests can be conducted at higher stresses and temperatures, and the rupture times under long-term service conditions (lower stresses and temperatures) can be predicted by extrapolation. An approach to this scheme can be achieved by writing the logarithmic form of Eqn. (12) as

$$\log t_r = \frac{P_1}{T} - P_2 \tag{13}$$

The correlation parameter advocated by Orr et al. (1954) is P_2. Thus, the stress-rupture data are plotted as log stress against (log t_r - P_1/T). Such data for a chromium-molybdenum-vanadium steel are shown in Figure 17(a), with P_1 = 17,300. An alternative, suggested by Larson and Miller (1952), is to use the P_1 parameter (i.e., a plot of log stress against T (log t_r + P_2)), also shown in Figure 17(b) with P_2 = 23.3. Using modifications of this approach, more than 30 alternative variants of P have been proposed. A selection of these (including P_1 and P_2), and their practical application, is described in the Metals Handbook (Voorhees 1985). The very existence of such a large number of proposed correlation parameters signals the lack of a definitive engineering design tool to project rupture times in a reliable fashion. This is partly due to the inherent scatter in the experimental data, e.g., there can be a hundred-fold spread in rupture times measured for a given stress and temperature. Furthermore, the correlation parameters themselves have significant limitations. Thus, the data in Figure 17 cover a wide range of stress and temperature and illustrate the point made above that such plots are generally non-linear. Thus, while these approaches can be useful for data collation and interpolation, parametric relationships cannot be used reliably for extrapolation, except over very limited time spans (an extrapolation factor of about 3).

An alternative engineering approach is to use a continuum mechanical concept of accumulated damage (Kachanov 1958, Rabotnov 1969). Damage is described by a generalized scalar parameter, ω, which varies from zero at the start of life, to unity at failure. The precise mechanistic nature of the damage is not specified, but we may relate it to the progressive development of internal cavities and cracks. Both damage and creep strain are assumed to increase as a function of stress, temperature and the current state of damage. The creep rate and damage rate are then expressed as

$$\dot{\epsilon} = A\sigma^n / (1 - \omega)^n \tag{14}$$

$$\dot{\omega} = B\sigma^r (1 - \omega)^s \tag{15}$$

where A, B, n, r and s are temperature-dependent constants. An examination of Eqn. (14), with a focus on its applicability to the accelerating tertiary stage (the essence of the ω parameter), will provide some understanding of the phenomenological nature of ω. Thus, the term $1 - \omega$ accounts for the increase in effective stress arising from grain-boundary decohesion. Explicitly, ω can be considered to be the number fraction of cavitated grain boundaries such that the stress operating on the remaining intact boundaries is $[\sigma/(1 - \omega)]$. In principle, then, ω can be evaluated at any strain, or time, by measuring the total cavity volume in a metallographic section. However, this is a somewhat impractical procedure. Alternatively, we could fit Eqn. (14) to the tertiary creep data to obtain an analytical expression for ω, hence obtaining estimates for A, r and s in Eqn. (15). However, there is no certainty that this provides a sound basis for extrapolation. In addition, Eqn. (14) predicts that $\dot{\epsilon} = \infty$ at the point of fracture, where $\omega = 1$. This is inconsistent with experimental observation, demonstrating that final rupture (plastic instability) occurs when $\omega < 1$, i.e., $\omega = 1$ is not a good fracture criteria. Despite these shortcomings, the damage-parameter concept does effectively represent the phenomenology of tertiary creep and we can proceed by integrating Eqns. (14) and (15), whence by simple manipulation, using the fact that the time to rupture (t_r) and the strain rupture (ϵ_r) are reached when $\omega = 1$, we obtain the following:

$$\frac{\epsilon}{\epsilon_r} = 1 - (1 - t/t_r)^{1/\lambda} \tag{16}$$

$$\dot{\epsilon} = (\epsilon_m / t_r)(1 - t/t_r)^{1/\lambda} \tag{17}$$

$$\omega = 1 - (t - t/t_r)^{\lambda - 1} \tag{18}$$

where ϵ_r is the strain to rupture, $\epsilon_m = \dot{\epsilon}_s t_r$ (i.e., the Monkman-Grant constant) and $\lambda = \epsilon_r/\epsilon_m$. In Eqns. (16) and (17), the parameter ω does not appear. The major utility of these equations has been to provide a means for relating the strain or strain rate measured in actual plant components to the life fraction consumed, or the remnant life fraction $(1 - t/t_r)$. Practical application of this approach is explained elsewhere (Cane and Aplin 1994, Metals Handbook 1985). The analysis also offers the concept of required creep ductility during tertiary creep.

Thus, λ is used as a creep-damage tolerance parameter. In terms of measurable creep properties, it can be shown that

$$\lambda = \epsilon_r / \epsilon_m = \epsilon_r / \dot{\epsilon}_s t_r \tag{19}$$

In engineering practice, $\lambda > 10$ is used as a design criterion that ensures sufficient ductility during tertiary creep to avoid premature failure of a component.

5. PROPOSED ANALYTICAL TOOLS

It should be evident from Sections 2 and 3 that the design of the container requires reliable analytical tools to predict the creep behaviour, particularly the time (and/or strain) to failure. Section 4 has reviewed alternative methodologies that have been typically used in engineering practice to extrapolate creep strains and creep-rupture lifetimes. However, the inadequacies of these processes have been highlighted. A cursory perusal of the core references of Section 4 will reveal the rather early origin of the underlying ideas and principles. This is perhaps to be expected within the mainstream of traditional engineering design. There are, however, more recent and innovative approaches to the problem. These have arisen from advances in the understanding of creep and creep-rupture processes, plus the incentives emerging from the high-performance challenges encountered in the advanced technologies being developed in industries such as aerospace. One might also observe that the advent of modern computers has facilitated the exploration of new data analysis techniques and exploitation of elaborate curve-fitting techniques.

It is from this milieu that we have selected two complementary analytical tools. One is, in essence, a constitutive equation that can be used to fit the full three-stage creep curve, but avoiding the problems outlined in Section 4.2. It is the θ Projection Concept developed by Evans and Wilshire (1985) and includes the capability of predicting time, or strain, to rupture, while avoiding the problems indicated in Section 4.3. This analytical procedure is described in Section 9, together with the supporting theoretical formulation that underlies the functional form of the constitutive equation.

The second analytical tool employs the concept of the Deformation Mechanism Maps developed by Frost and Ashby (1982) and their complementary Fracture Mechanism Maps (Ashby et al. 1979). These provide a vehicle, in concert with the θ Projection Concept, for ensuring that the overall approach is entrenched in a scientific understanding of creep processes. In fact, the Mechanism Maps are a convenient repository of the collective world-wide knowledge of creep behaviour and creep mechanisms. A detailed description will be found in Sections 7 and 8.

Because a central theme of our proposed approach is the understanding of creep behaviour, we will now present a summary of the major creep-deformation and creep-rupture mechanisms.

6. PRINCIPAL CREEP-DEFORMATION AND -RUPTURE MECHANISMS

6.1 THE ROLE OF DIFFUSION

The kinetics of creep deformation and creep rupture are controlled by thermally activated processes, hence the Arrhenius form of the temperature dependence contained in the typical strain-rate equation (given above):

$$\dot{\epsilon} = A\sigma^n \exp -(Q_c / kT) \tag{20}$$

The thermal energy, Q_C, is that required to activate the individual process responsible for producing a unit of creep strain. In many cases, as illustrated in Figure 14 (see Section 4.3), Q_C is equal to the activation energy for self-diffusion (as defined below), Q_{SD}, where the self-diffusion coefficient (D_{SD}) is given by

$$D_{SD} = D_o \exp -(Q_{SD} / kT) \tag{21}$$

where D_o is a constant. This establishes the fact that creep deformation is usually controlled by diffusion processes.

The relevant diffusion process involves the thermally induced migration of vacancies. The link between vacancy migration and deformation processes will be made clear below. The vacancy diffusion process can occur within various locations in the solid. Thus, diffusion in the crystal lattice is called self-diffusion, with a characteristic activation energy of Q_{SD}. Although $Q_C = Q_{SD}$ at higher temperatures, Q_C is significantly less than Q_{SD} at lower temperatures. This reflects the fact that there are diffusion paths other than the crystal lattice, where vacancy migration is much easier, i.e., the associated activation energy is much less than Q_{SD}. Such easy diffusion paths exist within grain boundaries and along the cores of dislocations (termed "pipe" diffusion), where the activation energies are Q_{GB} and Q_P, respectively (Q_{GB} and Q_P are equal to 0.5 Q_{SD}, or less).[7]

This effect is illustrated in Figure 18. It will be seen from this Arrhenius plot that whereas easy diffusion paths exist, they are dominant only at lower temperatures (below T on the diagram). They make a negligible contribution to the overall diffusion rate at higher temperatures because the effective volume of grain boundaries and dislocations is very small compared with the total volume of lattice. Hence, within the (low homologous temperature) container shell, we can anticipate low activation energies (low temperature dependence) for creep, with creep rates controlled by diffusion along grain boundaries and dislocations. Creep data for copper (Feltham and Meakin 1959), shown in Figure 19, illustrate this point.

6.2 DIFFUSIONAL CREEP

This term is used to describe a creep process that arises directly from the diffusion of vacancies. Figure 20 shows, schematically, a cube-shaped grain subjected to a system of

---

[7] Grain Boundaries and dislocation cores (central axis of the dislocation) define regions where the atomic arrangements are less regular than the crystal lattice.

tensile and compressive stress. Elongation of the grain in the tensile direction can be achieved by displacing an atom from a position just below the surface to a position on top of the surface. In doing this, the stress does an amount of work, $\sigma\Omega$, where Ω is the volume of the atom. The addition of atoms on the tensile surface creates vacancies in the sub-surface region. The resulting increase in concentration of vacancies, in equilibrium with the stressed surface is given by

$$C = C_o \exp(\sigma\Omega / kT) \tag{22}$$

where C_0 is the equilibrium concentration under zero stress. Concomitantly, the concentration of vacancies at the surface under compressive stress is reduced, according to

$$C = C_o \exp(-\sigma\Omega / kT) \tag{23}$$

The resulting concentration gradient causes a flow of vacancies from the surface under tension to the surface under compression. This is equivalent to a flow of atoms in the opposite direction. The overall result is that atoms are removed from the compression surface and added to the tension surface, thus producing the creep strain.

A polycrystalline material is, of course, an assembly of a large number of grains, of the type shown in Figure 20. The diffusional flow described above, occurs in each grain, the collective microscopic behaviour being the total macroscopic creep elongation of the specimen or component. The vacancy-producing or -absorbing "surfaces" referred to above are, actually, grain boundaries. The rate at which this diffusional creep occurs is now dependent on the diffusional path, in accordance with those described in Section 6.1.

If the diffusion path is primarily through the lattice (see Figure 20), this is called Nabarro-Herring creep (Nabarro 1948, Herring 1950). The application of standard diffusional theory, using the boundary values established by Eqns. (22) and (23), yields the following creep-rate expression:

$$\dot{\epsilon} = K_1 \frac{D_{SD}}{d^2} \cdot \frac{\sigma\Omega}{kT} \tag{24}$$

where K_1 is a constant (≈ 10), D_{SD} is the diffusion coefficient for lattice self-diffusion and d is the average grain diameter.

Alternatively, if the preferred/dominant diffusion path is the grain-boundary (see Figure 20), the process is called Coble creep (Coble 1963). The governing equation is

$$\dot{\epsilon} = K_2 \frac{D_{GB}}{d^3} \cdot \frac{\delta\sigma\Omega}{kT} \tag{25}$$

where K_2 is a constant (≈ 40), D_{GB} is the grain-boundary self-diffusion coefficient and δ is the width of the narrow zone in the grain boundary that contains the diffusive flow. Note that the grain size dependence of Coble creep is different from that of Nabarro-Herring creep.

Taking into account that the temperature dependence of the diffusion coefficient is given by Eqn. (15), both Eqns. (24) and (25) have the same form as that for the secondary creep rate given in Eqn. (10). The value of the activation energy, Q, will be that for self diffusion (Q_{SD}) for Nabarro-Herring creep (at higher temperatures), and that for grain-boundary diffusion (Q_{GB}) for Coble creep (at lower temperatures). However, the value for n will be unity in both cases. Referral to Figure 10 will show that power-law creep with $n \approx 1$ typically occurs at low stress levels, i.e., diffusional creep dominates at low stress and low creep rates. We may, therefore, anticipate this mechanism being present in certain regions of the container shell. The significance of a low value for n (i.e., a low stress dependence of the creep rate) will become apparent when we discuss creep rupture and creep ductility in Section 6.4.1.

6.3 DISLOCATION CREEP

The role of the diffusion of vacancies is less direct in dislocation-creep mechanisms than in diffusional creep. In the latter, the strain is produced directly by the selective deposition of atoms at grain boundaries. The strain arising from dislocation-creep mechanisms is produced by the generation and movement of dislocations in the crystal lattice. In this case, diffusion serves to assist the dislocations in their movement. Consequently, a much higher strain is produced per unit of diffusional flux and the creep rate is dominated by the dislocation processes at the higher levels of stress (where dislocation movement is encouraged). To better understand the dislocation processes, it will be useful to examine their phenomenological characteristics before looking at micromechanisms.

6.3.1 Work Hardening and Recovery

Dislocation mechanisms must fall into a general framework where two competing phenomena are occurring simultaneously, namely work hardening and recovery. This is a long-standing principle (Bailey 1926) that has been substantiated through extensive theoretical and experimental investigation. At low temperatures, where recovery is absent, continued plastic deformation requires an increase in the applied stress. This produces the familiar form of the stress-strain curve recorded in a tensile test, see Figure 21. At any stress level, it is possible to define a rate of work hardening, h, as the gradient of the stress-strain curve, where

$$h = \partial\sigma / \partial\epsilon \tag{26}$$

The hardening is due to the fact that the density of dislocations is increasing with increasing strain (i.e., the deformation is generating additional dislocations). Consequently, the dislocations interact with each other and hence become increasingly immobilized such that further deformation strain is possible only if the stress is increased.

If the strained metal is now heated to a higher temperature, the material gradually softens with time. This would result in a decrease in the stress necessary to produce further strain (i.e., the flow stress), see Figure 21. Such a process is called recovery and the rate of recovery (r) is defined as

$$r = - \partial\sigma / \partial t \tag{27}$$

Recovery occurs because the dislocation density decreases, as dislocations are annihilated by thermally activated processes.

During creep deformation, the creep strain increases by a small amount ($d\varepsilon$) during a small time interval (dt). Work hardening and recovery are taking place simultaneously and the change in flow stress ($d\sigma$) is a function of both strain and time and is dependent on the rate of work hardening, compared to the rate of recovery:

$$d\sigma = \frac{\partial \sigma}{\partial \epsilon} d\epsilon + \frac{\partial \sigma}{\partial t} dt = h d\epsilon - r dt \tag{28}$$

If the work-hardening rate is dominant, the flow stress will progressively increase and the creep rate will decrease with time/strain. This is the situation during the primary stage. In contrast, if the recovery process is dominating, the flow stress will decrease and the creep rate will accelerate, as in the tertiary stage. During the secondary stage, the rate of work hardening is exactly balanced by the rate of recovery, $d\sigma = 0$ and the creep rate is constant and is given by

$$\dot{\epsilon}_s = \frac{d\epsilon}{dt} = - \frac{\partial \sigma / \partial t}{\partial \sigma / \partial \epsilon} = \frac{r}{h} \tag{29}$$

This concept forms the basis of most dislocation theories. Furthermore, the dynamic competition between work hardening and recovery is the fundamental rationale underlying the θ Projection Concept presented in Section 9. It remains to investigate the details of the dislocation arrangements and interactions that determine the values of r and h.

6.3.2 Generic Dislocation Model

During creep, the microstructural distribution of dislocations develops in a non-uniform fashion. In some areas, there will be a high density of dislocation tangles and networks, forming barriers, or obstacles, to further dislocation flow. Adjacent to these will be areas that are comparatively free of dislocations. These regions are relatively soft and dislocation movement will be comparatively facile. The rate of continuing creep deformation will now be controlled by the ability of the mobile dislocations to overcome the hard-barrier regions.

Although the details of this process are complex, we will explore its generic kinetics because this illustrates the competing nature of the work-hardening and recovery processes outlined in Section 6.3.1. Furthermore, the desired equations form the basis of understanding that underlies the θ Projection Concept referred to in Section 5 and discussed more fully in Section 9. Our discussion will draw from the generalized dislocation-barrier theory of McLean (1966) and the dislocation microstructural model of Nix and Ilschner (1979). Further details will be found in Evans and Wilshire (1985 and 1993).

The basic strain-rate equation is obtained by considering the activation energy (q) necessary to overcome the obstacles:

$$\frac{d\epsilon}{dt} = B \exp(-q / kT) \tag{30}$$

where B is a constant and represents the detailed dislocation configuration.

If the applied stress, σ, is equal to the mechanical strength of the barrier, σ_b, the required activation energy will be zero (i.e., q = 0). When σ is less than this value, the thermal energy necessary to assist the stress in overcoming the barrier will be $q(\sigma_b - \sigma)/\sigma_b$. The rate equation then becomes

$$\frac{d\epsilon}{dt} = B \exp\left[-\frac{q}{kT}\left(1 - \frac{\sigma}{\sigma_b}\right)\right] \tag{31}$$

A key concept is that the strength of the barrier is being continuously modified by the work-hardening and recovery processes:

$$\sigma_b - \sigma = h\epsilon - rt \tag{32}$$

A consideration of the work done in overcoming the barrier (the force on the barrier x the distance moved in overcoming the barrier) leads to

$$q = \sigma_b b a \tag{33}$$

where b is the Burgers vector of the dislocation and a is the area of the slip plane swept out by the dislocation in overcoming the obstacle. Substitution of Eqns. (32) and (33) into (31) yields

$$\frac{d\epsilon}{dt} = B \exp\left[-\frac{ba}{kT}(h\epsilon - rt)\right] \tag{34}$$

In the early stages of creep (i.e., the primary creep stage), the exponential term can be approximated by the first two terms of its Taylor series, leading to the first-order differential equation

$$\frac{d\epsilon}{dt} + \frac{Bbah}{kT}\epsilon = B\left[1 + \frac{rba}{kT}t\right] \tag{35}$$

which has the solution

$$\epsilon = \frac{kT}{Bbah}\left[B + \frac{r}{h}\right]\left\{1 - \exp\left(-\frac{rba}{kT}t\right)\right\} + \frac{r}{h}t \tag{36}$$

In general form, Eqn. (36) can be written as

$$\epsilon = \theta_1(1 - e^{-\theta_2 t}) + \dot{\epsilon}_S t \tag{37}$$

with the θ_1 and θ_2 parameters describing the primary creep curve, where

$$\theta_1 = \frac{kT}{Bbah}\left[B + \frac{r}{h}\right] \quad \textit{and} \quad \theta_2 = \frac{rba}{kT}$$

Equation (37) (which is identical to Eqn. (7)) is a key element of the θ Projection Concept and will be discussed further in Section 9. At this point, it is worth noting that the θ parameters contain information on the detailed dislocation configuration, and the competing recovery and work-hardening processes. At very long times, Eqn. (37) shows that the total primary creep strain is limited to the value of θ_1, while θ_2 represents the rate of decay of the creep rate (i.e., the shape of the primary creep curve) and is often referred to as a process of "exhaustion", similar to the logarithmic form of Eqn. (3). However, the second term of Eqn. (37) predicts that the exhaustion process undergoes a gradual transition into the steady-state creep rate, $\dot{\varepsilon}_s$ (equal to r/h). In the next section, we examine more specific dislocation models that provide further understanding of recovery and work hardening.

6.3.3 Specific Dislocation Model

Numerous specific dislocation mechanisms have been put forward to describe creep phenomena. A review of these will be found in the textbook of Gittus (1975). We will examine one of these to illustrate their genus. This is the classical theory of Weertman (1955), based on the seminal idea that the recovery process is contained in the kinetics of dislocation climb. The mechanism is illustrated schematically in Figure 22.

Deformation has its origin in the generation of dislocations from numerous sources, one of which is shown in Figure 22. The emitted dislocations initially move relatively freely along their glide plane. However, the leading dislocations inevitably encounter an obstacle that prevents further glide. Subsequent dislocations emitted from the source interact with each other and become piled up against the obstacle. The resulting back-stress prevents the source from creating further dislocations: deformation ceases, this representing the strain hardening effect. Under the action of the stress (which modifies the local vacancy concentration in equilibrium with the dislocation in a manner identical to that represented in Eqn. (22)), diffusion causes vacancies to flow to or away from the dislocation, resulting in its climb motion normal to the slip plane. The released dislocation is now free to move on an adjacent slip plane, or may be annihilated by an encounter with another dislocation of opposite sign. In this manner, the obstacle is circumvented and the source can continue to operate. The climb process is the recovery event, controlled by diffusional kinetics.

When the details of this process are worked out, it is found that the climb rate of the dislocation is proportional to σ^2 and the ratio of the distance of dislocation glide to the height of dislocation climb is proportional to $\sigma^{2.5}$. This results in the following (steady-state) creep-rate equation

$$\dot{\epsilon} = A\sigma^{4.5} \exp(-Q_{SD}/kT) \tag{38}$$

which is identical to Eqn. (10), with n = 4.5. Other dislocation theories (which also depend on climb-induced recovery) predict values of n ranging from 2 to 10. Under low-temperature conditions, where dislocation-pipe diffusion is more effective than lattice self diffusion, Q_{SD} will be replaced by Q_P.

6.4 FRACTURE MECHANISMS

6.4.1 General Considerations

Materials subjected to tensile deformation may fail in a variety of ways. The broad classes of fracture are illustrated in Figure 23. For relatively ductile materials subjected to short-term tensile testing, failure is generally initiated by the development of a localized necked region, which progresses until the local cross-sectional area reduces to zero. Materials that have less ductility will form internal voids, usually transgranular, but sometimes intergranular when grain boundaries are weakened by impurities. These voids form by plastic tearing and are usually confined to regions of local necking. At low (usually cryogenic) temperatures, brittle cleavage fracture (transgranular or intergranular) can occur. Under creep conditions, voids and cracks can form by a combination of diffusion and creep plasticity. These are virtually always intergranular in nature, but can be transgranular at higher stresses.

Tertiary creep mechanisms are intrinsically linked with creep-rupture mechanisms. There is, however, one exception to this rule. An accelerating creep rate can occur as a result of microstructural instability, or softening. An example of this would be dynamic recrystallization, which effectively annihilates the dislocation microstructure by a process akin to annealing. Such behaviour is not expected to occur in the materials being considered for fuel-waste container construction because of the relatively low homologous temperature, which is below the recrystallization temperature. Another common source of softening would be the modification (particularly coarsening) of precipitates. This generally applies to high-strength alloys whose high creep resistance is achieved by precipitation hardening. Again, this does not apply to the candidate container materials, which are not precipitation-hardened materials.

Before we describe specific creep-rupture mechanisms, it is important to examine the general phenomenology of plastic instability. This is manifest as the development of a localized region of necking. Not only does this result in premature failure at low average creep strains, but the rapid local deformation occurring at the elevated stress present in the necked region produces an accelerating deformation rate. Although this is a localized plastic instability, it gives rise to an apparent macroscopic tertiary stage.

As the propensity for necking is highly dependent on the stress sensitivity of the creep rate, we must place this phenomenon in the context of the container shell. We start by representing the stress dependence of the creep rate (Eqn. (10)) in simplified form:

$$\dot{\epsilon} = B\sigma^n \tag{39}$$

As necking proceeds, the localized stress becomes higher, resulting in an increase in the local creep rate. An increase in the creep rate produces an acceleration of the reduction of load bearing area in the neck, giving rise to a runaway instability. The higher the value of n, the greater is the increase in the creep rate for a given reduction in the cross-sectional area, and

hence a greater tendency for necking. We can be more specific. Consider a creep specimen with a gauge length of x and a cross-sectional area of A. The strain rate can be written

$$\dot{\epsilon} = \frac{1}{x}\frac{dx}{dt} = -\frac{1}{A}\frac{dA}{dt} \tag{40}$$

Using Eqn. (39) and recognizing that $\sigma = L/A$, where L is the load on the specimen, the rate of decrease in specimen cross-sectional area is

$$-\frac{dA}{dt} = BL^n A^{1-n} \tag{41}$$

Thus, when $n \rightarrow 1$, the rate of decrease in cross-sectional area becomes independent of the area. Consequently, the rate of reduction in area is identical throughout the specimen gauge length, and localized necking is hence inhibited[8]. This has been confirmed in an extensive survey of creep-rupture data on a variety of materials (Woodford 1969). Over a range of n values from 200 to 1.6, the strain to rupture increased from 0.04 to 20. Similarly, Figure 24 (Evans and Wilshire 1985) illustrates the overall consequence of progressive neck development, and its dependence on the value of n. The average strain rate of a tensile specimen is plotted as a function of average strain, according to a simple finite element analysis of the necked region. This figure effectively demonstrates the increase in the measured creep rate as deformation progresses i.e., the development of a tertiary creep stage. As expected, the acceleration of the creep rate is more rapid for high values of n. When n = 1, the creep rate is essentially constant, in accordance with the analysis presented above. In principle, if n = 1, the material should extend indefinitely. This is the basis of the so-called superplastic materials, where $n \approx 1$ and extremely large strains of 1 to 10 are typically realized (Sherby and Wadsworth 1989).

As shown in Section 6.2, a creep process that is characterized by $n \simeq 1$ is that of diffusional creep. It would, therefore, be advantageous to operate the container under conditions where diffusional creep dominates. Plastic stability would then prevail. However, we could not guarantee that the extremely high strains characteristic of superplastic materials would be maintained. The intergranular fracture processes described in Section 6.4.2 could still occur, placing some limit on creep ductility. Actual superplastic materials are designed to avoid this problem by using extremely fine grain sizes to suppress grain-boundary cavitation. Nevertheless, conditions with n = 1 would favour high ductilities and long creep lives.

---

[8] In the general case, the effect of work hardening should be considered, in addition to the strain rate sensitivity. This is made explicit in the classical analysis of Hart (1967). Thus, if the rate of work hardening (h in Eqn. (26)) is high, the local deformation associated with necking causes a significant increase in the flow stress, hence resisting further neck formation. This would seem to be beneficial under creep conditions, where the values of h are typically very high (Evans 1973). However, as explained in Section 6.3.1, the hardening process is continuously being opposed by the recovery process. This makes it difficult to assess the benefit of work hardening in resisting neck formation under creep conditions.

6.4.2 Creep Fracture Mechanisms

The mechanisms of creep fracture are quite different from the time-independent ductile fracture processes occurring in short-term tensile tests. Whereas the latter usually fail by the development of transgranular cracks, creep rupture is more typically an intergranular phenomenon. These creep-rupture processes cause a marked reduction in strain to failure compared with short-term tensile tests. At higher creep stresses, microcracks form at grain-boundary triple-points (the point of intersection of three grain boundaries), and are wedge-like in shape, whereas at lower stresses, cracking occurs by the link up of spherical voids nucleated along the grain boundary. Both triple-point cracking and cavity formation occur primarily on grain boundaries lying normal to the tensile stress. They both nucleate fairly early in the creep life, but their growing presence is not evident until they are responsible for the accelerating creep of the tertiary stage. A comprehensive summary of creep-rupture mechanisms is provided in a book written by Evans (1984).

The formation of triple-point wedge-cracks is a direct result of the fact that adjacent grains within a polycrystalline material move relative to each other under creep conditions. This shearing process, termed grain-boundary sliding, is illustrated in Figure 25. Such sliding results in stress concentrations at triple-points, large enough to nucleate a crack. Continued sliding causes a wedge-shaped crack to grow along the grain boundary normal to the tensile stress. The relative movement of the adjacent grains must be accommodated by deformation in the surrounding grains. Grain-boundary sliding, and hence triple-point crack development, is then controlled by the rate of grain deformation by creep. This coupling of fracture and deformation is the basis of the Monkman-Grant relationship discussed in Section 4.3.

The grain-boundary shear stresses, and therefore the applied tensile stress, must be sufficiently high to decohere the grain boundary at the triple-point. At lower stress ranges, intergranular failure occurs by grain-boundary cavitation, depicted in Figure 26. As with triple-point cracking, the nucleation of grain-boundary cavities is typically caused by grain-boundary sliding. The stress-concentration sites are now associated with particles at the grain boundaries, or irregularities formed by the intersection of planes of deformation with the grain boundaries. Following nucleation, grain-boundary sliding can make a contribution to cavity growth, but evidence is in favour of diffusional growth being the major process. Thus, when a cavity has reached a critical size (dependent on the applied stress), growth continues by absorption of vacancies from the surrounding grain boundary (Balluffi and Siegle 1955).

In keeping with Eqn. (22), the vacancy concentration, C_b, at a grain boundary normal to the stress, σ, is given by

$$C_b = C_o \exp(\sigma\Omega / kT) \tag{42}$$

where C_o is the equilibrium concentration of vacancies at zero stress, and Ω is the atomic volume. However, the vacancy concentration near the cavity surface, C_c, is also increased above C_o. This is due to the presence of the surface tension, γ, such that the work done to form a vacancy at this location is $2\gamma\Omega/r$, where r is the cavity radius, and the local vacancy concentration is

$$C_c = C_o \exp(2\gamma\Omega / rkT) \tag{43}$$

For the cavity to preferentially absorb vacancies from the grain boundary, $C_b > C_c$. This condition is reached when the cavity size exceeds $r = 2\gamma/\sigma$. Based on the boundary conditions represented by Eqns. (42) and (43), a diffusional model (grain-boundary diffusion) was developed by Hull and Rimmer (1959), from which the rate of growth of a cavity is predicted to be

$$\frac{dr}{dt} = \frac{D_{GB}\delta\Omega(\sigma - 2\gamma/r)}{2kTa_c r} \tag{44}$$

where a_c is the spacing between cavities. Other variants and refinements of this equation have also been developed (Gittus 1975).

There are a number of difficulties in using equations such as (44) to calculate, for example, the time to rupture:

- The cavity spacing, a_c is not well characterized. Experiments show that it can vary with stress, temperature, strain and time in ways that are not well understood. This makes integration of Eqn. (44) very difficult.

- There is no definitive fracture criterion. This will be associated with cavity growth and interlinkage, but requires an understanding of the plastic failure of the inter-cavity ligaments. It is worth noting that the plastic instability phenomenon discussed in Section 6.4.1 plays a role in this context. Thus, creep rupture by cavitation is delayed in materials with $n = 1$.

- Surface diffusion plays a role. This has the effect of changing the spherical cavity into an elongated lenticular shape, a phenomenon that has an important influence on cavity linkage, and hence the fracture criterion.

- A plastic accommodation factor must be taken into account. This is discussed below.

In the description of the cavity-growth model above, emphasis was placed on the key role of vacancy diffusion. However, there is an equivalent counterflow of atoms, and these must be deposited on the grain boundary adjacent to the cavities. The volume increase associated with this plating out of atoms must be accommodated by local plastic deformation (Beere and Speight 1978). In addition, the ligaments separating the cavities and removed from the region of diffusional flow, will undergo creep deformation as shown in Figure 27. Such creep deformation contributes to the growth of the cavities and the overall elongation rate of the material. A second, related, phenomenon occurs because grain-boundary cavitation is inhomogeneous. The situation is illustrated in Figure 26. The atoms that are depositing on the cavitated grain boundary are "jacking" grains A and B apart. This jacking action is constrained by grains C and D. The rate at which A and B move apart, and hence the rate of cavity growth, is controlled by the creep deformation of C and D (Dyson 1976). Further information on this deformation-controlled fracture mechanism will be found in the discussion of Fracture Mechanism Maps, Section 8. Not only does this complicate the cavity-growth rate

and determination of the ultimate time to rupture, it provides the coupling between creep fracture and deformation, essential to explain the Monkman-Grant relationship.

Whereas the theory of creep rupture is highly complex, the associated strain/time behaviour in the tertiary stage is even more complicated. We have shown above how enhanced plastic creep strain is initiated by the cavity-growth process itself. Another factor is the effective increase in stress because of the net loss in cross-sectional area resulting from cavity formation. However, further discussion of the characteristic shape of the tertiary creep stage will be postponed until we return to this important issue in Section 9.

7. DEFORMATION MECHANISM MAPS

7.1 CONSTRUCTION OF THE MAPS

Although Ashby (1972) is the recognized champion of the deformation mechanism map concept, the basic diagrammatic format originated with Weertman (1963). However, it was Ashby and his co-workers at Cambridge university who refined the mapping process, collected vast amounts of data, and constructed maps for many metals and ceramics. A major collection of their work is to be found in the book by Frost and Ashby (1982). This book reviews the relevant creep mechanisms (i.e., a more detailed version of Section 6) and includes maps for titanium and copper, separately published by Sargent and Ashby (1982) and Cocks and Ashby (1982), respectively.

The deformation maps are drawn using axes of normalized stress (σ/E, or σ/G, where E and G are the Young's modulus and shear modulus of elasticity, respectively) and homologous temperature, as shown schematically in Figure 28. The various fields of the map (about five of them) represent the range of stress and temperature within which a particular mechanism is dominant. The boundaries of these fields represent the stress-temperature locus where the applicable creep rates of adjacent mechanisms are equal. The mechanisms considered in the construction of the maps conform with those described in Section 6. The creep rates are calculated from the corresponding constitutive equations, being a combination of theoretical prediction and empirical interpolation (see below). In addition to representing the stress-temperature regimes within which a given mechanism is expected to be dominant, contours of constant creep rate are superimposed on the map, these contour lines traversing the various mechanistic fields. These contour lines are shown on the specific maps for titanium and copper shown in Figures 29 and 30. In a similar manner, actual experimental creep data are plotted on the map. Thus, the deformation map is a compendium of theoretical and experimental information, represented in a compact, highly visual form.

As shown in Figure 28, the upper limit of the diagram is determined by yield-point phenomena, and is of no interest to us. The lower limit of the diagram is set by diffusional creep, with a distinction between Nabarro-Herring and Coble creep. Calculations within these regions are performed using Eqns. (24) and (25): the relevant parameters (diffusion coefficients, elastic moduli, etc.) for titanium and copper are collected in Table 1. The deformation equation used for the dislocation-creep field (termed power-law creep in Figures 29 and 30) is a modified form of Eqns. (10) and (38):

$$\dot{\epsilon} = A \frac{DGb}{kT} \left(\frac{\sigma}{G}\right)^n \tag{45}$$

where the diffusion coefficient, D, is put equal to D_{SD} for high temperatures and equal to D_P at lower temperatures. The parameters A and n are determined from actual experimental data, and are collected in Table 1.

A limitation of the deformation maps is that they represent steady-state (secondary creep stage) creep conditions only. Frost and Ashby (1982) have made an attempt to capture transient creep (primary creep stage) in the deformation map format. However, these are cumbersome and less useful as they come in multiple sets; each map is appropriate to a specified time. In addition, transient-creep data are rather limited in scope; the only set of maps provided by Frost and Ashby are for stainless steel. Furthermore, the deformation maps do not include information on tertiary creep. Some of this information is, however, contained in the complementary Fracture Mechanism Maps, discussed in Section 8.

7.2 APPLICATION OF THE MAPS

For our purposes, the attractive feature of the deformation maps is that they are based on established mechanisms for creep, supported by a wide-ranging set of experimental data. As a result, they contain the authority of the mainstream of international scientific knowledge on creep processes. Any selected subsection of the map is supported by the complete body of information subsumed into the map taken as a whole. It is from this that the utility of the maps emerge. Take titanium as an example (Figure 29). The container shell will operate at a homologous temperature (based on the β-phase melting temperature used in the map) of 0.2. We observe that experimental data at this temperature are confined to the region of very high stress. However, we can, with some degree of confidence, focus on the strain-rate contour of $10^{-12}s^{-1}$ (recalling that this would be the approximate range of acceptability discussed in Section 3.2). Such a strain rate would allow a design stress of about 10^{-3} G. The map tells us that this deformation rate falls in the area of power-law (i.e., dislocation) creep, with (see Table 1) a stress exponent of n = 4.3 and an activation energy of 97 kJ/mole (dislocation core diffusion). Such parameters facilitate the engineering design of the container, together with the experimental design of a test matrix for conducting additional creep tests in this region. The appropriate constitutive equation for steady-state creep would be that of Eqn. (45).

It might be judged advantageous to operate the titanium shell in the diffusional creep mode. This would allow benefit from the high ductility that is predicted from a stress exponent of n = 1, which prevents the onset of plastic instability. We discover from the map that this would require a stress level of about 10^{-4} G. The creep mechanism would be Coble creep, for which an accurate constitutive equation is known (Eqn. (25)), together with its relevant parameters (from Table 1). Using such an equation (or adding the appropriate strain-rate contours to the map), the preferred maximum creep strain rate of the particulate matrix could be determined.

Another general message contained in the maps is that the steady-state creep regimes (whether of dislocation or diffusion origin) extend throughout the entire temperature range, despite the fact that the actual deformation rates at homologous temperatures of 0.2 and below, are very low. This substantiates the arguments made in Section 4 that even at low temperatures we might expect (over very long time scales) the full expression of creep

behaviour typified by primary, secondary and tertiary stages. This position will be supported by similar consideration of Fracture Mechanism Maps described in Section 8.

The deformation map will also be useful when we consider the θ Projection Concept, elucidated in Section 9. Thus, it will allow us to exercise caution if the θ Projection is extended from one creep region to another, i.e., if we cross a field boundary from one dominant mechanism to its neighbour. The information in the map will also provide some ballpark comparison with the creep rates predicted by any θ Projection equations that are eventually developed. Such equations will require the generation of experimental creep data to extract the essential θ-parameters. The deformation map will provide useful guidance in setting the range of stress and temperature to be explored in these experiments. The relevance of these points will be more evident following the discussion of the θ Projection Concept in Section 9.

Finally, it must be acknowledged that although the Deformation Mechanism Maps summarize our current knowledge of steady-state creep, they undoubtedly are incomplete. Within the context of the long history of mechanical metallurgy, there is likely to emerge future modification of theoretical models and experimental data. We can, however, say with conviction that the maps currently represent the entire state of understanding of creep and plastic flow processes.

7.3 SPECIFIC CASE STUDIES

In their book on Deformation Mechanism Maps, Frost and Ashby (1982) provide several case studies illustrating the application of the deformation maps to practical problems. Examples from industrial metal-forming procedures, including rolling, forming and extrusion, fall into the upper end of the strain-rate range (10 - 10^5 s^{-1}). The maps are used for a variety of materials to obtain estimates for the forming forces that are required, and the way in which these forces will change if the rate of the process, or the temperature at which it is performed, are altered.

Maps constructed for tungsten have been used to improve the lifetime of electric light bulb filaments. For these to last ~1000 h, the filament creep rate must be $<10^{-9}$ s^{-1}. The maps show that for pure tungsten, the operating conditions place the filament in the power-law creep regime, with an unacceptable creep rate of 10^{-4} s^{-1}. However, doping the tungsten with minor alloy additions causes the power-law creep region to shrink, thus placing the filament in the diffusional creep area. The creep rate is now reduced to 4×10^{-10} s^{-1}, and ductility is also enhanced by the fact that $n = 1$. A similar scenario emerges for the analysis of nickel-based alloys used in high-temperature turbine blades (maximum acceptable creep rates of ~10^{-8} s^{-1}). Alloying again places the blade in the diffusional creep field, but with unacceptably high creep rates. The solution to this is to increase the grain size, thus reducing the diffusional creep rate. As a result, the power-law creep field expands such that it contains the turbine blade and precipitation-strengthening strategies can be used to lower the creep rate further.

Examples of application of the maps to longer time scales (~30 years) are taken from the nuclear industry. Reactor components made of stainless steel are considered. Allowable creep rates are in the range of 10^{-10} s^{-1}, placing them in the diffusional creep field. Because allowable strains are small, of the order of 0.01, transient-creep maps are found to be necessary to obtain accurate predictions.

Apart from the above examples, there are several case studies that deal with much longer time scales, of historical and geological proportion. As these are of greater significance to the waste-container problem, we will look at these separately, in greater detail.

7.3.1 Creep of Architectural Lead

Since pre-Roman times, lead has been used for roof coverings and water pipes. Because of its good corrosion resistance, ancient lead piping installations have survived in various architectural forms. Present-day inspections sometimes reveal that creep deformation has occurred, even under relatively low stress conditions. This is due to the fact that the low melting point of lead places room temperature in the range of 0.5 T_m homologous temperature. It has been observed that whereas Roman lead piping shows negligible creep over periods of about 2000 years, Victorian piping of about 75 years old has crept by significant amounts. Thus, an analysis of the sag of Victorian piping (drain pipe and hot-water pipe) showed that creep rates of about 5×10^{-12} s^{-1} had occurred under stresses of $\sim 5 \times 10^{-5}$ G. An examination of the relevant deformation map (Figure 31) shows that the observed creep rates are consistent with those predicted, falling in the field of diffusional creep (Coble creep).

Note that the grain size for this map is 50 μm, in keeping with the measured grain size of 10 - 100 μm in Victorian lead piping. In contrast, the grain size of Roman lead piping is >1 mm. This is a consequence of the fact that Roman piping was made by a casting process, whereas Victorian piping was produced by extrusion. Figure 31 also shows the deformation map for a 1 mm grain size (bearing in mind that diffusional creep is strongly dependent on grain size, as explained in Section 6.2). This places the water piping in a position straddling the diffusional creep and power-law creep boundary. The predicted creep rates are several orders of magnitude slower, adequately explaining the lack of creep deformation in Roman piping over a period of thousands of years.

7.3.2 Creep in the Polar Ice Cap

Studies of the South Polar Ice Cap show a maximum depth of 4000 m at its centre, sloping gently outwards for 1000 km or more, before falling steeply into the open sea. Based on this gradient and depth of ice, the shear stresses in the ice can be calculated. Similarly, borehole measurements have determined the temperature as a function of depth.

Deformation maps have been used to analyze the outward flow of the ice cap. The relevant map is shown in Figure 32, onto which is plotted the range of temperature and stress present in the ice cap (at the Byrd Station), as a function of depth. This shows that the Antarctic ice cap deforms by power-law creep, with the creep rate being greatest ($\sim 10^{-9}$ s^{-1}) next to the bedrock, where the stress and temperature are maximum.

7.3.3 Continental Drift

It is well established that the major continental plates positioned in the earth's upper mantle are drifting apart, over distances of about 5000 km in a period of 2×10^8 years. This translates to a creep strain rate of 10^{-12} - 10^{-15} s^{-1}. The major mineral phase present in the mantle and sustaining this creep strain is olivine, a silicate material. The deformation map is presented in Figure 33.

The creep-rate contours in Figure 33 have been modified to take into account the extreme pressures present in the earth's mantle (much larger than for the polar ice cap). The theoretical-creep equations facilitate this by including the effects of pressure on the creep-activation energies. The net effect is to reduce the creep rates by about 10^3, compared to creep rates at atmospheric pressure. The range of creep stress and temperature is uncertain, but is bounded by the hatched area shown in Figure 33. This shows that the predicted creep rates are consistent with those estimated from geological observation of continental drift. The map also predicts that the creep mechanism will be power-law creep at the higher stresses (deeper layers) and diffusional creep at lower stresses, based on a grain size of 0.1 mm. If the grain size is larger, say 1 mm, the dominant flow mechanism will be power-law creep.

8. FRACTURE MECHANISM MAPS

The format and layout of the Fracture Mechanism Maps is similar to that of the Deformation Mechanism Maps. However, during their historical development, the method of construction has progressed through two phases. The first of these (Ashby et al. 1979) followed a largely empirical process. The resulting map for copper (to the author's knowledge, no map for titanium has been published) is shown in Figure 34. The mechanistic fields of this map are derived from direct observation of the characteristic fracture mode from metallographic examination of creep specimens. Thus, the narrow region at the higher stress levels is designated "ductile fracture", or "transgranular creep fracture" (the differentiation between the two is rather arbitrary), based on observation of plasticity-induced voids and cracks. Below this is the extensive field of "intergranular creep fracture" characterized by the observation of intergranular voids and cracks. The upper right sector, at higher temperatures, marks the regime where extensive dynamic recrystallization is evident.

Also plotted on the map are contours of equal fracture times, the included numbers being the logarithm, to the base 10, of the time to rupture in seconds. Solid symbols mean that the fracture was identified as intergranular (open symbols, transgranular). The shaded areas indicate a mixed mode of fracture.

The information contained in such fracture maps is, in reality, rather limited. The diagram basically divides the microscopic observations into two classes: transgranular and intergranular. The experimental rupture times included on the maps provide supplementary information, necessarily of limited temperature and stress ranges. As such, the maps are largely of pedagogical value, at best. They provide little basis for extrapolation, having a very limited theoretical basis, somewhat at variance with the claim of a "mechanistic" map.

These fundamental limitations were partially improved in later versions of the maps (Cocks and Ashby 1982), the published version for copper (titanium unavailable) being shown in Figure 35. Such maps are now more firmly based on the mechanistic understanding outlined in Section 6.4. The boundaries of the map are derived from kinetic equations that describe cavity growth, mainly on grain boundaries. With the aid of these theoretical equations (with parameters such as diffusion coefficients and creep rates derived from experimental data), the map is divided into regions that are primarily controlled by surface diffusion, grain-boundary diffusion and power-law creep, as described in Section 6.4. The lower boundary on the map (the heavily dashed line) marks the threshold stress below which the voids are unstable (sub-critical) and therefore disappear by sintering, under the action of the surface tension. The

contours on the map represent constant values of damage rate, df_h/dt, where f_h represents the fractional area of cavities, r^2/ℓ^2, where r is the radius of the cavity and 2ℓ their spacing apart on the grain boundary. Note that the initial values of ℓ and f_h (and therefore r) have to be pre-designated. The authors use the values of df_h/dt to calculate the times to rupture, by integration. However, the considerable difficulties associated with this are pointed out in Section 6.4. Not least of these is the determination of a suitable fracture criterion. Cocks and Ashby adopt a value of $f_h = 0.25$. Clearly, when $f_h = 1$, the cavities are fully linked and fracture is guaranteed. The preferred (and rather arbitrary) value of $f_h = 0.25$ assumes that the remaining ligaments fail rapidly by plastic tearing. In addition, it is assumed that the inter-cavity spacing (2ℓ) remains constant. This is at variance with experimental information that typically demonstrates that cavity nucleation is an ongoing process as creep proceeds. In addition, the time required to nucleate the cavities has to be estimated (and may represent a significant fraction of the rupture time).

The integration procedure also yields the increasing creep strain resulting from the cavitation growth process. Thus, an expression is obtained for the tertiary creep stage, and the strain to failure. However, this procedure is subject to the same limitations underlying the assumptions used to calculate the times to rupture.

In summary, the Fracture Mechanism Maps (in contrast to the utility of the Deformation Mechanism Maps) are of limited practical use. In particular, their reliability is questionable for the purposes of extrapolation outside the experimental database. However, the theoretical analysis of Cocks and Ashby (1982) represents a superb representation of the current understanding of creep-fracture mechanisms. In fact, their paper serves the admirable task of emphasizing the enormous complexity of the fracture mechanisms, and their subtle coupling with the deformation process. As has been mentioned previously, this latter observation is a key characteristic of creep, being entrenched in the Monkman-Grant relationship (Section 4.3) and utilized in the θ Projection Concept (Section 9).

9. THE θ PROJECTION CONCEPT

9.1 GENERAL CONSIDERATIONS

The θ Projection Concept was introduced by Evans et al. (1982) in 1982 and has been a topic of intense investigation and application by the Swansea University research group. Extensive reviews of this development have been published in their 1985 textbook (Evans and Wilshire 1985) and a more recent update (Evans and Wilshire 1993).

The concept embraces the maxim that the creep behaviour of a material finds its full expression in the total creep curve, classically represented by the three stages of primary, secondary and tertiary creep. Thus, as pointed out in Section 4.3, creep and creep fracture have been traditionally described by reference to only a few standard parameters, the secondary creep rate ($\dot{\varepsilon}_s$), the time to rupture (t_r) and the strain to rupture (ε_r). While the values of t_r and ε_r precisely identify the point of creep failure, measurement of only the steady-state creep rate disregards the primary and tertiary stages, so that a major portion of the information available from a creep curve is totally ignored. The significance of this omission can be illustrated using Figure 36. Thus, the three curves have the same values of $\dot{\varepsilon}_s$, t_r and ε_r, but the curve shapes differ markedly, reflecting the different proportion of lifetime

spent in primary or tertiary. Actual examples of this, for the case of copper, are shown in Figure 37. In general, this shows the common trend for the primary stage to become less pronounced, and the tertiary stage to become more dominant, with decreasing applied stress (the likely scenario for the container shell). Such disparate behaviour is of crucial importance for the modelling of complex structures using finite element stress analysis codes. Clearly, then, a comprehensive description of creep behaviour requires constitutive equations that accurately describe the full creep-curve shape and its dependence on test conditions. Such a process will ensure that the constitutive equations contain the primary and fundamental phenomena that are universal to the creep behaviour of all classes of materials.

9.2 FORMULATION OF THE CONSTITUTIVE EQUATIONS

An early attempt by the Swansea group (Davies et al. 1969) to quantify the whole creep curve was based on the use of the exponential equation of Garofalo et al. (1963) to represent primary and secondary creep. This is Eqn. (7) of Section 4.2. This equation can be extended to include a tertiary term, as

$$\epsilon = \alpha_1(1 - e^{-\beta_1 t}) + \gamma t + \alpha_2 e^{\beta_2(t - t_i)} \tag{46}$$

where the constants α_2 and β_2 define the shape of the tertiary stage that begins after t_i. Unfortunately, the time to the onset of tertiary is subjective and can produce significant errors in long-term extrapolation. In addition, it was realized that the mechanistic precursors of the tertiary stage are present throughout the creep curve. Thus, for example, the onset of tertiary does not coincide with the nucleation of grain-boundary cavities. Such cavities form and grow early in the creep life, even during primary creep. Tertiary creep only becomes evident when the intergranular damage develops to an extent sufficient to cause an acceleration in the creep rate. This conceptual reasoning quickly leads to an alternative view of the form of conventional creep curves. We can consider the deformation behaviour to be a consequence of competing events, a primary creep process that decays throughout the entire creep life and a tertiary creep process that accelerates from the commencement of creep. This view is also in complete harmony with the idea of a competing work-hardening rate (h) and a recovery rate (r), as discussed in Section 6.3.1. Within this mechanistic framework, a minimum creep rate rather than a steady-state creep rate would be attained. Indeed, it seems fortuitous to expect that a perfect balance between r and h (bearing in mind that both r and h are themselves time-dependent quantities reflecting the evolution of the creep microstructure) will be maintained for any prolonged period to result in a protracted period of secondary creep. Depending on the precise rates of primary decay and tertiary acceleration, the minimum creep rate could appear to be essentially constant over the period of inflection. Examples of this will be given below.

We might consider a polynomial expression that is compatible with this concept, in keeping with Eqn. (5) and suggested by de Lacombe (1939)

$$\epsilon = \alpha_1 t^{\beta_1} + \alpha_2 t^{\beta_2} \tag{47}$$

with $\beta_1 < 1$ and $\beta_2 > 1$. However, as explained in Section 4.2, the coefficients of polynomial expressions vary erratically with stress and therefore are unsuitable for longer-term extrapolations. The evidence from experimental data indicates that the exponential form of equation holds more promise (Evans and Wilshire 1985).

We can begin the development of an exponential constitutive equation by examining that used to represent the primary and secondary stages:

$$\epsilon = \theta_1(1 - e^{-\theta_2 t}) + \dot{\epsilon}_s t \tag{48}$$

This, in its empirical form, is that suggested by Garofalo et al. (1963) (see Eqn. (7) in Section 4.2). We learned in Section 6.3.2 (Eqn. (37)) that this equation has full theoretical justification, being derived from a dislocation-creep mechanism applicable to primary creep, and based on the fundamental idea of the competing interaction between the work-hardening and recovery rates. Differentiation of Eqn. (48) then shows the creep rate decays as

$$\dot{\epsilon} = \theta_1\theta_2 e^{-\theta_2 t} + \dot{\epsilon}_s \tag{49}$$

which, on rearrangement becomes

$$\dot{\epsilon}_p = \theta_1\theta_2 e^{-\theta_2 t} = \theta_2(\theta_1 - \epsilon_p) \tag{50}$$

where $\dot{\epsilon}_p$ is the primary creep rate given by $\dot{\epsilon} - \dot{\epsilon}_s$.

In Eqn. (50), the primary creep rate ($\dot{\epsilon}_p$) decays linearly with increasing primary creep strain (ϵ_p). This means that primary creep obeys first-order reaction-rate kinetics, in keeping with the mechanistic predictions. A rationalization of this is as follows. The strain rate is a function of the pertaining microstructure (dislocation configuration, density of cavities, etc.), which evolves in proportion to the accumulated strain. A natural consequence is that $\dot{\epsilon}_p \propto \epsilon_p$. The kinetic rate constant is given by the parameter θ_2, while θ_1 determines the maximum primary strain as $t \rightarrow \infty$. This is illustrated in Figure 38. As shown in Eqn. (37), the θ parameters contain information on the dislocation configuration and the work-hardening/recovery rates. Equation (50) therefore describes a continuously decaying creep curve which, as the primary creep strain approaches θ_1 at long times, eventually attains a steady-state creep rate of $\dot{\epsilon}_s$.

We must now consider the tertiary creep stage. The required expression must recognize that the tertiary damage processes initiate early in the creep life and advance in a progressive manner. Thus, even when intergranular cavities and cracks nucleate early in the primary stage, the low initial damage levels will be insufficient to have any significant effect on the rapid decay in creep rate. However, as the size and number of cavities increase with increasing strain, the resulting acceleration in creep rate will offset the gradual decay in creep rate towards $\dot{\epsilon}_s$. This process can be modelled by introducing the damage parameter, ω, (see Section 4.3) which is initially zero for undamaged material (t = 0). The value of ω then

increases such that instead of approaching $\dot{\varepsilon}_s$, the creep rate will accelerate with the tertiary creep rate ($\dot{\varepsilon}_t$) given by

$$\dot{\epsilon}_t = \dot{\epsilon}_s (1 + \omega) = \frac{r}{h} (1 + \omega) \tag{51}$$

with the rate of damage accumulation $\dot{\omega}$ increasing as

$$\dot{\omega} = C (d\epsilon_t / dt) \tag{52}$$

where C is a constant. On integrating, we can then replace the steady-state term in Eqn. (48) to give

$$\epsilon = \theta_1(1 - e^{-\theta_2 t}) + (1/C)(\epsilon^{C\dot{\epsilon}_s t} - 1) \tag{53}$$

which can be written as

$$\epsilon = \theta_1(1 - e^{-\theta_2 t}) + \theta_3(e^{\theta_4 t} - 1) \tag{54}$$

Differentiation shows that the tertiary creep rate ($\dot{\varepsilon}_t$) increases linearly with increasing tertiary creep strain, $\varepsilon_t = \varepsilon - \varepsilon_p$ as

$$\dot{\epsilon}_t = \theta_3\theta_4 e^{\theta_4 t} = \theta_4(\theta_3 + \epsilon_t) \tag{55}$$

which is the same form as Eqn. (50) and demonstrates that the tertiary stage also obeys first-order reaction-rate kinetics. The significance of the θ_3 and θ_4 parameters is indicated in Figure 38.

Evans and Wilshire (1985) show that such first-order kinetics are inconsistent with a phenomenological explanation of tertiary creep based on the loss of load-bearing area. Thus, for example, Figure 24 shows that $\dot{\varepsilon}_t$ is <u>not</u> directly proportional to ε_t when the acceleration of creep deformation is the result of plastic instability arising from neck formation. Similarly, simple calculation shows that first-order kinetics would not be produced by the lack of grain-boundary load-bearing area resulting from the growth of cavities, regardless of the assumed cavity spacing. In addition, since the total cavity volume is usually less than 1%, the reduction in load-bearing area is insufficient to account for the typical magnitude of tertiary creep. Furthermore, experiments show that the deformation acceleration occurs only if the cavities are associated with grain boundaries (cavities produced within the grains do not increase the creep rate). However, the correct kinetics would derive from a micromechanism where dislocation climb is enhanced by the absorption of vacancies by the developing cavities

(Evans and Wilshire 1981). In this case, $\dot{\varepsilon}_t \propto \varepsilon_t$, in accordance with Eqn. (55). It is typically observed that significant necking occurs only in the final stages of tertiary creep.

9.3 INTERPOLATION OF EXPERIMENTAL DATA

Equation (54) is the primary constitutive equation emerging from the θ Projection Concept. Figure 39 demonstrates the capability of the equation to accurately represent experimental data obtained for a steel. This shows that the use of the four θ parameters allows a good fit to a creep curve that shows an apparent period of secondary creep, although the equation contains only a minimum creep rate. Through differentiation of Eqn. (54), the creep rate at any instant is given by

$$\dot{\epsilon} = \theta_1\theta_2\theta^{-\theta_2 t} + \theta_3\theta_4\theta^{\theta_4 t} \tag{56}$$

and the minimum creep rate is produced at a time t_m given by

$$t_m = \frac{1}{\theta_2 + \theta_4} \ln \frac{\theta_1\theta_2^2}{\theta_3\theta_4^2} \tag{57}$$

which, substituted with Eqn. (56) will yield the minimum creep rate, $\dot{\varepsilon}_m$. The value of $\dot{\varepsilon}_m$ will be greater than the secondary creep rate, $\dot{\varepsilon}_s$, in Eqn. (48), which would have been attained eventually in the absence of tertiary processes. Figure 37 shows some examples for copper (Brown et al. 1987), and demonstrates the capability of the equation to fit a variety of creep curves.

9.4 EXTRAPOLATION OF EXPERIMENTAL DATA

The major utility of Eqn. (54) lies in its capability for prediction and extrapolation. Such projection is achieved through the four θ parameters. The values of these (plus their statistical variability) can be extracted by fitting the equation to each experimental creep curve obtained for a particular material, using suitable computer programs (available from the Swansea group). The set of θ parameters for copper (obtained from creep curves such as those shown in Figure 37), plus their systematic variation with stress and temperature, is shown in Figure 40. This provides the basis for a quantitative description of the gradual change in curve shape with changing test conditions.

Figure 40 shows that a linear relationship is found in the plot of stress versus log θ. For the θ_1 and θ_3 parameters, the temperature dependence is represented by the temperature dependence of the short-term yield stress (σ_Y), whereas θ_2 and θ_4 are best fitted to an Arrhenius relationship. Both stress and temperature dependencies can thus be written as

$$\begin{aligned}
\theta_1 &= G_1 \exp H_1(\sigma/\sigma_Y) \\
\theta_2 &= G_2 \exp -[(Q_2 - H_2\sigma)/kT] \\
\theta_3 &= G_3 \exp H_3(\sigma/\sigma_Y) \\
\theta_4 &= G_4 \exp -[(Q_4 - H_4\sigma)/kT]
\end{aligned} \tag{58}$$

where G and H are constants and Q is the activation energy. The fact that $Q_2 = Q_4 = 110$ kJ/mol is consistent with the fact that the creep of copper is controlled by pipe diffusion (see Table 1). This applies to primary creep (θ_2) and tertiary creep (θ_4).

It is now necessary to verify whether the θ parameters facilitate long-term extrapolation. This has been demonstrated by an extensive investigation of a chromium-molybdenum-vanadium ferritic steel (Wilshire 1989, Wilshire and Evans 1994). This steel is used in the high-temperature (~550°C) steam generating section of a thermal-electric power station. The appropriate θ parameters are shown in Figure 41. The activation energy for θ_2 is equal to 224 kJ/mol, a value close to that for lattice self-diffusion in ferrite. The temperature dependence of θ_4 is more complex, a stress-dependent activation energy being required. This reflects the fact that, in addition to the formation of grain-boundary cavities, the tertiary creep in this material is affected by the coarsening of the carbide precipitates that are deliberately provided for added creep strength.

Figure 41 shows that the experimental stress range used to obtain the θ parameters for steel is 150 - 350 MPa. The θ parameters can now be used to extrapolate the creep data to much lower stresses. Thus, Figure 42 shows the complete curves predicted for the stress range 70 - 110 MPa. This demonstrates the capability of the θ Projection technique to extrapolate creep data obtained over a period of about one month to periods in excess of ten years.

The extrapolation capability is further illustrated by reference to Figure 10. This is a logarithmic plot of the minimum creep rate ($\dot{\varepsilon}_m$), obtained through Eqns. (56) and (57), versus stress. In Figure 10, the solid line is derived from short-term data (~1000 h), represented by the symbol, +. To this plot has been added long-term creep data (up to 100,000 h), subsequently obtained at lower stresses. It can be seen that the long-term data are remarkably well predicted by the θ parameters derived from short-term data. This is an impressive demonstration of the extrapolative power of the θ Projection Concept. It has been successfully applied (and verified) to project experimental data obtained from creep tests performed over several months to the 30-year lifetime conditions of an electricity generating plant.

Although this is far short of the levels of extrapolation (at least 500 years and possibly much longer) required for the waste-container shell, a glance at Figure 10 will show that the continued projection to a creep rate of $\sim 10^{-12}$ s^{-1} is a modest step. This is the range of the anticipated operating creep rate of the container shell (see Section 3.2).

Evans and Wilshire (1993) point out that the form of the θ equations represented by Eqns. (58) are not, in practice, convenient, particularly for use in finite element computer programs. They have therefore recommended the use of the following equation for long-term extrapolation:

$$\ln \theta_i = a_i + b_i\sigma + c_iT + d_i\sigma T \qquad (59)$$

This applies to conditions in which the experimental data used to derive the θ parameters do not depart significantly from the temperature of the intended application. Under such conditions, the 1/T relationship of Eqn. (58) is closely equivalent to a linear T dependence.

The constants a, b, c and d can be evaluated rapidly by a multilinear least-squares regression analysis. Their values for copper and steel are shown in Table 2.

The Swansea group has applied the θ Projection Concept to analyze the creep behaviour of a variety of materials, summarized as follows:

- oxygen-free high conductivity copper (Evans and Wilshire 1987a, Brown et al. 1987),
- three varieties of aluminum alloy used for airframe construction (Evans et al. 1990, Evans et al. 1993a),
- three high-performance structural steels (Brown 1987, Wilshire 1989, 1993a, Evans et al. 1984, 1993a, Wilshire and Evans 1994),
- oxide dispersion-strengthened steel (Evans et al. 1993, b and c), which has very high apparent values of n and Q_c: $n \approx 40$ and $Q_c \approx 3 \times Q_{SD}$,
- nickel-based superalloy (Brown et al. 1986a, Evans and Wilshire 1987b), and
- a variety of structural ceramics (Wilshire 1993b).

It will be noted from the above references that many of the papers were co-authored with collaborators from other laboratories. In addition, other workers, independent of the Swansea group, have utilized the θ Projection Concept. A selection of such studies includes

- four ferritic Cr-Mo-V steels (Maruyama and Oikawa 1987a),
- nickel-based superalloys (Li et al. 1987, Henderson and McLean 1984),
- low alloy steel (Shen and Plumtree 1990), and
- several high-temperature steels (Taylor et al. 1990, Li et al. 1990).

The further use of Eqn. (54) to extrapolate creep lifetimes (time, and strain to failure) will be discussed in Section 9.6, but first we pause to examine the relationship between the θ Projection Concept and the Deformation Mechanism Maps.

9.5 θ PROJECTION AND DEFORMATION MAPS

An inspection of Figure 10 shows that the stress dependence of the minimum creep rate follows a power law, with the stress exponent, n, varying with stress. We discussed the corresponding Norton law for steady-state creep in Section 4.3. Similar to the case of the secondary creep rate (Eqn. (10)), we can write

$$\dot{\varepsilon}_m = A\sigma^n \exp -Q_c/kT \tag{60}$$

In Figure 43, the plotted lines represent $\dot{\varepsilon}_m$ calculated from the θ parameters for copper. The data points (for a variety of temperatures) are measured from the actual creep curves, assuming that there exists a secondary stage, i.e., these are the "steady-state" creep rates, $\dot{\varepsilon}_s$. It can be seen that there is good agreement between the interpolated values of $\dot{\varepsilon}_m$ and the measured values of $\dot{\varepsilon}_s$, demonstrating (as expected) the equivalence between Eqn. (60) and Eqn. (10). At the higher stress levels, $n \approx 5$, in accordance with the climb mechanism represented by Eqn. (38) in Section 6.3.3. However, the n value decreases continually with decreasing stress, approaching $n = 1$, typifying the diffusional creep process, Section 6.2.

Using Eqn. (60), together with the θ data of Figure 40, the full range of Norton's n values can be plotted as in Figure 44, and range from n = 12 to 1 over the extrapolated stress field.

In a similar fashion, we can plot the full set of activation energies, Q_c in Eqn. (60). These are also shown in Figure 44.

Using the "rules" that correlate values of n and Q_c with the classical creep mechanisms in Section 6, we can superimpose the information in Figure 44 on the Deformation Mechanism Maps for copper shown in Figure 30 of Section 7. This is shown in Figure 45. It is evident that the predicted n = 1 contour separates the regions of dislocation power-law and diffusional creep. Similarly, the projected line for Q_c = 125 kJ/mol divides the map into the appropriate fields controlled by lattice self diffusion at high temperature and that controlled by preferential diffusion (grain-boundary or dislocation-core paths) at lower temperatures.

This is convincing demonstration of the consistent equivalency between the θ Projection Concept and the Deformation Mechanism Maps. However, it must be remembered that the two approaches (although complementary) are based on a fundamental difference of logic. The deformation maps are based on the concept of a true secondary creep region. In contrast, the θ Projection Concept focusses on the stress and temperature dependence of the characteristic shape of the entire creep curve. The fact that $\dot{\varepsilon}_m \approx \dot{\varepsilon}_s$ can be considered fortuitous, although it is a direct consequence of mechanistic viewpoint. Although this may seem a trivial point of graphical plotting perspective, there are deeper implications.

We have seen that the mechanistic base of the θ Projection Concept, Eqn. (8) is rooted in a consideration of creep deformation occurring via dislocation motion characterized by the work-hardening and recovery rates. The immediate question is why, then, does the projection of creep data based on the θ-parameter equation apparently enter the diffusional creep field, at lower stresses (outside the experimental database).

This apparent anomaly has encouraged the Swansea group to take a rather radical stance on mechanistic issues. First they reject the actuality of diffusional creep, in practical terms. They claim that even in stress-temperature regimes where n = 1, the governing mechanism is based on dislocations, not direct diffusion. They offer experimental support to their claims (Wilshire 1990). However, this contravention of extant understanding (and a holistic denial of published experimental evidence) is extreme and unnecessary (in this author's opinion). Indeed, personal discussion with Evans and Wilshire (R. Dutton, 1994, memorandum to J.L. Crosthwaite) has revealed some compromise on this position. Thus, an alternative (and preferred) viewpoint is as follows. From the inception of the deformation map concept, and entrenched in all mechanistic theory, it is always understood that all acceptable deformation mechanisms occur simultaneously. The fields of the mechanism maps represent, only, regions in the stress-temperature plane where an individual deformation mechanism is dominant. Therefore it is feasible (required, actually) that the θ parameters capture the concurrent existence of all relevant mechanisms. The variation of θ with stress and temperature reflects the moving contribution of all of these mechanisms. However, for this crucial information to be contained in the derived θ-parameters, it is vital to ensure that they are obtained from a data set that adequately samples the full expression of all of the deformation mechanisms. Thus, in the specific case of the container-shell material, particularly with long-term projection in mind, we must ensure that the range (particularly stress range) of our experimental database is sufficiently wide. This emphasizes the utility of combining the use of Deformation Mechanism Maps with the θ Projection Concept. The map

will force us to pay particular attention to extrapolation across mechanism field boundaries. The examples for steel and copper described above (and the referenced application to other materials, both metals and ceramics) clearly demonstrate that this is readily achieved in practice.

9.6 PROJECTION OF RUPTURE LIFETIMES

While Eqns. (54) and (59) appear to offer a highly satisfactory means of predicting creep curves, this type of analysis does not specifically refer to fracture. Hence, to complete the description of creep behaviour, it is necessary to define some suitable failure criterion. Although the mechanistic understanding of the precursors to fracture is in place (Section 6.4), the critical damage level at which final rupture occurs is ill-defined, as explained in Section 8. A convenient way of marking the termination of the creep curve (e.g., those shown in Figure 42) is to specify either the rupture time or the rupture strain. The Swansea group has recommended the limiting creep strain, or ductility, as the parameter more amenable to long-term projection. This choice is largely based on the observation that the creep ductility does not vary markedly with stress (Figure 46), whereas the creep life changes by several orders of magnitude over the same range of test conditions (Figure 47).

Figure 46 shows that the creep ductility, ε_f, decreases gradually with decreasing stress at each creep temperature. This suggests that the applicable relationship, equivalent to Eqn. (59), is

$$\epsilon_f = a + b\sigma + cT + d\sigma T \tag{61}$$

where the constants a, b, c and d can be evaluated by multilinear least squares regression analysis of the data shown in Figure 46. These values, for copper and steel are included in Table 2.

Having obtained the appropriate value for ε_f, the θ parameters can be used to estimate the time to rupture, t_r. This is the time taken for the accumulated creep strain to reach the total ductility, ε_f. For this purpose, the time (t') to reach some specified creep strain (ε') is obtained by solving (numerically) the equation

$$\theta_1(1 - e^{-\theta_2 t'}) + \theta_3(e^{\theta_4 t'} - 1) - \epsilon' = 0 \tag{62}$$

By setting $\varepsilon_f = \varepsilon'$, the rupture time is given at $t_r = t'$. Note also that the strain rate at any strain, ε', can be obtained simply by substituting t' into Eqn. (56).

Using the strain to failure criterion, a variety of creep-curve equations have been compared to assess their capability of predicting the rupture time (Brown 1987). The polynomial equations described in Section 4.2 were included. It was demonstrated that the θ Projection Concept provided the most accurate prediction.

It is expected that there will be relatively little error in the projection of rupture life, even if the material ductility does change unexpectedly at low-stress levels. Thus, in low stress tests, the creep curves are typically dominated by the tertiary process, defined by θ_3 and θ_4. The

strain/time behaviour may then be considered simply in terms of a gradually increasing creep rate throughout virtually the entire life. In the late stages of the tertiary process, the creep rate is accelerating very rapidly. As a consequence, even a substantial change in ductility should cause only a relatively small variation in rupture life under these conditions.

Using the coefficients in Table 2, the predicted stress-rupture curves for the 0.5Cr-0.5Mo-0.25V steel are shown in Figure 47. It is important to note that the experimental data used for the creep-curve analysis were from tests lasting less than 1200 h. Despite the short-term nature of these data, Figure 47 shows that the predictions are accurate for times in excess of 100,000 h, as confirmed by the long-term stress-rupture data (Johnson et al. 1967) included in the graph. Furthermore, the θ Projection Concept can be used to test the Monkman-Grant relationship. The relevant plot is shown in Figure 48, where again, the theoretical predictions are in excellent agreement with the experimental data. Although the extrapolated lines show appreciable curvature (reflecting the pronounced curvature of Figure 10), they are reasonably linear over quite extended times, and the plots obtained at different temperatures superimpose reasonably well.

Although the results described above on the 0.5Cr-0.5Mo-0.25V steel are impressive, the Swansea group did not consider them to be a definitive test of the θ Projection Concept because the creep tests (to obtain the θ parameters) were performed on a different batch of material to that used to measure the creep-rupture lives. In fact, the creep-rupture data (Johnson et al. 1967) were obtained from multi-laboratory testing (e.g., such as those shown in Figure 17), hence the relatively large scatter band (up to ± 20% in stress) indicated in Figure 47. Thus, even rather poor predictions may well have fitted within such broad scatter bands. To avoid this shortcoming, a large ongoing collaborative study (Swansea University, GEC, Babcocks Energy, National Power, Power Gen and Nuclear Electric) was undertaken on a 1Cr-Mo-V rotor steel. The initial results have been published (Evans et al. 1993c, Wilshire and Evans 1994), and are shown in Figure 49. The short-term data (up to about 1000 h), shown as open symbols, were used to extrapolate the times to rupture. These extrapolations are seen to be in excellent agreement with the long-term rupture data (full symbols). This comparison was conducted with a "double blind" protocol in place, to avoid any bias in the analysis. Note that the short-term creep tests were performed under constant-stress conditions and the long-term tests under constant-load conditions. Using the θ Projection Concept, it is relatively easy to produce predictive plots for either loading mode. It is instructive to observe the better agreement of the long-term experimental data with the appropriate constant-load prediction, a graphic illustration of the power and accuracy of the derived θ parameters.

Figures 47, 48 and 49 provide a convincing demonstration of the applicability of the θ Projection Concept to rupture times and creep ductility. It is clear that long-term rupture lives can be estimated from short-term measurements of creep behaviour. However, care should be taken in using the methodology to extrapolate outside the temperature range of the experimental data. This is due to the fact that although Eqn. (58) has a sound theoretical foundation (e.g., the activation energies of the rate parameters θ_2 and θ_4 are related directly to their controlling mechanisms), Eqns. (59) and (61) are essentially empirical (i.e., their coefficients have no mechanistic significance). In this regard, additional guidance can be obtained from the Deformation Mechanism Maps, and to a lesser extent, the Fracture Mechanism Maps.

10. CONCLUDING REMARKS

10.1 GENERAL COMMENTS

We have seen that the constitutive equation embedded in the θ Projection Concept is specifically formulated to capture the phenomenological shape of the entire creep curve. This axiomatic principle has immediate appeal. Through its representation of the complete creep behaviour, it facilitates the precise calculation of creep strain, deformation rates and times to failure. As the mathematical formulation is based on established mechanistic understanding, it lends confidence to long-term extrapolation outside of the experimental database. Whereas the classical approach is generally based on the concept of a single-valued steady-state creep rate, expressed as a function of stress and temperature, the θ Projection Concept employs four rate constants to represent the stress and temperature dependence of the complete creep-curve shape. Combined with a simple fracture criterion, this facilitates the computation of rupture life at any stress or temperature. The accuracy of this predictive capability has been well demonstrated. In their latest paper (Wilshire and Evans 1994), the Swansea group has shown that the predicted behavioural pattern determined from tests lasting up to 1000 h correlated extremely well with the independently measured long-term data for conditions that would have resulted in creep lives well in excess of 100,000 h. It is significant to note that this impressive projection was made for a 0.5Cr-0.5Mo-0.25V steel, which is known to exhibit marked changes in carbide precipitate dispersion during prolonged creep exposure. The θ-relationships are obviously capable of quantifying the complex long-term effects associated with such progressive changes in microstructure. Because of the simple single-phase composition of the relatively pure titanium and copper intended for the fuel waste container, these microstructural changes will not occur. Therefore, it is reasonable to expect that even longer-term extrapolations (up to ~5,000,000 h) for these materials will be reliable. A conservative fracture criterion will serve to provide added confidence. The level of confidence can be estimated from a statistical analysis of the θ-parameters. A formal procedure for accomplishing this has been published (Evans 1989, 1990).

Since its introduction in 1982, the θ Projection Concept has found international acceptance in the scientific and engineering communities. Thus, as shown in Section 9.4, the methodology has been applied to a wide range of materials, including pure metals, steels, superalloys and ceramics. The Swansea group has, naturally, spearheaded this effort. They have been successful in attracting substantial external financial support which has enabled them to develop a large and sophisticated creep laboratory, with over 50 modern creep machines and supporting equipment (Dutton 1994). As a result, extensive collaborative and contractual research is being conducted with major companies including Nuclear Electric, GEC, Babcocks Energy, National Power, Power Gen, Rolls Royce, Pratt and Whitney, etc. Whereas much of this work is published in the open literature, a large fraction of the data are protected by proprietary interests. Other European, North American and Japanese laboratories are also adopting the same approach. In some instances, the commercial interest is in data interpolation. An example would be in high-temperature gas turbine blades. The challenge is to predict creep strains and creep lives with great precision, and in a format suitable for complex finite element analysis. In this case, creep testing spans the actual operating temperatures, stresses, and the expected component lifetimes. In contrast, an emphasis on extrapolation of the creep data to longer service lifetimes is the focus of studies on high-temperature steam generating components used in thermal power plants. This widespread adoption of the θ Projection Concept reflects substantial endorsement of the technique as a

practical solution to a long-standing problem. Such interest and effort ensures the ongoing refinement and extension of the methodology.

The fact that the θ Projection Concept casts some doubt on the reality of a period of constant creep rate during the secondary stage, does not imply that we should discard the extensive body of literature dealing with steady-state creep mechanisms. A useful starting point to examine this issue is to revisit the role of the work-hardening rate (h) and the recovery rate (r), discussed in Section 6.3.1. Thus, Eqn. (29) can be rewitten as

$$\dot{\epsilon} = \left(\frac{\partial \epsilon}{\partial t}\right)_{\sigma} = -\left(\frac{\partial \sigma}{\partial t}\right)_{\epsilon} \Big/ \left(\frac{\partial \sigma}{\partial \epsilon}\right)_{t} = \frac{r}{h} \tag{63}$$

It has been pointed out by Davies and Stevens (1993) that Eqn. (63) should apply throughout the creep curve, not just in the steady-state region.[9] Primary and tertiary creep then arises because the values of r and h vary with time, or strain. Differentiation with respect to time gives

$$\frac{\partial \dot{\epsilon}}{\partial t} = \ddot{\epsilon} = \frac{h\dot{r} - r\dot{h}}{h^2} \tag{64}$$

where

$$\dot{r} = \left(\frac{\partial}{\partial t}\right)_{\sigma}\left(\frac{\partial \sigma}{\partial t}\right)_{\epsilon} \quad \textit{and} \quad \dot{h} = \left(\frac{\partial}{\partial t}\right)_{\sigma}\left(\frac{\partial \sigma}{\partial \epsilon}\right)_{t}$$

and since h > 0 for plastic stability, then during primary creep we have

$$\ddot{\epsilon} < 0 \qquad \frac{\dot{r}}{r} < \frac{\dot{h}}{h} \tag{65}$$

while during tertiary creep

$$\ddot{\epsilon} > 0 \qquad \frac{\dot{r}}{r} > \frac{\dot{h}}{h} \tag{66}$$

The condition prevailing in secondary creep is represented by

$$\frac{\dot{r}}{r} = \frac{\dot{h}}{h} \tag{67}$$

---

[9] In the context of Section 6.3.1, the rate of hardening is always balanced by the rate of recovery such that $d\sigma = 0$ applies throughout the creep curve. This is a necessary condition because under creep conditions, the flow stress is always equal to the applied stress.

This equality can be accomplished in two ways. The first is that Eqn. (67) is equal to zero. This would represent the fact that a state of constant structure exists, e.g., that the dislocation density is constant, leading to a finite period of constant creep, i.e., an extended steady-state secondary stage. The second possibility is that Eqn. (67) is not equal to zero. This would correspond to the situation where no steady-state creep exists, but rather the secondary creep is only a point of inflection. Such a minimum creep rate is the situation proposed within the θ Projection Concept. In actuality, within a dynamic system of interacting mechanisms, it would be fortuitous to expect the existence of an extended time period over which the microstructure (including the dislocation density) remains precisely constant. Regardless of whether Eqn. (67) is equal to zero, or not,[10] this analysis highlights the role of the evolving microstructure in determining the values of r and h, and their variation with time (or strain). This is the essence of the derivation of the primary creep mechanism described in Section 6.3.2. Within the theories of steady-state creep, the parameters characterizing the microstructure are generally contained in a preexponential constant. This is the constant A in the general creep equation (Eqn. (10)), the constant B in the generic dislocation-creep equation (Eqn. (34)), and the constant A in the specific creep equation based on dislocation climb (Eqn. (38)). Thus, the existence of a constant creep rate in the steady-state mechanisms discussed in Section 6 is contingent on the constancy of the preexponential structural parameter. This does not refute the reality, or application, of the established creep mechanisms, and their attendant rate equations. Indeed, we note that the values of the preexponential constants are evaluated directly from experimental creep-rate data, using the assumption that a steady state exists (within the limitation of current theoretical understanding, there is no a prior method to calculate the preexponential constant). Accordingly, to the extent that this represents a reasonable representation of experimental data, while retaining the essential mechanistic understanding, the Deformation Mechanism Maps described in Section 7 are valid and representational. Indeed, there has been no claim that the Maps capture the total creep behaviour, including primary and tertiary creep. This limitation is understood.

Within this framework, we are justified in using the mechanistic equations and the Deformation Mechanism Maps as a guide to interpretation and extrapolation. Thus, the Maps can be used to identify the prominent mechanism that prevails within prescribed boundaries of stress and temperature. Furthermore, the mechanistic equations will provide reasonable estimates of the characteristic creep rate. Accordingly, it is reasonable to use Figures 29 and 30 to determine that, at the maximum operating temperature (100°C) of the fuel-waste container, deformation at high stresses will occur by power-law creep and at lower stresses, by diffusional creep. In both instances, the creep rate will be controlled by diffusion along easy paths, such as grain boundaries or dislocations. Creep rates of 10^{-11} sec^{-1}, or less, are to be expected. Of course, these statements do not exclude the possibility that alternative mechanisms exist, and have not been identified on the Maps. In this context, we must bear in mind that there is a dearth of experimental data available within the extreme left-hand portion of the Maps. One of the objectives of our experimental creep program will be to provide some of these data. An analysis of the temperature and stress dependence of the θ-parameters will enable these mechanisms to be identified. For example, the work of Zeyfang et al. (1971) indicates that the creep rate of titanium at ~80°C is controlled by dislocations overcoming interstitial solute barriers in a (unspecified) thermally activated fashion. It is interesting to note that their data

---

[10] Davies and Stevens present some experimental evidence supporting the conclusion that $\dot{r}/r = \dot{h}/h = 0$ and hence it is "probable" that a secondary stage truly exists, at variance with the θ Projection Concept. However, they point out that this conclusion is "subject to some experimental uncertainty".

show that the change in strain rate during primary creep was proportional to the strain, i.e., that it followed the first-order rate kinetics predicted by the θ Projection Concept. However, the creep rates examined were quite high, ~10^{-4} sec^{-1}. This would place (quite appropriately) the mechanism within the obstacle-controlled plasticity region of the Deformation Map in Figure 29. It will be important to establish, for our material, the stress level that defines the lower boundary of this deformation field. At this juncture, it is important to emphasize that the θ Projection Concept makes no assumption regarding the precise deformation micromechanism that controls the creep rate. Thus, the rate equation developed in Section 6.3.2, on which the formulation of primary creep (i.e., θ_1 and θ_2) is based, is generic in nature. It is only necessary to assume that deformation occurs when thermally activated events manage to overcome internal activation barriers, and that when such events occur, they are governed by Boltzmann statistics. If the activation barriers are allowed to have strengths that can increase by work hardening, or decrease by recovery processes, the general form of primary creep behaviour can be derived, and the kinetics obey first-order rate theory. In a similar manner, the representation of the tertiary region, through the θ_3 and θ_4 parameters, is based on the assumption that damage mechanisms are becoming prominent. Furthermore, the rate of damage accumulation is linked to the deformation rate (and hence the work-hardening and recovery rates), as explained in Sections 4.3 and 9.2, and obeys first-order rate kinetics.

The θ Projection approach is not unique in its use of the mechanistic understanding of creep mechanisms to develop a constitutive equation describing the complete creep curve. Thus, Chandler (1990) has modified the steady-state deformation equations from the Deformation Mechanism Maps to describe primary creep. This was achieved by replacing the applied stress by a driving stress that is progressively reduced in strength by a work-hardening term that is essentially introduced as a microstructural factor within the preexponential parameter. Similarly, the equations derived from the Fracture Mechanism Maps are added to introduce the accelerating tertiary stage. A similar procedure is used by Dyson and McLean (1990), as discussed further below. A hybrid approach was used by Shen and Plumtree (1990). They used the standard θ-equation to describe the primary stage, but a modified formulation to describe the tertiary stage. In this case, a damage accumulation parameter was used to represent a continual increase in the effective stress due to a progressive loss of load-bearing area. Such an approach is parallel to that of Kachanov (1958) and Rabotnov (1969), discussed in Section 4.3. The resulting equation gives a better fit to tertiary creep that exhibits a rapid acceleration of creep rate, a phenomenon described in Section 10.3. However, similar to the form of Eqn. (17), the rupture time enters the equation as an essential parameter, hence somewhat defeating the objective of predicting the lifetime.

Of the alternative analytical approaches mentioned above, that of Dyson and McLean (1990) warrants further discussion. This work represents the development of a creep analysis methodology by the National Physics Laboratory (NPL) in the UK. Their constitutive equations are based on strain <u>rate</u> expressions (rather than strains as in the θ Projection Concept), the creep curve then being obtained via numerical integration. Despite this difference, the NPL group also consider the shape of the creep curve to be determined by the decreasing creep rate of the primary stage being superseded by an accelerated tertiary stage, leading to fracture. Similar to the θ Projection Concept, four parameters are used to capture this overall process. These include parameters that represent the strain hardening and recovery processes. Most of the creep modelling emphasis is placed on those recovery, or "softening", processes that characterize the tertiary creep stage. Within the mathematical formulation, the creep damage parameter of Kachanov (1958) and Rabotnov (1969) is used. Depending on

the material, a wide range of damage mechanisms can be included in the tertiary softening process. These have been classified by Dyson (1992) and include cavity growth, microstructural instability and corrosion processes. Based on these considerations, NPL has developed a software package called CRISPEN (Dyson and McLean 1990) to extract the four constitutive parameters from experimental creep data, integrate the rate equations to obtain the creep curves, and facilitate predictive extrapolation. More complex conditions, such as those involving multiaxial stress states can be handled by the more sophisticated numerical integration schemes contained in the CREEPSIM software package (Osgerby et al. 1992).

The NPL group have used their methodology to analyze the creep behaviour of high-strength steels (Dyson and Osgerby 1993, Osgerby and Dyson 1994a) and nickel-based superalloys (McLean et al. 1992). The creep curves of all of these materials are dominated by tertiary creep, most of which is characterized by softening due to precipitate coarsening. Using the CREEPSIM software, the creep data have been used to predict stress-strain (Osgerby and Dyson 1993) and stress relaxation (Osgerby and Dyson 1994b) behaviour. Within all of these applications, the NPL group has not demonstrated the capability of their methodology to perform long-term projection of creep data, equivalent to that of the θ Projection Concept, as described in Section 9.6. In fact, based on the fact that both methods use four parameters to describe similar strain hardening and softening phenomenon, Dyson and McLean (1990) acknowledge the equivalence of the two approaches, but claim an advantage of using CREEPSIM for more complex multiaxial bonding conditions.

10.2 DATA ANALYSIS AND PERFORMANCE PROJECTION

As mentioned earlier, a program of creep testing of titanium has been initiated at the Whiteshell Laboratories. At the time of writing, one of these tests, conducted at 100°C and 187 MPa, has proceeded to failure after a total lifetime of about 24,000 h. The creep curve is shown in Figure 50. This confirms that at this temperature considerable creep strain (>0.2) occurs in titanium and the classical three-stage behaviour is evident. Most of the creep life is composed of primary creep, with a rather abrupt onset of the tertiary stage: a definitive secondary stage is not apparent. There will be more detailed discussion of this and other current creep data in a future report.

The creep data, such as those shown in Figure 50, will be subsequently analyzed using the θ Projection Concept. This will be facilitated by employing a commercial computer software package, the "Theta Projection Analysis Suite", acquired from Swansea University. This package consists of a suite of 19 computer programs (including a comprehensive user manual), which is designed to accomplish tasks such as:

- edit the experimental data,
- plot the experimental creep curves,
- fit the theoretical θ-parameter creep curves,
- extract the θ parameters,
- statistical analysis of the parameters,
- determine stress and temperature dependence of parameters, and
- predict long-term creep strains, rates and rupture times.

These capabilities are precisely those needed to analyze our experimental creep data, provide a constitutive equation suitable for the finite element code we are developing, and extrapolate the creep behaviour characteristics over the lifetime of the container. The software suite is

being used by a significant number of other researchers, and hence is well tested and has found general acceptance in the scientific/engineering community.

Since the θ Projection Concept, supported by the software package, allows any creep-strain or creep-rate parameter to be calculated in a highly computer-efficient manner, it is ideally suited to engineering design and assessment. In many circumstances, the thermal and mechanical conditions vary in some structural components during operation: the prevailing conditions often change with time. With the computer-based finite element methods, procedures must be developed for handling changes in stress and temperature during service.

If the operating conditions change from $\sigma_1 T_1$ to $\sigma_2 T_2$, there is no practical difficulty in computing the θ values at $\sigma_2 T_2$, and hence in constructing the new creep curve. However, it is not immediately apparent how the new creep rate is to be calculated from the new curve. The problem is illustrated in Figure 51 where two schematic creep curves are shown for the conditions $\sigma_1 T_1$ and $\sigma_2 T_2$. It is possible to proceed from the first curve to the second along many alternative paths, the extreme cases being referred to as time-hardening (A) and strain-hardening (B). In many circumstances, studies of the effects of changes in stress and temperature have shown that the strain-hardening path is very nearly correct and a simple constitutive relationship can be constructed on this basis (Evans and Wilshire 1987, Wilshire 1989). Thus, if a strain ε_1 has been attained at $\sigma_1 T_1$, then the corresponding θ-values are (from Eqn. 59) θ_i such that

$$\log \theta_i = f(\sigma_1 T_1) \tag{68}$$

and (see Eqn. (56))

$$\dot{\epsilon}_1 = \theta_1\theta_2 \exp(-\theta_2 t^*) + \theta_3\theta_4 \exp(\theta_4 t^*) \tag{69}$$

where, from Eqn. (62), t^* is the root of

$$\theta_1(1 - e^{-\theta_2 t}) + \theta_3(e^{\theta_4 t} - 1) - \epsilon_1 = 0 \tag{70}$$

When the operating conditions are changed to $\sigma_2 T_2$, the new creep rate $\dot{\varepsilon}_2$ will be given by

$$\dot{\epsilon}_2 = \theta_1'\theta_2' \exp(-\theta_2' t') + \theta_3'\theta_4' \exp(\theta_4' t') \tag{71}$$

where $\log \theta_i' = h(\sigma_2 T_2)$ and t' is the root of

$$\theta_1'(1 - e^{-\theta_2' t}) + \theta_3'(e^{\theta_4' t} - 1) - \epsilon_1 = 0 \tag{72}$$

In this way, the θ Projection Concept provides the complete constitutive relationship for the material, which is required to be able to apply the computer-based analysis to conditions of various stresses and temperatures. This method was used (Evans et al. 1993c) to convert constant-stress creep data into constant-load creep-rupture data, as shown in Figure 49. Similar examples are presented by Taylor et al. (1990). The technique has also been used successfully in the design of, and service lifetime calculations for superalloy turbine blades (Evans and Wilshire 1987).

In Section 3.1, it was pointed out that for the packed-particulate container to be used for storing fuel waste, the deformation rate of the container shell may be controlled by the creep rate of the particulate. An understanding of material behaviour (such as the container shell) under conditions of constant strain rate is frequently required for the design of components subjected to creep deformation. However, the experimental acquisition of such constant strain-rate data is expensive compared to the procurement of creep data, because of the more sophisticated test equipment required. Fortunately, methods have been developed to predict constant strain-rate behaviour from creep data. A recent example comes from the work of Osgerby and Dyson (1993). The methodology uses the fact that the total strain rate, $\dot{\varepsilon}_T$, under changing stress conditions is given by

$$\dot{\epsilon}_T = \frac{\dot{\sigma}}{E} + \dot{\epsilon} \tag{73}$$

where E is the elastic modulus. The rate of change of stress under constant strain-rate conditions, $\dot{\varepsilon}_T = K$ is then given by

$$\dot{\sigma} = E\,(K - \dot{\epsilon}) \tag{74}$$

By numerically integrating the constitutive equation for $\dot{\varepsilon}$, under the constraint imposed by Eqn. (74), the stress-strain curve appropriate to the constant strain rate K is obtained. Osgerby and Dyson did not employ the θ Projection equation. However, they used the constitutive equation developed at NPL (see Section 10.1), which is similar to the θ Projection Concept. An example creep curve for the Nimonic 101 alloy is shown in Figure 52, with the fit to their constitutive equation. Such creep data was then used to construct the stress-strain curve shown in Figure 53. Also shown on this figure is an actual experimental plot of a constant strain-rate test. As can be seen, there is good agreement between the experimental data and the behaviour predicted from the model that utilized the constant-load creep data. The model can be used to predict the stress-strain curve for any given constant strain rate. Figure 53 shows the stress rising initially to a peak value, corresponding to the hardening-dominated primary creep behaviour. Then, as the softening processes accompanying tertiary creep become more dominant, the stress decays monotonically. A similar procedure can be carried out using the θ-equation.

The above examples demonstrate the capability and flexibility of the θ Projection Concept in analyzing and predicting creep strains and creep rates. As has already been discussed, to be in a position to project creep-rupture times, there is a need to specify a fracture criterion. This is the topic of the next section.

10.3 FRACTURE CRITERION

The discussion of fracture mechanisms in Section 6.4 and Fracture Mechanism Maps in Section 8 pointed out that the micromechanisms responsible for fracture can be varied and complex. Consequently, the form of the tertiary stage cannot be defined with the same precision as that of the primary stage, reflecting the generally poorer qualitative understanding of rupture processes and their coupling with tertiary deformation. The θ Projection Concept assumes that the rate-controlling process follows first-order kinetics. However, for example, Figure 24 shows that if gross necking is prevalent, first-order kinetics does not apply, the acceleration of the creep rate proceeding in a more rapid fashion. This effect is illustrated by the creep curve for titanium, shown in Figure 50. Thus, compared with the creep curve for steel shown in Figure 39, the later stage of tertiary creep in titanium accelerates much faster, due to the early onset of necking. These inherent uncertainties can cause some error in the prediction of times to rupture based on the derivation of the θ_3 and θ_4 parameters from the experimental data. In particular, it is the rate constant θ_4 that loses its capability of fitting the complete tertiary stage when the apparent creep rate increases rapidly under the rising stress conditions in the necked region. These deficiencies have been addressed by several workers.

In a study of four ferritic steels, Maruyama and Oikawa (1987a) used the θ Projection Concept to identify the nature of the creep mechanisms. The later stages of tertiary creep deviate from the θ-equation, because of gross necking instability. This deficiency was solved by truncating the experimental data before fitting the θ-equation. Not only did this improve the fit with the tertiary stage, but also improved the fit in the earlier primary stage. To avoid arbitrariness in the truncation, the values of θ_2 and θ_4 were calculated over a range of cut-off strains. The strain at which $\theta_2 = \theta_4$ was chosen as a standard criterion (Maruyama and Oikawa 1987b). Such a constitutive equation that equates θ_2 and θ_4 has been criticized by Brown et al. (1986b), who revealed several analytical inadequacies. This procedure was also found to be inapplicable for a nickel-based superalloy (Li et al. 1987). The values of θ_1, θ_2, θ_3 and θ_4 become constant above a specific cut-off strain. This characteristic, together with an examination of the standard error of fitting, was used for the truncation criterion.

The utilization of the truncation strategy has also been used for the projection of creep properties and times to rupture for steels (Taylor et al. 1990, Li et al. 1990). Again, it was observed that in the absence of truncation, the θ_3 and θ_4 parameters were so scattered that their predictive capability was poor. The situation was significantly improved by truncating the creep curves to eliminate the period of gross necking. An investigation of the sensitivity of the calculated θ values to the level of truncation showed that provided the final stage of the creep curves was removed, the results were not significantly affected by the cut-off point. A standard truncation criterion of the strain at seven times the minimum creep rate was established, and was found to be successful in offering accurate predictability.

The problem of the shape of the tertiary creep stage being disturbed by necking has been recognized by the Swansea group. To overcome this difficulty, their θ Projection software suite includes a data truncation criterion based on the onset of rapid creep-rate acceleration. In addition, they have prepared (Evans and Wilshire 1993) a modified form of the θ Projection equation for a material that displays little or no tertiary creep, as depicted in Figure 54. Such behaviour is related to the necking phenomenon, but in this case the instability is a result of an intolerance to tertiary damage. For example, in an exceedingly brittle material (a ceramic would be a primary case) internal damage is likely to result in the formation of a microcrack that propagates very rapidly, in an unstable manner. This causes premature termination of

the primary creep stage so that little tertiary stage is discernable. To accurately describe such a creep curve, Eqn. (54) must be modified by expanding the tertiary exponential term by means of its Taylor series so that

$$\epsilon = \theta_1(1 - e^{-\theta_2 t}) + \theta_3\theta_4 t \tag{75}$$

This equation is identical to that of Garafalo et al. (1963), shown as Eqn. (7) in Section 4.2. It consists of a primary stage that enters a steady-state secondary stage. Such an equation has been successfully used to analyze the creep behaviour of ceramics (Wilshire 1993b).

In Section 9.6, we saw how the θ Projection Concept employs a fracture criterion based on the total strain to rupture following the ultimate termination of tertiary creep. The rupture time, which is the primary engineering parameter used to predict the useful lifetime of a component, is obtained by using the θ-based deformation equation to compute the time required to reach the rupture strain. However, we have seen from the discussion presented above that in many cases there is reduced confidence in the capability of the θ_3 and θ_4 parameters to predict the total shape of the complete tertiary stage. This uncertainty is associated with the complexity and coexistence of multiple damage processes leading to fracture. In addition, the precise quantitative understanding of the detailed micromechanisms of intergranular cavity and crack formation is imperfectly understood. In many practical instances, these shortcomings are offset by the fact that the errors of prediction are not significant. This fortunate circumstance arises because in a condition of rapid acceleration of the creep rate, an uncertainty in the rupture strain does not have a large effect on the calculated rupture time. Notwithstanding the general validity of this conclusion, we think it prudent to employ a more conservative fracture criterion into the design of the fuel waste container. We don't wish to operate the container under extended periods of tertiary creep, particularly recognizing that at the relatively low operating temperatures, premature instability due to the necking phenomenon is a likely scenario. Recognizing that we will forfeit available lifetime, we will adopt a fracture criterion where the maximum allowable design strain is less than the actual rupture strain. A considerable safety margin would be secured by setting this limiting strain to that which exists at the onset of tertiary creep, i.e., the strain to reach the minimum creep rate. The θ-based equation is ideally suited to the determination of this condition. Thus, the lifetime would then be defined by the employment of Eqn. (57). However, our experimental program, and the θ Projection equation that arises may show that the majority of the long-term creep curve is actually dominated by the tertiary stage. In this case, the onset of tertiary creep may represent a criterion that is unsatisfactorily limiting, excessively conservative. Under such circumstances, a more suitable, yet acceptible criterion may be set by choosing a creep strain where the creep rate has increased to some modest level, e.g., three times the minimum creep rate[11]. In this context, we may recall the truncation criterion of Taylor et al. (1990) and Li et al. (1990) of seven times the minimum creep rate, as described above. The eventual decision on the precise value of the multiplying factor can be made after we have completed our experimental creep program and formulated our appropriate θ-equation. Whatever

---

[11] This criterion strictly applies to creep conditions, where the prevailing stress is less than the yield-stress. As discussed in Section 2.3, it is possible that small-scale plastic deformation may initially occur in localized areas where the yield-stress is exceeded. Under these rapid strain-rate conditions, the appropriate maximum strain criterion is obtained from short-term tensile tests, as described by Teper (1988).

criterion we ultimately set, the θ Projection Concept, supported by the complementary Deformation Mechanism Map, provides an immediate tool to compute the container lifetime. In addition, the Fracture Mechanism Map will provide a comparative estimate of rupture time, from which we can extract a supplementary evaluation of the safety factor.

ACKNOWLEDGEMENTS

This document was prepared in support of the Canadian Nuclear Fuel Waste Management Program, which is funded jointly by AECL and Ontario Hydro under the auspices of the CANDU Owners Group.

The author would like to thank Drs. B. Wilshire and R.W. Evans of Swansea University, and Drs. R.N. Stevens and C.K.L. Davies of the University of London for extensive and penetrating discussions on the θ Projection Concept and Deformation Mechanism Maps. While these researchers offered valuable insight into these methodologies, the author is solely responsible for any nuances of interpretation that might deviate from their viewpoint. Within this spirit, the carefull review of the manuscript, and the useful comments provided by my colleagues, J.L. Crosthwaite, B.W. Leitch and B. Teper, are gratefully acknowledged.

REFERENCES

Adenstedt, H. 1949. Creep of titanium at room temperatures. Metal Progress 56, 658-660.

Andrade, E.N. da C. 1910. The viscous flow in metals, and allied phenomena. University College, London. Proceedings of the Royal Society, London (A) 84, 1-12.

AECL (Atomic Energy of Canada Limited). 1994. Environmental impact statement on the concept for disposal of Canada's nuclear fuel waste. Atomic Energy of Canada Limited Report, AECL-10711, COG-93-1. Available in English and French.

Ashby, M.F. 1972. A first report on deformation-mechanism maps. Acta Metallurgica 20, 887-897.

Ashby, M.F., C. Gandhi and D.M.R. Taplin. 1979. Fracture-mechanism maps and their construction for F.C.C. metals and alloys. Acta Metallurgica 27, 699-729.

Bailey, R.W. 1926. Note on the softening of strain-hardened metals and its relation to creep. Engineering 121, 351-352.

Balluffi, R.W. and L. Siegle. 1955. Effect of grain boundaries upon formation and dimensional changes during diffusion. Acta Metallurgica 3, 170-177.

Beere, W. and M.V. Speight. 1978. Creep cavitation by vacancy diffusion in plastically deforming solid. Metal Science Journal 12, 172-176.

Brown, S.G.R. 1987. Extrapolation by creep-curve shape analysis. In Creep and Fracture of Engineering Materials and Structures (B. Wilshire and R.W. Evans, editors), Proceedings of the Third International Conference, University College, Swansea, 1987, 829-838.

Brown, S.G.R., R.W. Evans and B. Wilshire. 1986a. Creep strain and creep life prediction for cast nickel-based superalloy IN-100. Materials Science and Engineering 84, 147-156.

Brown, S.G.R., R.W. Evans and B. Wilshire. 1986b. Exponential descriptions of normal creep curves. Scripta Metallurgica 20, 855-860.

Brown, S.G.R., R.W. Evans and B. Wilshire. 1987. New approach to creep of pure metals with special reference to polycrystalline copper. Materials Science and Technology 3, 23-27.

Cane, B.J. and P.F. Aplin. 1994. Creep life assessment methods. The Journal of Strain Analysis 29, 225-232.

Carpenter, G.J.C. 1971. Diffusion coefficient as a guide to prospects for high temperature zirconium alloys. Atomic Energy of Canada Limited Report, AECL-3967.

Chandler, H.D. 1990. Creep-curve descriptions in terms of deformation and damage accumulation mechanisms. In Creep and Fracture of Engineering Materials and Structures (B. Wilshire and R.W. Evans, editors), Proceedings of the Fourth International Conference, Swansea, 1990, 975-984.

Coble, R.L. 1963. A model for boundary diffusion controlled creep in polycrystalline materials. Journal of Applied Physics 34, 1679-1682.

Cocks, A.C.F. and M.F. Ashby. 1982. On creep fracture by void growth. Progress in Materials Science 27, 189-244.

Conrad, H. 1981. Effect of interstitial solutes on the strength and ductility of titanium. Progress in Materials Science 26, 123-403.

Conway, J.B. 1967. Numerical Methods for Creep and Rupture Analyses. Gordon and Breach Science Publishers, Incorporated, Newark, N.J.

Crosthwaite, J.L. 1994. The performance, assessment and ranking of container design options for the Canadian Nuclear Fuel Waste Management Program. Atomic Energy of Canada Limited Technical Record, TR-500, COG-93-410.

Crosthwaite, J.L., J.N. Barrie and K. Nuttall. 1982. Design, fabrication and testing of a prototype stressed-shell fuel isolation container. Atomic Energy of Canada Limited Report, AECL-6823.

Davies, C.K.L. and R.N. Stevens. 1993. Constant steady-state creep in a Cu-9 atomic % Al alloy? In Creep and Fracture of Engineering Materials and Structures (B. Wilshire and R.W. Evans, editors), Proceedings of the Fifth International Conference, Swansea, 1993, 31-40.

Davies, P.W., W.J. Evans, K.R. Williams and B. Wilshire. 1969. An equation to represent strain/time relationships during high temperature creep. Scripta Metallurgica 3, 671-674.

de Lacombe, J. 1939. Method for expressing creep curves. Revue de Metallurgie 36, 178-188.

Dutton, R. 1969. A survey of compression creep testing of metals. Materials Research and Standards 9, 11-17.

Dyson, B.F. 1976. Constraints on diffusional cavity growth rates. Metal Science Journal 10, 349-353.

Dyson, B.F. 1992. Materials data requirements, creep damage mechanisms, and predictive models. In High Temperature Structural Design (L.H. Larson, editor). Mechanical Engineering Publications, London, 335-354.

Dyson, B.F. and M. McLean. 1990. Creep deformation of engineering alloys - developments from physical modelling. Iron and Steel Institute of Japan International 30, 802-811.

Dyson, B.F. and S. Osgerby. 1993. Modelling and analysis of creep deformation and fracture in a 1 Cr ½ Mo ferritic steel. National Physics Laboratory Report, DMM(A)116.

Evans, H.E. 1973. A model of strain hardening during high-temperature creep. Philosophical Magazine 28, 227-230.

Evans, H.E. 1984. Mechanisms of Creep Fracture. Elsevier Applied Science Publishers, London.

Evans, R.W. 1989. Statistical scatter and variability of creep property estimates in theta projection method. Materials Science and Technology 5, 699-707.

Evans, R.W. 1990. Statistics of creep property estimation. In Creep and Fracture of Engineering Materials and Structures (B. Wilshire and R.W. Evans, editors), Proceedings of the Fourth International Conference, Swansea, 1990, 1017-1028.

Evans, R.W. and B. Wilshire. 1981. The role of grain-boundary cavities during tertiary creep. In Creep and Fracture of Engineering Materials and Structures (B. Wilshire and D.R.J. Owen, editors), Proceedings of the International Conference, Swansea, 1981, 303-314.

Evans, R.W. and B. Wilshire. 1985. Creep of Metals and Alloys. The Institute of Materials, London. Ashgate Publishing Company, Brookfield, VT.

Evans, R.W. and B. Wilshire. 1987a. Power-law creep of polycrystalline copper. In Creep and Fracture of Engineering Materials and Structures (B. Wilshire and R.W. Evans, editors), Proceedings of the Third International Conference, Swansea, 1987, 59-70.

Evans, R.W. and B. Wilshire, 1987b. Creep behaviour of superalloy blade materials. Materials Science and Technology 3, 701-705.

Evans, R.W. and B. Wilshire. 1993. Introduction to Creep. The Institute of Materials, London. Ashgate Publishing Company, Brookfield, VT.

Evans, R.W., I. Beden and B. Wilshire. 1984. Creep life prediction for ½Cr½Mo¼V ferritic steel. In Creep and Fracture of Engineering Materials and Structures (B. Wilshire and D.R.J. Owen, editors), Proceedings of the Second International Conference, Swansea 1984, 1277-1290.

Evans, R.W., A.A. Fadlalla and B. Wilshire. 1990. Prediction of long-term creep rupture properties for an aluminum alloy for airframe application. In Creep and Fracture of Engineering Materials and Structures (B. Wilshire and R.W. Evans, editors), Proceedings of the Fourth International Conference, Swansea, 1990, 1009-1016.

Evans, R.W., E.A. Little, J.A. Preston and B. Wilshire. 1993. Rationalization of the creep behaviour of oxide-dispersion-strengthened alloys. In Creep and Fracture of Engineering Materials and Structures (B. Wilshire and R.W. Evans, editors), Proceedings of the Fifth International Conference, Swansea, 1993, 565-572.

Evans, R.W., J.D. Parker and B. Wilshire. 1982. An extrapolation procedure for long-term creep strain and creep life prediction, with special reference to 0.5Cr0.5Mo0.25V ferritic steels. In Recent Advances in Creep and Fatigue of Engineering Materials and Structures (B. Wilshire and O.R.J. Owen, editors), Pineridge Press, Swansea, U.K., 135-167.

Evans, R.W., I. Pearce, B. Wilshire, R.I. Butt and R.N. Wilson. 1993a. Creep fracture of aluminum airframe alloys. In Creep and Fracture of Engineering Materials and Structures (B. Wilshire and R.W. Evans, editors), Proceedings of the Fifth International Conference, Swansea, 1993, 109-116

Evans, R.W., J.A. Preston, B. Wilshire and E.A. Little. 1993b. Creep and creep fracture of an oxide-dispersion-strengthened 13% chromium ferritic steel. Materials Science and Engineering A167, 65-72.

Evans, R.W., M.R. Willis, B. Wilshire, S. Holdsworth, B. Senior, A. Fleming, M. Spindler and J.A. Williams. 1993c. Prediction of long-term creep and creep fracture data for 1 CrMoV Rotor steel. In Creep and Fracture of Engineering Materials and Structures (B. Wilshire and R.W. Evans, editors), Proceedings of the Fifth International Conference, Swansea, 1993, 633-642.

Evans, W.J. 1984. Low-temperature creep and fracture of near α titanium alloys. In Creep and Fracture of Engineering Materials and Structures (B. Wilshire and D.R.J. Owen, editors), Proceedings of the Second International Conference, Swansea, 1984, 395-406.

Evans, W.J. 1987. Creep-fatigue interactions in Ti-6Al-4V at ambient temperatures. In Creep and Fracture of Engineering Materials and Structures (B. Wilshire and R.W. Evans, editors), Proceedings of the Third International Conference, Swansea, 1987, 603-613.

Feltham, P. and J.D. Meakin. 1959. Creep in face-centred cubic metals with special reference to copper. Acta Metallurgica 7, 614-627.

Frost, H.J. and M.F. Ashby. 1982. Deformation-Mechanism Maps: The Plasticity and Creep of Metals and Ceramics. Franklin Book Company, Incorporated, Elkins Park, PA.

Garofalo, F. 1965. Fundamentals of Creep-Rupture in Metals. Macmillan Publishing Co., Inc., New York, NY.

Garofalo, F., C. Richmond, W.F. Domis and F. von Gemminger. 1963. Joint International Conference on Creep, Institute of Mechanical Engineering, London.

Gittus, J. 1975. Creep, Viscoelasticity and Creep Fracture in Solids. Elsevier Science, Inc., New York, NY.

Graham, A. and K.F.A. Walles. 1955. Relationships between long and short-time creep and tensile properties of a commercial alloy. Journal of the Iron and Steel Institute, 179, 105-120.

Hart, E.W. 1967. Theory of the tensile test. Acta Metallurgica 15, 351-355.

Henderson, P.J. and M. McLean. 1984. An evaluation of the factors influencing tertiary creep in nickel-based superalloys. In Creep and Fracture of Engineering Materials and Structures (B. Wilshire and D.R.J. Owen, editors), Proceedings of the Second International Conference, Swansea, 1984, 319-332.

Henderson, P.J., J-O. Österberg and B. Ivarsson. 1992. Low-temperature creep of copper intended for nuclear waste containers. Swedish Institute for Metals Research. Swedish Nuclear Fuel and Waste Management Company Report, SKB-TR-92-04.

Herring, C. 1950. Diffusional viscosity of a polycrystalline solid. Journal of Applied Physics 21, 437-445.

Hosaluk, L.J., H.Y.S. Ko and K.J. Truss. 1987. The effects of creep on the long-term performance of titanium stressed-shell fuel isolation containers. Atomic Energy of Canada Limited Technical Record, TR-402.

Hull, D. and D.E. Rimmer. 1959. The growth of grain-boundary voids under stress. Philosophical Magazine 4, 673-687.

Johnson, L.H., J.C. Tait, D.W. Shoesmith, J.L. Crosthwaite and M.N. Gray. 1994. The disposal of Canada's nuclear fuel waste: Engineered barriers alternatives. Atomic Energy of Canada Limited Report, AECL-10718, COG-93-8.

Johnson, R.F., M.J. May, R.J. Trueman and J. Mickleraith. 1967. Elevated-temperature tensile, creep, and rupture properties of 1%Cr-½%Mo, 2¼%Cr-1%Mo, and ½%Cr-½%Mo-¼%V steels. In High Temperature Properties of Steels, Proceedings of the Joint Conference, Eastbourne, 1966, 229-264.

Kachanov, L.M. 1958. Long-time strength and creep. Izvestiya Akademii Nauk. SSSR, Otdelenie Tekhnicheskikh Nauk, 8, 26-31.

Kiessel, W.R. and M.J. Sinnott. 1953. Creep properties of commercially pure titanium. Transactions A.I.M.E., Journal of Metals, 5, 331-338.

Larson, F.R. and J. Miller. 1952. A time-temperature relationship for rupture and creep stresses. Transactions ASME 74, 765-771.

Li, G., T. Sakai and T. Endo. 1987. An application of creep time law to the life prediction of a nickel-base superalloy. In Creep and Fracture of Engineering Materials and Structures (B. Wilshire and R.W. Evans, editors), Proceedings of the Third International Conference, Swansea, 1987, 803-813.

Li, Y.Z., M.C. Nguyen and H.H. Over. 1990. Creep and creep crack growth evaluation within the European High Temperature Materials Databank, PETTEN. In Creep and Fracture of Engineering Materials and Structures (B. Wilshire and R.W. Evans, editors), Proceedings of the Fourth International Conference, Swansea, 1990, 961-974.

Luster, D.R., W.W. Wentz and D.W. Kaufmann. 1953. Creep properties of titanium. Materials and Methods 37, 100-103.

Maruyama, K. and H. Oikawa. 1987a. On physical bases of the modified θ projection concept. In Creep and Fracture of Engineering Materials and Structures (B. Wilshire and R.W. Evans, editors), Proceedings of the Third International Conference, Swansea, 1987, 815-828.

Maruyama, K. and H. Oikawa. 1987b. Comments on "exponential descriptions of normal creep curves by S.G.R. Brown, W.R. Evans and B. Wilshire". Scripta Metallurgica 21, 233-237.

McLean, D. 1966. The physics of high temperature creep in metals. Reports on Progress in Physics 29, 1-33.

McLean, M., B.F. Dyson and R.N. Ghosh. 1992. Recent evaluation of gas turbine materials and the development of models for life prediction. In Mechanical Behaviour of Materials, Volume 2, Pergamon Press, Oxford, 49-57.

Monkman, F.C. and N.J. Grant. 1956. An empirical relationship between rupture life and minimum creep-rate in creep-rupture tests. Proceedings ASTM 56, 593-605.

Nabarro, F.R.N. 1948. Deformation crystals by the motion of single ions. In Report on Conference on Strength of Solids, The Physical Society, London, 75-90.

Nix, W.D. and B. Ilschner. 1979. Mechanisms controlling creep of single phase metals and alloys. In Strength of Metals and Alloys (P. Haasen, V. Gerold and G. Kostorz, editors), Proceedings of the Fifth International Conference, Aachen, West Germany, 1979, Pergamon Press, New York, NY, 1503-530.

Orr, R.L., O.D. Sherby and J.E. Dorn. 1954. Correlations of rupture data for metals at elevated temperatures. Transactions American Society for Metals 46, 113-128.

Osgerby, S and B.F. Dyson. 1993. Constant strain-rate testing: Prediction of stress-strain curves from constant-load creep data. In Creep and Fracture of Engineering Materials and Structures (B. Wilshire and R.W. Evans, editors), Proceedings of the Fifth International Conference, Swansea, 1993, 53-61.

Osgerby, S. and B.F. Dyson. 1994a. Validation of a constitutive model for creep deformation and fracture in a 1 Cr ½ Mo ferritic steel. In Materials for Advanced Power Engineering, Part 1 (D. Coutsouradis et al., editors) 573-582.

Osgerby, S. and B.F. Dyson. 1994b. Physically-based modelling of stress-relaxation in superalloys and ferritic steels. In Proceedings of Conference on Performance of Bolting Materials in High Temperature Plant Applications, York, June 1994, to be published.

Osgerby, S.,A. Barbosa and B.F. Dyson. 1992. CREEPSIM-2: a software package for numerical integration of 1st order differential equations. National Physics Laboratory Report, DMM(A)35.

Rabotnov, Y.N. 1969. Creep rupture (Creep rupture and fatigue growth in solid body mechanics, considering triaxial stress state and simplified creep rupture theory variant). In Applied Mechanics, Proceedings of the 12th International Union of Theoretical and Applied Mechanics, Stanford University, CA, 1968, Springer-Verlag, New York, 342-349.

Rigby, G.L. 1994. A finite element model for creep in titanium. Atomic Energy of Canada Limited Technical Record, TR-647, COG-I-94-365.

Sargent, P.M. and M.F. Ashby. 1982. Deformation maps for titanium and zirconium. Scripta Metallurgica 16, 1415-1422.

Shen, G. and A. Plumtree. 1990. Combination of continuum damage mechanics and θ-projection concept for creep life prediction. In Creep and Fracture of Engineering Materials and Structures (B. Wilshire and R.W. Evans, editors), Proceedings of the Fourth International Conference, Swansea, 1990, 999-1008.

Sherby, O.D. and P.M. Burke. 1968. Mechanical behavior of crystalline solids at elevated temperature. Progress in Materials Science 13, 325-390.

Sherby, O.D. and J. Wadsworth. 1989. Superplasticity - Recent advances and future directions. Progress in Materials Science 33, 169-221.

Simmons, G.R. and P. Baumgartner. 1994. The disposal of Canada's nuclear fuel waste: engineering for a disposal facility. Atomic Energy of Canada Limited Report, AECL-10715, COG-93-5.

Taylor, N.G., B.R. Twaddle and R.C. Hurst. 1990. Prediction of alloy 800H and 2¼Cr 1 Mo component creep behaviour from uniaxial specimen data. In Creep and Fracture of Engineering Materials and Structures (B. Wilshire and R.W. Evans, editors), Proceedings of the Fourth International Conference, Swansea, 1990, 985-998.

Teper, B. 1985. Test programs of the prototype of the TWPP container: Part 2 - Post-hydrostatic tests. Ontario Hydro Research Division Report, 85-313-K.

Teper, B. 1987a. Test program of the prototype of the thin-wall particulate-packed (TWPP) container 1. Hydrostatic tests. Atomic Energy of Canada Limited Technical Record, TR-369-1. Also available as Ontario Hydro Research Division Report, 84-293-K.

Teper, B. 1987b. Test program of granular materials for the thin-walled, particulate-packed container. Ontario Hydro Research Division Report, 87-154-K.

Teper, B. 1988. Test program of the prototype of the TWPP container: Part 3 - Detailed stress analysis and comparison with test results. Ontario Hydro Research Division Report, 87-296-K.

Teper, B. 1990. Long-term creep assessment of candidate metals for high-level nuclear waste containers - interim report. Ontario Hydro Research Division Report, 90-241-K.

Teper, B. and S.A. Reid. 1989. Recent developments in design of containers for disposal of high-level waste from CANDU reactors. In Waste Management '89, Proceedings of the Symposium on Waste Management, Tucson, AZ, 1989, Volume 1, 623-631.

Voorhees, H.R. 1985. Assessment and use of creep-rupture properties. In Metals Handbook, Ninth edition, Volume 8, Mechanical Testing. ASM International, Metals Park, OH, 329-342.

Weertman, J. 1955. Theory of steady-state creep based on dislocation climb. Journal of Applied Physics 26, 1213-1217.

Weertman, J. 1963. An empirical relationship defining the stress dependence of minimum creep rate in metals. Metallurgical Society of AIME Transactions, 227, 1475-1476.

Wilshire, B. 1989. New high-precision creep procedures for accurate life extension of plant. International Journal of Pressure Vessel and Piping 39, 73-82.

Wilshire, B. 1990. On the evidence for diffusional creep processes. In Creep and Fracture of Engineering Materials and Structures (B. Wilshire and R.W. Evans, editors), Proceedings of the Fourth International Conference, Swansea, 1990, 1-9.

Wilshire, B. 1993a. Creep data prediction for high-performance steels. In Advanced Materials (T. Kishi, N. Tanaka and Y. Kagawa, editors), Proceedings of the Third Japan International SAMPE Symposium, Tokyo, 1993, 2011-2018.

Wilshire, B. 1993b. High temperature properties of monolithic ceramics. Materials and Design 14, 39-43.

Wilshire, B. and R.W. Evans. 1994. Acquisition and analysis of creep data. Journal of Strain Analysis 29, 159-165.

Woodford, D.A. 1969. Strain-rate sensitivity as a measure of ductility. Transactions of the ASM 62, 291-293.

Zeyfang, R., R. Martin and H. Conrad. 1971. Low-temperature creep of titanium. Materials Science and Engineering 8, 134-140.

---

* Internal report, available from SDDO, AECL Research, Chalk River Laboratories, Chalk River, Ontario K0J 1J0.

** Unpublished report available from the principal author at Ontario Hydro Research Division, 800 Kipling Avenue, Toronto, Ontario M8Z 5S4.

TABLE 1

VALUES OF THE PARAMETERS USED TO CONSTRUCT THE DEFORMATION MECHANISM MAPS (Frost and Ashby 1982)

Materials	α-Titanium	Copper
Crystallographic and thermal data		
Atomic volume, Ω (m^3)	1.76×10^{-29}	1.18×10^{-29}
Burç r's vector, b (m)	2.95×10^{-10}	2.56×10^{-10}
Melting temperature, T_m(K)	1933	1356
Modulus*		
Shear modulus at 300 K, G_o (MN/m^2)	4.36×10^4	4.21×10^4
Temperature dependence of modulus, $\frac{T_m}{G_o}\frac{dG}{dT}$	-1.2	-0.54
Lattice diffusion		
Pre-exponential, D_o (m^2/s)	8.6×10^{-10}	2.0×10^{-5}
Activation energy, Q_{SD} (kJ/mole)	150	197
Boundary diffusion		
Pre-exponential, δD_o (m^3/s)	3.6×10^{-16}	5.0×10^{-15}
Activation energy, Q_{GB} (kJ/mole)	97	104
Core diffusion†		
Pre-exponential, $a_c D_o$ (m^4/s)	7.3×10^{-29}	1.0×10^{-24}
Activation energy, Q_P (kJ/mole)	97	117
Power-law creep		
Exponent, n	4.3	4.8
Constant, A	7.7×10^4	7.4×10^5
Activation energy, Q_C (kJ/mole)††	242	-
Pre-exponential for creep, D_o (m^2/s)	1.3×10^{-2}	-

* $$G = G_o\left(1 + \frac{T - 300}{T_m}\right)\frac{T_m}{G_o}\frac{dG}{dT}$$

† a_c = effective diffusive section of a dislocation core.

†† for titanium, these values were used for power-law creep, the activation energies Q_{SD} or Q_P giving a poor fit to the data.

TABLE 2

COEFFICIENTS FOR ln θ and ε_r ACCORDING TO EQNS. (59) AND (61)
(Units are in s, K and MPa)

COPPER				
Parameter	a_i	b_i	c_i	d_i
$\log_e \theta_1$	-15.8241	-0.02419	0.01190	0.0001392
$\log_e \theta_2$	-23.3920	-0.09676	0.01359	0.0003669
$\log_e \theta_3$	-12.9852	-0.06501	0.00766	0.0001495
$\log_e \theta_4$	-22.7161	-0.05707	0.01336	0.0002519
ε_r	-0.02247	-0.03668	-0.16511	0.04695
½ Cr ½ Mo ¼ V STEEL				
Parameter	a_i	b_i	c_i	d_i
$\log_e \theta_1$	-20.11538	0.01060	-0.00103	0.0001569
$\log_e \theta_2$	-54.01865	0.00051	0.00051	-0.0000449
$\log_e \theta_3$	-4.30353	-0.00468	-0.00127	0.0001840
$\log_e \theta_4$	-37.83147	0.02107	-0.00109	0.0001644
ε_r	-2.58580	0.00349	0.00126	-0.0000011

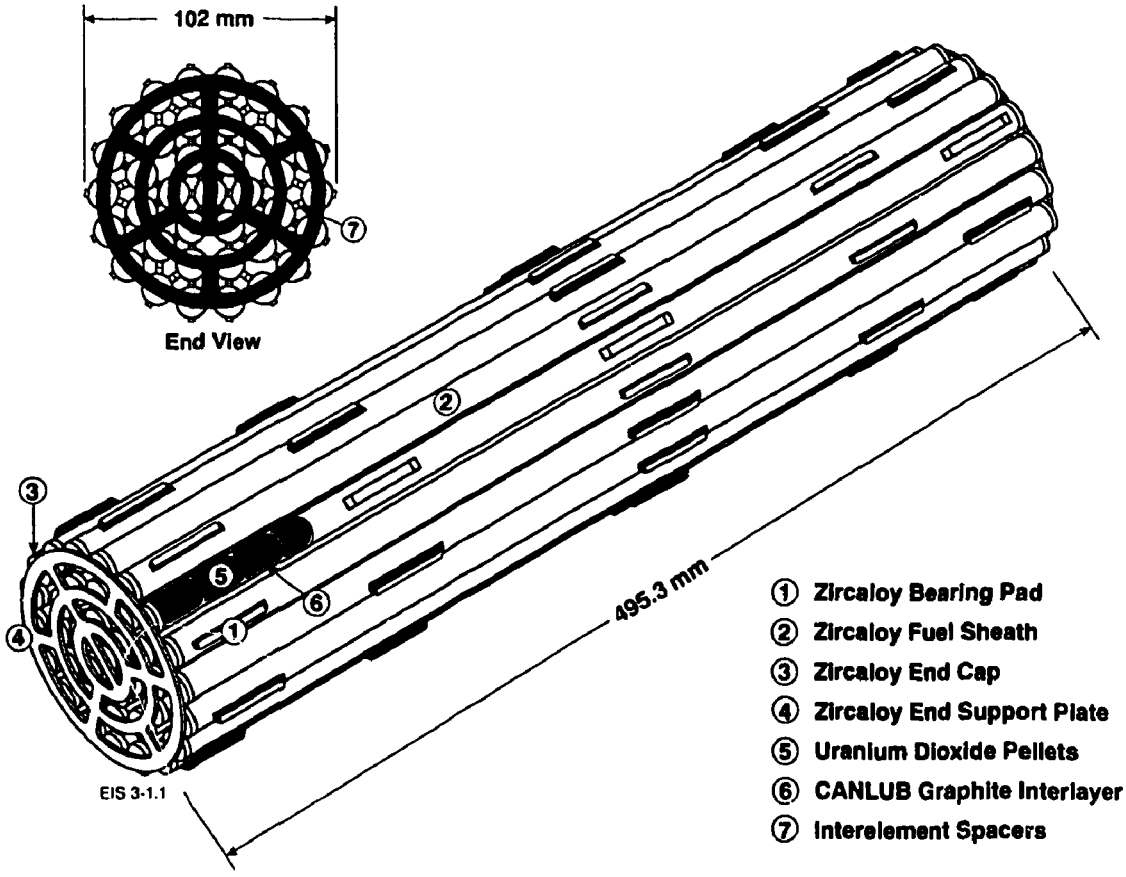

FIGURE 1: A CANDU 37-Element Fuel Bundle

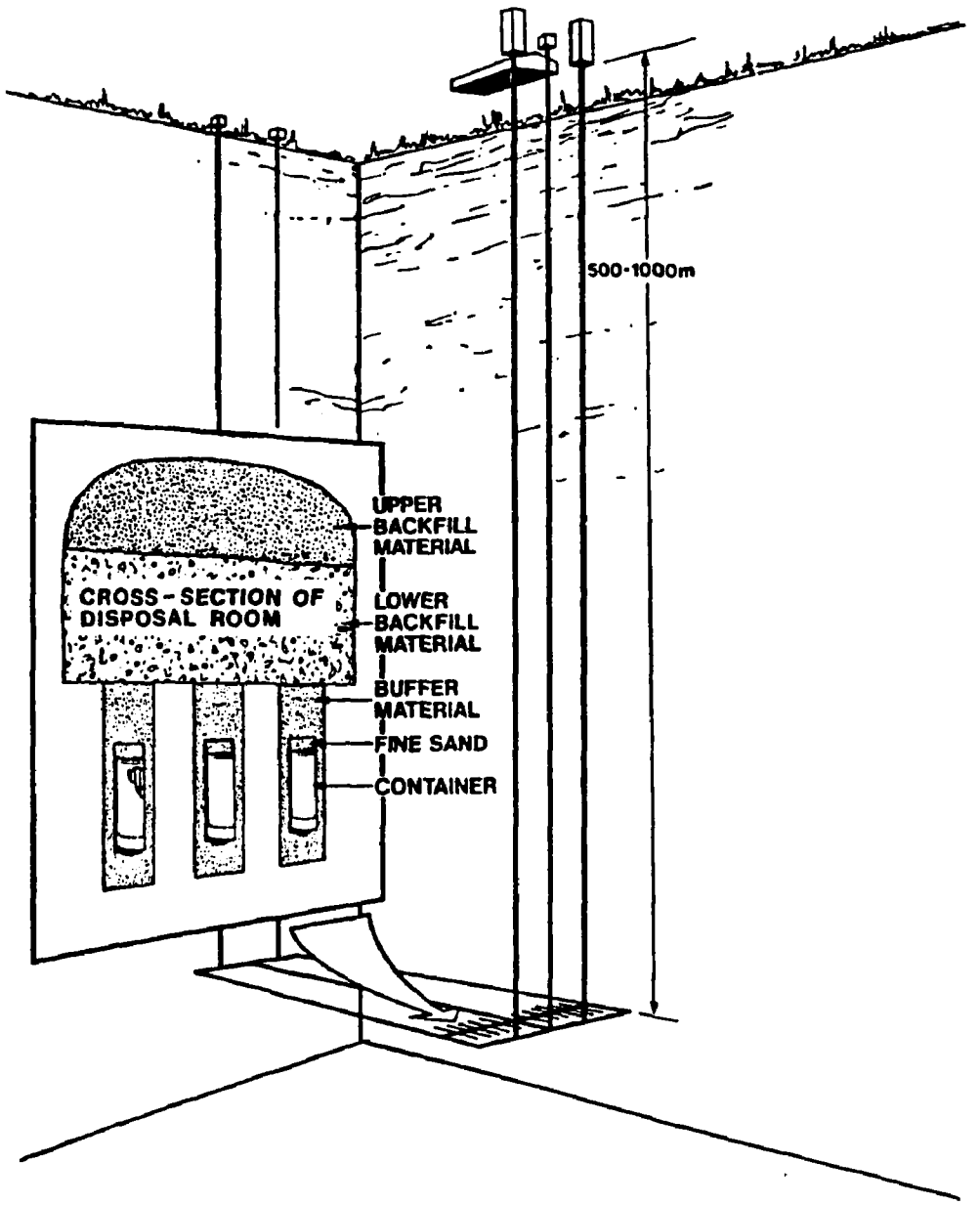

FIGURE 2: Conceptual Disposal Vault Design

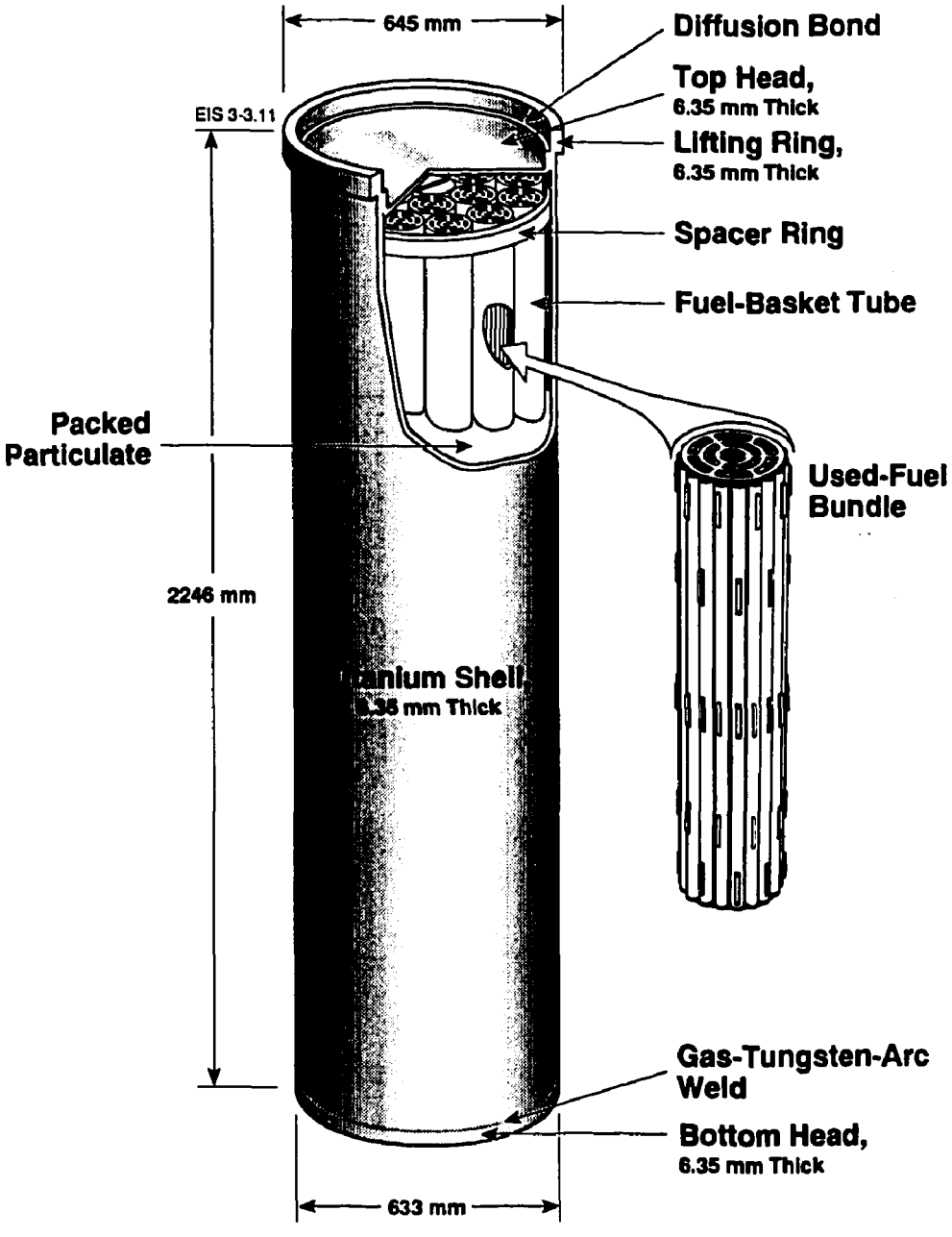

FIGURE 3: Titanium-Shell, Packed-Particulate Fuel Disposal Container

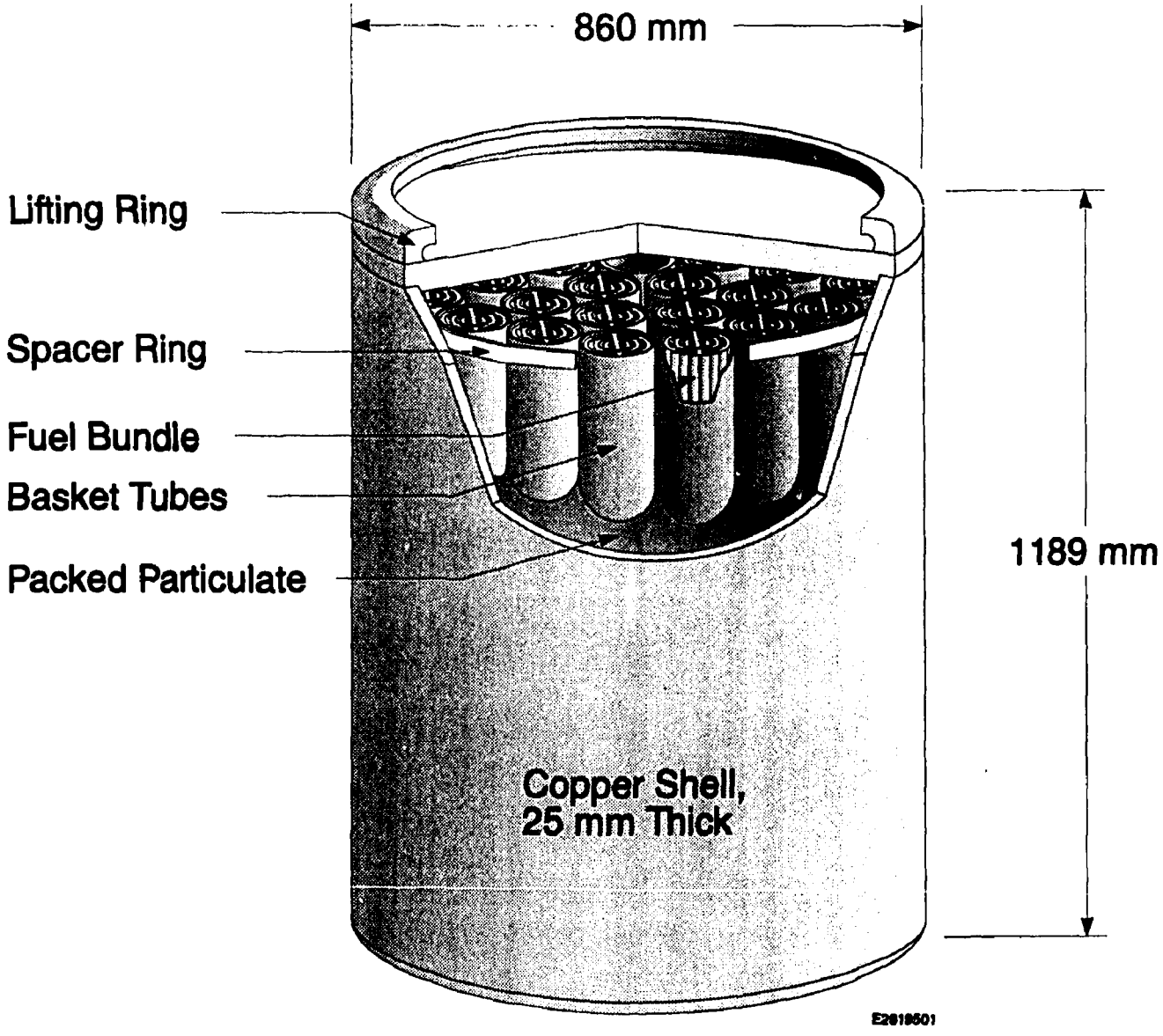

FIGURE 4: Copper-Shell, Packed-Particulate Container Designed for In-Room Emplacement

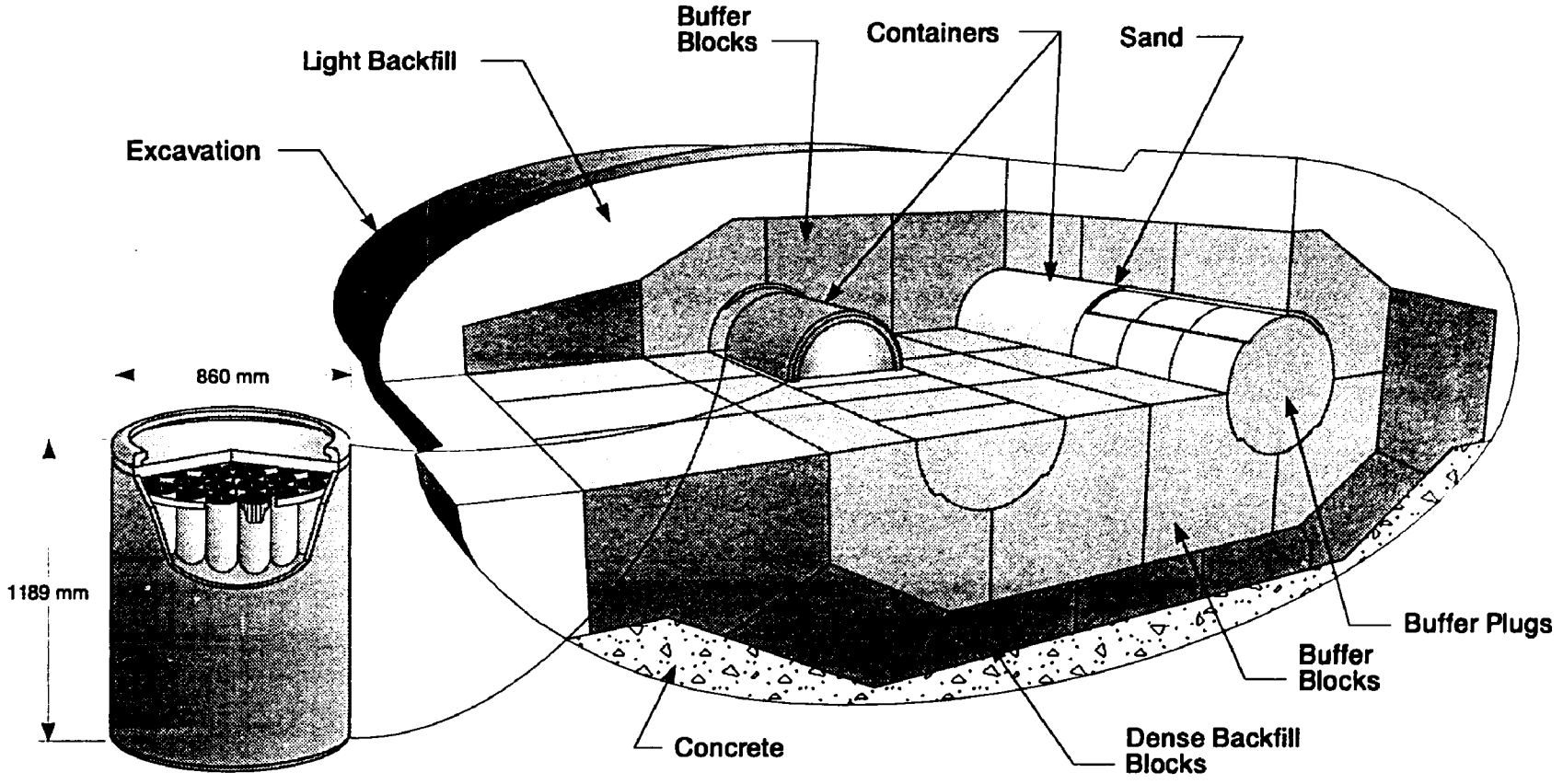

FIGURE 5: Disposal Room Showing the In-Room Emplacement of Disposal Container

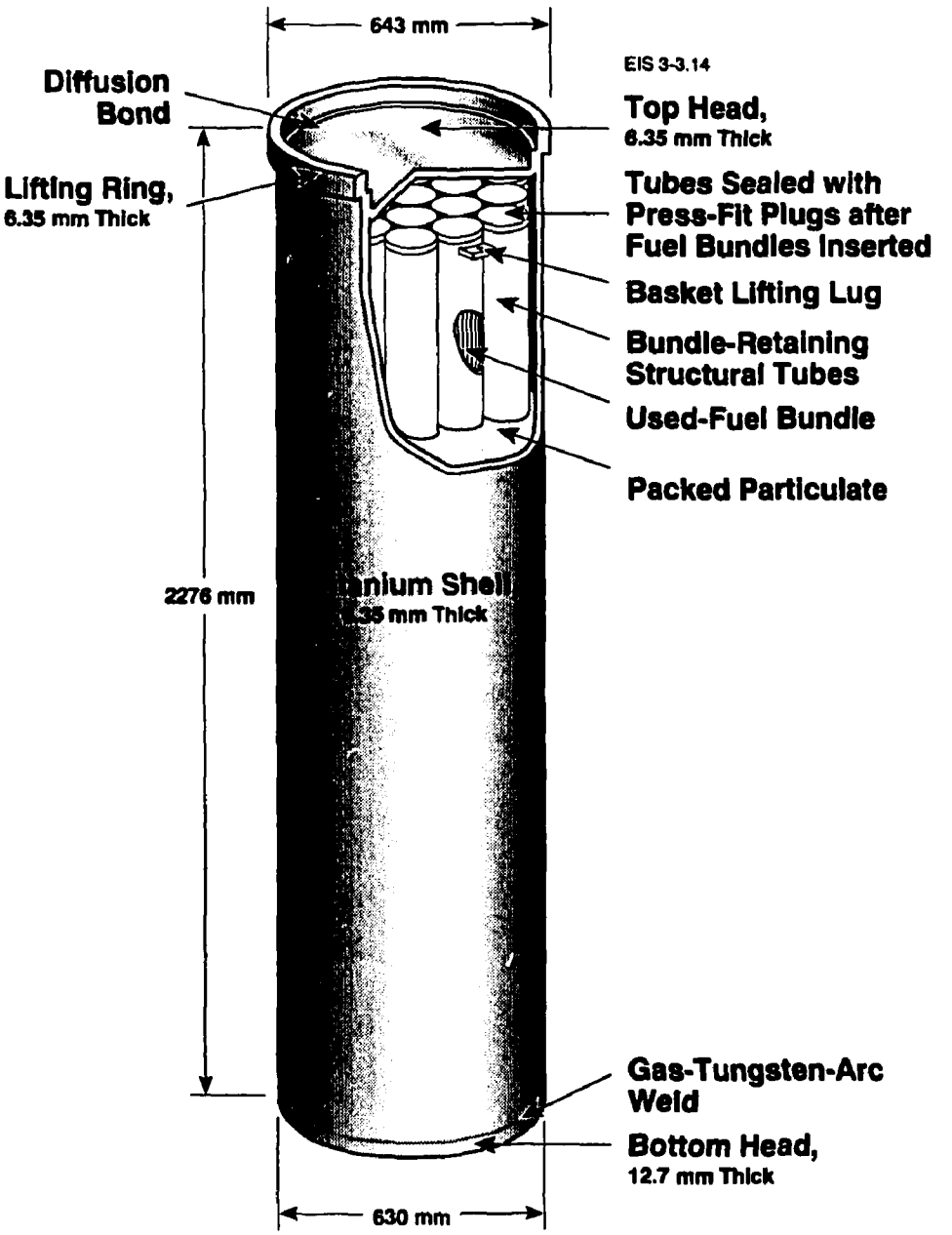

FIGURE 6: Titanium-Shell, Structurally Supported Fuel Disposal Container

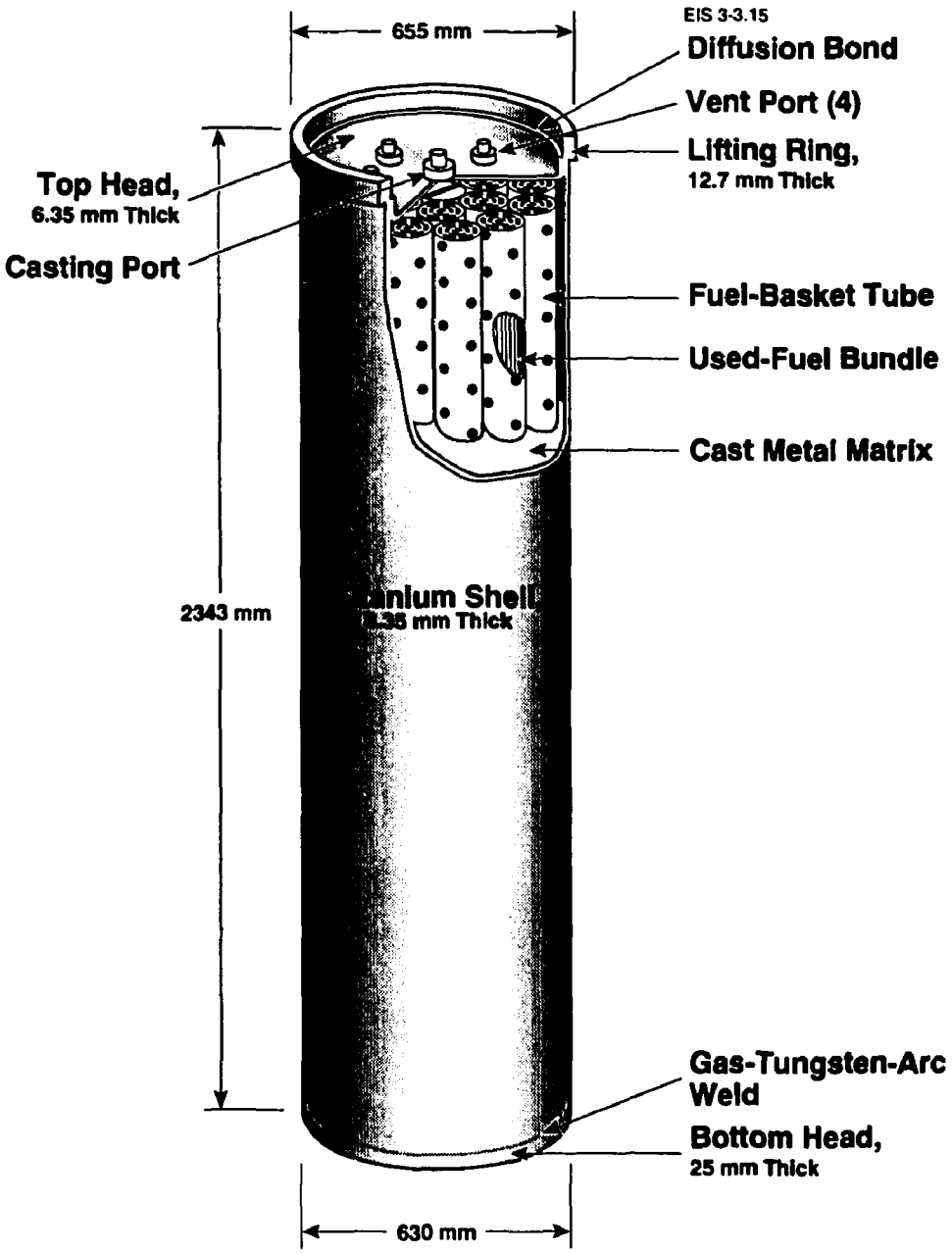

FIGURE 7: Titanium-Shell, Metal-Matrix Fuel Disposal Container

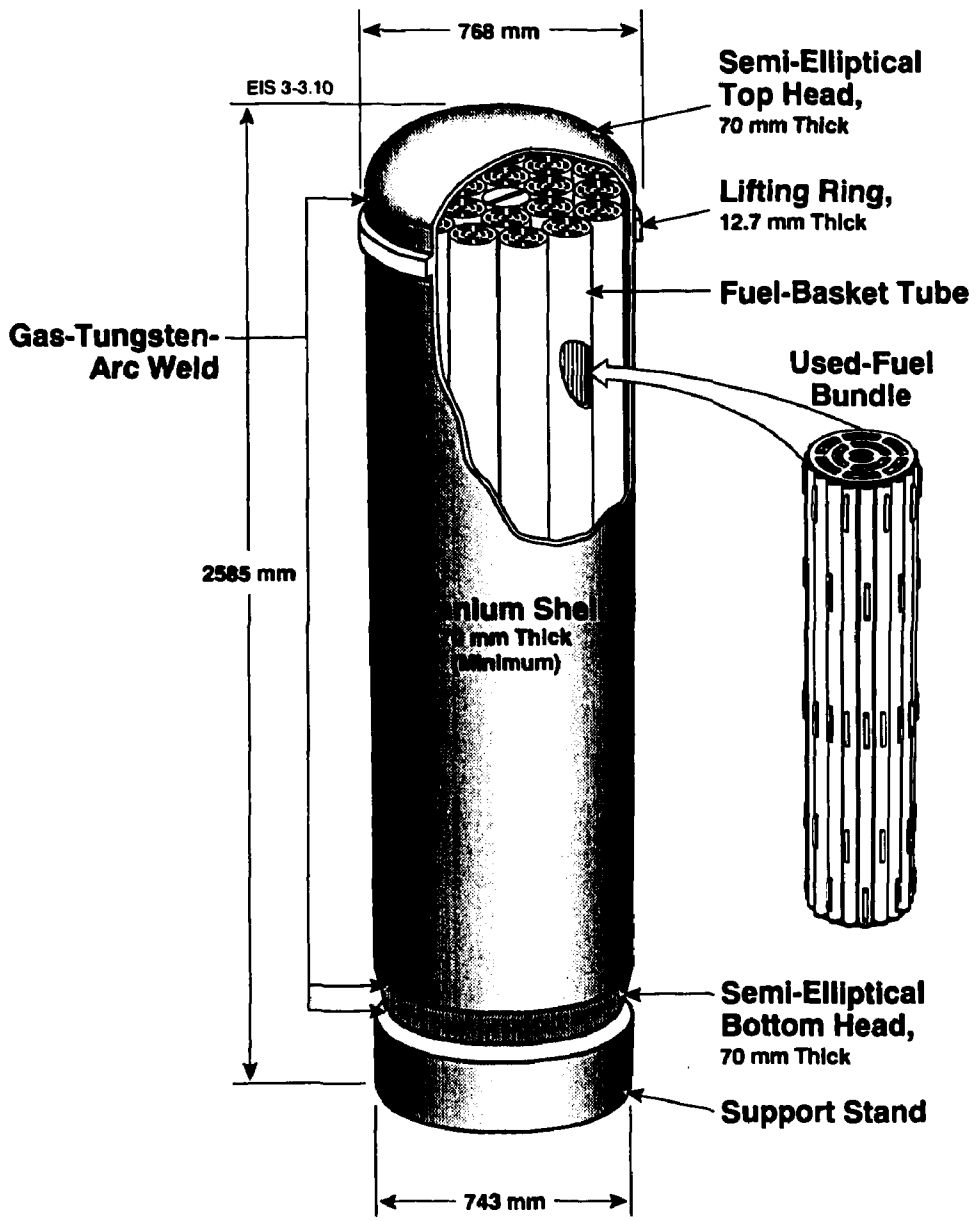

FIGURE 8: Titanium Stressed-Shell Fuel Disposal Container

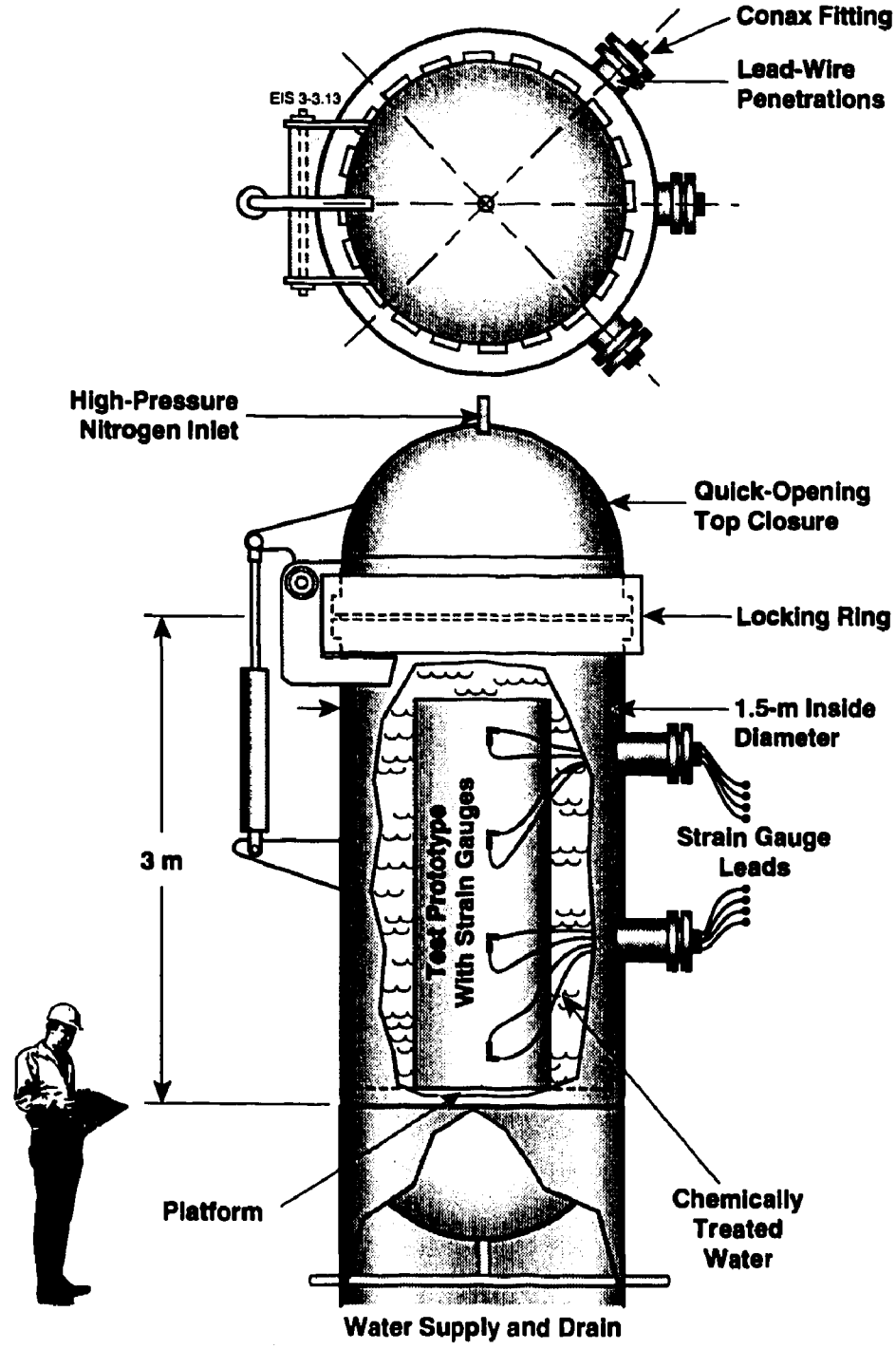

FIGURE 9: Whiteshell Laboratories Hydrostatic Test Facility

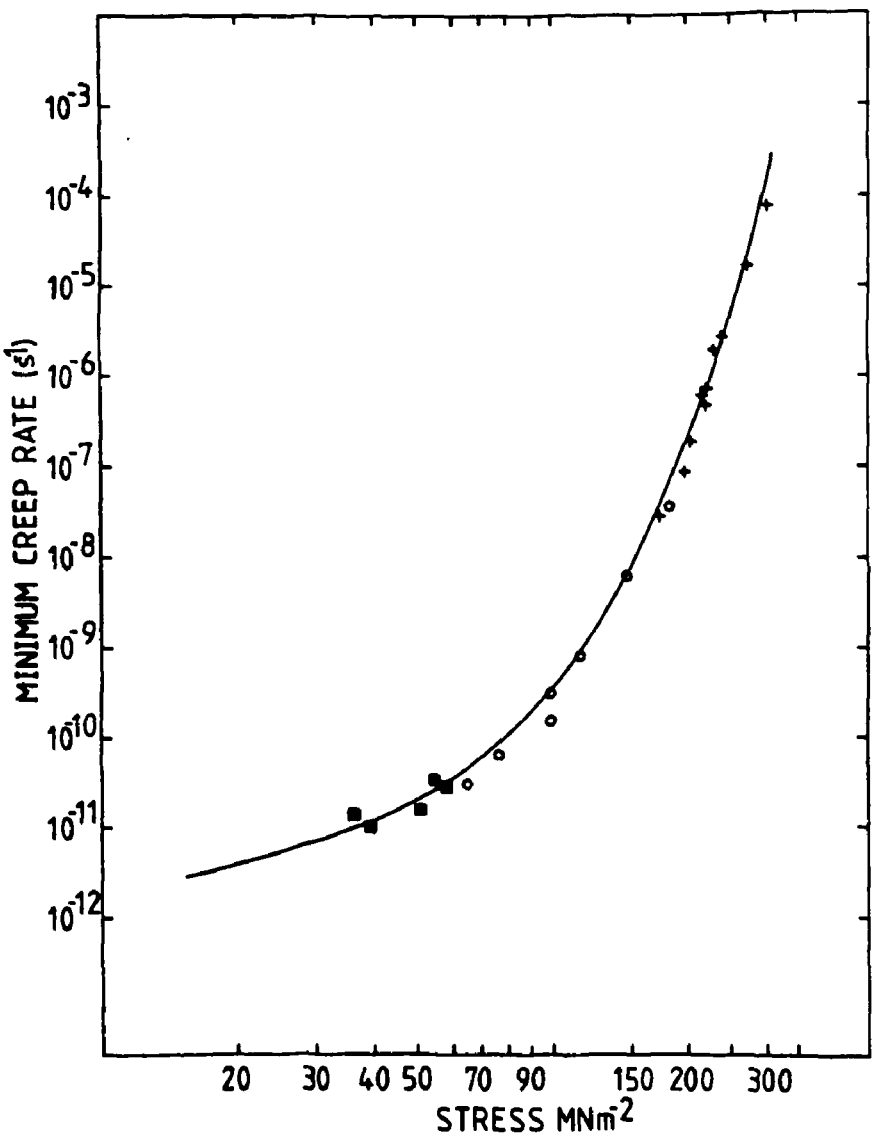

FIGURE 10: The Stress Dependence of the Minimum Creep Rate of 0.5Cr-0.5Mo-0.25V Ferritic Steel at 565°C. The solid line is calculated from the short-term data (marked +), using the θ Projection methodology (Section 9). The long-term data (marked o and ■) was subsequently obtained (Evans and Wilshire 1985).

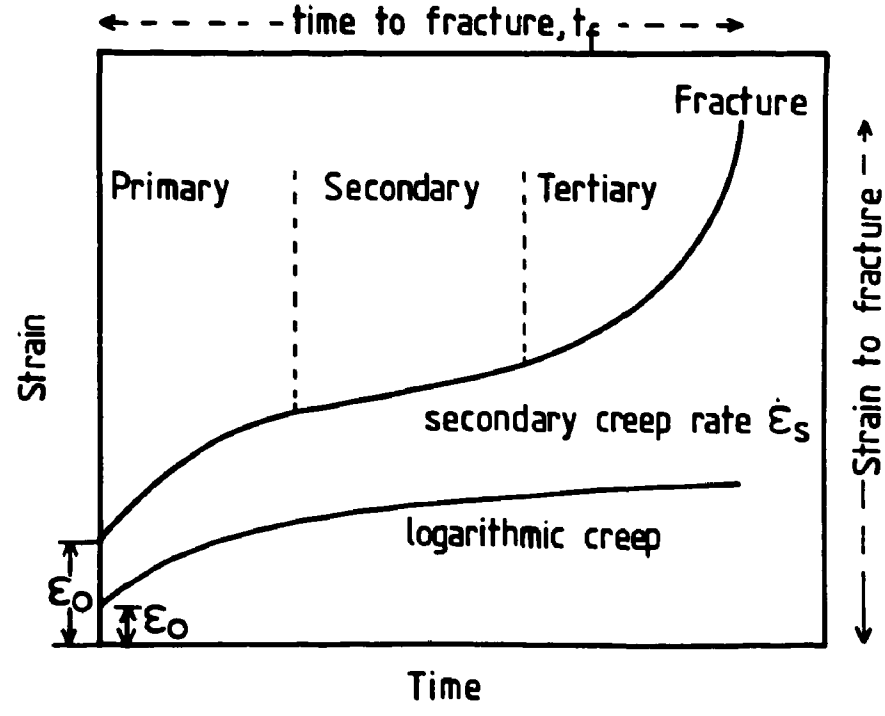

FIGURE 11: Schematic Creep Curves Illustrating Logarithmic Behaviour at Lower Temperatures and Normal Three-Stage Behaviour at Higher Temperatures

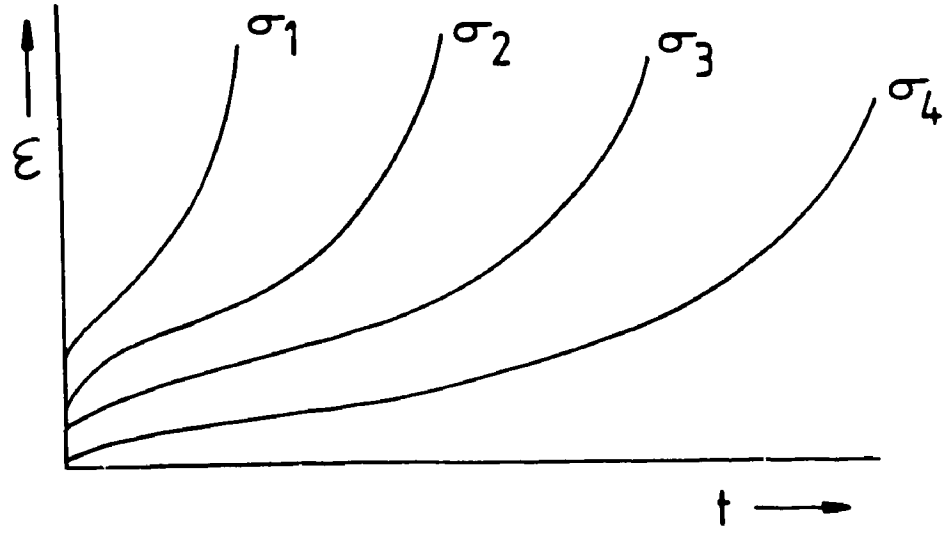

FIGURE 12: Schematic Creep Curves at the Same Temperature, but Various Stresses (σ), Where $\sigma_1 > \sigma_2 > \sigma_3 > \sigma_4$

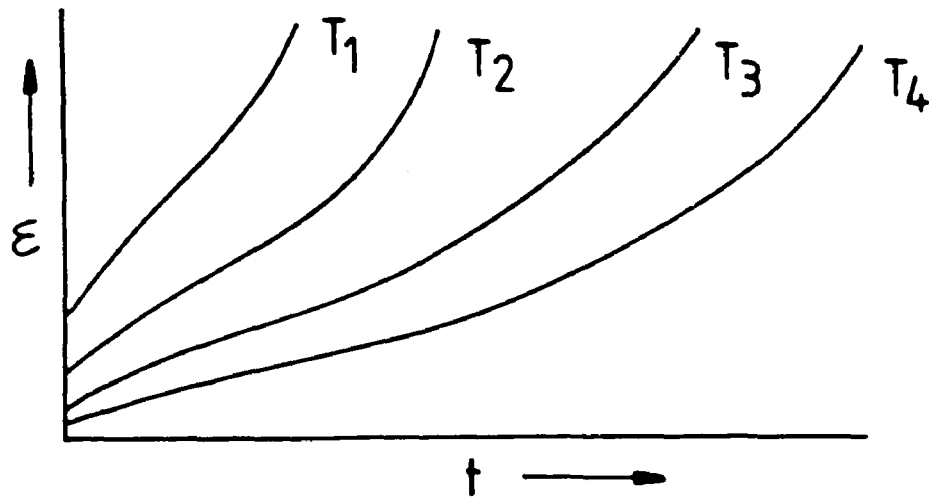

FIGURE 13: Schematic Creep Curves at the Same Stress, but Various Temperatures (T), Where $T_1 > T_2 > T_3 > T_4$

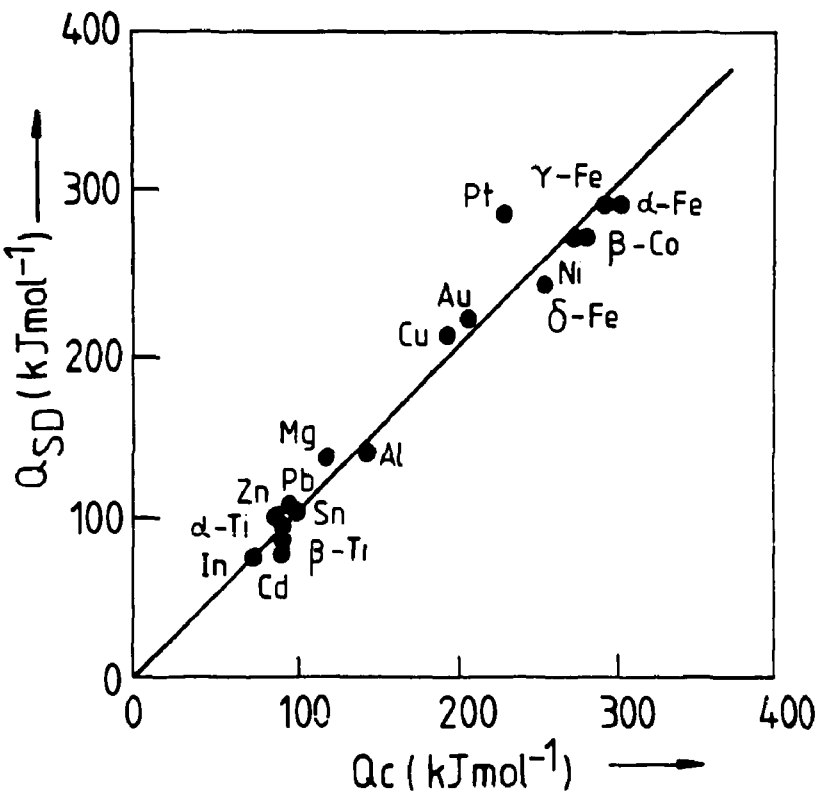

FIGURE 14: The Relationship Between the Activation Energy for Creep (Q_c) and the Activation Energy for Lattice Self Diffusion (Q_{SD}) for a Number of Pure Metals at High Temperature (Sherby and Burke 1967)

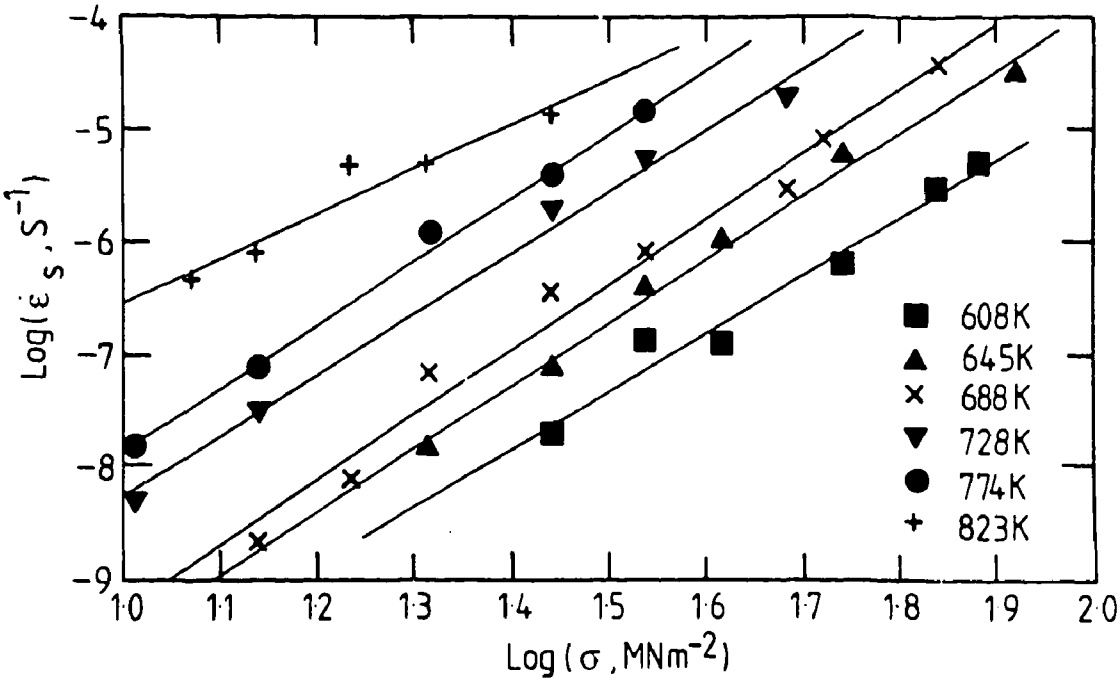

FIGURE 15: Power-Law Form of Steady-State Creep Rates Measured at Various Temperatures for Polycrystalline Copper. Stress exponent (n) is about 5 (Evans and Wilshire 1993).

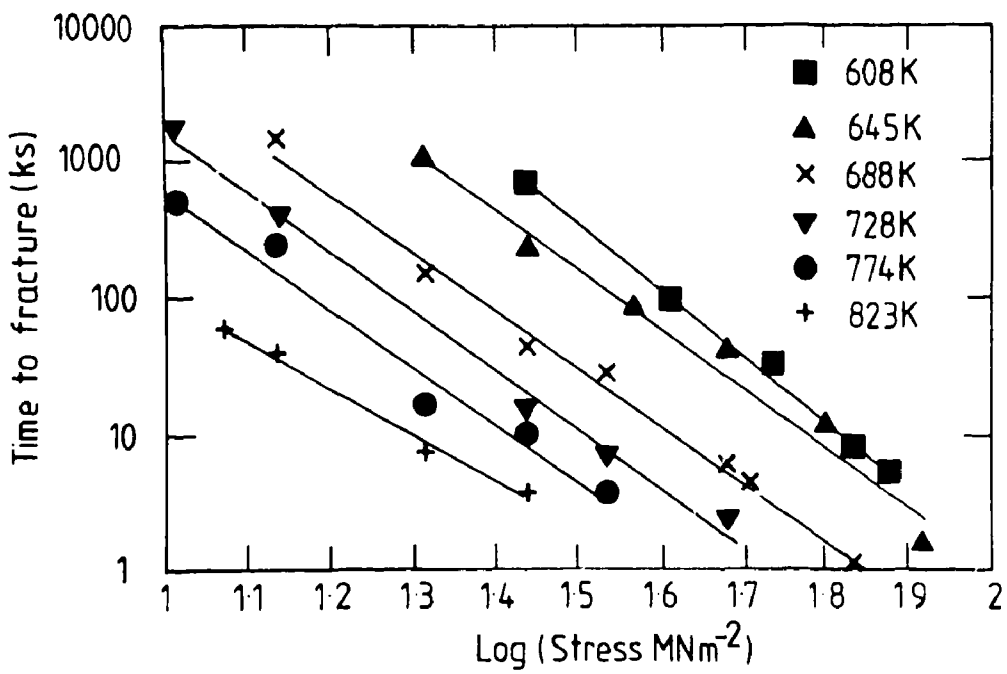

FIGURE 16: Dependence of Time to Rupture on Stress, at Various Temperatures, for the Polycrystalline Copper Data Shown in Figure 15 (Evans and Wilshire 1993)

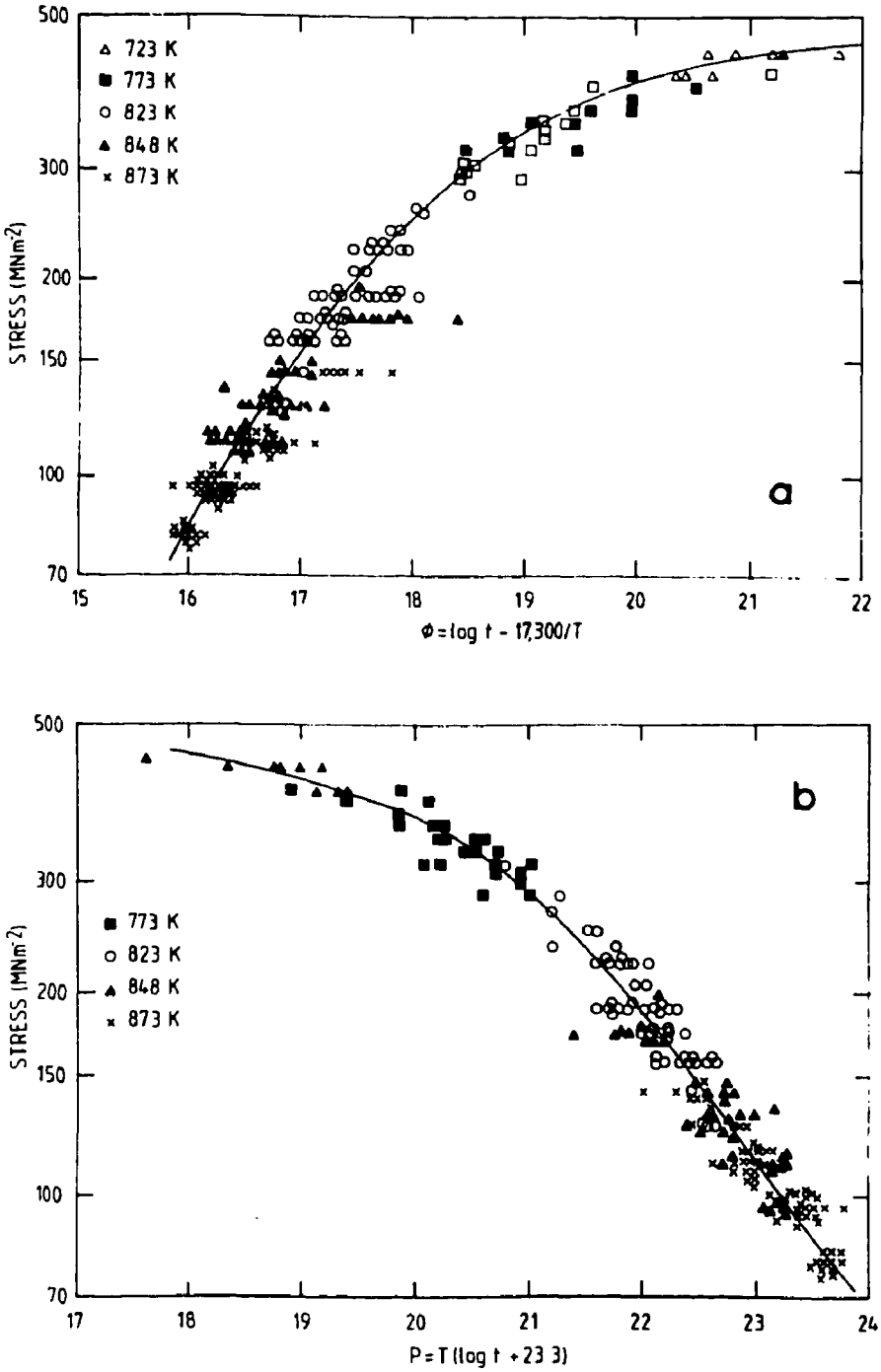

FIGURE 17: Stress-Rupture Data for 0.5Cr-0.5Mo-0.25V Steel, Using the Parametric Relationship Suggested by (a) Orr, Sherby and Dorn (1954) and (b) Larson and Miller (1952)

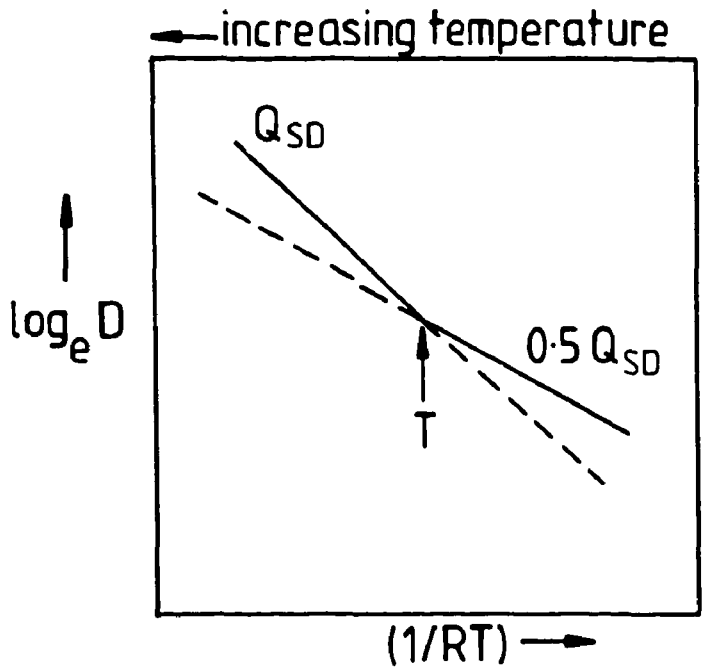

FIGURE 18: Schematic Illustration of the Variation in Diffusion Rate with Temperature for Lattice Diffusion ($Q = Q_{SD}$) and for Preferential Diffusion Along Preferred Paths ($Q = 0.5\,Q_{SD}$)

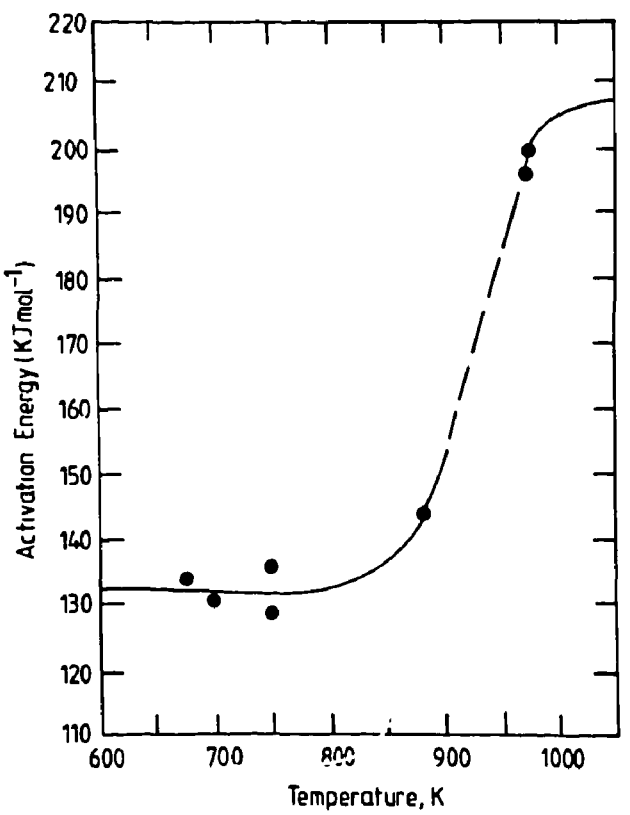

FIGURE 19: The Temperature Dependence of the Activation Energy for Creep of Polycrystalline Copper (Feltham and Meakin 1959)

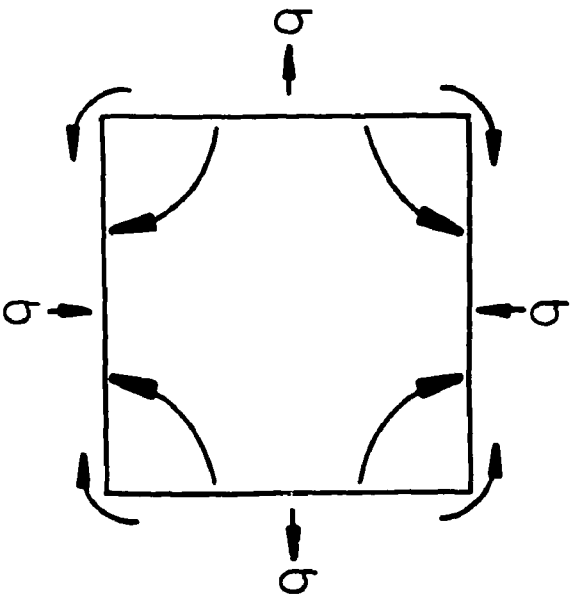

FIGURE 20: Schematic Representation of Diffusional Creep. The flow of vacancies may be through the grains (Nabarro-Herring creep) or along the grain boundaries (Coble creep)

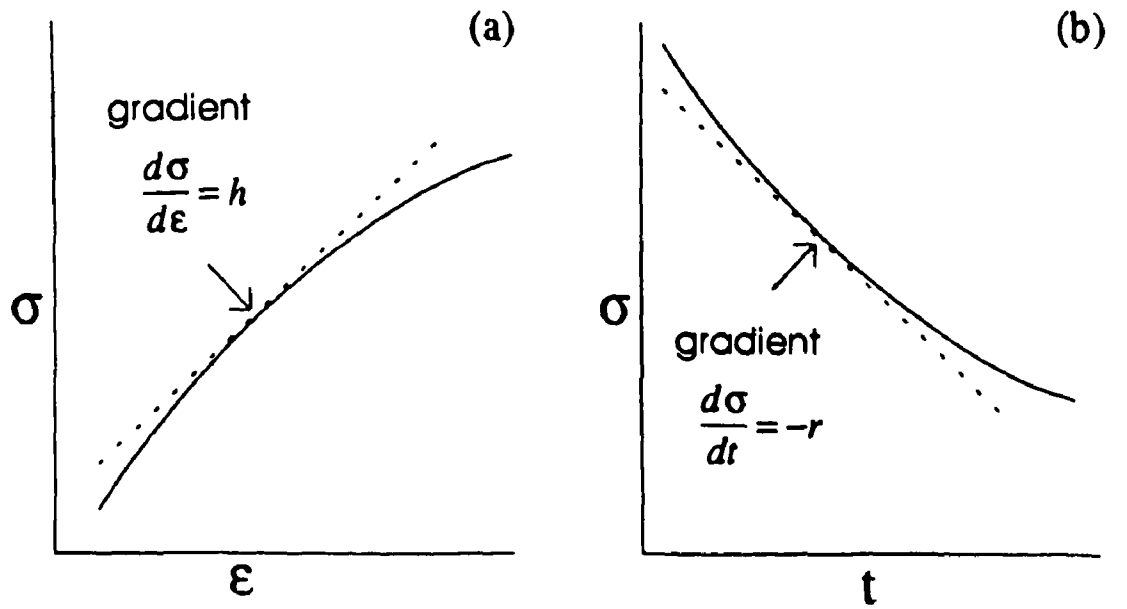

FIGURE 21: Graphical Representation of the Work-Hardening Rate (h) and Recovery Rate (r)

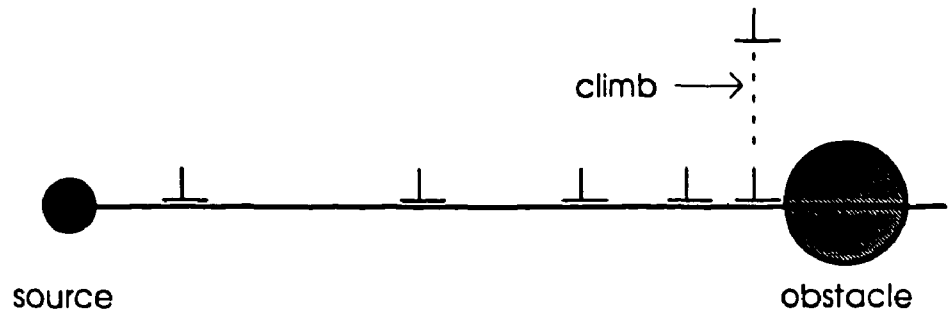

FIGURE 22: Schematic Representation of Climb of the Leading Dislocation in a Pile Up Against an Obstacle on the Slip Plane

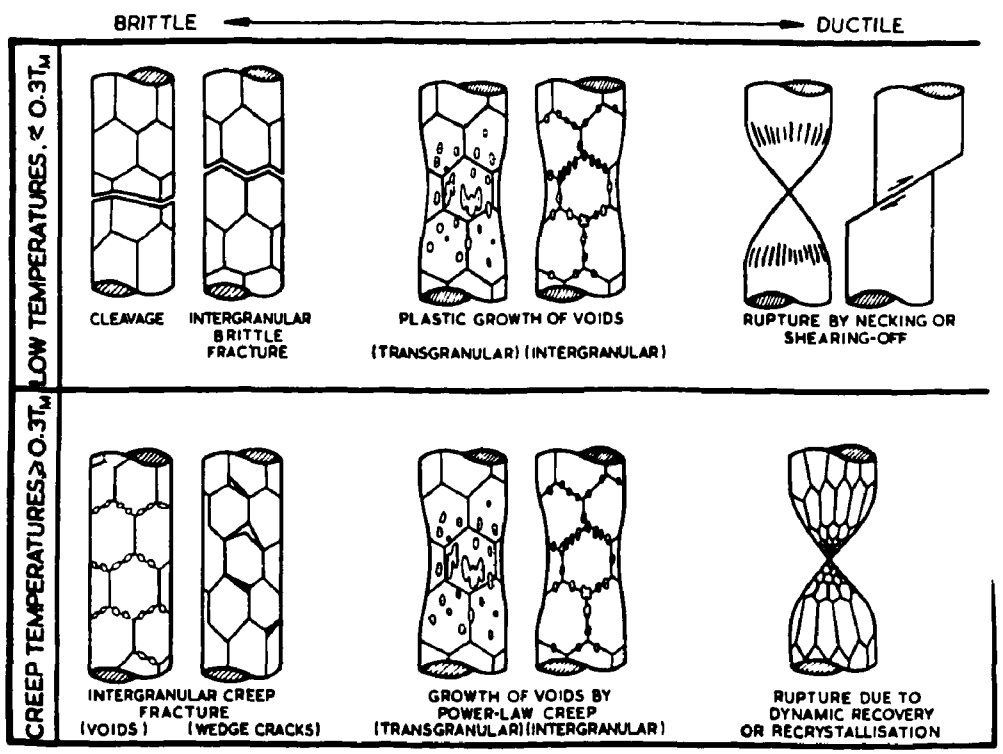

FIGURE 23: Schematic Diagram Showing the Broad Classes of Fracture Mechanisms (Ashby et al. 1979)

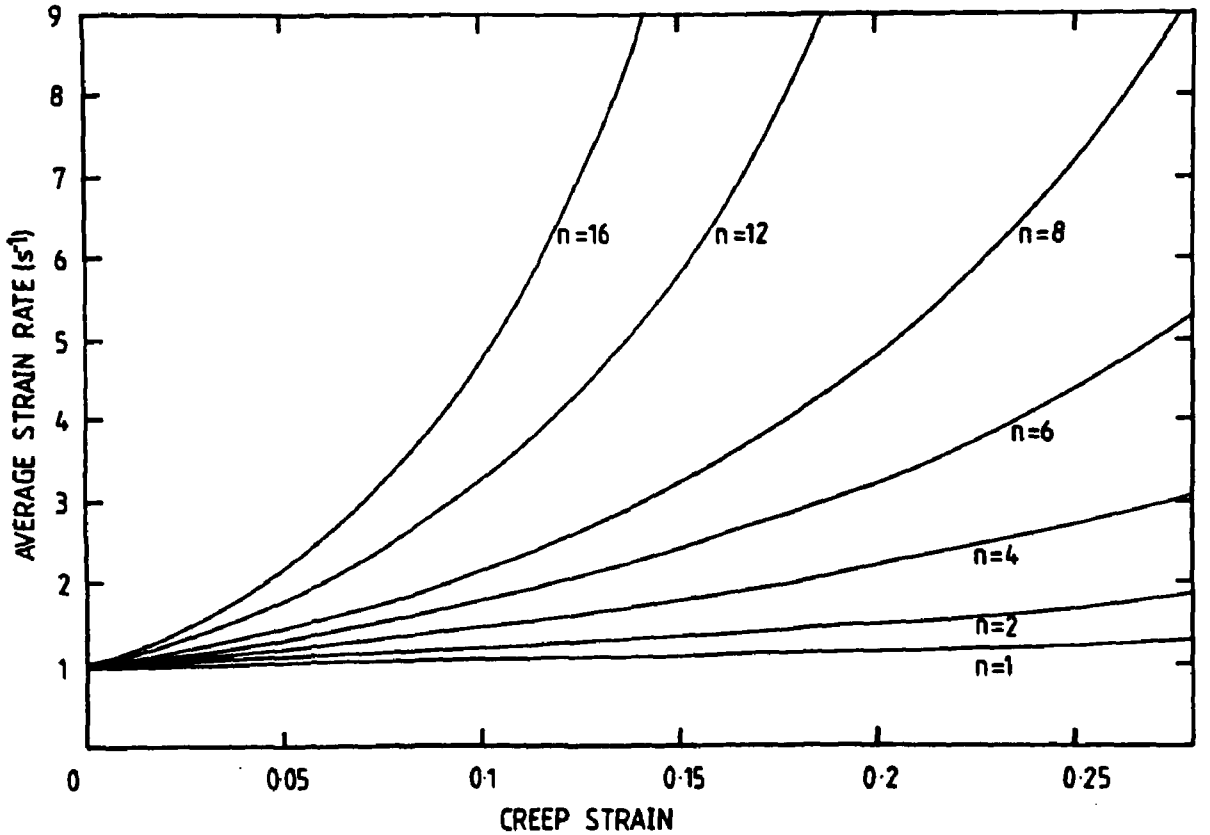

FIGURE 24: Average Specimen Strain Rate as a Function of Average Strain for a Tensile Creep Specimen Undergoing Progressive Necking for Various Values of the Stress Exponent, n (Evans and Wilshire 1985)

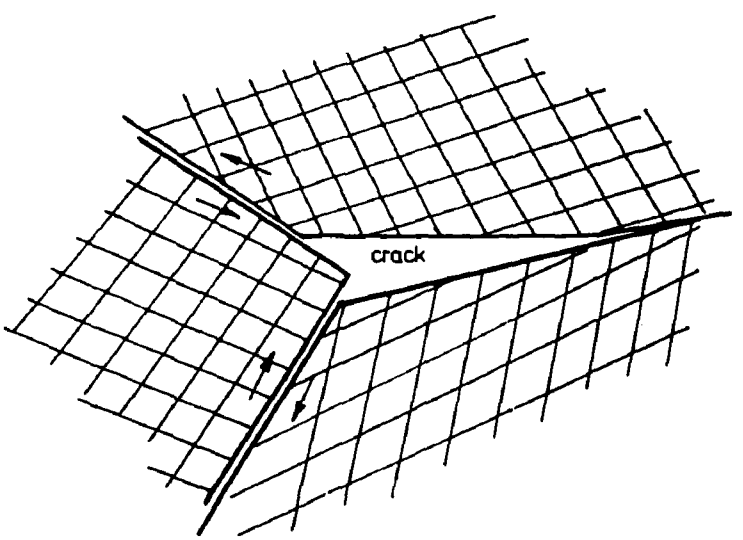

FIGURE 25: Schematic Representation of the Development of Wedge-Cracks at a Triple-Point, Due to Grain-Boundary Sliding

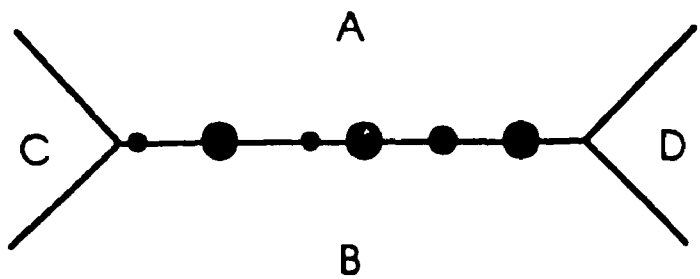

FIGURE 26: Depiction of a Series of Cavities Growing by Vacancy Absorption on a Grain Boundary Under a Tensile Stress

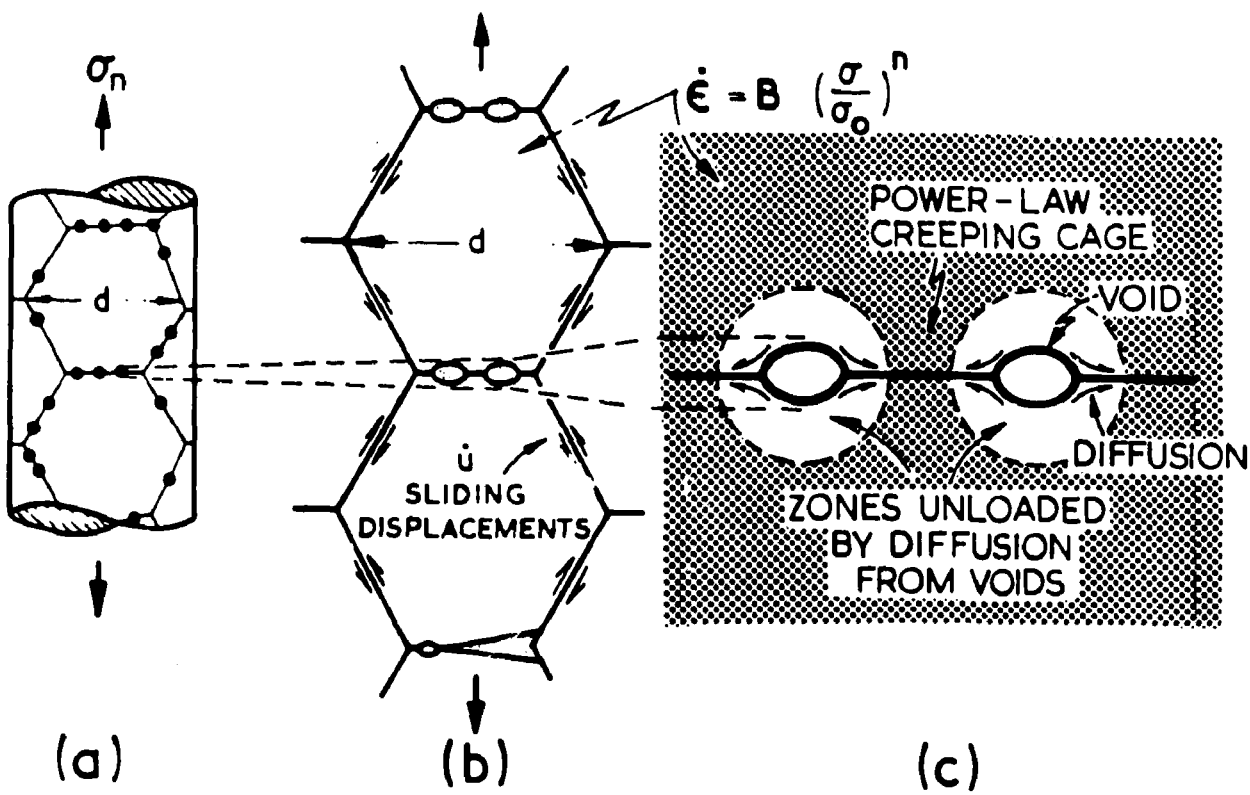

FIGURE 27: Diagrams (a) and (b) Show the Development of Grain-Boundary Voids, Accompanied by Grain-Boundary Sliding. In (c) the diffusional growth of voids is indicated. The diffusion fields of neighbouring voids do not, in general, overlap, so that each void is contained in a cage of material deforming by power-law creep (Ashby et al. 1979).

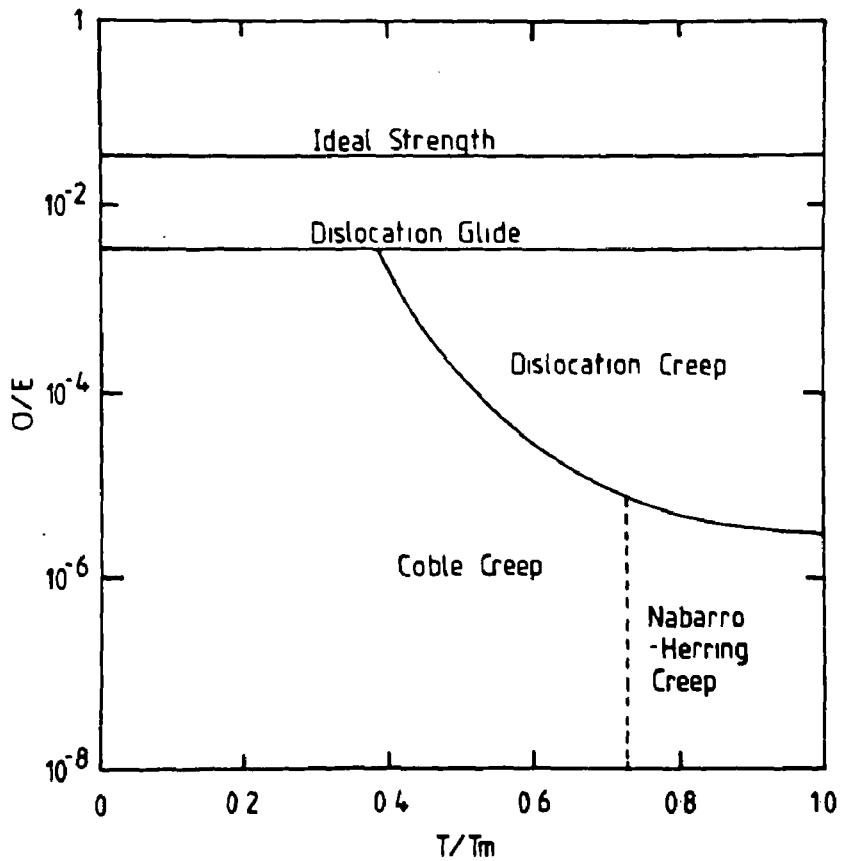

FIGURE 28: Schematic Version of a Deformation Mechanism Map, Showing Regions in the Stress/Temperature Plane Where Various (Steady-State) Creep Mechanisms Dominate the Deformation Process

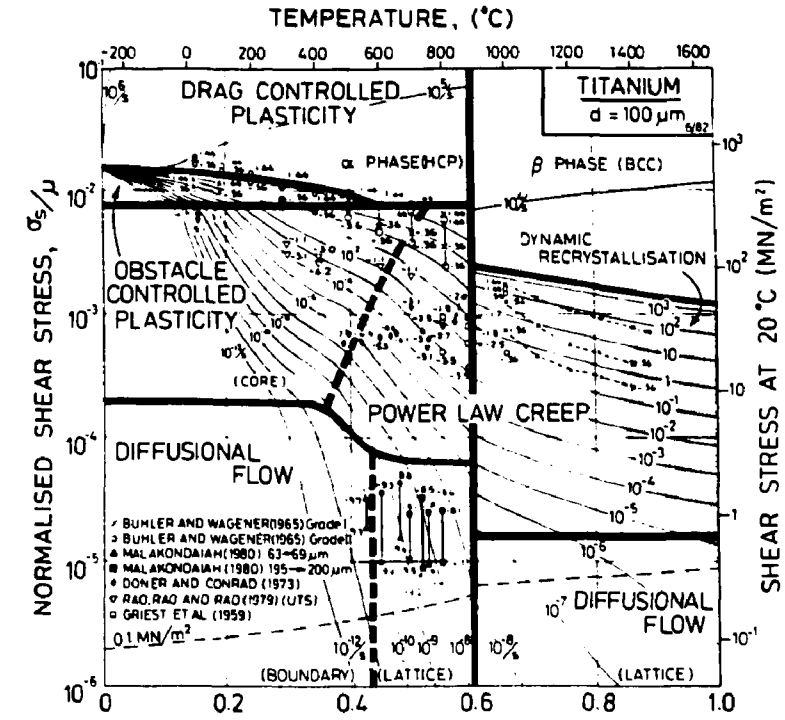

(a)

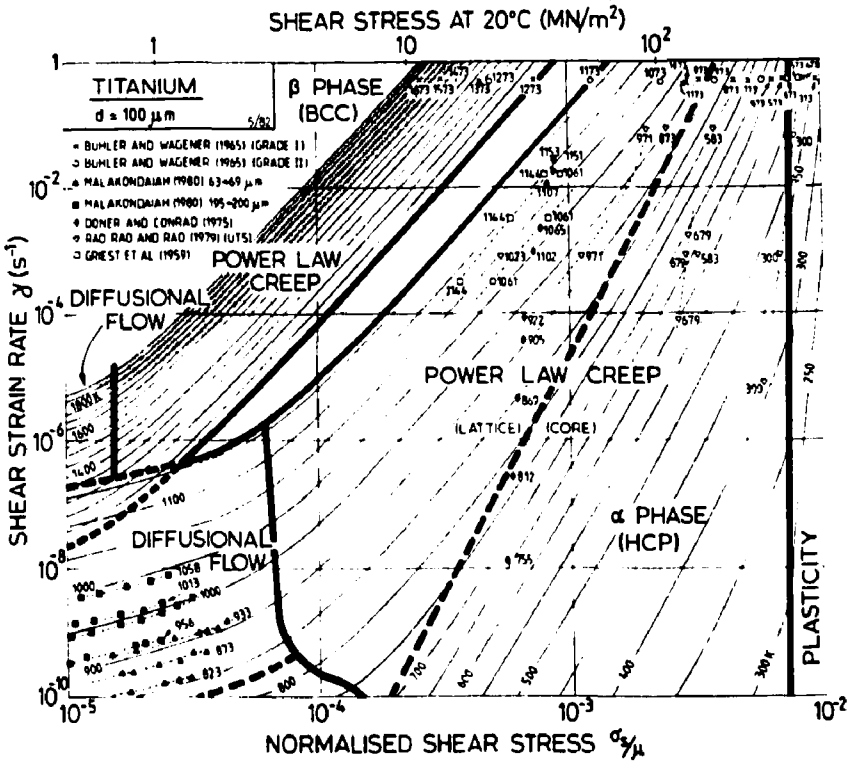

(b)

FIGURE 29: Deformation Mechanism Map for Titanium with a Grain Size of 100 μm. Diagram (a) is the normal form of the Map, corresponding to Figure 28. In this stress/temperature plane, contours of constant strain rate are plotted, and the experimental data indicated by various symbols. An alternative (but equivalent) form is shown in (b), using the strain-rate/stress plane, where the contour lines represent equal temperature conditions. Note the symbol μ is used for the elastic shear modulus, rather than G in the text. (Sargent and Ashby 1982).

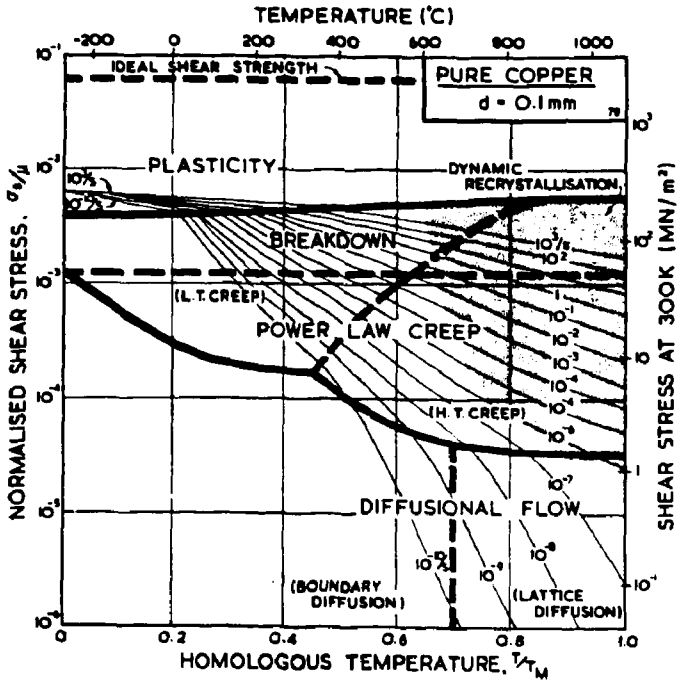

(a)

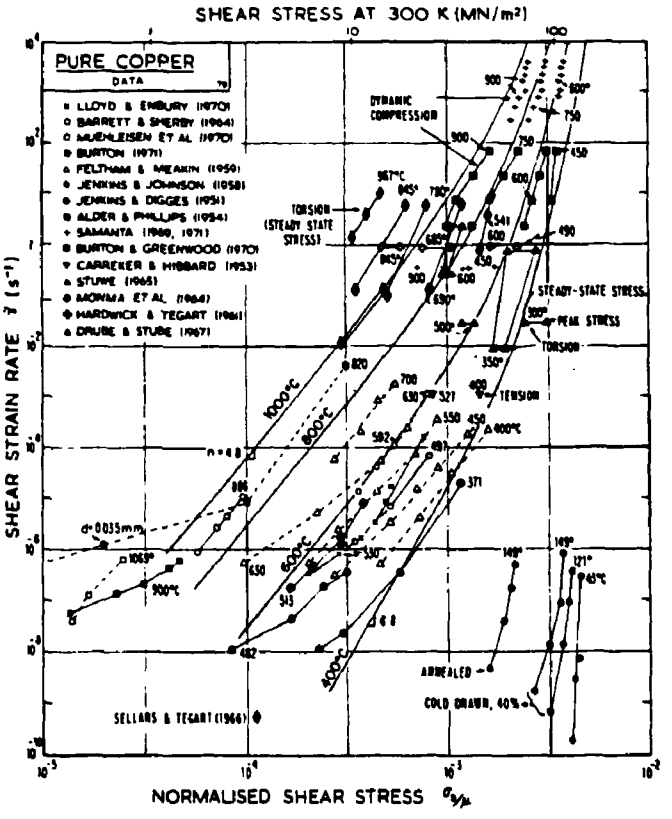

(c)

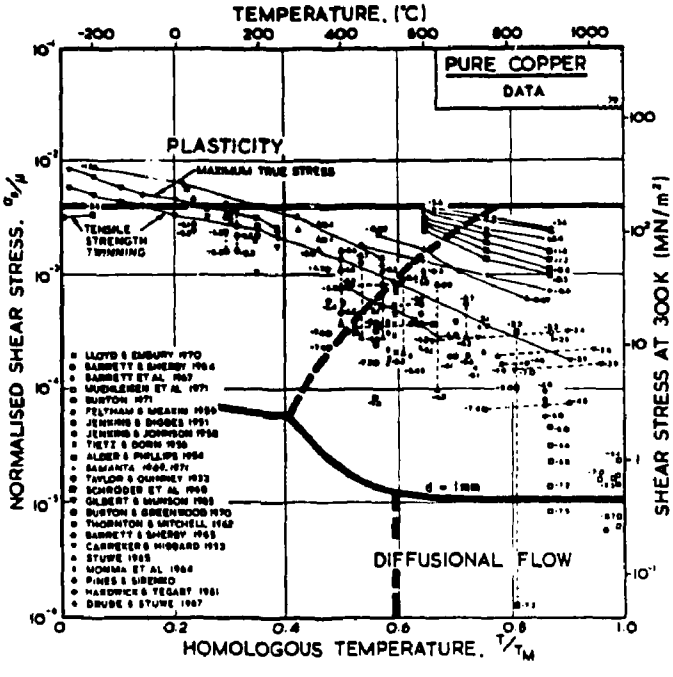

(b)

FIGURE 30: Deformation Mechanism Map for Copper with a Grain Size of 0.1 mm, Shown in (a). Diagram (b) shows the experimental data superimposed on the Map, while (c) shows the data in the strain-rate/stress plane. Note the symbol μ is used for the elastic shear modulus, rather than G in the text. (Frost and Ashby 1982).

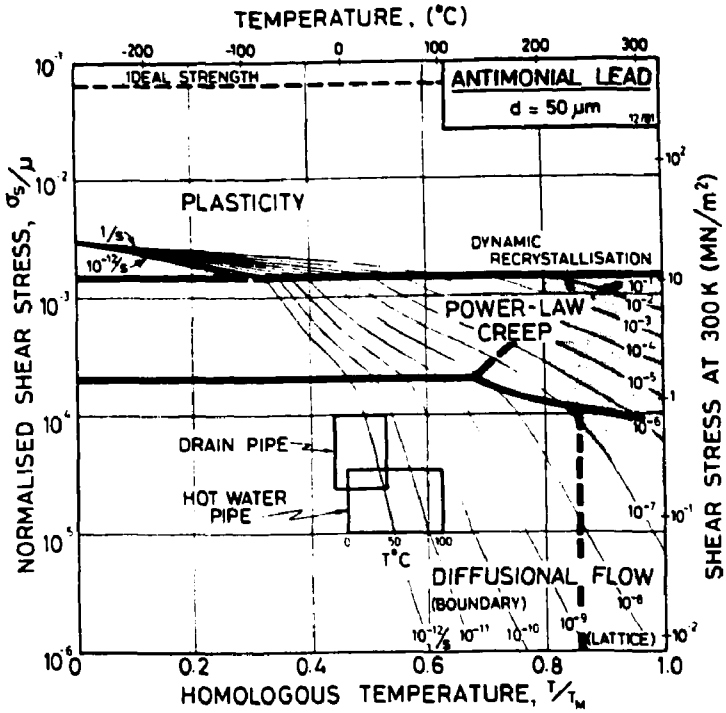

(a)

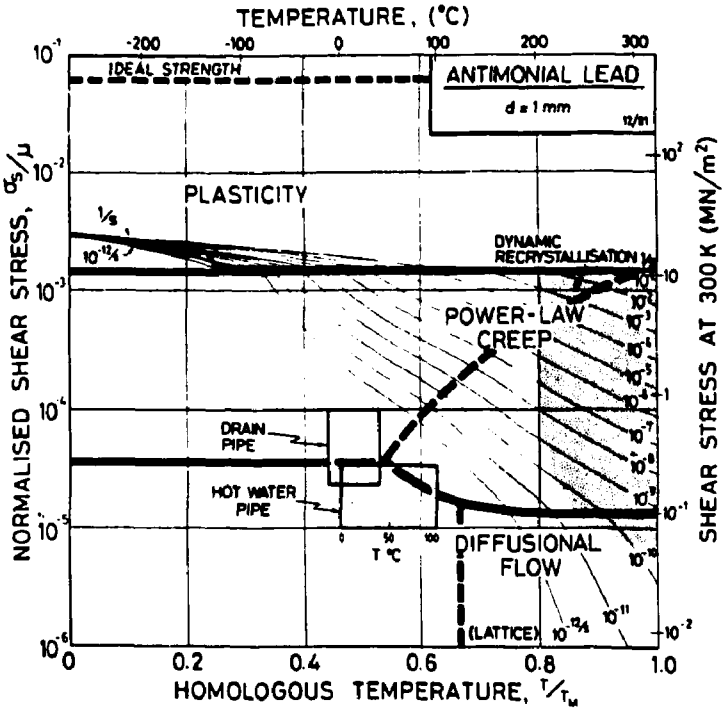

(b)

FIGURE 31: Deformation Mechanism Map for Antimonial Lead with a Grain Size of 50 μm (a) and 1 mm (b). On each of these Maps is plotted the stress/temperature range of the water pipes. Note the symbol μ is used for the elastic shear modulus, rather than G in the text. (Frost and Ashby 1982).

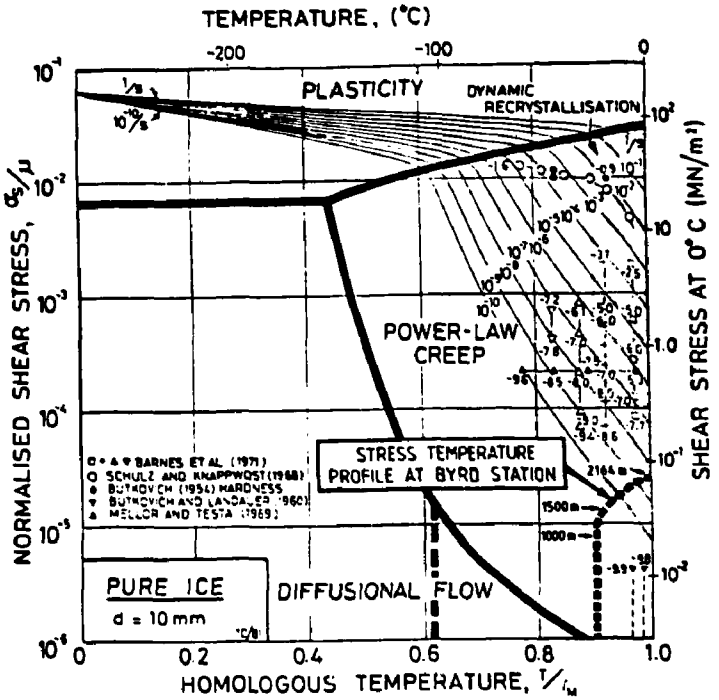

FIGURE 32: Deformation Mechanism Map for Ice with a Grain Size of 10 mm. The stress-temperature profile of the Antarctic ice derived from boreholes at the Byrd Station is also plotted, showing deformation in this region is mainly by power-law creep. Note the symbol μ is used for the elastic shear modulus, rather than G in the text. (Frost and Ashby 1982).

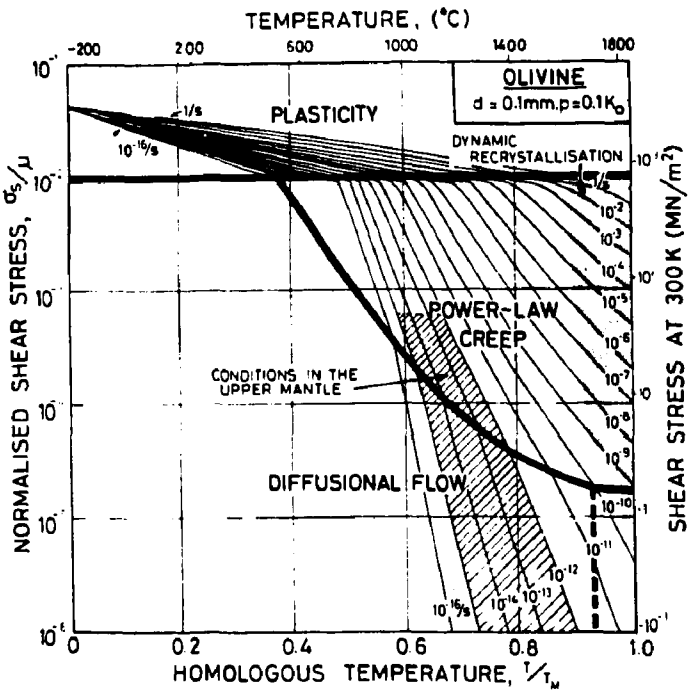

FIGURE 33: Deformation Mechanism Map for Olivine (Grain Size of 0.1 mm) Relevant to a Hydrostatic Pressure of 1.3×10^4 MPa, Corresponding to a Depth of 380 km. The range of conditions in the earth's upper mantle is shown. Note the symbol μ is used for the elastic shear modulus, rather than G in the text. (Frost and Ashby 1982).

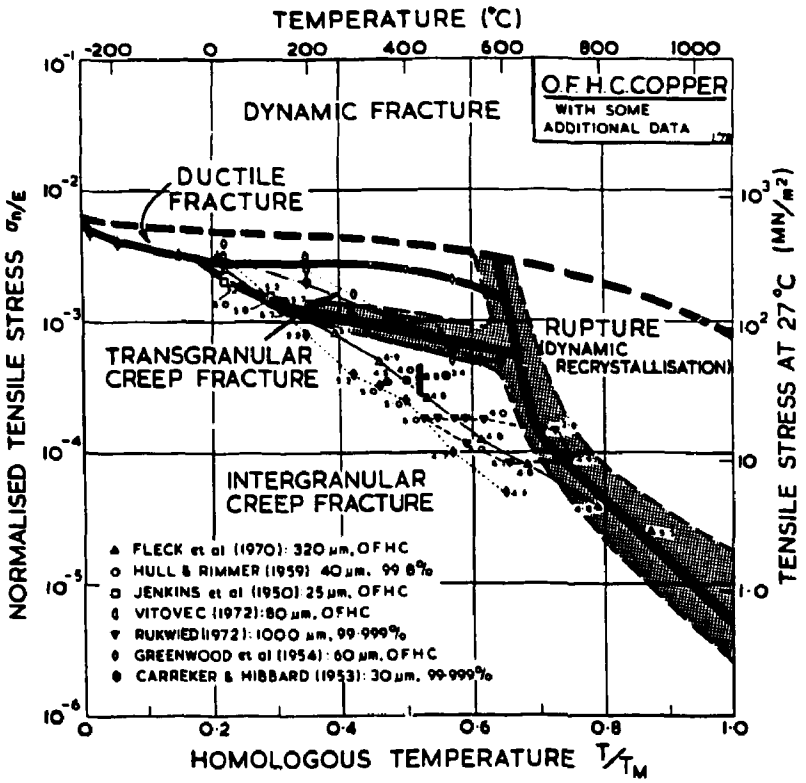

FIGURE 34: Fracture Mechanism Map for OFHC Copper, Based on Empirical Metallographic Evidence from the Experimental Data Indicated (Ashby et al. 1979)

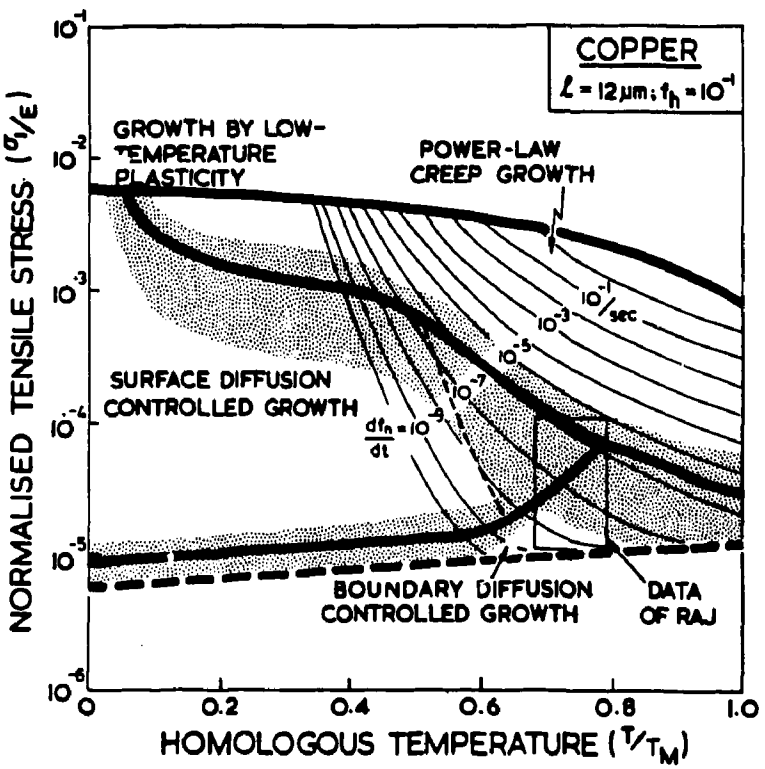

FIGURE 35: Fracture Mechanism Map for Copper, Based on Intergranular Creep Cavity Growth Mechanisms Where f_h is the Fractional Area of Cavities, Spaced 2 ℓ Apart (Cocks and Ashby 1982)

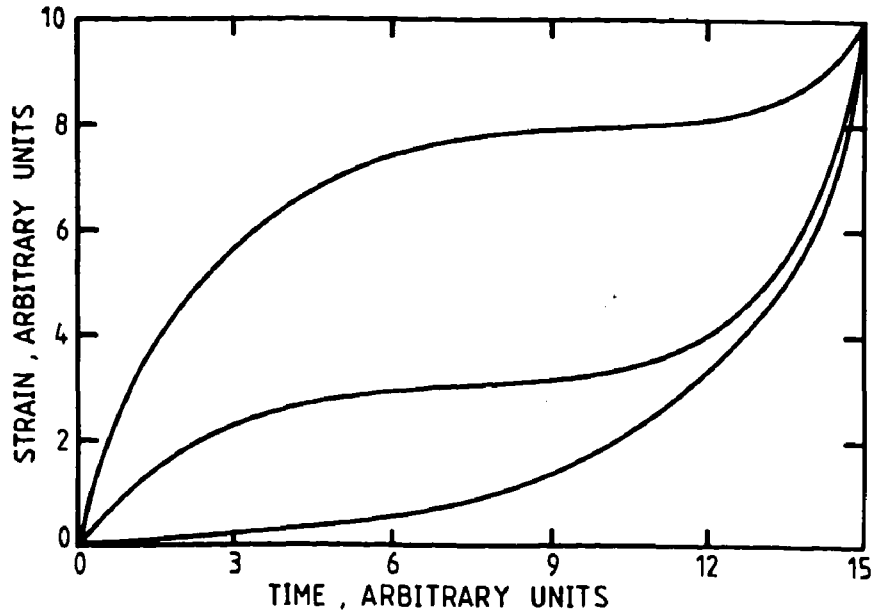

FIGURE 36: Schematic Creep Curves of Different Shape but Characterized by the Same Steady-State Creep Rate, Time and Strain to Fracture (Evans and Wilshire 1993)

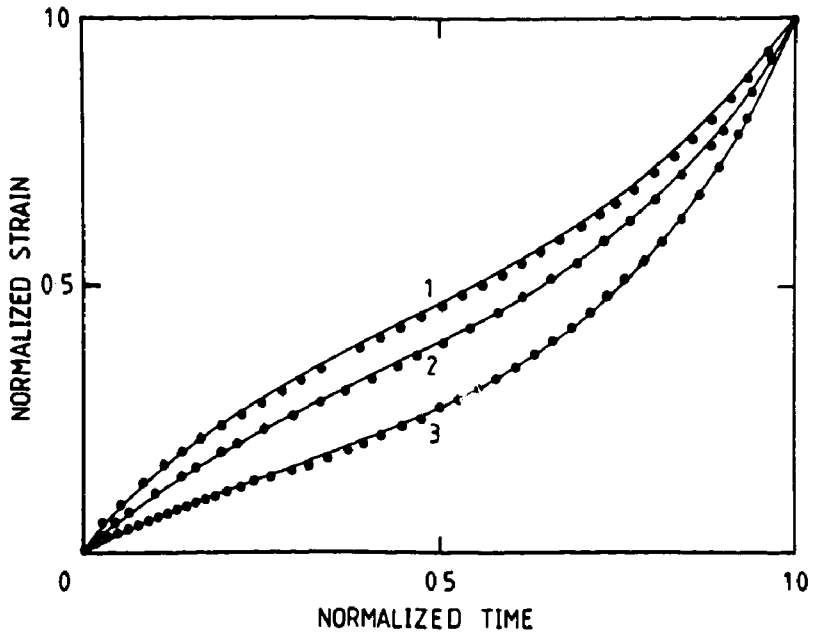

FIGURE 37: Constant-Stress Creep Curves for Copper Plotted as Normalized Strain ($\varepsilon/\varepsilon_f$) Against Normalized Time (t/t_f) for Stresses of (1) 48, (2) 34 and (3) 14 MPa at 455°C. The points are experimental data, while the lines are constructed using the θ Projection Concept (Evans and Wilshire 1993).

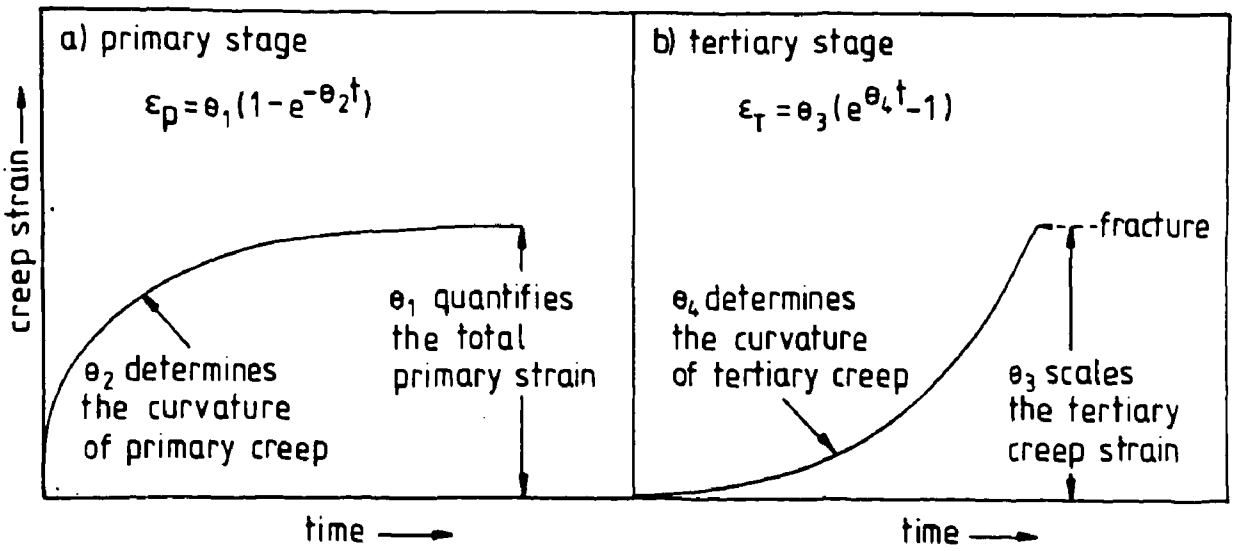

FIGURE 38: This Illustrates that the θ Projection Concept is Based on the Principle that Normal Creep Curves Comprise a Decaying Primary Component (ε_p) and an Accelerating Tertiary Concept (ε_t). The parameters θ_1 and θ_3 scale the primary and tertiary stages with respect to strain. The terms θ_2 and θ_4 are then rate parameters that describe the curvatures of the primary and tertiary stages, respectively (Evans and Wilshire 1993).

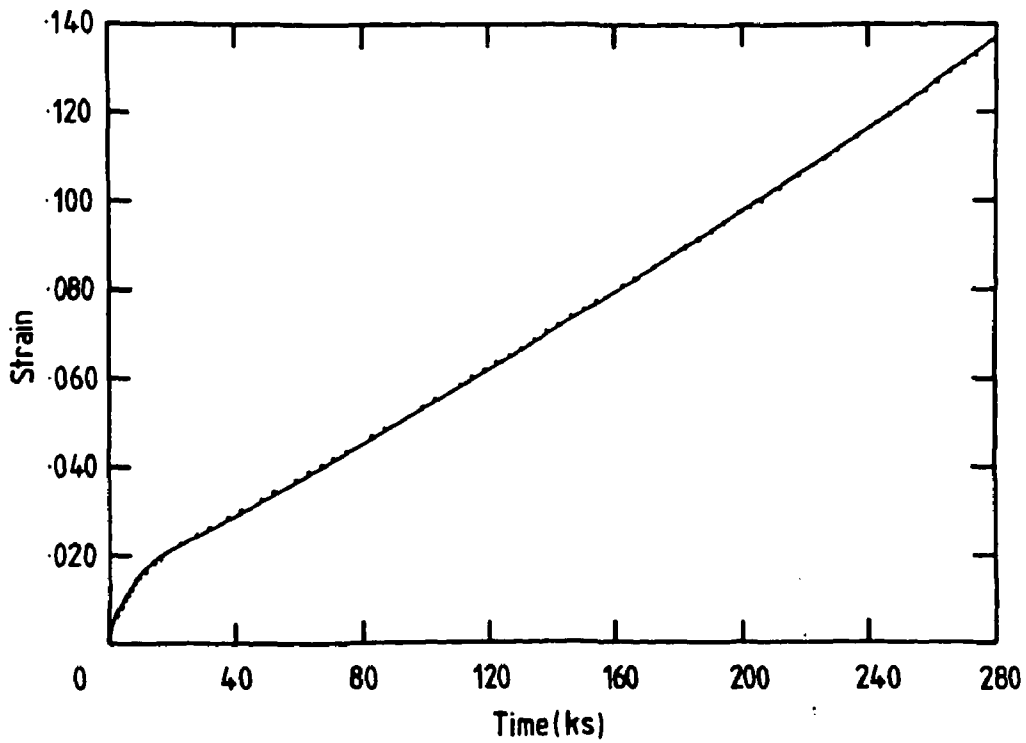

FIGURE 39: Actual (Data Points) and Predicted (θ Projection) Creep Curve for 0.5Cr0.5Mo0.25V Steel Tested at 310 MPa and 530°C (Evans et al. 1984)

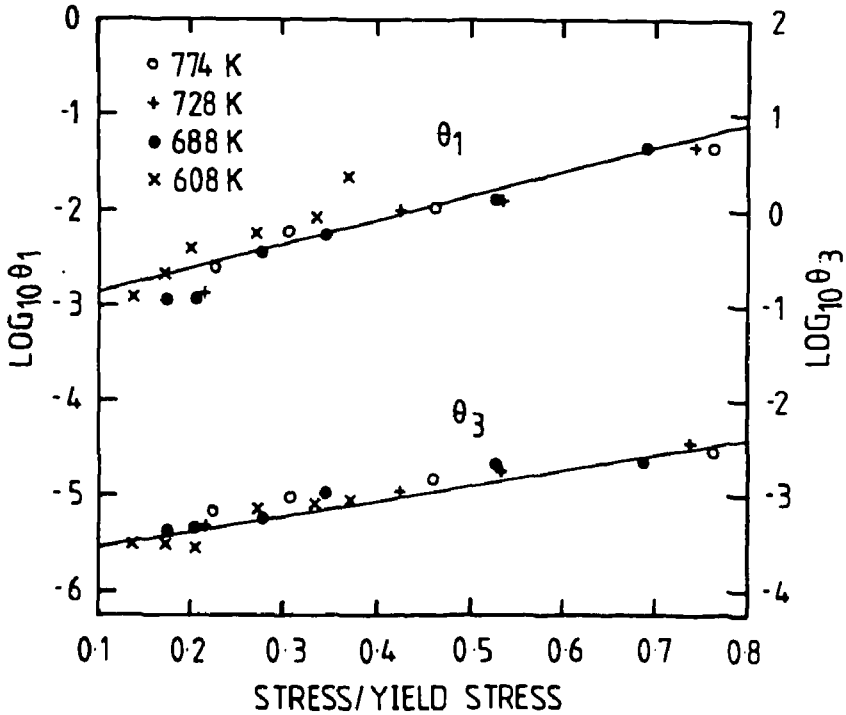

(a)

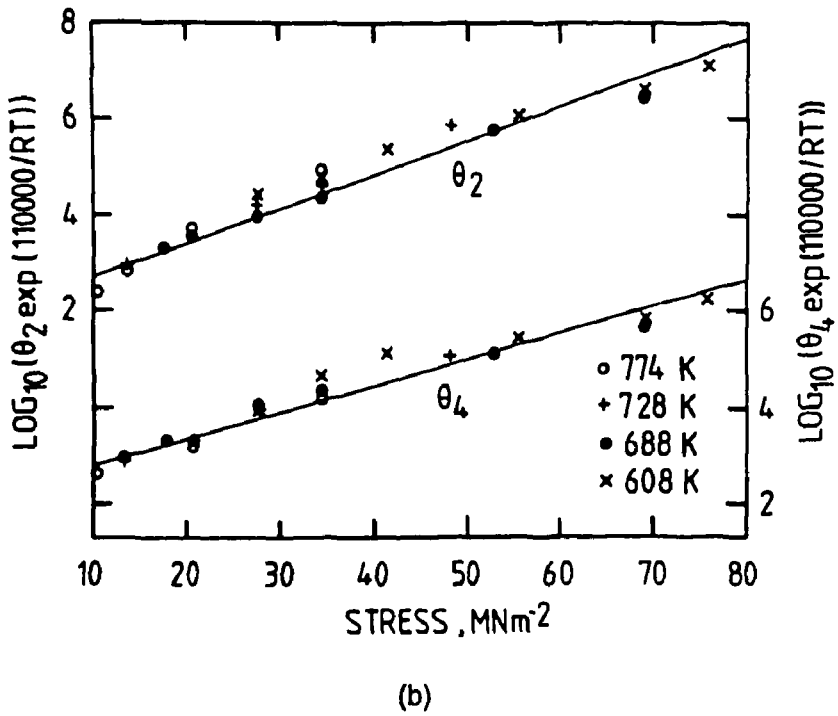

(b)

FIGURE 40: The Stress and Temperature Dependencies of (a) the Strain-Like Parameters θ_1 and θ_3, and (b) the Rate Constants θ_2 and θ_4 for Copper (Evans and Wilshire 1983)

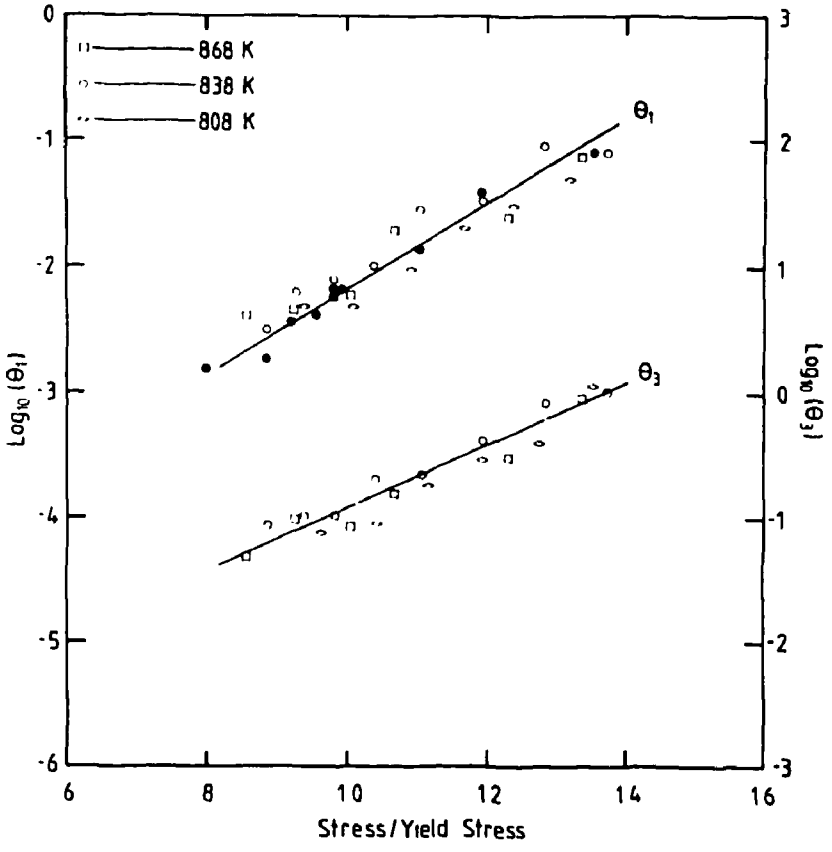

(a)

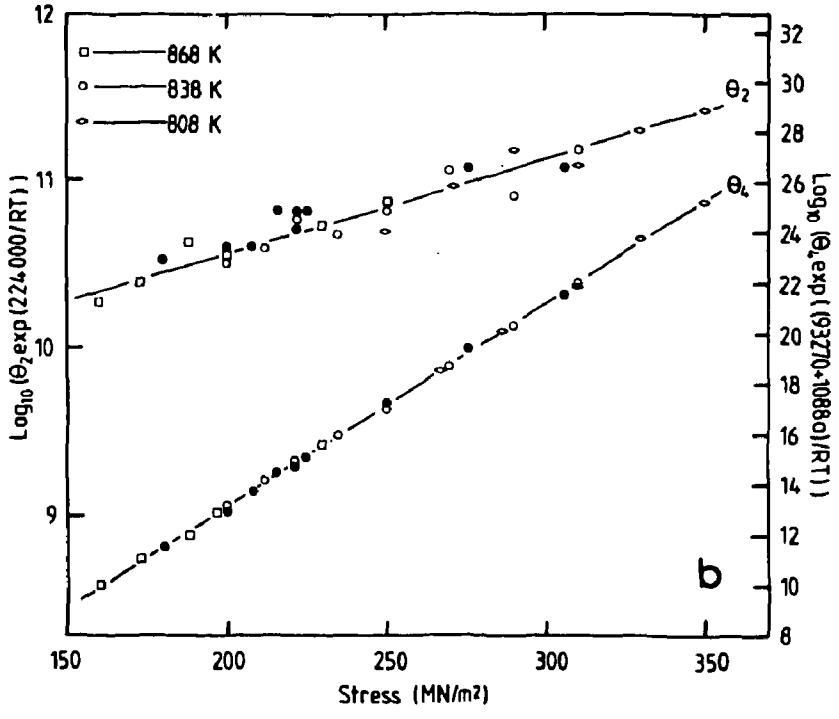

(b)

FIGURE 41: The Stress and Temperature Dependencies of (a) θ_1 and θ_2, and (b) θ_3 and θ_4 for 0.5Cr-0.5Mo-0.25V Steel (Evans and Wilshire 1993)

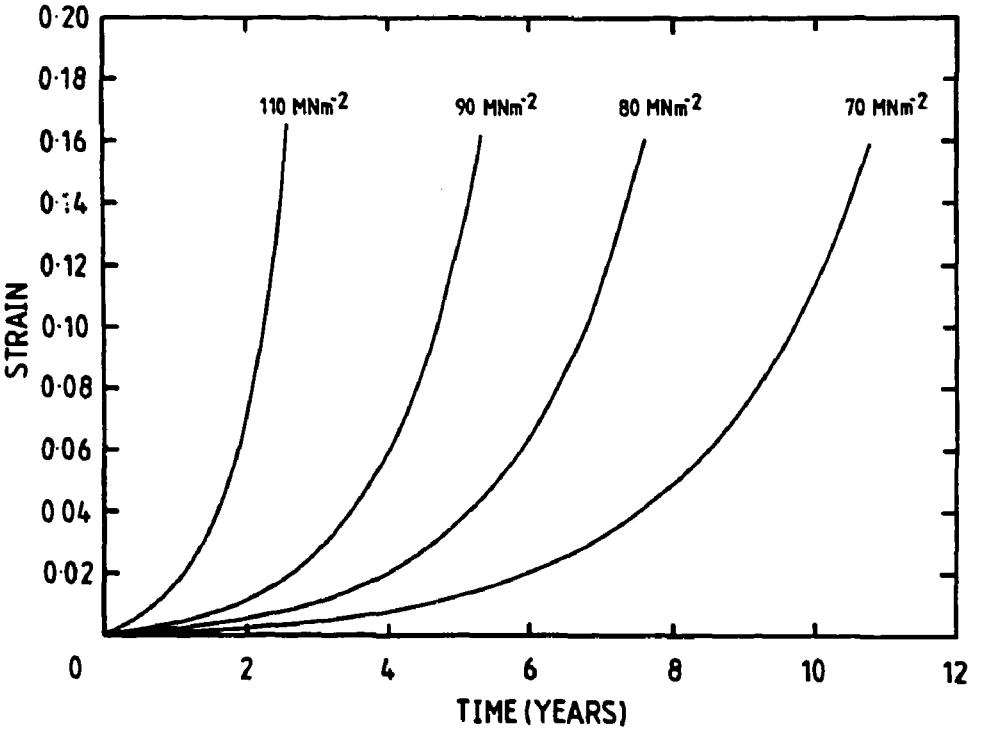

FIGURE 42: Long-Term Creep Curves Calculated from the θ Data (Figure 41) for 0.5Cr0.5Mo0.25V Steel at 565°C (Evans and Wilshire 1985)

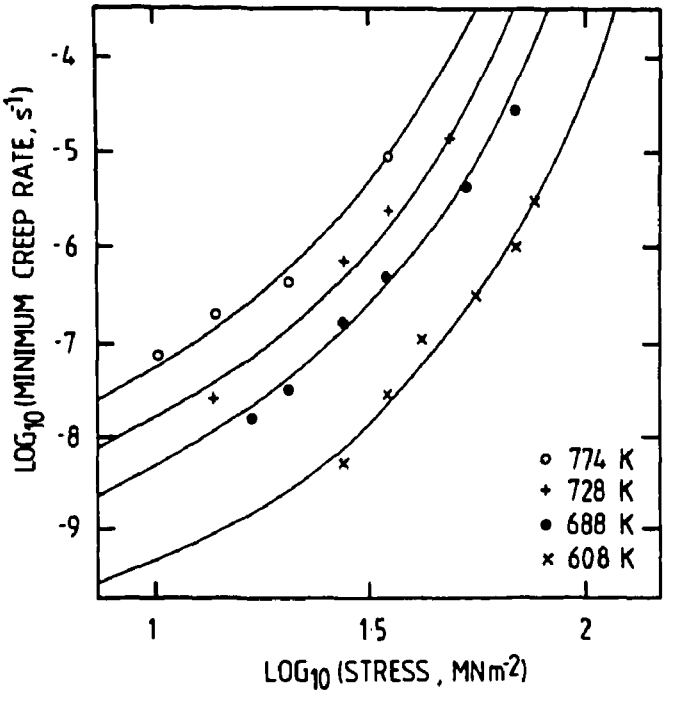

FIGURE 43: Stress Dependence of the Minimum Creep Rate for Polycrystalline Copper. The lines predicted from the stress dependence of the θ parameters (Figure 40) are compared with experimental data at various temperatures (Evans and Wilshire 1993).

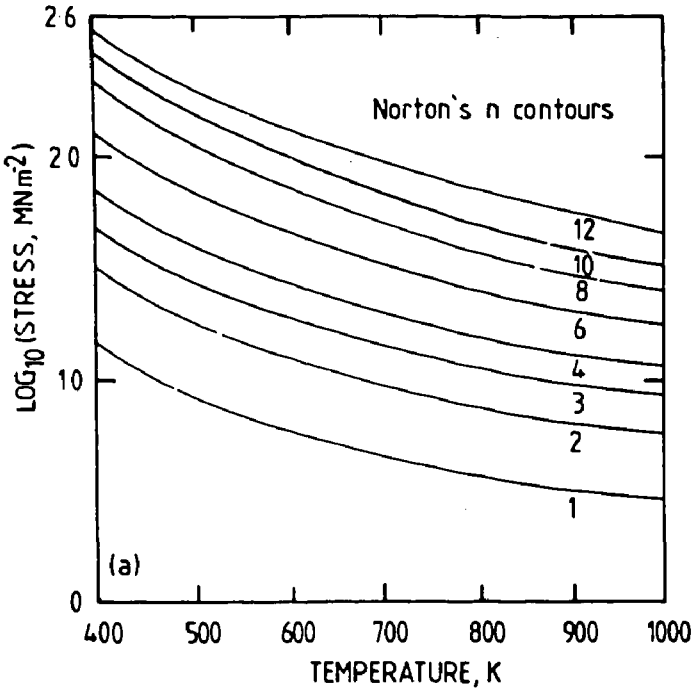

(a)

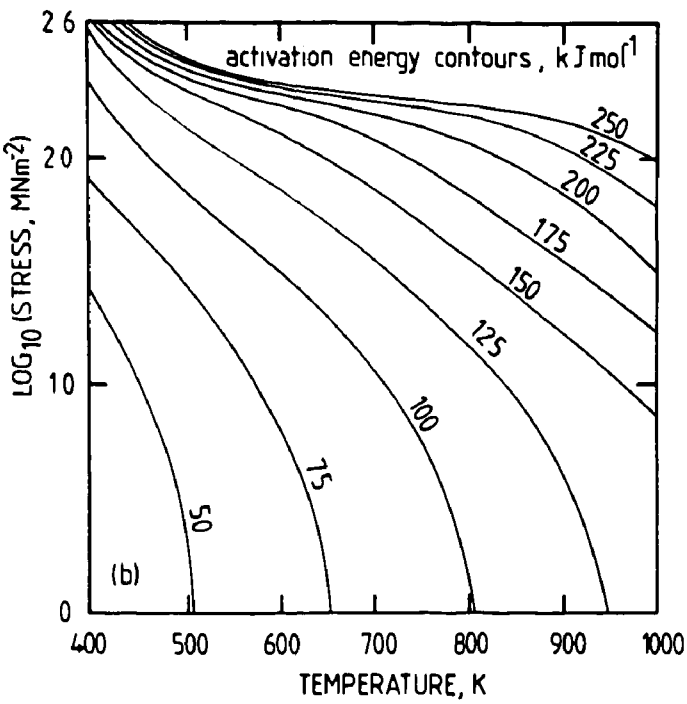

(b)

FIGURE 44: Variation of (a) the Stress Exponent, n, and (b) the Activation Energy for Creep, Q_c, of Polycrystalline Copper. The plots were derived from minimum creep rates calculated from a knowledge of the stress and temperature dependencies of the θ parameters shown in Figure 40 (Evans and Wilshire 1993).

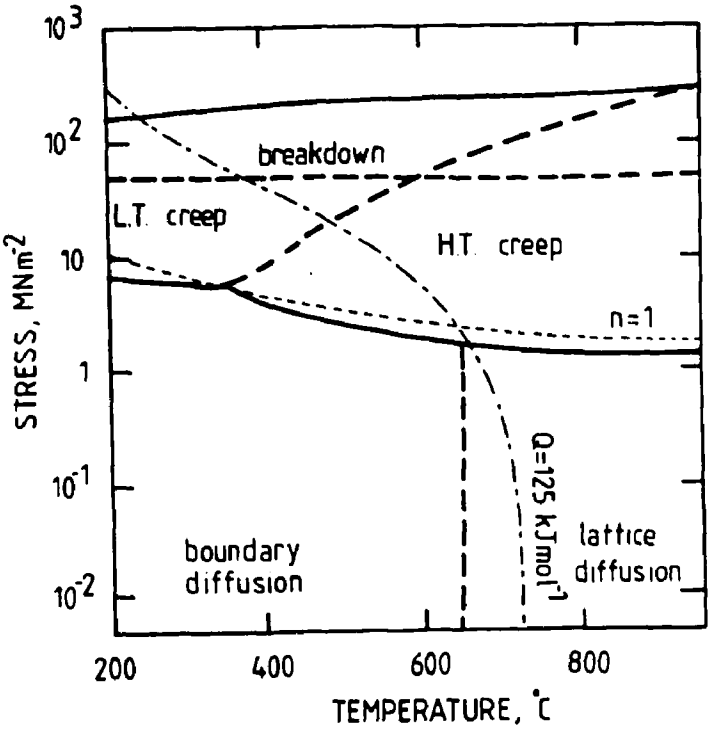

FIGURE 45: Deformation Mechanism Map for Polycrystalline Copper (see Figure 30) with Lines of $n \approx 1$ and $Q_c = 110$ kJ mol^{-1} Calculated from the Stress and Temperature Dependencies of the θ Parameters (Figure 40). LT and HT indicate the regimes where dislocation creep is controlled by core diffusion and lattice diffusion at low and high temperatures, respectively (Evans and Wilshire 1993).

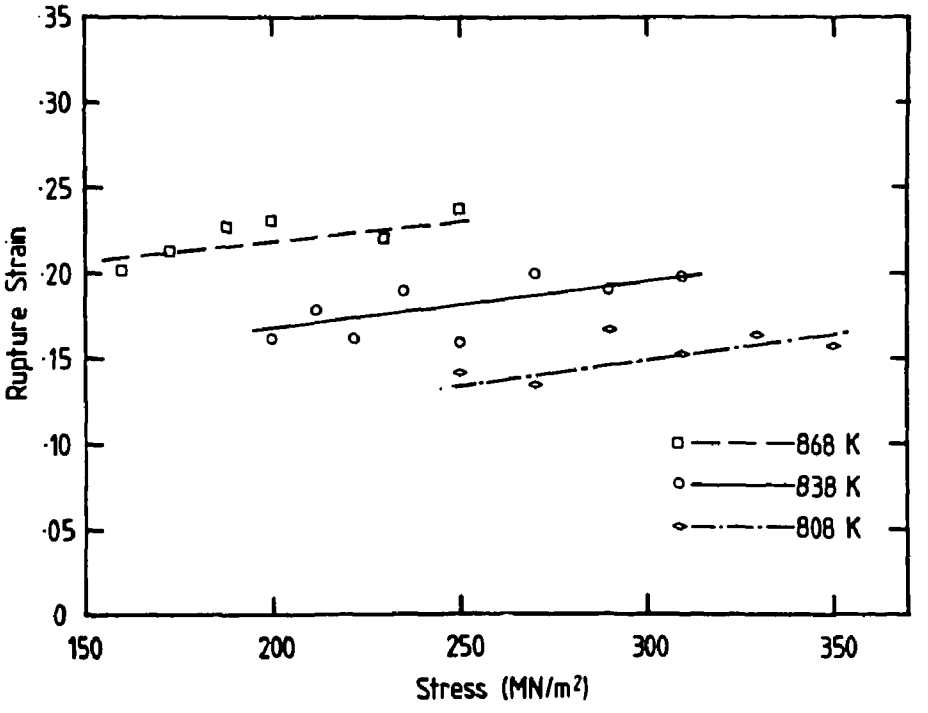

FIGURE 46: The Variation of the Creep Ductility, ε_f, with Stress and Temperature for 0.5Cr0.5Mo0.25V Steel (Evans and Wilshire 1993)

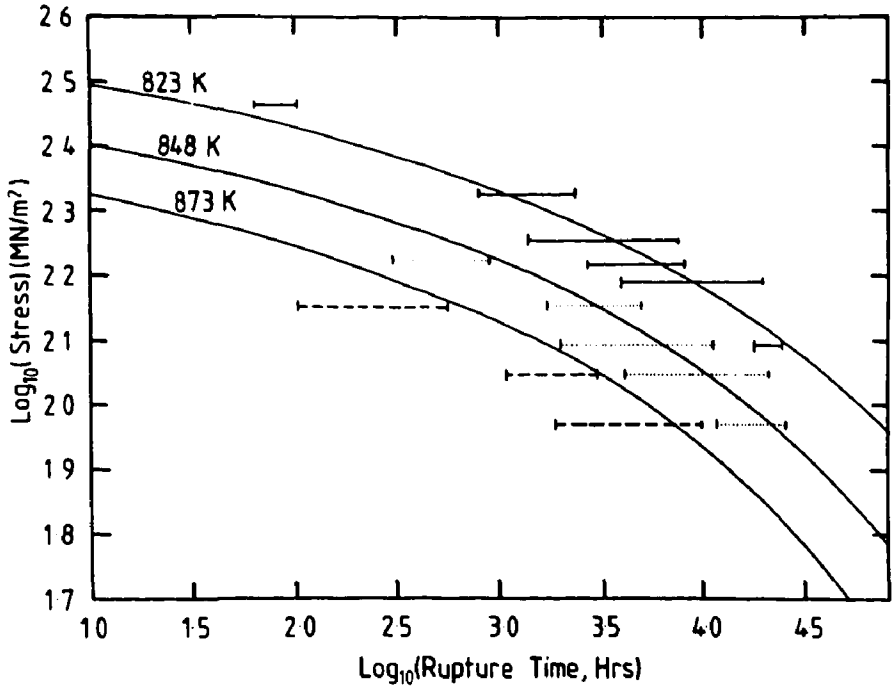

FIGURE 47: Predicted Stress-Rupture Curves for 0.5Cr-0.5Mo-0.25V Steel. The error bars represent the scatter for various stress/temperature conditions in multi-laboratory long-term stress-rupture data (Evans and Wilshire 1993).

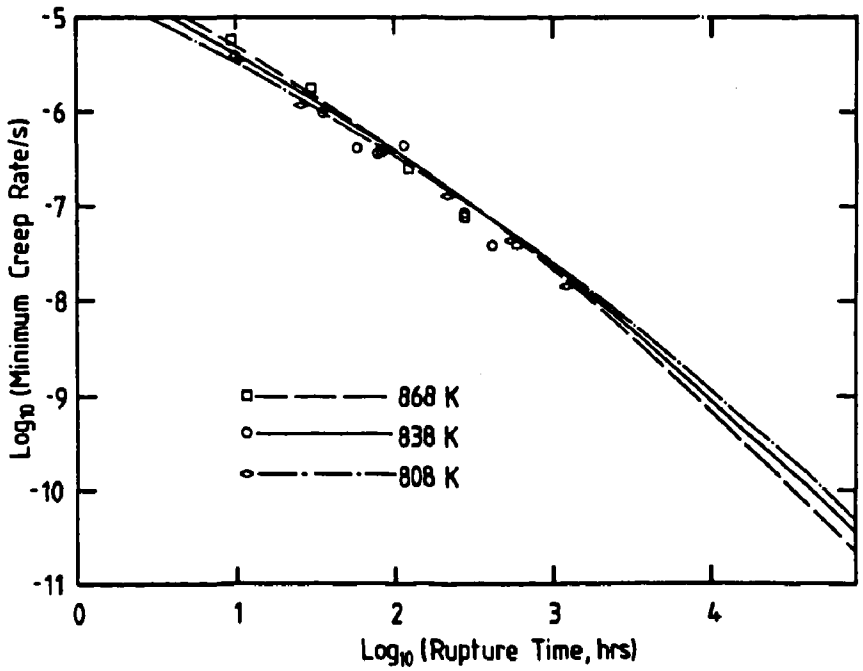

FIGURE 48: The Relationship Between the Minimum Creep Rate- and the Rupture Life of 0.5Cr0.5Mo0.25V Steel Calculated from the θ Data (lines), Together with the Available Experimental Points (Evans and Wilshire 1985)

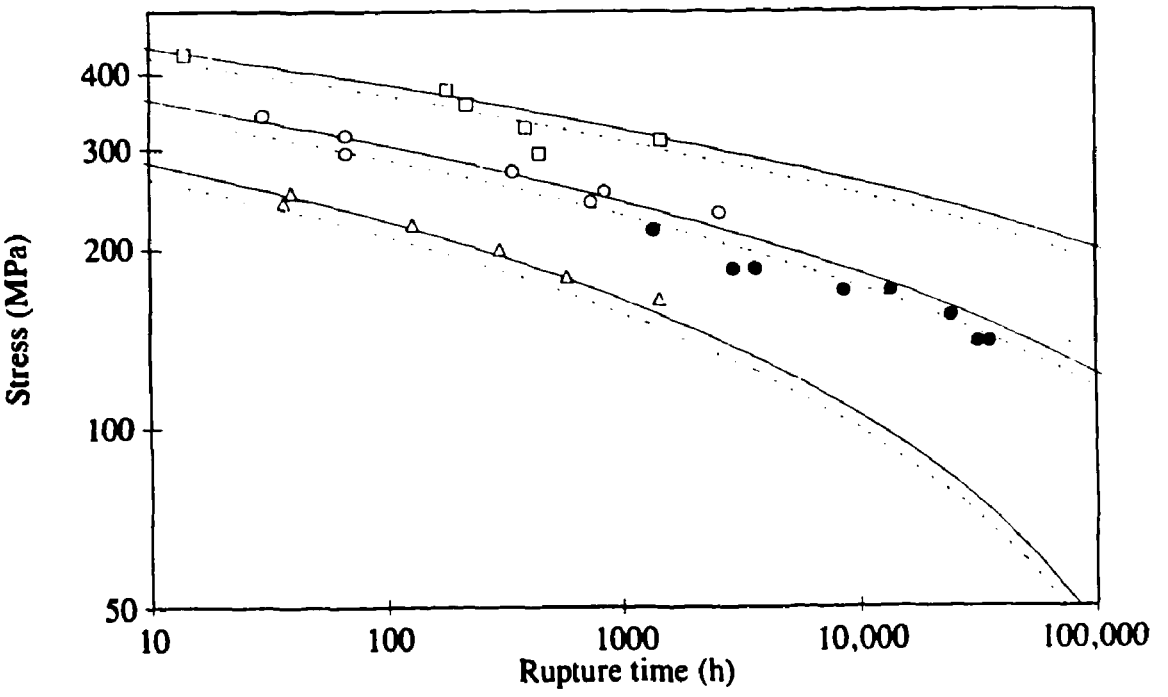

FIGURE 49: Predicted (θ Parameter) log σ/log t_r Plots for Constant-Stress (Solid Lines) and Constant-Load (Broken Lines) Conditions, Compared with Measured t_r Values Obtained from Short-Term Constant-Stress Tests at 510, 550 and 590°C (Open Symbols) and Long-Term Constant-Load Tests (Full Symbols) at 550°C, for 1CrMoV Steel (Wilshire and Evans 1994)

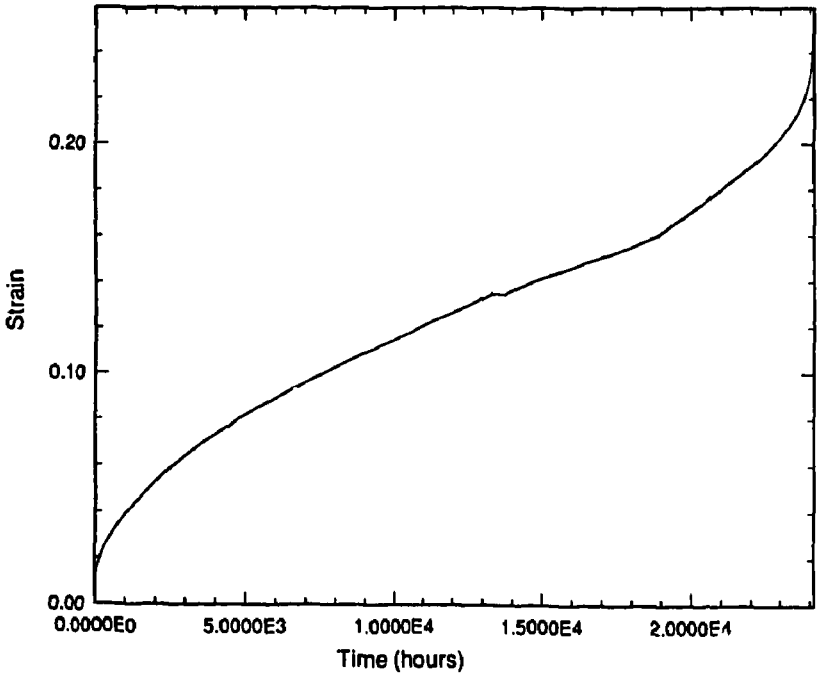

FIGURE 50: Creep Curve for ASTM Grade 2 Titanium, Tested at 100°C and 187 MPa

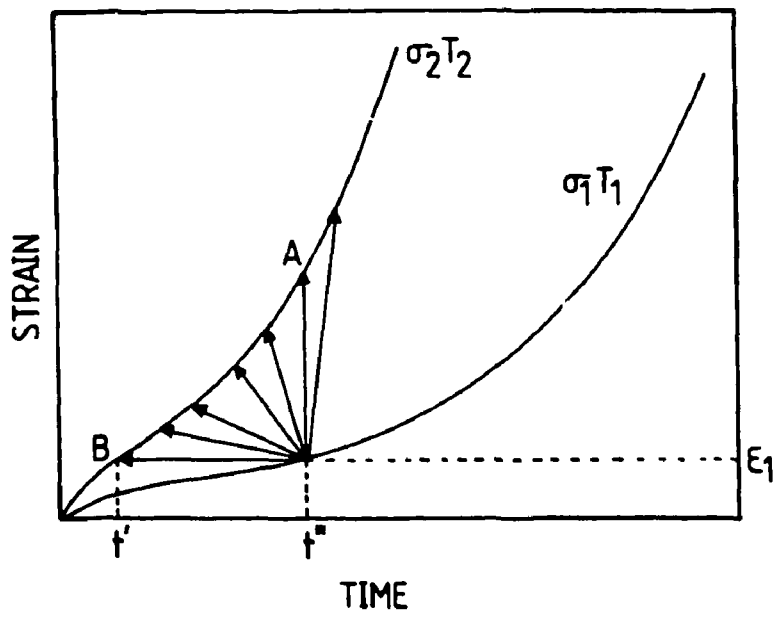

FIGURE 51: Schematic Diagram Showing Alternative Paths when Prevailing Conditions Change from $\sigma_1 T_1$ to $\sigma_2 T_2$ (Evans and Wilshire 1987b)

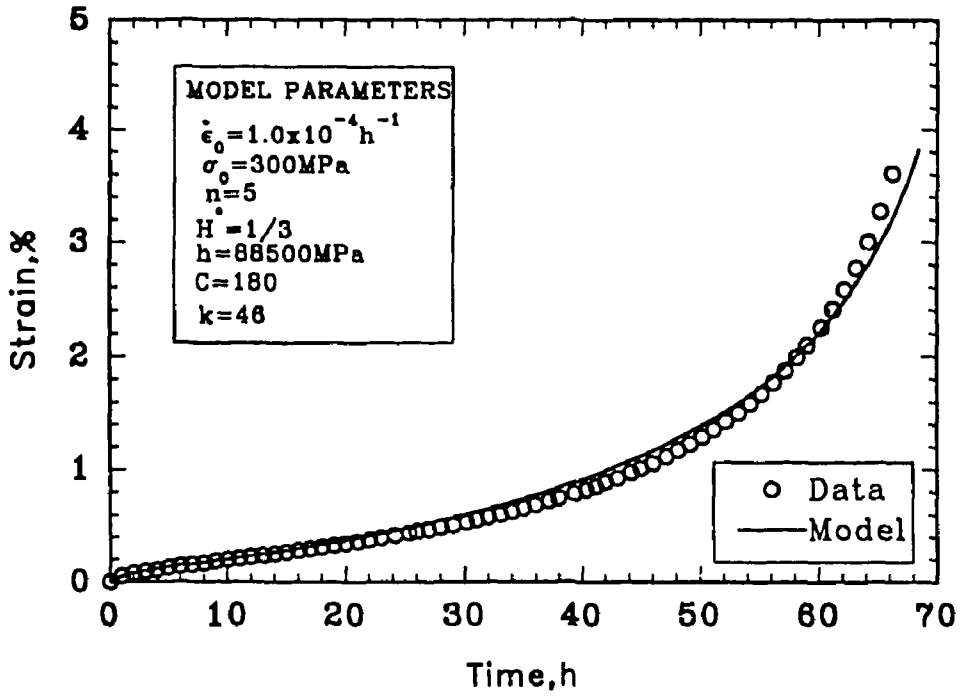

FIGURE 52: Creep Curve for Nimonic 101 Alloy (Osgerby and Dyson 1993)

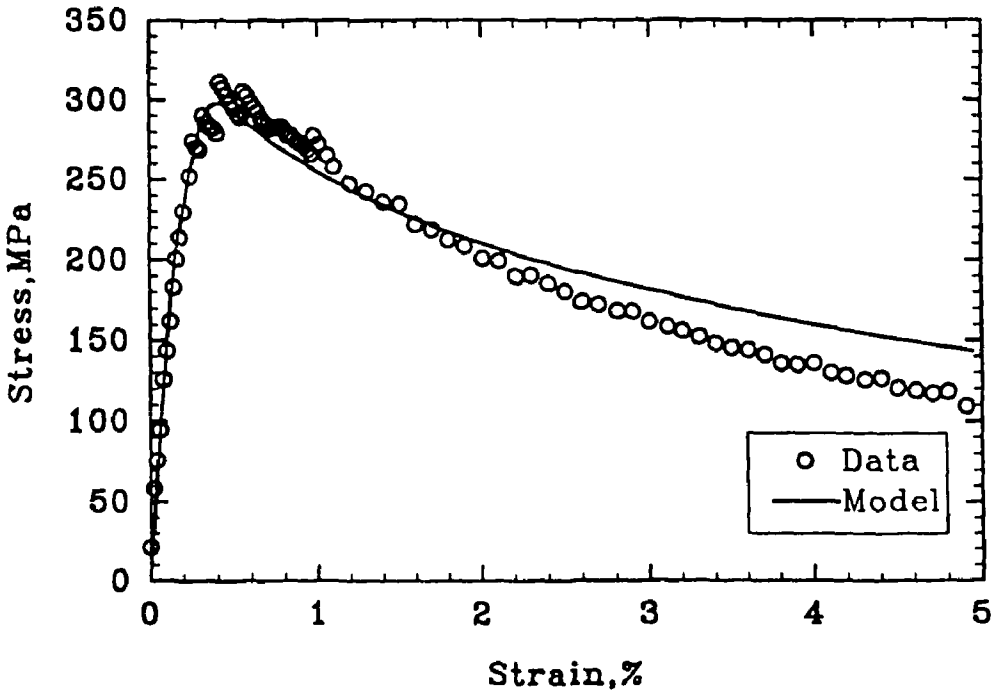

FIGURE 53: Stress-Strain Curve (Constant-Strain Rate of 1.4 x 10^{-4} h^{-1}) for Nimonic 101 Alloy, Predicted from Creep Data and Compared with Experiment (Osgerby and Dyson 1993)

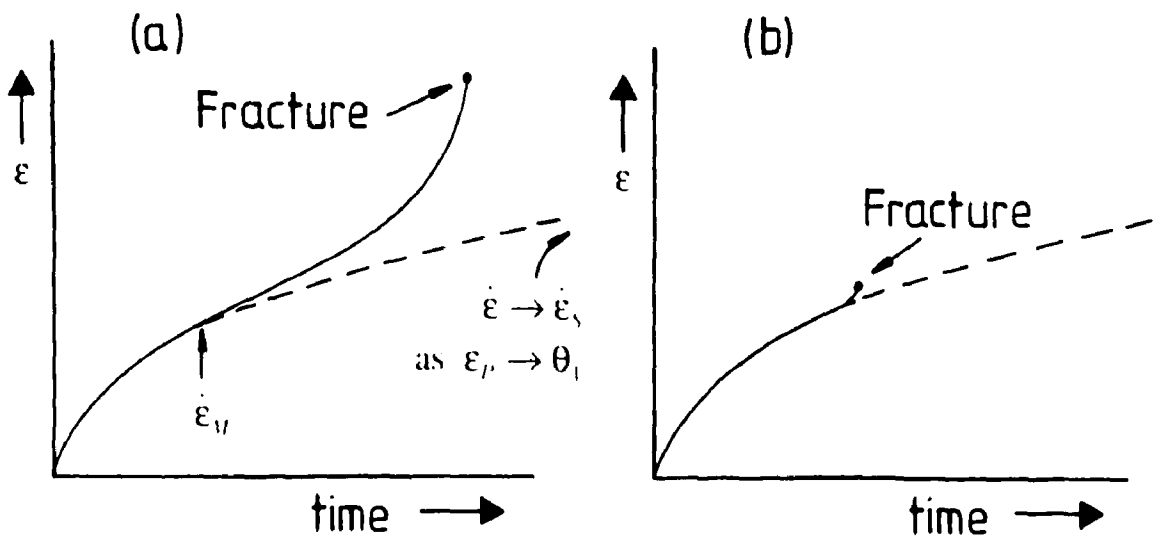

FIGURE 54: Schematic Representation of (a) Extensive Tertiary Stage for Creep-Ductile Materials and (b) Contracted Tertiary Stage for Creep-Brittle Materials (Evans and Wilshire 1993)

Cat. No. / N° de cat.: CC2-11249E
ISBN 0-660-16281-4
ISSN 0067-0367

To identify individual documents in the series, we have assigned an AECL- number to each. Please refer to the AECL- number when requesting additional copies of this document from

Scientific Document Distribution Office (SDDO)
AECL
Chalk River, Ontario
Canada K0J 1J0

Fax: (613) 584-1745 Tel.: (613) 584-3311
ext. 4623

Price: C

Pour identifier les rapports individuels faisant partie de cette série, nous avons affecté un numéro AECL- à chacun d'eux. Veuillez indiquer le numéro AECL- lorsque vous demandez d'autres exemplaires de ce rapport au

Service de Distribution des documents officiels (SDDO)
EACL
Chalk River (Ontario)
Canada K0J 1J0

Fax: (613) 584-1745 Tél.: (613) 584-3311
poste 4623

Prix: C